INVESTIGATION OF PLATINIUM-BASED NANOPARTICLES ON BORON-DOPED DIAMOND SUBSTRATE FOR APPLICATIONS IN ELECTROCATALYSIS

PAR

Guillaume SINÉ

DEA SMPM, Université de Bordeaux 1, France
et de nationalité française

EPFL

ÉCOLE POLYTECHNIQUE
FÉDÉRALE DE LAUSANNE

Suisse
2006

Remerciements

Je tiens tout d'abord à remercier le Professeur Christos Comninellis pour m'avoir accueilli au sein de son groupe et m'avoir encadré tout au long de la thèse. Son enthousiasme et sa rigueur scientifique m'ont été d'un grand secours pour mener ce travail à bien. Je remercie également les membres du jury, les Prof. Bleuler, De Battisti et Kuhn d'avoir accepté d'apprécier la qualité de ce travail.

Je remercie également toutes les personnes qui ont contribué à l'accomplissement de la thèse ; Donya et David, que j'ai pu encadrer lors de leurs travaux dans notre groupe et dont certains des résultats figurent dans ce manuscrit, et le Dr. György Fóti pour m'avoir aidé à établir et développer le modèle théorique, ainsi que le Prof. Buffat, Lassiné Ouattara, Nicholas Xanthopoulos, Igor Stolichnov, et Kurt Schenk . L'aide de José Solla-Gullón, du groupe du Prof. Aldaz à l'Université d'Alicante, a été déterminante et appréciée à sa juste valeur.

Un grand merci aussi et aux membres du groupe pour la bonne ambiance et les moments de détente pendant et en dehors du travail. Je pense plus particulièrement à Alain, Arnaud et Bahaa pour leur amitié et les bons moments passés ensemble. Je n'oublie pas Aga, Gabriele, Erika, Alexandre, Mériadec et les « plus anciens », Ivan, Ilaria, Béatrice, Elena, et Justyna. Un petit mot aussi aux amis et connaissances : Eric et Sandy, Flo, Mariam et tous les autres que j'ai oublié de citer mais qui je l'espère se reconnaîtront.

Je remercie aussi ma famille et mes parents pour leur soutien tout au long de mes études.

Enfin, merci pour tout Carole.

Table of contents

Abstract

The search of new energy sources has motivated during the last few years numerous research projects due to environmental, economical and political reasons. One of the main subjects of these works is the development of fuel cells. Within this framework the Direct Alcohol Fuel Cell (DAFC), mainly fed with methanol or ethanol, has received great attention. However one of the major limitations of the DAFC is the electrocatalysis of fuel oxidation; the electrocatalyst (dispersed Pt-based particles) is indeed readily poisoned by adsorbed intermediates, hence decreasing the fuel cell efficiency. Consequently the electrocatalysis of methanol and ethanol oxidation on different types of Pt-based nanoparticles, deposited on synthetic boron-doped diamond (BDD) thin film, has been studied during this thesis. This substrate has been chosen due to its outstanding properties of chemical inertness, illustrated by a very low capacitive current.

In the first part of this thesis, electrodeposited Pt particles on BDD have been studied. Electrodeposition of Pt particles has been carried out both on bare BDD and on diamond pre-modified with gold nanoparticles deposited via a thermal decomposition technique. In both cases it was established that Pt particles were electrodeposited following a progressive mechanism during which formation of new nuclei and growth of primary nuclei simultaneously occur. The electrocatalytic activity of electrodeposited particles was also studied, and it was shown that the presence of Au particles together with Pt particles does not influence markedly the electrocatalytic behaviour of the later ones. Preliminary calcination of the co-deposit results in a dramatic decrease of its electrocatalytic activity, presumably due to the formation of a core (Pt)-shell (Au) structure less capable of alcohols dehydrogenation. Finally electrodeposition of Pt on BDD leads to particles of diameter in the 150-700 nm domain with very large size distribution. Obviously such particles are not consistent with the definition of nanoparticles in catalysis and electrocatalysis.

In a second part of this work, Pt-based nanoparticles synthesized via the microemulsion method have been investigated once deposited on a diamond substrate. Attention has been mainly focused on Pt, Pt/Ru and Pt/Sn nanoparticles. All the synthesized nanoparticles are in the 2-5 nm size range with narrow size distribution. Moreover the compositions of bimetallic particles were very close to those expected. The electrocatalytic behaviour of bimetallic Pt-based nanoparticles toward both methanol and ethanol electrooxidation has been investigated. Bimetallic nanoparticles are more efficient than pure Pt, and it was shown that Pt/Ru nanoparticles were more indicated for electrocatalysis of methanol oxidation whereas

Abstract

Pt/Sn were more efficient in the case of electrocatalysis of ethanol oxidation. Both cooperative and electronic effects are involved in the enhancement of the electrocatalytic activity of bimetallic nanoparticles, and Pt-rich nanoparticles are the most efficient ones due to their superior alcohols adsorption properties. However the electronic effect is not of same nature in Pt/Ru than in Pt/Sn (Pt/Ru nanoparticles are alloyed ones, on the contrary of Pt/Sn), and this may explain the probable activation of the ethanol C-C bond scission by Pt/Sn electrocatalysts. Due to the different action modes of Pt/Ru and Pt/Sn electrocatalysts, a ternary Pt/Ru/Sn sample has also been synthesized by the microemulsion technique. This ternary electrocatalyst has exhibited very good activity toward methanol electrooxidation whereas that toward ethanol electrooxidation was significantly lower. It is believed that the electronic effect mainly occurs between Sn and Ru components of the sample, creating a new state of adsorbed oxygenated species that should be of higher mobility and reactivity than on bimetallic surfaces.

In addition, a model for methanol electrooxidation at Pt/M (M = Ru, Sn...) surfaces has been developed in order to generalise the obtained results. The concepts and theories of heterogeneous catalysis have been extended to the specific case of this electrochemical reaction involving adsorbed intermediates. The donor-acceptor theory of heterogeneous catalysis has been more particularly considered and adapted, and within this framework Pt has been considered as the acceptor whereas Sn was regarded as the donor. The development of this model has made the establishment of a relation between the measured current to the applied potential possible in a number of real limiting cases. Validity and limitations to the proposed model has in due course been discussed in view of the obtained results.

Version abrégée

La recherche de nouvelles sources d'énergie a motivé pendant les dernières années de nombreux projets de recherche en raison de problèmes environnementaux, économiques et politiques. Un des sujets principaux de ces travaux est le développement des piles à combustible. Dans ce cadre la pile à combustible directe à alcool (Direct Alcohol Fuel Cell, DAFC), principalement alimentée par le méthanol ou l'éthanol, a attiré la plus grande attention. Cependant une des principales limitations des DAFC est l'électrocatalyse de l'oxydation du combustible ; l'électrocatalyseur (particules dispersées à base de Pt) est en effet rapidement empoisonné par des intermédiaires adsorbées, diminuant par conséquent l'efficacité de la pile. En conséquence l'électrocatalyse de l'oxydation du méthanol et de l'éthanol sur différents types de nanoparticules à base de Pt, déposées sur des couches minces de diamant synthétique dopé au bore (Boron-Doped Diamond, BDD), a été étudiée pendant cette thèse. Ce substrat a été choisi en raison de ses propriétés d'inertie chimique, illustrées par un courant capacitif très faible.

Dans la première partie de cette thèse, des particules de Pt électrodeposées sur BDD ont été étudiées. Le dépôt électrochimique de particules de Pt a été effectué à la fois sur le diamant nu et préalablement modifié par des nanoparticles d'or déposées via une technique de décomposition thermique. Dans les deux cas il a été établi que les particules de Pt étaient électrodeposées suivant un mécanisme progressif pendant lequel la formation de nouveaux noyaux et la croissance de noyaux primaires se produisent simultanément. L'activité électrocatalytique des particules a été également étudiée, et il a été montré que la présence simultanée de particules d'Au et de particules de Pt n'influence pas de façon très nette le comportement électrocatalytique de ces dernières. La calcination préliminaire du co-dépôt a eu pour résultat de diminuer très fortement son activité électrocatalytique, vraisemblablement en raison de la formation d'une structure de type cœur (Pt)-coquille (Au) moins à même de procéder à l'adsorption dissociative des alcools. Enfin le dépôt électrolytique du Pt sur BDD donne des particules de diamètre de l'ordre de 150-700 nm avec une distribution de tailles très large. Évidemment de telles particules ne sont pas conformes à la définition d'une nanoparticule en catalyse ou électrocatalyse.

Dans une deuxième partie de ce travail, des nanoparticules à base de Pt synthétisées par l'intermédiaire de la méthode des microémulsions ont été étudiées après avoir été déposées sur un substrat de diamant. L'attention a été principalement

concentrée sur les nanoparticles de Pt, Pt/Ru et Pt/Sn. Toutes les nanoparticules synthétisées sont de l'ordre de 2 à 5 nm en diamètre avec une distribution de tailles étroite. Par ailleurs les compositions des particules bimétalliques étaient très proches de celles qui étaient attendues. Le comportement électrocatalytique des nanoparticules bimétalliques à base de Pt envers l'électrooxidation du méthanol et de l'éthanol a été étudié. Les nanoparticules bimétalliques sont plus efficaces que le Pt pur, et il a été montré que les nanoparticules de Pt/Ru sont davantage indiquées pour l'électrocatalyse de l'oxydation du méthanol tandis que celles de Pt/Sn sont plus efficaces dans le cas de l'électrocatalyse de l'oxydation de l'éthanol. Des effets coopératifs et électroniques sont impliqués dans l'augmentation de l'activité électrocatalytique des nanoparticules bimétalliques, et les particules riches en Pt sont les plus efficaces à température ambiante en raison de leurs propriétés d'adsorption supérieures. Toutefois l'effet électronique n'est pas de même nature dans Pt/Ru et dans Pt/Sn (les nanoparticules de Pt/Ru sont des alliages, au contraire de celles de Pt/Sn), et ceci peut expliquer l'activation probable de la scission de la liaison C-C de l'éthanol par les électrocatalyseurs de Pt/Sn. En raison des modes d'action différents des électrocatalyseurs de Pt/Ru et de Pt/Sn, un échantillon ternaire de Pt/Ru/Sn a été également synthétisé par la technique de microémulsion. Cet électrocatalyseur ternaire a montré une très bonne activité envers l'électrooxidation du méthanol tandis que son activité envers l'électrooxidation de l'éthanol était sensiblement inférieure. Il a été suggéré que l'effet électronique se produit principalement entre l'étain et le ruthénium, créant ainsi un nouvel état d'espèce oxygénée adsorbée pouvant être d'une mobilité et d'une réactivité plus élevées que sur les surfaces bimétalliques.

En outre, un modèle pour l'électrooxidation du méthanol sur des surfaces de Pt/M (M = Ru, Sn…) a été développé afin de généraliser les résultats obtenus. Les concepts et théories de la catalyse hétérogène ont été étendus au cas spécifique de cette réaction électrochimique faisant intervenir des intermédiaires adsorbées. La théorie dite de donneur-accepteur en catalyse hétérogène a été plus particulièrement adaptée, et dans ce cadre le platine a été considéré comme accepteur tandis que l'étain a été considéré en tant que donneur. Le développement de ce modèle a permis l'établissement de relations entre le courant mesuré et le potentiel appliqué dans un certain nombre de vrais cas limites. La validité et les limitations au modèle proposé ont évidemment été discutées au vu des résultats obtenus.

Chapter 1 Introduction

Today, the search of new catalysts for fuel cells applications is a very active field. Present anode Direct Alcohol Fuel Cell (DAFC) catalysts still exhibit some problems, thus limiting the practical applications of DAFC for instance as an alternative for internal combustion engines. Platinum nanoparticles, most commonly dispersed in a Nafion® membrane, indeed undergo surface poisoning by reaction intermediates (CO) that are strongly bonded to the surface, block the active sites, and dramatically decrease the catalytic activity and the cell's working time [1, 2]. The use of Pt-based alloys rather than pure Pt nanoparticles allows improvement of the catalytic activity, due to the combination of two effects, *i.e.* the cooperative effect [3] and the electronic (or ligand) effect [4].

Platinum-based alloys with numerous transition metals have been prepared using a wide range of experimental techniques, and it is now well accepted that among all the combinations tested Pt/Ru [5] and Pt/Sn [6] appear as the most appropriate ones for the electrocatalysis of methanol and ethanol electrooxidation, respectively. These new catalytic surfaces have exhibited enhanced electrocatalytic properties and higher CO tolerance than pure Pt. However, there are still some limitations, which come from both from the anode and cathode (kinetics of oxygen reduction) catalysts and from the membrane (alcohol crossover), in the practical use of DAFC.

The aim of this work was to synthesize and characterize various novel Pt-based bimetallic nanocatalysts for applications in the anode compartment of a DAFC. The problem was attacked from a fundamental point of view, the main objectives being an understanding of the enhancement modes as well as the oxidation mechanisms realized on Pt-based bimetallic surfaces. For this reason, the operating conditions of a real fuel cell were not reproduced in this work, and the Pt-based particles were electrochemically characterized as particles deposited on a boron-doped diamond (BDD) substrate electrode. This substrate was chosen due to its unique and remarkable properties of chemical inertness, low background current, high mechanical resistance to chemical and electrochemical attacks... [7, 8]. Due to these properties, BDD is a promising alternative to other common substrate electrodes that may undergo oxides formation (Au and Ti substrates) or corrosion (graphite and glassy carbon substrates).

The different methods of synthesis of Pt and Pt-based particles and nanoparticles are presented in the experimental part (Chapter 3). The experimental conditions used in the synthesis of nanoparticles via the microemulsion method [9] and electrodeposition [10] are presented. The characterization techniques (both

electrochemical and physical) used in this work are listed, and their principles are briefly summarized. Major information that can be extracted from such measurements is presented. Further analysis of the results is described.

Chapters 4 to 8 of this manuscript deal with the deposition of various Pt-based nanoparticles on the BDD electrode, with the aim of practical use in the electrocatalysis of alcohols (methanol and ethanol) oxidation. The particles studied here differ in their synthesis method (electrodeposition or microemulsion method) and in their nature (Pt, Pt/Ru, Pt/Sn, Pt/Ru/Sn and Au/Pt). Chapter 4 more specifically deals with the electrodeposition of Pt particles both on bare BDD electrodes ("BDD") and BDD electrodes modified by pre-deposited Au nanoparticles ("BDD-Au"). Attempts to combine Pt and Au particles on the same substrate were motivated by the outstanding electrocatalytic properties of Au nanoparticles for CO oxidation [11]. It was also attempted to realize an alloy between the two metals by heating the BDD-Au/Pt electrode.

Chapters 5 to 8 describe how various Pt-based nanoparticles, synthesized via the microemulsion method, are deposited on BDD electrodes and used in electrocatalysis. Pure Pt nanoparticles are treated in Chapter 5, where particular attention is given to their activation by hydroxyl radicals electrogenerated on BDD. Pt/Ru and Pt/Sn bimetallic nanoparticles are treated in Chapter 6 and Chapter 7, respectively. Electrocatalytic application of Pt/Ru nanoparticles is more focused on methanol electrooxidation, whereas ethanol electrooxidation was chosen for the electrocatalytic application of Pt/Sn nanoparticles. Some preliminary results obtained in the characterization of a ternary Pt/Ru/Sn type of nanoparticles synthesized via the microemulsion route are presented in Chapter 8.

The particles and nanoparticles were both physically and electrochemically characterized. Physical characterization was performed by means of Electronic Microscopies (SEM with particles supported on the diamond substrate, TEM with particles supported on a microscope grid), XPS and XRD. Electronic interactions between the metals included in bimetallic samples were also evaluated by XPS. Electrochemical and electrocatalytic characterization of these particles was performed using cyclic and linear sweep voltammetries, chronoamperometry and electrochemical impedance spectroscopy. All these measurements have been normalized with respect to the total amount of deposited metals on diamond according to AAS experiments (microemulsion-synthesized nanoparticles) or to the charge exchanged during electrodeposition events.

In the theoretical part (Chapter 9), the concepts and definitions of heterogeneous catalysis are extended to electrocatalysis. The case of electrocatalysis of methanol

oxidation at Pt-based surface is more specifically emphasized. The donor-acceptor theory of heterogeneous catalysis has been applied to the electrocatalysis of methanol oxidation at Pt/Sn surfaces. It has been postulated that hydroxyl radicals, believed to be formed from water discharge at M (M = Ru, Sn...) sites, can be considered as species that spillover through the donor phase (M) to the acceptor phase (Pt) where they react with adsorbed CO from methanol dehydrogenation. The rates of the different steps involved in the entire oxidation process have been expressed in terms of the donor-acceptor theory, and the measured currents have been linked to the applied potential for several limiting cases. The results obtained experimentally during this work have also been generalized with respect to this model.

Chapter 10 constitutes a general discussion of the present work. The choice of the BDD substrate is justified and the suitability of the microemulsion method as the synthesis technique of catalyst nanoparticles is discussed. The results obtained in this thesis for the different types of Pt-based particles and nanoparticles, and most particularly their electrocatalytic characterization, are linked together and placed in the current scientific context. The results are also discussed with respect to the model proposed for methanol electrooxidation at a surface composed of a donor (Sn, or generally M) and an acceptor (Pt) phase.

Finally some further prospects opened up by this work are outlined in Chapter 11. The question of the role of the substrate in the supported particles response is for instance of great importance (metal-support interactions). The BDD electrode surface have thus been treated by different ways (plasma fluorination, electrochemical polishing). It was also attempted to synthesize Pt nanoparticles using the dendrimeric method [12]. However these experiments can only be considered as preliminary tests for which different parameters have to be optimized. New approaches from literature about new catalyst formulations are also mentioned in conclusion.

1. REFERENCES

[1]   C. Lamy, E. M. Belgsir, in: W. Vielstich, H. A. Gasteiger, A. Lamm (Eds.), *Handbook of Fuel Cells - Fundamentals, Technology and Applications*, John Wiley & Sons, Ltd., New York (2003), p. 323.

[2]   A. Hamnett, in: W. Vielstich, H. A. Gasteiger, A. Lamm (Eds.), *Handbook of Fuel Cells - Fundamentals, Technology and Applications*, John Wiley & Sons, Ltd., New York (2003), p. 305.

[3]   M. Watanabe, S. Motoo, *J. Electroanal. Chem.* **60** (1975), 267.

[4] K.-W. Park, J.-H. Choi, B.-K. Kwon, S.-A. Lee, Y.-E. Sung, H.-Y. Ha, S.-A. Hong, H. Kim, A. Wieckowski, *J. Phys. Chem. B* **106** (2002), 1869.

[5] G. Méli, J.-M. Léger, C. Lamy, R. Durand, *J. Appl. Electrochem.* **23** (1993), 197.

[6] F. Delime, J.-M. Léger, C. Lamy, *J. Appl. Electrochem.* **29** (1999), 1249.

[7] Y. V. Pleskov, *Russ. Chem. Rev.* **68** (1999), 381.

[8] Y. V. Pleskov, in: R. C. Alkire, D. M. Kolb (Eds.), *Advances in Electrochemical Science and Engineering*, Wiley-VCH, Weinheim (2002), p. 209.

[9] I. Capek, *Adv. Colloid Interface Sci.* **110** (2004), 49.

[10] M. Paunovic, M. Schlesinger, *Fundamentals of Electrochemical Deposition*, John Wiley & Sons, Inc., New York (1998).

[11] G. C. Bond, *Gold Bull.* **34** (2001), 117.

[12] H. Ye, R. W. J. Scott, R. M. Crooks, *Langmuir* **20** (2004), 2915.

Chapter 2   Bibliography

1. INTRODUCTION

The electrochemical investigations of diamond and of nanoparticles are relatively new lines of research that have attracted considerable attention due to their numerous possible applications. In this chapter, the state of the art achieved in this research will be presented, and some specific points will be developed. The first of these points is the synthesis of boron-doped diamond electrode by the hot-filament chemical vapour deposition (HF-CVD) process, including the influence that parameters such as crystallographic structure, boron doping level or surface functional groups can have on the electrochemical properties of diamond. The electrochemical properties and applications of diamond such as waste water treatment or strong oxidant production will be presented. Diamond-supported particles as the main subject of this thesis will receive particular emphasis, and the major results in this field will be presented and discussed. The two areas constituting this work, *i.e.* electrochemistry of diamond and electrochemistry of nanoparticles, will be linked. Advances in nanoparticles science including the understanding of their different and novel properties as compared to those of bulk materials will be highlighted. The methods of synthesis of particles (*i.e.* electrodeposition and the microemulsion method) that have been used in this work will then be presented. Principles, advantages, limitations and more spectacular results obtained by these methods will be detailed. Aspects of the electrochemistry of Pt-based surfaces and of alcohols electrooxidation on this type of catalysts will also be examined.

2. HF-CVD SYNTHESIS OF THIN-FILM DIAMOND

Diamond is a unique material with fascinating properties. It exhibits an extraordinarily high atomic density, hardness, thermal conductivity, broad optical transparency, biological compatibility and chemical inertness [1], properties that have motivated scientific interest in diamond. Diamond is also a good electrical insulator but becomes a semiconductor when doped (it has a band gap of 5.4 eV), and is very resistant to chemical corrosion [2]. Several attempts have been made since the end of 19th century to fabricate synthetic diamond, mainly under conditions of high pressure and high temperature (HPHT). Success in synthetic diamond synthesis has been claimed by a number of laboratories, but the first work acknowledged by publication was that of researchers at General Electric [3] published in 1955 (see Figure 2.1). After that, the major effects in research on diamond synthesis were directed at optimizing parameters such as the substrate or the doping level.
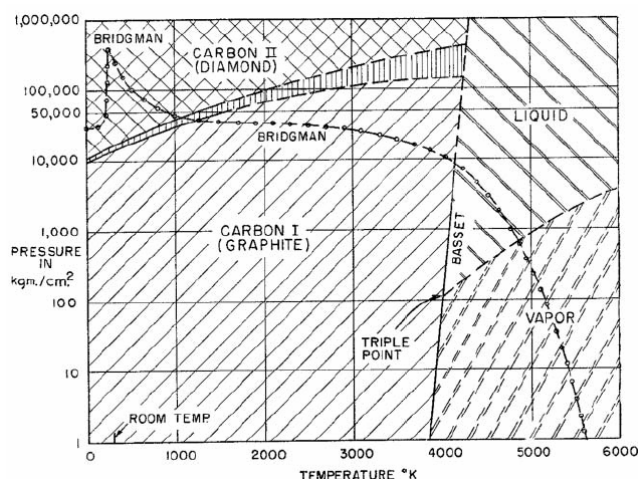
Figure 2.1: Phase diagram of carbon [3].

In the early sixties, it was pointed out that diamond could be synthesized from the gas phase at lower pressures than used in the HPHT technique. Important advances in the chemical vapour deposition (CVD) process are associated with the works of Derjaguin *et al.* [4-6]. Deposition occurs from an activated gas phase composed of a volatile carbon-containing compound and hydrogen, at pressures lower than atmospheric. Activation of the gas-phase is needed, *(i)* to generate a sufficiently high concentration of active carbon-containing species and *(ii)* to generate an agent that will efficiently prevent deposition of non-diamond carbon (graphite and amorphous carbon) on the substrate.

Methods of gas activation are mainly thermal and electrical. Electrical activation includes various types of electric discharge (arc, glow discharge); both dc and ac regimes are used (microwave, pulse current and high-frequency). The most common thermal activation technique is the hot filament technique (HF-CVD). This was the method used by CSEM (Swiss Center for Electronics and Microtechnology, Neuchâtel) to produce the BDD electrodes used in the present work, and hence will be the only technique discussed in detail here. It allows diamond to be deposited on large and three-dimensional surfaces. Relative to other techniques, it is considered as a "cheap" method for which inexpensive equipment will suffice. The deposition involves a gas-phase chemical reaction that occurs above a solid surface. Basically, a hydrocarbon precursor (usually methane) is diluted in a large excess of hydrogen. The mixture is then passed along a hot filament wire. The substrate temperature and surface pre-treatment, the concentration of hydrogen atoms and the nature of the hydrocarbon precursor are key parameters for the deposition and resulting properties of diamond.

6

2.1. Reactor

The reactor (see Figure 2.2) consists of a vacuum chamber (10-50 mbar) continuously pumped with a rotary pump. The process gases are introduced at controlled rates (typically a few hundreds of cm^3 min^{-1}). The distance between the sampled to be coated and the hot filament (2200-2600 °C) is about a few millimeters in order to keep the substrate at the desired temperature (700-925 °C).
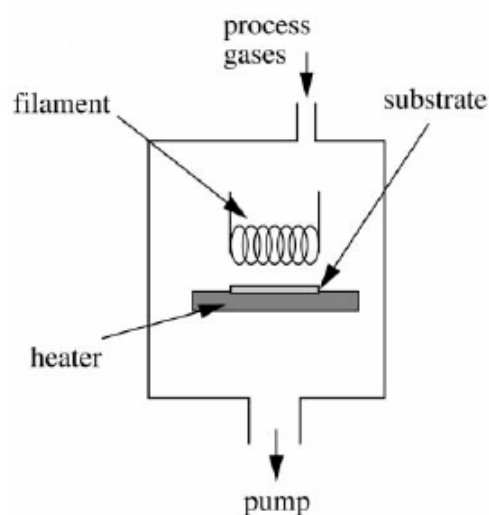
Figure 2.2: Schematic representation of a HF-CVD reactor [2].

The gas phase is a mixture of methane (0.5-2.5 %) in hydrogen. HF-CVD is based on the thermal activation of gaseous species. The role of the filament is to produce such active species and thus its choice must fulfil some conditions. Firstly, the melting point of the filament material must be very high. Second, the reactivity of the filament metal must be low, since a carburisation of the filament occurring during activation of the gaseous species will modify its properties. For these considerations, tungsten and tantalum are commonly used. However, the exact role of the filament is still not very clear. It can be concluded that the filament acts as an energy supplier and/or catalyst in the dissociation of H_2.

2.2. Substrate

The substrate is of course an important parameter that can influence the porosity, the adhesion and the quality of the diamond layer. Requirements for the substrate are chemical, electrochemical, and mechanical stability under the deposition conditions, a low thermal expansion coefficient, and a good electrical and thermal conductivity. Moreover, the substrate must be able to form a diffusion barrier (to avoid hydrogen embrittlement) and a conductive layer at the substrate/diamond interface. Good chemical bonding should be created (covalent σ-bonding) at the interface in order to

ensure good adhesion and ohmic contact. Among the usual substrates, one can distinguish:

- metallic substrates: Ti, W, Zr, Nb, Ta, etc.
- conductive ceramic substrates: carbon allotropes, silicon, etc.

The choice of the substrate depends on the desired electrochemical application (anode, cathode or bipolar electrode), each kind of substrate having its advantages and disadvantages. Silicon remains the only satisfactory anodic substrate for diamond electrodes. In this work, the diamond films were grown on p-Si substrates.

2.3. Nucleation and growth

How diamond is able to grow on non-diamond surfaces is certainly the most important question. Individual carbon atoms have to nucleate on the substrate surface in a way that allows the initiation and construction of a tetrahedrally coordinated sp^3 network. In the commonly accepted theory, steps on the substrate serve as nucleation sites [7]. Substrate surface are pretreated in order to increase its defect density, thus providing additional nucleation sites and enhancing the nucleation density. This can be done by abrasion (mechanical polishing) of the substrate surface with a diamond powder, or by ultrasonication in a diamond powder suspension. Two effects arise from these treatments: *(i)* creation of scratched steps at the surface, which will act as the high-energy sites preferred for nucleation, and *(ii)* incorporation of diamond particles or other types of carbonaceous fragments in the polished surface, which will also act as suitable nucleation sites for diamond growth.

Nucleation can only begin on saturated carbon surfaces. The precursor gases are dissociated by thermal energy from the hot filament, resulting in the formation and diffusion of reactive species (mainly methyl radical) toward the substrate surface. A carbon film is then formed by absorption and coalescence. However, the precise mechanism of diamond growth is not fully understood. It is suggested that atomic hydrogen from the gas phase abstracts a hydrogen atom from the surface, yielding a surface radical where a methyl radical can add. These two steps are repeated until the lattice formation is completed. The surface is finally formed of tertiary carbon atoms having just a single C-H bond [8].

2.4. Diamond doping

Intrinsically, diamond is an electrical insulator, as had already been stated, yet behaves like a semi-metal when properly doped with boron, fluorine or nitrogen, for instance. At higher dopant concentrations, diamond displays metallic behaviour. For electrochemical purposes, the doping level must be sufficient to guarantee low ohmic

drop within the diamond layer (quasi-metallic conduction), and at the same time sufficiently low, so as not to disturb the crystalline structure and induce the formation of a graphitic phase. Two types of doping are possible: positive and negative. Positive doping consists in substituting some carbons by an atom of similar size, but having a slightly higher energy level than the valence bond of diamond and for which an electron is missing in the electronic layer compared to diamond (boron). In negative doping, the doping atom will have an excess electron and a slightly lower energy level (nitrogen). The diamond electrodes used in this work were boron-doped, therefore only this type of doping will be considered in detail.

Boron doping is performed adding traces of a boron-containing species (trimethylboron) to the gas mixture during the HF-CVD process. The boron dopant atoms, which are electron acceptors, form a band located 0.35 eV above the valence band edge of diamond. At room temperature, some of the valence band electrons are thermally promoted to the boron acceptors, leaving free electrons in the dopant bond and holes or vacancies in the valence bond to support the current flow [9]. Typical boron concentrations range from 500 to 8000 ppm; the electrical resistivity depends on the boron concentration in the diamond layer. From an electrochemical point of view, lower boron concentrations lead to an excessive electrical resistivity and higher levels result in the anodic consumption of the electrode, presumably due to secondary nucleation of diamond and formation of sp^2 carbon species. The boron-doped diamond electrode exhibits a polycrystalline, rough, randomly oriented structure with small quantities of non-diamond carbon impurities. Individual crystallites measure approximately 200 to 800 nm (see Figure 2.3).
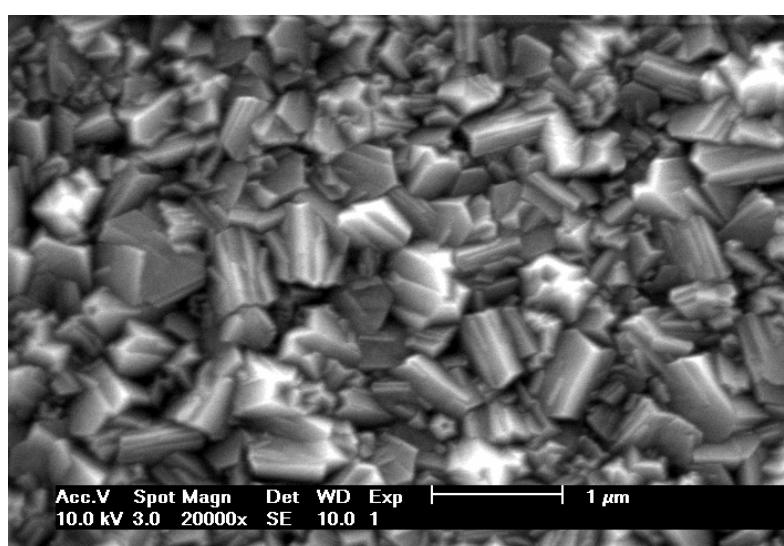
Figure 2.3: SEM micrograph of the polycrystalline BDD electrode surface.

3. ELECTROCHEMICAL PROPERTIES AND APPLICATIONS OF BDD

3.1. Properties

The electrochemistry of diamond is a field that started to expand about fifteen years ago [1]. Since then this field has attracted increasing interest, and at present the properties of boron-doped diamond electrodes are investigated by many groups. Electrochemical properties of boron-doped diamond electrodes have been investigated with techniques such as cyclic voltammetry, electrochemical impedance spectroscopy, and steady-state polarization. This electrochemical characterization is generally supplemented by surface analysis with methods such as XPS, Raman spectroscopy, X-Ray diffraction or electron microscopy. Boron-doped diamond electrodes exhibit some very promising properties for electrochemistry. The inertness of the diamond surface leads to a very good mechanical resistance to chemical and electrochemical attacks, as compared to other carbon electrodes such as graphite or glassy carbon, which is very useful in some applications (batteries, fuel cells). The BDD electrode exhibits a very large potential window between hydrogen and oxygen evolution (see Figure 2.4). It is established that a diamond film of good quality possesses a potential window of about 4 V and very low background currents.
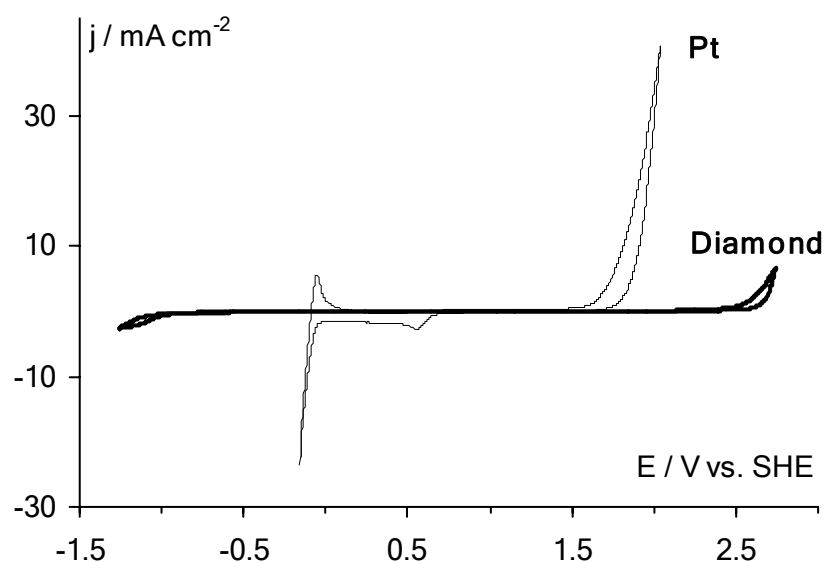
Figure 2.4: CV and potential window available for BDD (thick line) and platinum (thin line) electrodes recorded in 1 M $HClO_4$ at 100 mV s^{-1}.

These low background currents have been attributed to three main factors: *(i)* the relative absence of electroactive carbon-oxygen functionalities on the hydrogen-terminated diamond surface, *(ii)* the lower density of surface electronic states close to the Fermi level (due to the semi-conductor nature of BDD), and *(iii)* the structure of

diamond that can be regarded as a collection of microelectrodes. It is generally assumed, in fact, that the surface of a diamond electrode is composed of electrochemically active sites separated by more insulating regions. The wide potential window of BDD electrodes allows the study of electrochemical reactions occurring at high overpotentials. It has also been pointed out that the presence of non-diamond C sp^2 impurities may play a significant role in the electrochemical response of BDD electrodes [10].

3.2. Applications

Properties of BDD electrodes, such as the high anodic stability under acidic conditions, the high oxygen evolution potential, and the formation of hydroxyl radicals during water discharge [11] make them an attractive candidate for numerous electrochemical applications such as electroorganic synthesis, the production of strong oxidants, or wastewater treatments.

The feasibility of electroorganic synthesis was investigated in our laboratory using a variety of organic substances. A typical example was the oxidation of 3-methylpyridine (3-MP) to nicotinic acid [12]. Bulk electrolysis of 3-MP in 0.5 M $HClO_4$ at low current density (2.5 mA cm^{-2}) and for low 3-MP conversion has shown that the partial oxidation of 3-MP to nicotinic acid can be achieved at a BDD electrode. Hydroxyl radicals generated from water discharge at a BDD anode are certainly involved in the partial oxidation of 3-MP to nicotinic acid, and there was no evidence of electrode surface deactivation under these experimental conditions.

Oxidants can be produced at BDD, either via a fast direct reaction that involves one-electron transfer, or via an indirect mechanism assisted by electrogenerated intermediates (hydroxyl radicals). The first type of reaction can lead to the formation of powerful oxidants, and redox couples such as Ag^{II}/Ag^{I}, Ce^{IV}/Ce^{III} or Co^{III}/Co^{II} have been exploited with high current efficiencies not observable at other electrodes such as Pt, Au, or Sb-SnO_2. The oxidation of Ag^{I} to Ag^{II} at BDD anode was investigated in our laboratory [13] in concentrated nitric acid; the formation of an anodic peak of intensity proportional to the Ag^{I} concentration can be observed by means of cyclic voltammetry (CV). The formation of peroxydisulfate, one of the strongest oxidising agents known, may serve to illustrate the second pathway. A high-overpotential anode for O_2 evolution is needed to perform the oxidation with minimization of the oxygen evolution reaction. During peroxydisulfate production at platinum electrodes, problems are encountered because of the high corrosion rate, the need for removal of the corrosion products, and the effect of additives on the Pt surface. This reaction has been also investigated in our laboratory [14]. The production of peroxydisulfate at

BDD was performed with high current efficiencies, and the process was assumed to be indirect, *i.e.* assisted by hydroxyl radicals as described in Equation 2.1:

$$2\ HSO_4^- + 2\ {}^\bullet OH \rightarrow S_2O_8^{2-} + 2\ H_2O \qquad\qquad (2.1)$$

Electrochemical treatment of waste water is a very attractive alternative to biological ones in the case of refractory organic pollutants. The oxidation of some model organic compounds on the BDD electrode has been investigated in our group [15-19]. According to their behaviour towards electrooxidation at BDD, the organic compounds studied could be divided into two main classes: *(i)* simple carboxylic acids and *(ii)* phenolic compounds. The electrochemical oxidation of carboxylic acids was performed in the region of water stability: no electrochemical activity could be observed and the only difference caused by the added organics being a lowering of the starting potential of water discharge. This phenomenon was explained by the presence and mediation of hydroxyl radicals, and confirms the indirect mechanism [16]. The oxidation of phenolic compounds was studied in the region of water decomposition, and revealed a different behaviour. An anodic peak attributable to the formation of phenoxy radical was observed, but polymerization led to the formation of a polymeric film and deactivation of the surface [19]. The surface could only be reactivated by applying strong anodic polarization (high anodic potentials) to the electrode.

The electrochemical oxidation of organics in the region of water discharge was studied at BDD anodes on a wide variety of compounds including carboxylic acids, ketones, alcohols, phenolic compounds or soluble polymers. In all cases, oxidation could be achieved with high current efficiencies.

3.3. Diamond-supported catalytic particles

Recently, BDD electrodes have been discussed as possible substrates for the electrochemical characterization of electrocatalytic particles and nanoparticles. In fact, the substrates most commonly used for this type of studies can produce some interference such as corrosion (glassy carbon and graphite substrates) or surface oxide formation (gold substrates). The remarkable properties of synthetic diamond electrodes (low background currents and capacitance, high mechanical resistance, surface chemical inertness) can help to solve the above problems. Moreover, the high mechanical resistance of BDD surfaces may allow synthesis techniques to be used that can be constrained for the substrate, such as thermal decomposition. "Soft" synthesis methods can of course be employed to yield a BDD-supported particles composite electrode suitable for further electrochemical characterization of the particles.

Thus, BDD electrodes have been used as a substrate for the deposition of metal particles and nanoparticles differing in their nature and composition. Metal oxide particles such as the dioxides of lead [20] and titanium [21], or the hydrous oxides of ruthenium [22] and iron [23] have been deposited on diamond substrates. It was shown that lead dioxide particles and hydrous ruthenium oxide particles were efficient electrocatalysts for ethylene glycol oxidation and hydrogen evolution, respectively. It has also been shown that thermally decomposed IrO_2 nanoparticles (size about 10 nm) on a BDD substrate strongly affect the electrochemical response of the diamond electrode, the observed behaviour of the composite electrode in fact being solely attributable to the electrochemical properties of the particles [24], even at very low loadings of deposited IrO_2. Such BDD-IrO_2 composite electrode was regarded as a diamond matrix on which particles were deposited more or less homogeneously. The reaction under study (oxygen evolution reaction or oxidation of organic) takes place on diamond as well as on the deposited IrO_2, with distinct reaction rates being associated with each process, and the reaction rates being higher on the IrO_2 nanoparticles than on diamond.

Pure metal particles such as gold [25-27] and platinum [28-31] have also been deposited on BDD substrates for their potential utility in the electrocatalytic reduction of oxygen and in the electrocatalytic oxidation of methanol, respectively. The BDD-Au and BDD-Pt composite electrodes were shown to be efficient in these applications. In the deposition of microemulsion-synthesized Pt nanoparticles on BDD, one can use the diamond's ability to electrogenerate highly reactive hydroxyl radicals from water discharge at high overpotentials [11] for cleaning the nanoparticles (which are stabilized by a protective Nafion® layer) from residual surfactant that was left over from the synthesis process itself [29]. These electrogenerated radicals were also shown to assist the oxidation process. Swain *et al.* have trapped Pt particles into the diamond film, by performing an additional diamond layer deposition step after the deposition of particles on the substrate, or by introducing Pt in the gas mixture during the CVD process [32, 33]. They tested this type of "sandwich" electrode in the oxygen reduction reaction. This type of composite electrode is extremely resistive to harsh chemical and electrochemical conditions, but important loss of electrocatalytic activity of the particles occurs owing to a decrease in accessible active area. The surrounding diamond layer presumably blocks the surface of the particles, thus preventing attainment of the same level of activity as that of similar particles directly deposited onto the surface.

Due to their mechanical hardness and resistance, the BDD substrates allow a wide range of nanoparticles synthesis methods to be applied. The most common

ones are thermal decomposition for oxides and electrodeposition for oxides and pure metals, respectively.

For electrodeposition of Pt particles on BDD, a platinic ion solution was used. It was determined that the process follows a progressive nucleation mechanism during which new nuclei formation and primary nuclei growth occur in parallel [28]. The electrodeposition particles had a very wide size distribution (150-700 nm) and were preferentially located at defect sites, presumably non-diamond impurities, grain boundaries, or kink sites [31]. With such a size, however, these particles could not strictly be considered as nanoparticles for electrocatalysis.

Using a two-step preparation method involving sputtering followed by thermal decomposition [25] as well as the microemulsion method of synthesis [29], our group have succeeded in depositing nanoparticles of Au and Pt on diamond substrates. The average size of the Pt nanoparticles was 2 to 5 nm for microemulsion synthesis, that of Au particles was approximately 10 nm in the two-step method. The particles have exhibited good adhesion and stability on the substrate. The spontaneous deposition of metal nanoparticles on BDD from acidic solutions of metal ions or complex metal ions has also been reported [34]. Particles of Ag, Cu, Au, Pd and Pt having diameters in the 50-400 nm range could be obtained by simple immersion of the substrate into the precursor solution. Some control in the particles size by adjusting the immersion time and the precursor concentration. An enhanced hydrogen evolution activity could be observed in the case of Pd particles deposited on BDD. The authors argued that electrons necessary for metal ion reduction were provided by the conductive Si substrate.

Summarizing, one can point out that the boron-doped diamond electrode can be used as substrate for the study of nanoparticles differing in their nature and composition, and having diameters as low as 2 nm. Throughout, due to the inert character of diamond, the electrochemical response of the BDD-particles composite electrode was solely attributable to the supported particles. The active particles were used as electrocatalysts.

4. GENERAL CONSIDERATIONS ON NANOPARTICLES

The nano-size range covers particles having dimensions intermediate between those of atoms and those of the macroscopic particles characteristic of bulk material. In this size range, matter exhibits some specific physical properties that can significantly differ from those of bulk materials. These new properties have different origins: *(i)* large fraction of surface atoms, *(ii)* high surface energy, *(iii)* spatial confinement, and *(iv)* reduced imperfections. This may give rise to modifications in

the melting point, mechanical strength, optical and magnetic properties or electrical conductivities of the materials. In many cases a correlation between the trends in a given property and the size of the nano-object can be established. Consequently, research in the field of nanoscience, both fundamental and applied, has attracted rapidly increasing interest during recent decades and expanded to subjects in areas as different as optics, magnetism, physics, electronics, or catalysis and electrocatalysis. Some of the new properties of nanomaterials are well known, but many more certainly will be discovered. In this section of the manuscript, some new properties of nanomaterials and nanoparticles, as compared to those of bulk materials, will be highlighted as illustrating examples.

Nanoparticles of metals or semiconductors generally are found to have lower melting points than bulk materials at diameters below 100 nm. This is illustrated in the case of gold nanoparticles in Figure 2.5, where it can be seen that the melting point rapidly decreases for particles with diameter below 5 nm [35]. Similar observations have been made in the case of lead [36] and other metals. Such observations are not easy to make, owing to the difficulty of accurately recognizing the melting of the nanoparticles. The surface properties of a particle are not the same as those of the bulk material, and enhanced evaporation from the particle surface would lead in a reduction of diameter, and therefore to a lower melting temperature. Generally, the lowering of the melting points of metals is explained by the fact that the surface energy increases with decreasing particle size.
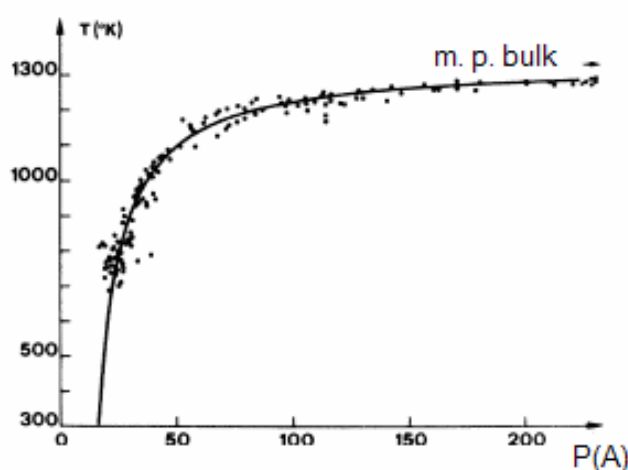
Figure 2.5: The melting points of gold nanoparticles as a function of their diameter. The plots include experimental data (the individual points) and the results of a least-squares fits (the solid line) [35].

The electronic structure of a material would also be modified by decreasing particle size of the material. A change in electronic structure involving a widening of the band gaps and the formation of discrete band gaps occurs when the dimensions

of an object drop below a critical value, *i.e.* the electron's de Broglie wavelength. Thus, the electronic structures of the nanomaterials should differ significantly from those of their bulk counterpart. This phenomenon is also known as "quantum size effect": electrons and holes are spatially confined, electric dipoles are formed, and discrete energy levels will arise in the material. These effects involve systematic changes in density of the electronic levels with size, and produce strong variations in both the optical and electrical properties [37]. For instance, some metal nanowires become semiconducting as their diameter drops below a certain level, and semiconductors may become insulators [38]. Modifications of the optical properties of a material with decreasing particle size can be produced, both by surface plasmon resonance and by increased energy levels spacing as the system becomes more confined (again the so-called quantum size effect). This effect is more pronounced in the case of semiconductor nanoparticles than in that of metal ones, which is due to the higher density of energy levels in metals. A noticeable separation of the energy levels within the conduction band will occur when the metal nanoparticle consists of approximately 100 atoms.

The most spectacular change in character induced by a decrease in particle size is certainly demonstrated by the catalysis exhibited by gold nanoparticles. While bulk gold commonly is considered as a weak chemisorber, and consequently as a weak catalyst, gold nanoparticles exhibit surprisingly high catalytic activity [39, 40]. Thus, high catalytic activity towards CO oxidation was obtained even at very low temperature [41, 42]. Of course, the catalytic properties of the Au particles depend on the support and the preparation method, but they particularly strongly depend on the size of the Au particles. It has been suggested that the unusual catalytic properties of supported metal clusters were observable when one dimension of the cluster becomes smaller than three atomic spacings [43]. Extraordinary catalytic properties were not seen only at gold nanoparticles; similar observations were made for platinum nanoparticles. Pt nanoparticles have for instance been used in the catalysis of oxygen electroreduction [44, 45] or in the oxidative dehydrogenation of ethanol [46]. In these cases a correlation between catalytic activity and particles size could be established. The same was found in methanol electrooxidation, where the specific activity of particles decreased with decreasing particled size in the range from 4.5 to 1.2 nm [47]. By now, nanoscience has now a considerable impact on catalysis. Colloids and nanoclusters are widely used as catalysts in a broad range of both heterogeneous and homogeneous reactions [48, 49].

Summarizing, it can be said that reducing the size of a particle down into the nano-range will significantly influence the properties of the material. Not only the

properties that were discussed above, but also other ones such as ferromagnetism, optical and mechanical properties will be affected by the decreasing particle size. For a more detailed discussion of the mechanisms and consequences of such modifications, the reader is encouraged to consult some books and reviews [50, 51]. The new properties exhibited by nanomaterials are now used or contemplated for a broad range of applications. Nanotechnology has become a reality in fields as different as electronics, optics, magnetism, materials science, or catalysis and electrocatalysis, and in the future will shape more and more aspects of our life.

5. SYNTHESIS OF NANOPARTICLES

From the catalysis and electrocatalysis points of view, nanoparticles and nanoparticulate materials are objects of diameter typically below 10 nm. Depending on the desired composition, shape, uniformity, dimension, size distribution, and intended use of particles, a variety of techniques can be considered for the synthesis of such materials. Practicability of a given method is an important parameter to be considered. Ideally, the synthetic approach should come close to satisfying the following requirements: *(i)* identical size of all particles (monosized), *(ii)* identical shape and morphology, *(iii)* identical chemical composition and crystal structure, and *(iv)* individually dispersed or monodispersed (no agglomeration).

The different synthesis methods of nanomaterials can be divided into the two main groups of *(i)* thermodynamic equilibrium and *(ii)* kinetic approaches [50]. In the thermodynamic approach, the synthesis proceeds via *(i)* generation of supersaturation, *(ii)* nucleation and *(iii)* growth. In the kinetic approach, the formation of nanoparticles is achieved, either by limiting the amount of precursors available or by confining the process in a limited space.

This section is not intended to provide the details of all the synthesis techniques. Only those used in this work (electrodeposition and microemulsion method) will here be detailed. Information about other methods of nanoparticles synthesis are available in some special reviews [50-52]. This part of the manuscript is conceived as an overview of basic theories and of the most representative results obtained with the methods listed above.

5.1. Electrochemical deposition

Electrodeposition of metal is a very practical method of synthesis of metallic particles or films on substrates. It consists in applying a potential perturbation (potential step or linear variation of potential) to an electrode sitting in a precursor solution so as to attain a potential at which reduction and deposition of the material

will occur. Deposition thus occurs directly on the electrode surface, and the nature of the substrate material is one of the key parameters for the electrodeposition process, as well as the nature of the precursor salt. From a practical point of view, electrodeposition is more economic and facile than physical deposition techniques (CVD...), even if the deposits generally are inferior in their quality [53].

In this section, aspects of the theory of electrodeposition will be presented. Basically, electrodeposition consists in the electrochemical reduction of a metallic ion dissolved in an electrolyte that can be aqueous, organic, or mixed aqueous-organic. In aqueous media, the ion reduction into its metallic form is followed by its deposition on the electrode surface as described in the overall Equation 2.2:

$$M^{z+}_{sol} + ze^- \rightarrow M_{ads} \hspace{4cm} (2.2)$$

This reaction can be made to occur, either by classical electrodeposition, where the electrons are purchased by an external source, or by electroless deposition, where the deposition may occur spontaneously (autocatalysis) or with the participation of electrons provided by a reducing agent is added to the solution. In a strict sense, electrochemical deposition processes may consist of both processes at once; however, in this Chapter, only classical electrodeposition will be analyzed.

The understanding of metal electrodeposition mechanisms on an atomic scale has been limited for a long time by the resolution of the imaging techniques available to electrochemists. Thus, investigations of this crucial aspect were limited to kinetic studies at the electrode (analysis of current-time transients) and to an optical characterization of electrodeposits. It is pertinent to point out here that the relevant kinetic parameters cannot be determined in an easy or straightforward way, since the substrate surface continuously changes during the process [54]. With the development of scanning tunnelling microscopy (STM) in a solution environment, it finally became possible to visualize in real time the events taking place during the electrodeposition [55, 56], and obtain direct confirmation for assumptions and models developed earlier on the basis of kinetic and optical studies.

Electrodeposition occurs in two principal, distinct stages that should not be confused: nucleation and growth [57]. Nucleation is the stage during which atoms from the mother-phase (here the solution) regroup themselves to form cores or nuclei, and growth corresponds to the stage during which the atoms from the solution are directly incorporated in existing nuclei. It is well-known now that surface defects play a key role in the electrochemical deposit characteristics, particularly by providing the preferential sites on which the deposit will start to form. It is known, too, that the various crystalline planes of a polycrystalline sample do not have the same physical and electrochemical properties. The overall mechanism of electrodeposition can be

viewed as the reduction and incorporation of a metal ion on the electrode surface occurring at the level of defects known as kink sites (Figure 2.6) [58]. Two different sequences of events occurring on an atomic scale can lead to this same result. In the first one, the metal atoms are adsorbed on edges of the substrate where they become "adatoms", then diffuse towards the kinks (2.6.B) on the substrate surface. In the second one, the atoms are initially adsorbed on the substrate on sites known as "terraces", then diffuse as adatoms, first towards the edges and then towards the kink sites (2.6.C).
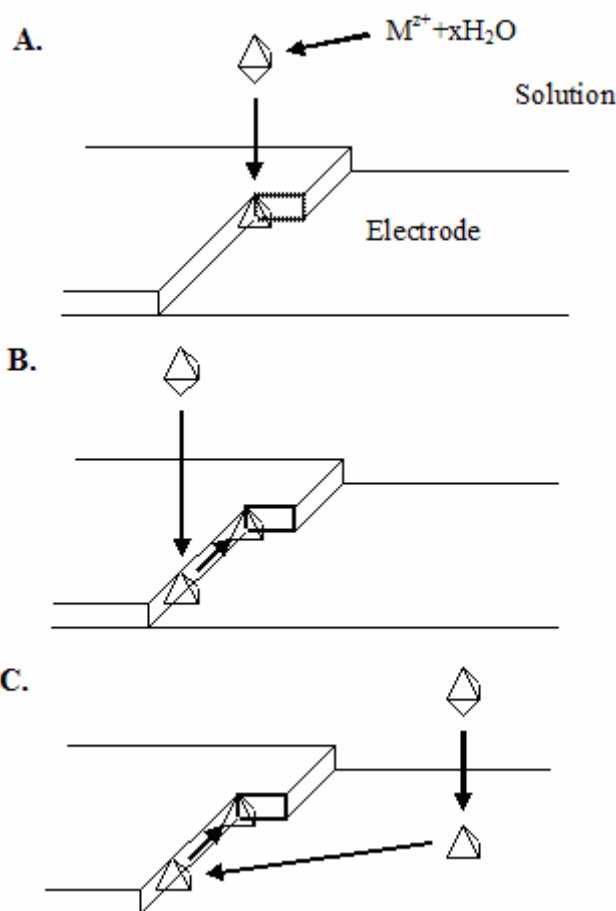
Figure 2.6: Schematic view of possible mechanisms of electrodeposition.
A: Overall mechanism of deposition, **B**: adsorption at an edge followed by diffusion to a kink site, **C**: adsorption at a terrace and diffusion to an edge, then to a kink site.

The first event of the process is electronucleation: the ions in solution are brought up to the polarized electrode by various modes of transfer: diffusion of the species being consumed by reaction at the electrode, from the bulk of the solution towards the electrode surface; migration of solvated ions; convection. These metal ions can become adsorbed on the substrate, supposed to be plane and single-crystal. These adsorbed metal atoms, M_{ad}, also denoted adatoms, are not yet fully linked to the

substrate, and still have the possibility of being reoxidized to adions $M_{ad}^{z'+}$. Stabilization and integration of the adatoms involve several physical phenomena. In fact, an isolated atom weakly bonded to the surface would not remain adsorbed, and could not constitute the beginning of a new phase. Thermodynamics showed that new atoms can be incorporated into the network of surface only on nuclei having a minimal size (critical nuclei).

The general theory of nucleation can be applied to describe the case of electrochemical nucleation, by introducing the electrochemical quantities describing the deposit into the general thermodynamic and kinetic relations. For a simple initial idea of formulation of these phenomena, consider nuclei in the shape of discs of radius r on the substrate in the gas phase. Formation of a nuclei at constant T occurs with the free enthalpy change:

$$\Delta_n G = 2\pi r \varepsilon_i - \frac{\pi r^2}{A} RT \ln \frac{p}{p_0}$$
(2.3)

where ε_i is the free energy of incorporation by surface unity, A is the surface occupied by one mole of the deposit atoms, p is the pressure at the interface, and et p_0 is the equilibrium pressure between the solid and gas phases; ratio p/p_0 represents the supersaturation. The value of $\Delta_n G$ attains a maximum at $r = r_c$, r_c being the critical radius of the nucleus (value of r above which nuclei are stable). For three-dimensional nuclei, r_c is given by:

$$r_c = \frac{\varepsilon_i A}{RT \ln \frac{p}{p_0}}$$
(2.4)

This relation can be used for the electrochemical case, by merely replacing the ratio p/p_0 ratio by the ratio a/a_0, where a is the activity of adsorbed M^{z+} at the interface, a_0 is the activity of the same ions adsorbed at the equilibrium. It is a significant advantage of electronucleation that the degree of supersaturation (ratio a/a_0) can be controlled by controlling the applied overpotential η. From Equation 2.5:

$$\eta = \frac{RT}{zF} \ln \frac{a}{a_0}$$
(2.5)

it can be deduced that:

$$r_c = \frac{\varepsilon_i A}{zF\eta}$$
(2.6)

so that the free enthalpy of formation of one nucleus of critical size r_c is given by:

$$\Delta_n G_c = \frac{\pi \varepsilon_i^2 A}{zF\eta}$$
(2.7)

It can be seen here that electronucleation is very sensitive to overpotential. Therefore, potentiostatic electrochemical methods are the methods of choice for kinetics studies of the process. Thus, the nucleation rate at stationary state, J_{st}, which is the number of aggregates larger than the critical size formed per units of time and surface, can be written as follows:

$$J_{st} = N_0 D_c \Gamma \exp(-\frac{\Delta_n G_c}{RT}) \tag{2.8}$$

where N_0 is the number of possible nucleation sites at the surface, Γ is a hydrodynamic factor, and D_c is the adatoms flow necessary to form a nucleus of critical size. Combining Equations 2.7 and 2.8, one finds:

$$J_{st} = K_1 \exp(-\frac{K_2}{\eta}) \tag{2.9}$$

where K_1 and K_2 are constants. Equation 2.9 again reveals the strong dependence of electronucleation on overpotential. It can be seen that the nucleation rate remains negligible below a minimal value of overpotential (the critical overpotential, of the order of a few mV). In two-dimensional nucleation, it must be remembered that nuclei are flat and adhere to the surface. Atoms can therefore spread out over the surface without be hindered, implying that inhibition phenomena do not occur. However, inhibition is frequent in electrocrystallisation because of the large number of species such as H^+, OH^- or impurities that can be adsorbed in competition with the metal at the metal-electrolyte interface. Two.dimensional spread out is no longer possible then, and with increasing inhibition, the system evolves from a two-dimensional to a three-dimensional nucleation.

Formation of a new phase during an electrochemical reaction at an electrode in solution implies that steps similar to those occurring during crystallisation from a saturated solution take place. A nucleus is primarily formed from a critical number of adatoms, supposed randomly distributed over the surface. The formation of such a nucleus can be a slow phenomenon, just like the formation of primary nuclei in crystallisation; it can be represented by Equation 2.10:

$$n \, M_{ad} \leftrightarrow (M_n)_{nucleus} \tag{2.10}$$
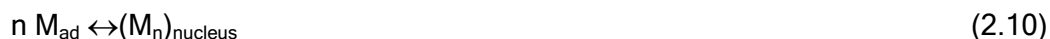
However, the electrocrystallisation process can be accelerated by supersaturation. Increasing adatom concentrations favour supersaturation, and equilibrium (2.10) is shifted to the right. The production of adatoms M_{ad} needs at least one electron-transfer step; it is possible, therefore, to increase the adatom concentration, just by increasing the absolute value of overpotential η. In two-dimensional nucleation, the rate constant $k_{n,2}$ is linked to the overpotential η by Equation 2.11:

$$k_{n,2} = k^0_{n,2} \exp(-\frac{a}{\eta}) \qquad (2.11)$$

while the rate constant for a three-dimensional nucleation is given by:

$$k_{n,3} = k^0_{n,3} \exp(-\frac{b^2}{\eta}) \qquad (2.12)$$

where a et b are constants. If the absolute value of overpotential is increased, the rate constants will increase up to the limit values $k^0_{n,2}$ and $k^0_{n,3}$.

The number of nuclei formed is a function of time, which has been taken into account by several hypotheses. Fleischmann and Thirsk [59] assumed that all possible sites of nucleation are active sites of identical reactivity toward nucleation, and that the probability of conversion of these sites to nuclei is constant over time. The nucleation rate can then be described as the rate of disappearance of available active sites according to a first order kinetic expression:

$$\frac{dN(t)}{dt} = k_n(\eta)[N_0 - N(t)] \qquad (2.13)$$

where η is the overpotential, $k_n(\eta)$ is the rate constant of nucleation for one site (s^{-1}), N_0 is the number of active sites available per unit surface area (cm^{-2}), which is regarded as independent of η. Integrating Equation 2.13 and taking into account the initial conditions (N = 0 at t = 0), N(t) can be expressed as follows:

$$N(t) = N_0[1-\exp(-k_n(\eta)t)] \qquad (2.14)$$

The value of N increases with time and tends toward the limiting value N_0. This law admits two limiting cases:

i) at large values of k_n, the nucleation rate is very high and given by:

$$\frac{dN}{dt} = N_0\delta(t) \qquad (2.15)$$

where $\delta(t)$ is the Dirac function, which is equal to 0 when t > 0 and tends toward infinity for t = 0 while its integral between t = 0 et t $\rightarrow \infty$ equals 1. Crystallisation takes place simultaneously at t = 0 on all active sites; this is the *instantaneous nucleation*.

ii) at very low values of k_n, the exponential term can be linearised, and the following expression, applicable at short times, is obtained:

$$N(t) = k_n N_0 t \qquad (2.16)$$

The number of nuclei increases linearly with time, and the nucleation rate is given by:

$$\frac{dN}{dt} = N_0 k_n \qquad (2.17)$$

In this case nuclei are formed continuously during a given time span; this is the *progressive nucleation* mechanism. It should be pointed out that relations 2.13 to 2.17 are applicable to two-dimensional nucleation as well as to three-dimensional

nucleation; one merely must replace k_n in these equations by the relevant expressions of $k_{n,2}$ or $k_{n,3}$.

Starting from this basic model, we may now assume that several types of active sites with different critical overpotential of nucleation η_c the coexist at the electrode surface. The theory of Markov and Kashchiev [60] is based on this hypothesis; in this case the maximum number of nuclei is precisely equal to the number of active centres at a given value of supersaturation:

$$N_s = \int_0^n z(\eta_c)d\eta_c \qquad (2.18)$$

where η is the applied overpotential, η_c is the critical overpotential at which a potentially active site will be activated, and $z(\eta_c)$ is the function that expresses the density of active sites for which the critical overpotential has the value of η_c. This general equation can also be written as follows:

$$N(t) = N_s(\eta)[1-\exp(-k_n(\eta)t] \qquad (2.19)$$

where $N_s(\eta)$ is the number of saturated active sites, which depend on η [61]. Fletcher and Lwin [62] have then improved this model by considering that due to the substrate surface imperfections, its properties were not homogeneous. Thus, the following approximations were made: *(i)* there is a random distribution of surface energies between nuclei and active sites, *(ii)* all active sites have the same nucleation overpotential, and *(iii)* the total number of active sites is independent from η. These assumptions lead to the following equation:

$$N(t) = \int_0^\infty N_\infty (1 - \exp[-k_n(\eta)t]) \Theta(k)dk \qquad (2.20)$$

where N_∞ is the total number of active sites at the surface, $k_n(\eta)$ is the kinetic constant at nucleation sites, and $[\Theta(k)dk]$ is the fraction of active sites with a rate constant between k and (k + dk). Extrapolation to long times gives:

$$\lim_{t\to\infty} N(t) = N_\infty \qquad (2.21)$$

This model is said to be "polykinetic", since the distribution of energies at the electrode surface is supposed to be linked to the distribution of nucleation rates over all active sites of the electrode. In the case of "monokinetic" behaviour of all nucleation sites, one comes back to the law of Fleischmann and Thirsk, and to Equation 2.14.

Following nucleation, the formed nuclei will grow. Assuming that there are at the substrate surface crystals of sufficient size, the growth of such grains is described by a direct reaction on the nuclei:

$$(M)_{n,cryst} + M^{z+} + ze^- \leftrightarrow (M)_{n+1,cryst} \qquad (2.22)$$

This process will depend on the size and geometry of the crystals already formed. Considering growth of the deposit subsequent to the formation of nuclei in the shape of discs measuring one atomic monolayer in height, and assuming that growth is two-dimensional at the disc periphery, the growth rate will be given by the rate of disc radius increase. If the electrodeposition rate-determining step is the adatoms incorporation at the periphery of the nuclei, the current corresponding to the growth of one site can be written as:

$$i = zFk2\pi rh \tag{2.23}$$

where k is the rate constant of incorporation (mol cm^{-2} s^{-1}), h is the nucleus height, and r is the radius of the nucleus. The electrical charge needed to form a cylindrical nucleus is:

$$Q(r) = \frac{\pi r^2 hzF\rho}{M} \tag{2.24}$$

where ρ is the metal density (g cm^{-3}) and M is its molar mass (g mol^{-1}). Combining the derivative of this expression with Equation 2.23 we obtain:

$$i(r,t) = \frac{2\pi hzF\rho}{M} r(t) \frac{dr(t)}{dt} \tag{2.25}$$

The rate of increase of the disc radius can be derived as:

$$\frac{dr(t)}{dt} = \frac{Mk}{\rho} \tag{2.26}$$

while the value of the radius at any time t is given by:

$$r(t) = \frac{Mk}{\rho} t \tag{2.27}$$

It follows that the current associated with the growth of an isolated, cylindrical nucleus varies linearly with time according to Equation 2.28:

$$i(t) = \frac{2\pi zFk2hM}{\rho} t \tag{2.28}$$

However, if two different nuclei grow in a two-dimensional lattice, they will inevitably overlap. Then the hypothesis of independently growing nuclei is no longer valid, and overlap of the diffusion zones of different nuclei must be taken into account as shown in Figure 2.7.
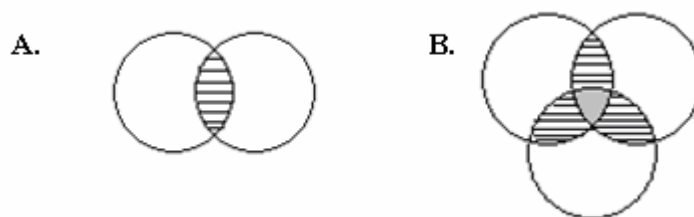
Figure 2.7: Schematic view of overlapping diffusion zones between growing nuclei. **A:** overlap between those of two nuclei (hatched), **B:** overlap between those of two (hatched) and three nuclei (grey area).

In a situation where N_0 nucleation centres of identical activity are statistically distributed over the electrode surface, an analysis of the Kolmogorov-Avrami type can be carried out in order to evaluate the influence of overlapping diffusion zones of the nuclei:

$$S(t) = S_0[1 - \exp(-\frac{S_{ex}}{S_0})]$$
(2.29)

where $S(t)$ is the surface covered by nuclei at time t, S_{ex} is the real surface that would be covered by individual nuclei formed after a time t if overlapping was neglected, and S_0 is a normalisation factor.

As concluding remark, it should be pointed out that the electrodeposition of alloys follows the same laws and principles as that of pure metals [63]. However, it must be kept in mind that the electrodeposition of alloys needs a mixture of two different ions in solution, and that these two ions will not require the same overpotentials for reduction and deposition.

5.2. The microemulsion method

5.2.1. Introduction on microemulsions

A microemulsion basically is a mixture of two non-miscible liquids (water and an organic), stabilized by a surfactant at the water-oil interface, which displays remarkable properties. A water-in-oil (w/o) microemulsion is a thermodynamically stable, isotropic, and optically transparent dispersion of water stabilized by a surfactant layer around water droplets in a continuous organic oily phase [64]. Dispersions of oil in a continuous aqueous phase are oil-in-water (o/w) microemulsions. The dispersed phase is present as small colloids with conformations that can vary depending on the components of the microemulsion, their volume ratio, and the temperature. For an understanding of the nature of a microemulsion it is of extreme importance to analyze all interrelated association structures occurring in the system and not just the microemulsion as an isolated association phenomenon [65].

Since their discovery by Schulman *et al.* in 1943 [66], these systems have been the subject of numerous studies related to their physico-chemical properties, mechanisms of formation, and potential applications. The term "microemulsion" was only introduced in 1959 by Schulman [67], he and his co-workers have extensively studied these transparent liquid mixtures using a wide range of experimental techniques [67-70]. They demonstrated that these systems are formed by spherical droplets having almost homogeneous diameters that can vary between 8 and 80 nm. Winsor found that three different system types can exist in mixtures composed of an organic, water and a non-ionic surfactant [71]. In the Winsor I system, o/w microemulsions coexist with an excess of organic. In Winsor systems of type II, w/o microemulsions coexist with an excess of water. In these systems spherical microdroplets dispersed in the continuous phase have been detected. Finally in Winsor systems of type III, one microemulsion coexist with an excess of water and organic. Type I is favoured at low temperatures, type II is mostly present at high temperatures, while type III is favoured at medium temperatures.

One of the great challenges in microemulsion research was that of elucidating the important changeover between the turbidity observed in emulsions and the absolute transparency of microemulsions. It seems obvious that large droplets present in the emulsion will spontaneously divide into small ones leading to an increase in the interface surface. Schulman has interpreted this phenomenon as the result of a temporary, negative interfacial free energy, expressing it as a superficial pressure [72]. However, some problems remained in view of the rather high superficial pressures (≈ 50 mN m^{-1}) required for this phenomenon. This question was resolved in later works [73, 74] in which the water/oil interface was considered as a double film with two types of tensions on the surface, one toward the water phase and the other toward the organic phase. The interface could then assume an optimum radius of curvature at which the superficial tension attains a minimum.

Phase transitions in ternary water/organic/surfactant systems usually are illustrated with triangular phase diagrams, in which each corner of the triangle represents one of the components of the system. In further analysis, surfactants are rationally classified according to their structure, into ionic (one type of charge), zwitterionic (two types of charge) and non-ionic (no charge on their molecule). Surfactants can also be classified according to their micelle-forming properties or to their swelling capacity. Microemulsions can be present in different forms such as water droplets in oil, oil droplets in water, bicontinuous mixtures, ordered droplets or lamellar mixtures, with an ample array of phase equilibria between them. This wide variety of systems is mainly governed by the variations of the system composition.

Microemulsion systems are used in a wide range of applications, most often in relation with the recovery of organics, with pharmaceutics processes, cosmetics, food products, or as liquid membranes and detergents.

5.2.2. Synthesis of nanoparticles in microemulsions

One of the most interesting applications of microemulsion systems is their use in the synthesis of metal nanoparticles with very narrow size distributions, as first reported by Boutonnet *et al.* [75]. Following this pioneering work, the microemulsion method has been successfully used to synthesize various types of nanoparticles including metal oxides [76], polymers [77], metals [29, 78-81], and metal alloys [82-85]. The principle of the method is that of providing a confined, nanosized reaction medium (the micelles) within which the reduction of dissolved metallic precursors will take place so that the process is isolated and limited to the medium dimensions. When using a w/o microemulsion as initial template, the way to be followed in order to achieve reduction of the metal precursors and synthesis of nanoparticles, simply consists in mixing equal volumes of two microemulsions having identical formulations (in order to have inverse micelles of identical typical size); the first one contains the metallic precursor and the second one the reducing agent dissolved in their respective aqueous phases. The commonly accepted scheme of this synthesis method is illustrated in Figure 2.8. Due to their small size, the aqueous nanodroplets are subject to Brownian motion, and therefore collide continuously, forming dimers and higher aggregates. These are short-lived, and rapidly disintegrate into droplets of the original size. As a result of the continuous coalescence and decoalescence process, the content of the aqueous nanodroplets will be distributed over the entire droplet population and reaction (nucleation and growth) will occur within the droplets that control the final size of the particles. The interchange of the reactants (dissolved metal salt(s) and reducing agent) occurs during the collisions between water droplets. This reactant interchange is very fast [86] and generally takes place just during the mixing step. The interchange of nuclei or particles between "nucleated" droplets is hindered, because it would imply the formation of a big hole during droplet collisions. This would require a great change in curvature of the surfactant film that is not energetically favourable. Microemulsions fit for nanoparticles synthesis must be formulated in such a way that the curvature radius is similar to the natural droplet radius; otherwise the surfactant film could be opened during collisions leading to an interchange of particles and nuclei, so that control over growth could not be achieved [87]. By the time the final size of the particles is attained, the surfactant is attached to the particles and protects them against further growth and agglomeration. Since the

starting droplets contained a dilute solution of a metal salt, and the particles formed have a size of the same order as the starting droplets, the final reaction mixture will consist of a relatively small amount of particles and a higher amount of empty droplets (*i.e.* nanodroplets free of salt or particles).
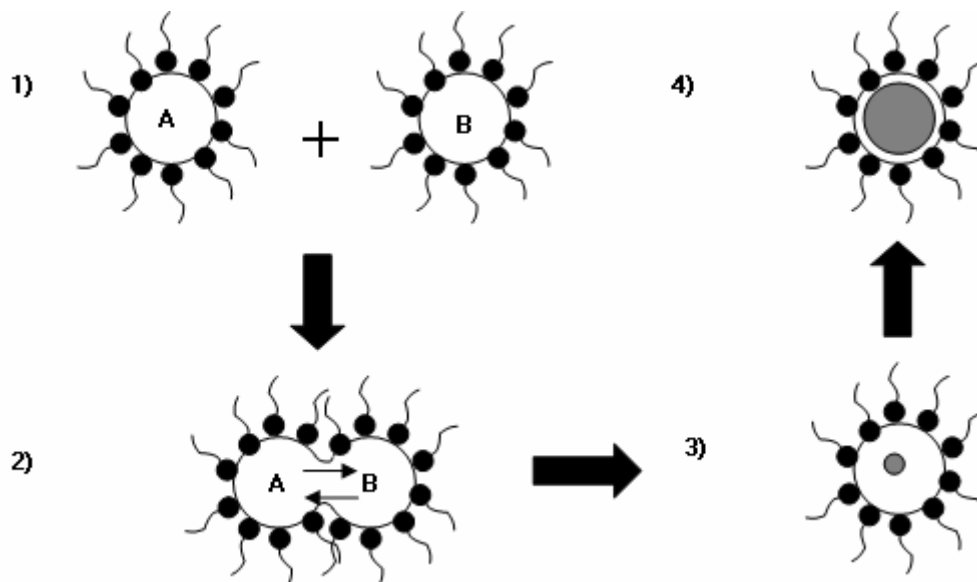
Figure 2.8: General scheme of synthesis of nanoparticles by mixing of two microemulsions. Steps of the process: **1)** mixing of the microemulsions, **2)** collision between aqueous nanodroplets, exchange of reactants, reaction, **3)** nucleation, **4)** growth of the particles in the inverse micelles. A = metal precursors, B = reducing agent, both dissolved in aqueous phases of the microemulsions.

The synthesis of nanoparticles in microemulsion systems has been the subject of numerous studies, both theoretical and experimental [78, 88], performed to better understand the reaction mechanisms and to more efficiently control the size and shape of the resulting particles that are important parameters in catalysis and electrocatalysis. It has already been stated that an exchange of reactants take place during collisions between droplets, and that this process is very fast. The dynamic exchange of reactants between droplets via the continuous oily phase is strongly depressed due to the restricted solubility of inorganic salts in the organic phase. This is a reason why the attractive interactions (percolation) between droplets play a dominant role in the particle nucleation and growth. The possibility of direct transfer of reactants between their pools would be enhanced in the case of more energetic and strongly interactive collisions. It has indeed been shown that inter-droplet communication is very rapid ($\approx$ 1 msec.) and takes place via the formation of a transitory "dimer" resulting from droplet collision [89]. Generally, the chemical reaction between reactants (metal salt and reducing agent) at the interior of the nanodroplets is very fast, and therefore the rate-determining step (rds) of the overall

reaction is the initial communication step of droplets containing different reactants. The rate of communication (k_{com}) has been expressed in terms of a second-order communication-controlled rate constant related to the droplet concentration in the continuous oily phase. This rate constant is analogous to a diffusion-controlled rate constant in a homogeneous medium, and is the highest possible rate constant in the system. Fisher *et al.* [90] have estimated k_{com} to be around 10^6-10^7 dm^3 mol^{-1} s^{-1} for the AOT (sodium bis(2-ethylhexyl)sulfosuccinate) / water / heptane microemulsion; this means that approximately 1 in 10^3 collisions between droplets lead to exchange of the reactants. The use of anionic surfactants such as AOT for instance can decrease the reaction rate or inhibit the reaction. In this case the interface is negatively charged, and the metal cations will be preferentially located close to this interface whereas the hydrophilic co-reactants will prefer to be located in a region away from this interface. This can lead to the separation of reactants in large droplets; but in microemulsion with small water cores (water-to-oil molar ratio $\omega_0 < 5$) no effective separation within the pools could be observed, and no retardation due to this effect is possible. The reverse is true for the larger pools (maximal separation for $\omega_0 \approx 20$). In the case of very large pools, the effect of surface/volume ratio is reduced and partitioning caused by this effect should be less pronounced.

Control of size of the microemulsion-synthesized nanoparticles has been the subject of many investigations. From a general point of view, it can be said that the size of the water pools in a microemulsion is a function of the value of ω_0 used in the formulation: for constant surfactant concentration there is a linear relationship between ω_0 and the size of the aqueous droplets. It follows that the size of the particles may be proportional to ω_0. Many groups have tried to correlate the size of the aqueous droplets of the starting microemulsion with that of the obtained particles. Such a correlation could be established in some cases where AOT was used as surfactant [91],but in general there was straightforward correlation between the size of droplets and particles. It seems that, at low water content (*i.e.* low values of ω_0), there is this type of relation between the two in the case of cadmium salts [92], platinum [79], silver [91] and copper [80]. In these cases, larger droplet size will lead to increasing particle diameter, only up to a certain value which then will remain constant while ω_0 is further increased [93]. Moreover, the choice of the surfactant seems not to be important in size control [79]. A range of important experimental findings concerning particle size control in microemulsion systems has recently been summarized as follows [94]: *(i)* particle size increases with reactant concentration, *(ii)* particle size decreases if the concentration of one of the reactants is increased far beyond the concentration of the other one, *(iii)* particle size increases with an

increase in surfactant film flexibility, and *(iv)* particle size may increase with an increase in microemulsion droplet size. These experimental findings are in good agreement with recent Monte Carlo (MC) simulations [95-99]. The MC simulations were made under the assumption that the chemical reaction in the nanodroplets is faster than exchange of reactants within the droplets. The possibilities of autocatalysis of the reaction by sub-nanoparticles formed and of ripening were included in the simulations.

Another intriguing issue is that of shape control of the nanoparticles synthesized via the microemulsion route. It has been postulated that the structure of obtained particles is mainly governed by the shape of dispersed aqueous cores in the microemulsion (*i.e.* spherical droplets, elongated droplets, rodlike channels...). Pileni and co-workers have prepared copper nanoparticles in microemulsions of variable internal structure [100, 101]. Reaction in a microemulsion consisting of spherical water droplets gave spherical particles the diameter of which is increased with increasing value of ω_0. Reaction in a microemulsion consisting of interconnected water cylinders led to cylindrical copper nanocrystals and some spherical particles. A reaction performed in a complex system consisting of a w/o microemulsion coexisting with a lamellar phase gave a mixture of spherical, cylindrical, and flat particles. Numerous studies exist in which no evidence was found for a correlation between template structure and resulting particle shape. There must be other parameters influencing the crystallization behaviour, such as the presence of salts or the nature of the anion. It is also possible to achieve the reduction of metallic salts dissolved in the aqueous cores of a w/o microemulsion by adding a solid reducing agent, such as sodium borohydride, to the microemulsion. The reducing agent will diffuse into the dispersed aqueous nanodroplets, so that the reduction and growth processes will then take place inside the water pools (see Figure 2.9). In this case again, growth of particles will be stopped by the stabilizing surfactant layers, and thus narrow size distribution of nanoparticles can be obtained.
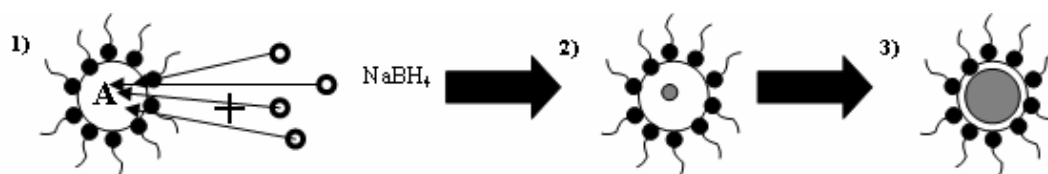

Figure 2.9: General scheme for the synthesis of nanoparticles when adding a solid reducing agent to a w/o microemulsion. Steps of the process: **1)** mixing of the microemulsion with solid $NaBH_4$, diffusion into the inverse micelles, reaction, **2)** nucleation, **3)** growth of the particles. A = metal precursors.

Despite the fact that the microemulsion method is an excellent way to synthesize metal and metal alloy nanoparticles of extremely small dimensions, some limitations to the use of this technique still exist. A prime limitation is cost: the formulation of microemulsions requires large amounts of surfactant (sometimes 20-30 % by volume) that is generally quite expensive. The second limitation comes from the surfactant molecules that coat the final particles and ensure colloidal stability, hence altering their surface and catalytic properties. This limitation could be lifted by using less surfactant or no surfactant at all, and working with two-dimensional structures such as clay minerals [102]. However, cleaning procedures for microemulsion-synthesized nanoparticles have recently been proposed as well. A first cleaning procedure involves the oxidative stripping of a CO monolayer adsorbed on the particles, and has been used for decontaminating microemulsion-synthesized Pt nanoparticles without loss of crystalline structure [103]. This method has also been applied for the decontamination of Pt-based alloys nanoparticles [104]. In our group, we have used the electrogeneration of free, highly reactive hydroxyl radicals at high overpotentials on BDD to clean microemulsion-synthesized Pt nanoparticles supported on diamond and stabilized by an additional Nafion® layer [29]. It has been observed that these hydroxyl radicals could also participate in the methanol oxidation process.

In summary, it can be said that the microemulsion method is a very powerful and efficient tool to produce metal, metal oxide, and metal alloy nanoparticles. This technique allows nanoparticles of controlled size and composition to be synthesized, can be applied to a broad range of compounds, and is very simple to perform from a practical point of view. The reduction of metal precursors (salts) takes place in compartmentalized nanoreactors (inverse micelles) limiting the growth of particles to their own dimensions, thanks to the stabilizing surfactant layer. Moreover the surfactant layer prevents particle from aggregating.

6. THE ELECTROCHEMISTRY OF PLATINUM

In this section the electrochemical and electrocatalytic behaviour of Pt-based electrodes that are well-known catalytic surfaces will be reviewed. Special attention will be paid to the electrooxidation of alcohols (mainly methanol and ethanol), given the importance of this reaction type in the technology of Direct Alcohol Fuel Cells (DAFC) [105-107]. Mechanisms proposed in the literature and the problems associated with these processes (mainly those of surface poisoning) will be presented, as well as the solutions to these problems currently being developed in this field, together with the action modes hypothesized. For this purpose, the DAFC will first be briefly presented. The electrochemical response of Pt electrodes in the

presence and absence of alcohols will be analyzed and interpreted. The overall reaction mechanism will be discussed in greater detail, with particular emphasis on the importance of factors such as reaction kinetics, adsorbed intermediates, or the potential of OH discharge. In conclusion, the effects of alloying (or mixing) of Pt with another transition metal will be highlighted.

## 6.1. Introduction to the Direct Alcohol Fuel Cell (DAFC)

The development and application of *Fuel Cells* (FC) certainly constitutes one of the topics that has motivated, and still is motivating, numerous efforts of the electrochemical community. This technology fundamentally seeks to provide a viable solution to the problems of limited availability and atmospheric pollution inherent in the use of fossil fuels. One of the most important components for the development of FC is the electrocatalyst. Finding new and better electrocatalysts undoubtedly is one of the keys to the development of FC able to compete with the internal combustion engines in cars, to batteries fit for portable systems (mobile phones and computers), and to FC-based electricity and heat generation systems.

The first true fuel cell was developed by Sir William Grove in the first half of 19th century. Grove demonstrated that electricity could be generated from the electrochemical reactions of hydrogen oxidation and oxygen reduction taking place at separate electrodes. This "primary" FC has since been improved continuously, and new types of FC were established. The FC existing today usually are according to the nature of their electrolytes: *(i)* Alkaline FC, *(ii)* Proton Exchange Membrane FC, *(iii)* Phosphoric Acid FC, *(iv)* Molten Carbonate FC, and *(v)* Solid Oxide FC. Which type FC recommended will depend on the application and environment selected by the user.

The operating mode of all of these FC is basically the same. Oxidation of the fuels (hydrogen, methanol...) takes place at the anode generating electrons and protons. Reduction of oxygen occurs at the cathode. The overall process yields water and electrical current, as well as CO_2 when an alcohol is used as the fuel. The subject of this thesis is the synthesis and characterization of different Pt-based nanoparticulate electrocatalysts that can be used in alcohol-fed FC, therefore, only the Direct Alcohol Fuel Cell (DAFC) will be presented in greater detail below. The use of liquid fuels (methanol or ethanol) is one of the most interesting solutions to avoid problems in the storage and handling of the fuel that are decisive for practical applications in vehicles and portable instrumentation. Important aspects for a possible industrial application of the DAFC (based on PEMFC) are the development of better catalysts, both for the cathodic and anodic processes, so as to reduce the required overpotentials and also

the surface poisoning that occurs at the anode, as well as improvements of the separating membranes, so as to avoid the leakage of alcohol from the anode compartment to the cathode causing lower working potentials and loss of fuel.

A schematic view of a direct ethanol fuel cell (DEFC) is shown in Figure 2.10. The catalytic material (in general Pt-based nanoparticles) is dispersed on a convenient substrate so as to stabilize the catalyst nanoparticles and to reduce the amount of precious metal used. High-surface-area, electrically conducting substrates (graphite, carbon blacks, and activated carbon) are chosen in order to achieve high dispersion of the electrocatalyst. Other supports are feasible, particularly so the proton exchange membranes (PEM) that are solid electrolytes. When a DEFC is operating an ethanol-water mixture (a few percent by weight to make a 1 to 2 M ethanol solution) is circulated through the anode compartment while oxygen from air flows through the cathode compartment. The PEM (usually Nafion$^®$) remains wet when in contact with the ethanol solution used as the anolyte, which is particularly important when working at high temperature (100-130°C). Under these conditions some pressure is applied in order to prevent the solution from boiling off. A direct methanol fuel cell (DMFC) follows exactly the same principle, the only difference being that methanol rather than ethanol is used as fuel. The oxidation of the fuel takes place at the anode following Equations 2.30 and 2.31 for a DMFC and a DEFC, respectively:

$$CH_3OH + H_2O \rightarrow CO_2 + 6e^- + 6H^+ \tag{2.30}$$

$$C_2H_5OH + 3H_2O \rightarrow 2CO_2 + 12e^- + 12H^+ \tag{2.31}$$
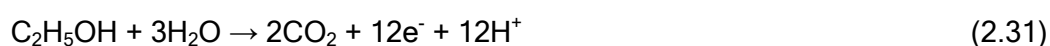
From a knowledge of the overall reactions, reversible anode potentials under standard equilibrium conditions can be calculated from thermodynamic data. This yields values of E^- of 0.046 V vs. SHE and 0.084 V vs. SHE for DMFC and DEFC, respectively. In both cases the reduction of oxygen occurs at the cathode (see Equation 2.32):

$$1/2O_2 + 2H^+ + 2e^- \rightarrow H_2O \tag{2.32}$$

for which the electrode potential is E^+ = 1.229 V vs. SHE. The standard electromotive force (emf) of the different cells can be calculated as follows:

$$E_{emf} = E^+ - E^- \tag{2.33}$$

giving values of E_{emf} of 1.183 V and 1.145 V for the DMFC and the DEFC, respectively. Taking into account the overall combustion reactions the theoretical mass energy density (W_e) of both the two fuels can be calculated, and values of 6.09 kWh kg^{-1} and 8.01 kWh kg^{-1} can be obtained for methanol and ethanol, respectively. The relatively good energy density of the alcohols, as compared to those of hydrocarbons and gasoline (10-11 kWh kg^{-1}) makes them viable alternative energy vectors for electric vehicles, for instance.
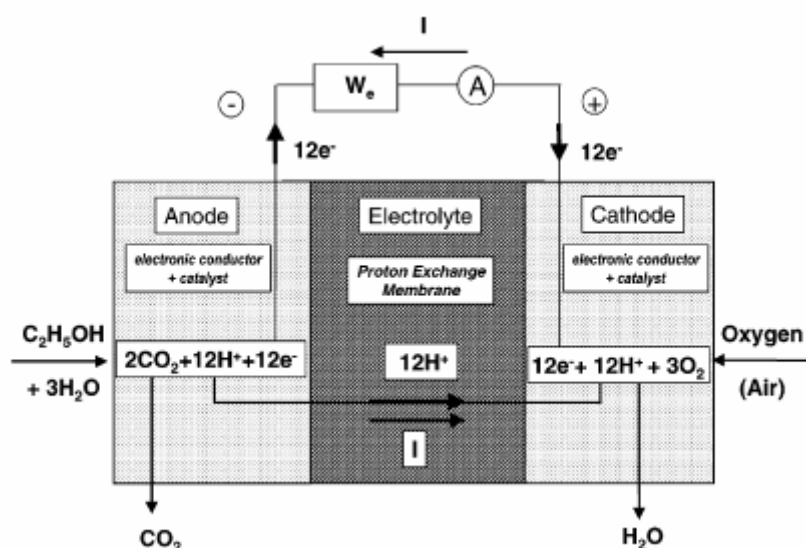
Figure 2.10: Schematic of a direct ethanol fuel cell [108].

These thermodynamic data look attractive, but the kinetics of alcohol oxidation is quite complicated, leading to high anodic overpotentials, particularly at platinum electrodes. Without any doubt, therefore, a practical DAFC critically depends on more efficient electrocatalysts, which must fulfil a series of essential requirements. First, they must by highly active toward the electrochemical oxidation of the fuel at the anode, as well as toward the oxygen reduction at the cathode. The number of reactive sites must be as high as possible. Secondly, they must have a long life and high stability in order to maximize the working life of the batteries. Thirdly, a good electrical conductivity must exist between the electrocatalysts and their supports. Lastly, they must be as cheap as possible per watt produced, and available in large amounts with a high reproducible quality. The reactions that occur at the anode and cathode must take place as close as possible of their thermodynamic potentials.

On a clean platinum electrode, initially a high activity for the oxidation of methanol is seen, but it quickly decreases due to the formation of intermediates (CO_{ads}) that are strongly adsorbed on the surface. Once formed, these intermediates can only be eleiminated by their oxidation at higher potentials. In the conversion of these adsorbates to CO_2, the Pt-CO bond must be broken by hydroxyl radicals. For this reason new electrocatalysts based on Pt (which is necessary to produce breakage of the C-H bonds in methanol), and modified with a second metal (Ru, Sn, W, Re...) able to form $^{\bullet}OH_{ads}$ at lower potentials than Pt, have been developed. The $^{\bullet}OH_{ads}$ must be generated from water discharge near Pt sites blocked by CO, to facilitate the reaction between this adsorbate and the OH, resulting in elimination of the poison and its transformation to CO_2 (bifunctional mechanism, see ref. [109]).

6.2.   Electrochemical response of Pt

Both in pure supporting electrolytes and in the same electrolytes containing an alcohol, the electrochemical response of Pt is the result of complex consecutive surface transitions: adsorption and desorption processes, oxide formation, or surface rearrangement. Platinum being a rather universal catalyst, its electrochemistry has been widely studied during recent decades, also in view of the applicability of Pt surfaces in DAFC technology.

A typical cyclic voltammogram (CV) of a polycrystalline Pt electrode is shown in Figure 2.12. This CV can be divided in four different domains (labelled 1 to 4 on Fig. 2.12) reflecting the surface transitions occurring on Pt during potential cycling. In this picture, the peaks are numbered according to their order of appearance with increasing potential. At cathodic potentials (0-0.3 V), reversible peaks H_A and H_C due to the adsorption and desorption of hydrogen on different crystallographic planes of the Pt surface are observed (region 1). The following flat feature can be attributed to the double-layer region during which water is adsorbed on Pt (region 2). It was shown that at 0.35 V, orientation of adsorbed water on Pt(111) electrode in $HClO_4$ solutions changes from hydrogen down to oxygen down indicating that the potential of zero charge is close to this potential value [110]. Increasing anodic potential results in the formation of successive O_A peaks indicative for the formation of different Pt oxides (region 3). After these peaks a plateau appears (region 4 in Fig. 2.12); this plateau precedes a strong current increase due to the evolution of O_2 on Pt (not shown in Fig. 2.12). In the reverse scan, Pt oxides are all reduced during a unique and irreversible process (peak O_C) [111].
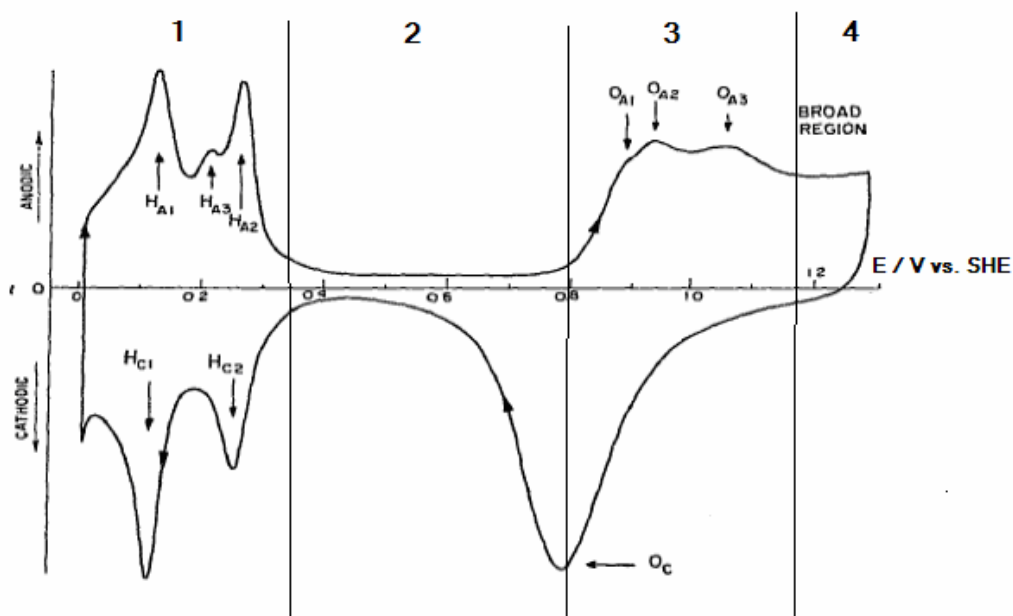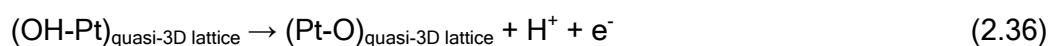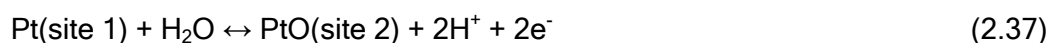
Figure 2.12: Typical CV profile of a polycrystalline Pt surface recorded in 0.5 M H_2SO_4 at 100 mV s^{-1}. Adapted from [111]. Region 1 corresponds to the adsorption and desorption of hydrogen on different crystallographic planes of the Pt surface, region 2 corresponds to the double-layer region, region 3 corresponds to the formation of different Pt oxides and region 4 corresponds to the plateau of Pt oxides preceding the evolution of O_2 (not shown). During the reverse scan, Pt oxides are all reduced in a unique and irreversible process (peak O_C).

The mechanism of the formation of surface Pt oxides is of crucial importance, and has been the subject of numerous studies. It is basic to an understanding of the electrocatalytic oxidation of organics on this metal. It is well established and reasonable that the presence of an oxide film on a noble metal will affect the mechanism and kinetics of anodic processes at the surface, by *(i)* affecting the thermodynamics of the reaction at the double layer, *(ii)* changing the electronic properties of the metal surface, *(iii)* imposing a barrier to charge transfer across the surface oxide film, and *(iv)* influencing the adsorption behaviour of reaction intermediates and/or products at the catalytic surface [112]. Earlier explanations on these phenomena have had to be revised on the basis of new experimental insights. Initially, it was considered that oxide growth at Pt electrodes produced by potential cycling or potentiostatic polarization proceeds via the formation of hydroxide species. It has also been recognized now that the crystallographic orientation at the surface and the electrolyte composition define a unique interface with specific metal-anion interactions which in due course determine the beginning potential of oxide growth. In aqueous H_2SO_4, oxide formation on Pt begins at 0.85 V vs. SHE, and the following oxide formation mechanism was proposed for this medium [111, 113]:
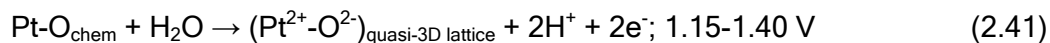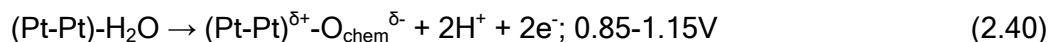
$$Pt + H_2O \rightarrow Pt\text{-}OH_{ads} + H^+ + e^- \qquad\qquad (2.34)$$

$$Pt\text{-}OH_{ads} \rightarrow (OH\text{-}Pt)_{quasi\text{-}3D\ lattice} \qquad (2.35)$$

$$(OH\text{-}Pt)_{quasi\text{-}3D\ lattice} \rightarrow (Pt\text{-}O)_{quasi\text{-}3D\ lattice} + H^+ + e^- \qquad (2.36)$$

where Eq. 2.34 refers to the oxidation of H_2O molecules with formation of adsorbed hydroxyl groups (OH_{ads}) between 0.85 and 1.10 V vs. SHE, Eq. 2.35 represents the interfacial place exchange between OH_{ads} and surface Pt atoms, and Eq. 2.36 represents the subsequent oxidation of OH within the quasi-3D lattice resulting in the departure of H^+ (potential in the 1.10-1.40 V range). This mechanism was proposed in view of reversibility of Pt surface oxidation in its initial stage, *i.e.* for surface coverages (θ) by OH_{ads} given by $\theta_{OH} \leq 0.20$. The different CV peaks in the 0.85-1.10 V potential domain were attributed to different surface compounds (such as Pt_4OH, Pt_3OH and Pt_2OH) and were not considered to originate from the polycrystalline nature of the electrode. This mechanism was questioned by Birss *et al.* [114], who reasoned, that it would require two distinct regions of mass response, one corresponding to the addition of 17 g mol^{-1} in the first step (Eq. 2.34) and the other one corresponding to a mass change of -1 g mol^{-1} caused by the departure of H (Eq. 2.36). In their electrochemical quartz-crystal microbalance (EQCM) measurements, however, a continuous mass increase in the 0.85-1.40 V potential region was observed [114], thus contradicting the above mechanism. A two-electron mechanism of Pt oxide formation excluding OH_{ads} as an intermediate was proposed by Harrington on the basis of simulation of the ac voltammograms recorded across the region of Pt oxide film formation [115]. This simpler mechanism was presented as follows:

$$Pt(site\ 1) + H_2O \leftrightarrow PtO(site\ 2) + 2H^+ + 2e^- \qquad (2.37)$$

$$PtO(site\ 2) \leftrightarrow PtO(site\ 3) \qquad (2.38)$$

where it was supposed that the rate-determining step (rds) was the two-electron oxidation of a Pt atom with concomitant migration of the atom out of its metal lattice (Eq. 2.37), and that the oxidized species diffuses across the surface until it gets stuck at a growing oxide island (Eq. 2.38) or is reduced back to Pt metal. The earlier mechanism expressed by Eqs. 2.34 to 2.36 cannot be reconciled with the EQCM and ac voltammetry results.

The mechanism of initial Pt oxidation has been recently re-examined by combined CV and electrochemical quartz-crystal nanobalance (EQCN) measurements where nanogram interfacial mass changes can be measured and directly correlated with the CV features [112]. This corresponds to an in-situ determination of the molecular weight increase of the Pt surface oxide. A value of 15.8 g mol^{-1} was found, which suggests that one O-atom is added to the surface, and PtO is the oxide species formed. It was also ascertained that the surface oxide was anhydrous, and that the process did not involve OH_{ads} as an intermediate. It was

suggested that surface oxidation proceeds via a progressive coordination of chemisorbed O adatoms (O_{chem}) to the Pt substrate. Therefore, the following mechanism of Pt surface electrooxidation was proposed (Eqs. 2.39 to 2.41):

$$Pt + H_2O \rightarrow Pt^{\delta+}\text{-}O^{\delta-}H_2; \ 0.27\text{-}0.85 \text{ V} \tag{2.39}$$

$$(Pt\text{-}Pt)\text{-}H_2O \rightarrow (Pt\text{-}Pt)^{\delta+}\text{-}O_{chem}^{\delta-} + 2H^+ + 2e^-; \ 0.85\text{-}1.15V \tag{2.40}$$

$$Pt\text{-}O_{chem} + H_2O \rightarrow (Pt^{2+}\text{-}O^{2-})_{quasi\text{-}3D \ lattice} + 2H^+ + 2e^-; \ 1.15\text{-}1.40 \text{ V} \tag{2.41}$$

The first step is an interaction of H_2O molecules with the Pt electrode at potential values between 0.27 and 0.85 V vs. SHE. At these potentials the Pt surface atoms carry a partial positive charge that attracts the negatively charged oxygen atoms in the dipolar water molecules (Eq. 2.39). In the second step, the discharge of half a monolayer (ML) of H_2O molecules takes place and results in the formation of 0.5 ML of O_{chem}. (Eq. 2.40). This process is accompanied by charge transfer. The third step is discharge of the second half-monolayer of H_2O molecules exhibiting strong interfacial interactions with the Pt surface. As the second half-monolayer of O_{chem} starts to build up, strong lateral repulsive dipole-dipole interactions set in which involve the dipole moment of the $(Pt\text{-}Pt)^{\delta+}\text{-}O_{chem}^{\delta-}$ surface compound. These interactions lead to an interfacial place exchange process of the initial half-monolayer of O_{chem} adatoms with the Pt surface atoms producing a surface PtO lattice in which the repulsive interactions are minimized. This place exchange is accompanied by completion of the charge transfer from Pt to O_{chem}, which leads to a quasi-3D surface lattice built up from Pt^{2+} and O^{2-}. Another important mechanistic aspect is the role co-adsorbed anions might play in the development of surface oxide. It is believed now that co-adsorbed anions slightly affect the interfacial mass change in the double-layer region, and have practically no impact on the oxide growth. It was shown by radio-tracer studies, for instance, that the anions ((bi)sulfate and perchlorate), absorbed either on polycrystalline or on single-crystal Pt electrodes, desorb at the onset of the surface-oxide formation and do not influence the growth process [116, 117]. Therefore, the surface-oxide formation mechanism described above (see Eq. 2.39 to 2.41) appears not to be obscured by concurrently occurring processes involving anions. As a final remark, it must be pointed out that potential cycling on a Pt electrode can result in more or less severe modifications of the metal surface (and its properties) due to phenomena such as dissolution or activation [118].

6.3. Effects of alloying

It has already been stated that the electrochemistry of Pt was widely studied in the past, amongst other reasons, because of the utility of Pt as an electrocatalyst for methanol and ethanol electrooxidation that are reactions of prime interest for DAFC

technology. However, during methanol electrooxidation on Pt the catalytic surface is readily poisoned by strongly adsorbed reaction intermediates (mainly CO) that block the active sites [119]. An approach to circumvent this problem consists in alloying Pt with a second transition metal (Ru, Sn, Mo, Ni...). Ternary and even quaternary Pt-based alloys have also been suggested [120-123]. The role of the alloying metal in alcohol electrooxidation will be developed in the following Sections 6.3.1 and 6.3.2 below; suffice it here to say that the alloying metal enhances the electrocatalytic activity of pure Pt via a cooperative effect [109] or a ligand effect [124].

The second metal, M, in the Pt-M alloys can be selected from a wide range of candidates. Watanabe and co-workers, for instance, in a series of papers have systematically tested the effect of various "deposited adatoms" including As [125], Au [126], Ru [109, 127], Sn [128-130] or Ge [128], on the electrocatalytic activity of Pt. As a general trend, they observed that the electrocatalytic activity of Pt was increased by the addition of "oxygen-adsorbing adatoms". Anderson *et al.* later undertook a theoretical study of an extended range of alloying metals with the aim of defining those that would lead to enhanced methanol fuel cell performance [131]. For this purpose, they evaluated the ability of substitutional atoms in the Pt(111) surface to attract a water molecule and become substrates for adsorbed OH (OH_{ads}). It was found that transition metals to the left of the coinage metals exhibit activity for generating OH_{ads}. The early metals of the first transition series appeared especially promising, and the early metals of the second transition looked potentially active for attracting and dissociating H_2O. It was suggested to experimentally verify these findings via modern alloy preparation and surface characterization techniques.

Considering the results of all these studies, the Pt/Ru system still stands out as the most efficient electrocatalyst for methanol electrooxidation. It had actually been found over 40 years ago already that alloying Pt with Ru could result in a significant enhancement of the efficiency of methanol electrooxidation [132]. This has been explained by OH_{ads} being produced by water dissociation at lower potentials than on Pt [109]. Subsequently, this system has attracted very wide interest (see for example refs. [133-135] and references therein). Almost 20 years ago it was found that with tin added to platinum could reduce the potential required for the oxidation of organic fuels by several hundred of millivolts [136]. The reasons for this enhancement of electrocatalytic activity are still controversial, and under debate. These two systems, Pt/Ru and Pt/Sn, will be more closely analyzed in the following two subsections. The focus will be on the oxidation mechanisms and kinetics of organic substances.

6.3.1. Pt/Ru alloys

Alloys of Pt/Ru are up to now the most efficient system for the electrocatalysis of methanol and CO oxidation. The Pt/Ru anodes exhibit a lower CO oxidation potential and, as a consequence, an enhanced CO tolerance and a lower poisoning rate than Pt anodes. This is commonly explained in terms of the bifunctional mechanism according to oxygen-containing species (OH) are present on Ru at much lower potentials than on Pt [109]. The electronic effect, or weakening of the Pt-CO bond strength by a modification of the electronic structure of Pt that is induced Ru, can also play a role in this behaviour.

The Pt/Ru alloys have been mainly studied in two directions: *(i)* as real catalysts, or *(ii)* as model electrodes in basic studies. Highly different types of alloys have been used, and a variety of preparation methods were used. The most common preparation methods were the chemical [137] and electrochemical [138] reductive co-deposition of the constituents, as well as the deposition of Ru particles with different sizes on a Pt substrate [109]. Catalysts intended for practical applications were more often prepared by impregnation of high-surface-area substrates with metal salts [139]. In most of the cases the exact composition of the external catalyst layer was unknown. Moreover, often some kind of "surface activation" of the electrode by heating in a gas stream or oxido-reduction in the electrolyte was applied. Even if the alloy surface composition was known at the initial stage, it is obvious that such treatments alter the surface properties; for instance, heating results in surface segregation of either Pt or Ru, depending on the gas atmosphere [140], while Ru starts to be oxidized at a potential of 0.95 V vs. SHE and is lost by corrosion at 1.3 V [141]. It is evident, then, that the surface composition should be checked after the activation treatments. The structures of Pt/Ru could be determined in the pure supporting electrolyte from the peaks ascribed to adsorption and desorption of hydrogen and oxygen species. Contrary to the well-known CV recorded at polycrystalline Pt, the CV for pure Ru exhibits a structureless hydrogen region and a higher current density in the double-layer region (between 0.4 and 0.8 V). The latter observation is due to the adsorption of oxygenated species at potential values as low as 0.25 V vs. SHE [141]. The CV of the alloys change slowly from the shape found at pure Ru to that found at pure Pt surface concentration is increased. Thus, cyclic voltammetry is a powerful tool providing information as to the alloy component (Pt or Ru) dominating the surface properties of a given alloy.

In summary, it can be stated that the addition of Ru decreases the overpotential for CO oxidation on Pt. This makes Pt/Ru alloys good electrocatalysts for of CO and methanol oxidation. Pre-treatments (activations) of the alloy surface can dramatically

alter its properties; it is well-known, for instance, that Ru oxides are formed and Ru dissolution occurs when the potential is cycled to values beyond 0.95 V vs. SHE, or that exposure to a gas stream can induce surface segregation of either Pt or Ru, depending on the conditions. When the potential window is limited to a domain in which no corrosion of Ru can take place, cyclic voltammetry allows the determination of the dominating surface character (Pt or Ru). This can give some preliminary insights on the electrocatalytic activity of the different alloys, since Pt is the only metal capable of dissociatively adsorbing methanol.

6.3.2. Pt/Sn alloys

Alloys between Pt and Sn have attracted wide interest for their use as electrocatalysts for methanol, ethanol and CO oxidation. Such systems are known to be among the more efficient ones for the electrocatalysis of methanol oxidation, but have been most widely studied as electrocatalyst for ethanol oxidation. It is believed, in fact, that catalysts of this type can activate scission of the C-C bond in the ethanol molecule; however, results reported in literature are quite controversial and still subject of discussions. Large differences observed between the results obtained by several groups point to the importance of a controlled preparation mode of the catalytic surface. The surface composition of Pt/Sn alloys can for instance be determined by chemical titration of carbon monoxide [142]. In this method, a gas is used that is selectively adsorbed on one of the components (here CO on Pt), and the assumptions must be made that *(i)* the number of adsorbed molecules per surface atom does not change when the element is diluted in the surface and *(ii)* chemisorption does not change the surface composition (through surface segregation). As in the case of Pt/Ru alloys, CV can be used to determine the dominating surface character (either Pt or Sn) of a given alloy. However, a crucial point in the case of Pt/Sn surfaces would be the surface distribution of elements rather than the true composition, since intermediates generated by methanol dissociative adsorption on one hand and water decomposition on the other hand are separately adsorbed on Pt (CO) and Sn (OH) [143] (see the section below).

6.4.   Alcohols electrooxidation on Pt and Pt-based alloys

The electrooxidation of alcohols being important for DAFC technology, this reaction has been the subject of numerous studies published over a number of decades [144]. Much of this work was done at Pt and Pt-based electrodes. Methanol has been the preferred fuel, mainly because of its availability, ease of oxidation, simple molecular structure (no C-C bonds) [145-148]. The electrooxidation of

alcohols having a longer aliphatic chain has been studied as well; among them, ethanol has attracted special attention owing to certain advantages over methanol: lower toxicity, production from biomass, and a higher theoretical mass energy density [149-152]. Some efforts were made toward the electrooxidation of 2-propanol [153-155]. However, C-C bond scission is necessary in these cases in order to achieve the complete oxidation to CO_2 and H_2O. After many decades of research, this still remains problematic [151, 156]. The present section will focus on the electrooxidation of methanol and ethanol at Pt and Pt-based alloys electrodes. Among Pt-based alloys, Pt/Ru and Pt/Sn will be more specifically highlighted as electrocatalysts.

6.4.1. Methanol electrooxidation

The electrooxidation of methanol at Pt has been studied and reviewed over a long period of time [119, 157, 158]. The overall oxidation reaction involves the release of six electrons, and can be described by the following equation:

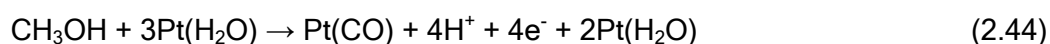$$CH_3OH + H_2O \rightarrow CO_2 + 6H^+ + 6e^- \tag{2.42}$$

The electrochemical environment of Pt has been studied experimentally in the presence of methanol as a function of the applied potential, by infra-red spectroscopy [159, 160] and sum frequency generation (SFG) [161-163]. It was the aim of these studies to elucidate the nature of the adsorbed species on the Pt surface by the electrosorption of methanol, and thus to clarify the adsorption mode of the alcohol and its oxidation mechanism. It appears from these studies that adsorbed CH_3OH cannot be detected on Pt; methanol chemisorption on platinum is dissociative, and mainly leads to adsorbed CO acting as a poison for the direct electrocatalytic oxidation of methanol, since it blocks the reactive sites on the Pt surface. These studies revealed that methanol adsorption on Pt is a surface-sensitive process, so that methanol electrooxidation on Pt also is surface-sensitive. Carbon monoxide was the mainly detected adsorbate. However, its nature (linearly or bridge-bonded) was seen to depend on the crystallographic orientation of the Pt electrode and on the applied potential, as well as on methanol concentration [159-163]. Methanol adsorbs at Pt surface as soon as hydrogen is desorbed, and is readily dehydrogenated into CO and COH/CHO [164]. Fourier-transform infra-red spectroscopy (FTIR) measurements involving labelled methanol (CD_3OH) indicated that the COH/CHO species actually was COH [165]. Other adsorbates such as CH_xO (x = 1, 2, 3) have been identified at low methanol concentrations and short reaction times. Adsorbed CO is then oxidized to CO_2 when the potential reaches values of 0.5 V approximately. The activity of the different Pt planes increases in the order Pt(111) < Pt(110) < Pt(100) [160]. This is in good agreement with CV results on single-crystal electrodes

[166], from which it was stated that the response of a polycrystalline electrode only poorly results from those of Pt(111). It can be reasonably concluded that the irreversible adsorption of methanol on Pt is accompanied by the simultaneous and spontaneous dehydrogenation of the molecule (combined with charge transfer) that is catalytically activated by Pt. Methanol adsorption on Pt should be regarded as a sequence of fast, consecutive dehydrogenation steps as described in Equation 2.43, rather than a simple adsorption phenomenon. All the steps listed in Eq. 2.43 are accompanied by the release of one proton and one electron, and this sequence leads to the formation of adsorbed CO:

$$CH_3OH \rightarrow CH_2OH_{ad} \rightarrow CHOH_{ad} \rightarrow COH_{ad} \rightarrow CO_{ad} \qquad (2.43)$$
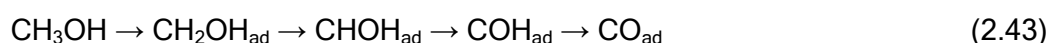
It must be pointed out here that polycrystalline bulk Pt and Pt nanoparticles do not behave in exactly the same manner with respect to methanol adsorption. It was shown by Christensen *et al.* [167] who compared the behaviour of Pt particles (15 nm) with that of bulk surfaces that methanol adsorption takes place at a lower potential on particles (< 50 mV, as compared to 150 mV for bulk Pt). These authors postulated that migration of singly bonded CO from terraces to edge or kink sites occurred on particles, and that the appearance of triply bonded CO was much more pronounced on particles. Overall methanol oxidation including dehydrogenation followed by oxidation of the poisoning surface residue can thus be described in terms of Equations 2.44 to 2.46:

$$CH_3OH + 3Pt(H_2O) \rightarrow Pt(CO) + 4H^+ + 4e^- + 2Pt(H_2O) \qquad (2.44)$$

$$Pt(H_2O) \rightarrow Pt(^\cdot OH) + H^+ + e^- \qquad (2.45)$$

$$Pt(CO) + Pt(^\cdot OH) \rightarrow 2Pt + CO_2 + H^+ + e^- \qquad (2.46)$$

The reaction described by Eq. 2.45 is commonly accepted, but the nature of the oxygen-containing species that oxidize CO_{ads} remain debated. As to the potential required for this reaction, one may also imagine that removal of the poison occurs as the result of a direct surface reaction with water molecules or reversible Pt surface oxides (Equations 2.47 and 2.48)

$$Pt(CO) + H_2O \rightarrow Pt + CO_2 + 2H^+ + 2e^- \qquad (2.47)$$

$$Pt(CO) + PtO_x \rightarrow Pt + PtO_{x-1} + CO_2 \qquad (2.48)$$

This complex overall mechanism is well summarized in the catalytic cycle of methanol electrooxidation at Pt presented in Figure 2.12. All the steps described by Equations 2.44 to 2.48 are clearly distinguishable in this picture, while the successive dehydrogenation steps are pictured in more detail.
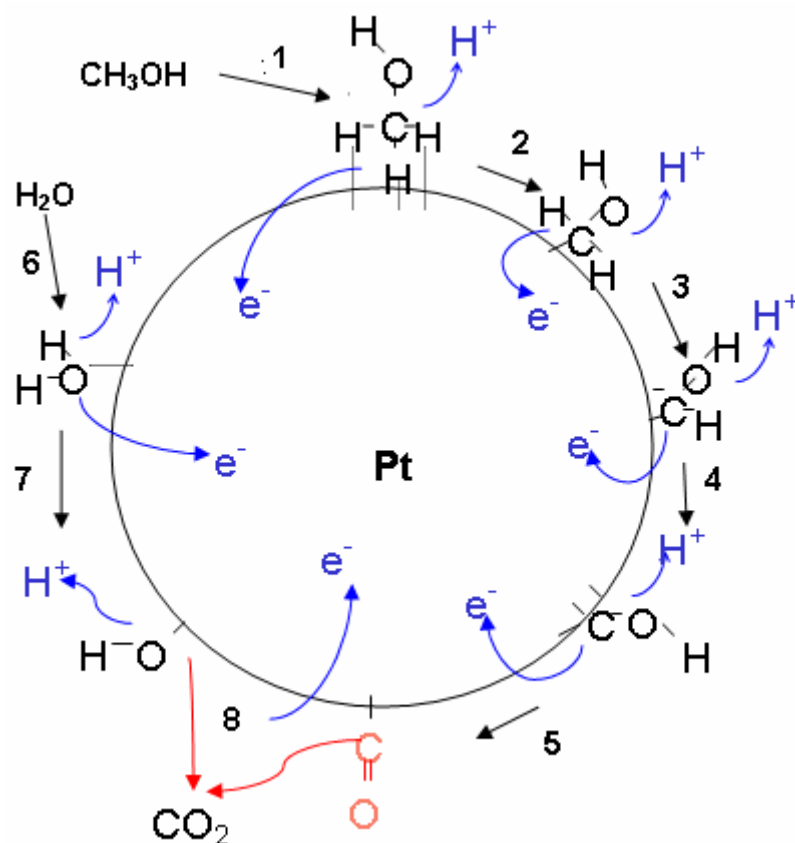
Figure 2.12: Catalytic cycle of methanol electrooxidation at a Pt electrode. This cycle involves the following steps: adsorption (1) of one methanol molecule on three adjacent Pt sites, followed by the four successive, fast dehydrogenation steps (2-5) of adsorbed methanol leading to CO. In parallel water activation and adsorption (6) of hydroxyl radicals at Pt sites (7) take place in parallel. The surface reaction between adsorbed CO and ˙OH finally yields free sites and CO_2 (8).

However, the limitations of the Pt electrocatalyst derive from the fact that water activation on this metal (Eq. 2.45) will not occur at potential values lower than 0.5 V vs. SHE, while the dissociative adsorption of methanol takes place as early as 0.046 V vs. SHE. Therefore, the rate-determining step (rds) of this mechanism is the activation of water on Pt. It follows that the surface is poisoned by adsorbed CO that blocks the active sites and the efficiency of the catalytic surface may dramatically decrease. This fact, taken together with the changes induced on the Pt surface by potential cycling (see section 6.2 of this Chapter), also provide the explanation for the unusual profile of cyclic voltammograms recorded during methanol electrooxidation an Pt (see Figure 2.13).

These CV exhibit two well-defined oxidation peaks, the first peak occurring during the forward scan, the second peak occurring at lower potential than the first peak during the reverse scan (Fig. 2.13.B). For sake of clarity, a CV recorded at a Pt electrode in the absence of methanol is reported in Figure 2.13.A, and the thermodynamic potential of methanol electrooxidation on Pt is marked on Fig. 2.13.B

by an arrow. As already stated, dehydrogenation of MeOH on Pt takes place at potentials as low as 0.05 V vs. SHE (Eqs. 2.43 and 2.44). It follows that the catalytic surface is blocked by adsorbed CO (poison); no further dissociative adsorption steps are possible, and the oxidation current is very low. At 0.5V, water is activated on Pt (Eq. 2.45). Adsorbed hydroxyl radicals are produced by water activation; these radicals can react with adsorbed CO to yield the final product CO_2 as well as free Pt sites for further methanol adsorption. Hence methanol oxidation can take place again, and the oxidation current increases. Continuing the potential scan results in the formation of Pt surface oxide around 0.8 V (see Eqs. 2.39 to 2.41). Methanol adsorption is not possible on Pt oxides, hence the current decreases, explaining the current drop in the forward-scan oxidation peak. As the potential is scanned in the reverse direction, the Pt oxides are reduced during a unique and irreversible process, so that methanol adsorption once again is possible and the oxidation current can increase; but when a potential value of 0.5 V is reached, water is no longer activated and the oxidation current decreases again, which leads to the reverse-scan oxidation peak.
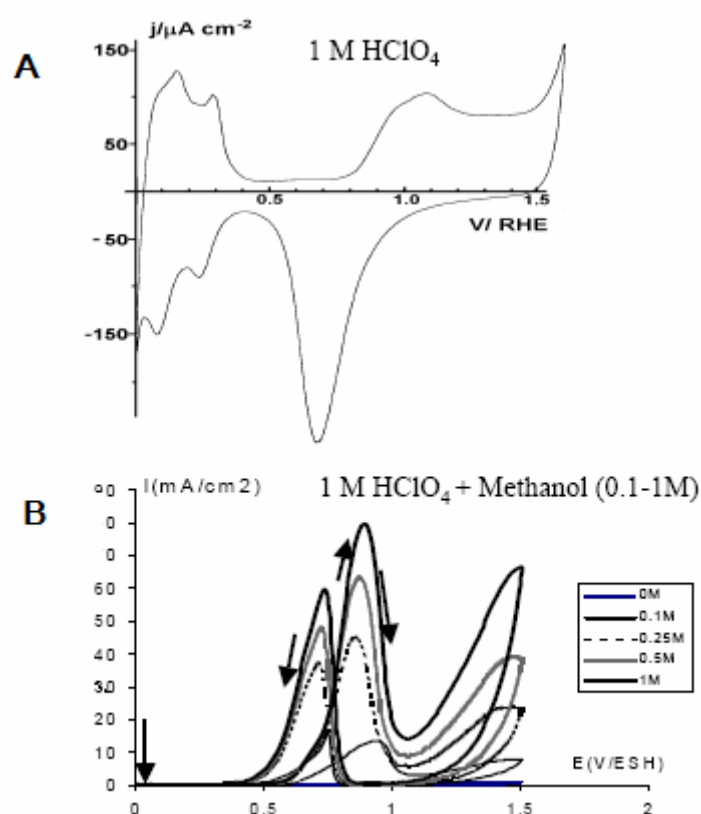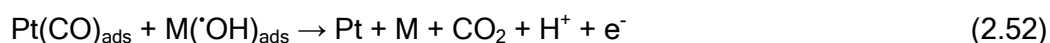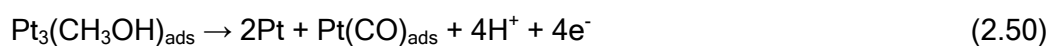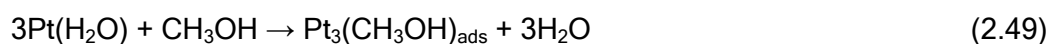

Figure 2.13: CV of a Pt electrode in the absence (**A**) and presence of methanol (**B**).

It is crucial, therefore, to find new catalysts capable of solving the problem of surface CO poisoning at low potentials. The characteristics of these new catalysts should be twofold: *(i)* decreasing the overpotential needed for water activation, and

(ii) weakening the Pt-CO bond to favour poison removal. Efficient Pt/M alloy catalysts for electrocatalysis of alcohols oxidation will fulfil these two requirements to an extent that depends on the surface. Appropriate alloying metals will serve to decrease the overpotential needed for water activation and the generation of hydroxyl radicals able to oxidize adsorbed CO. The ability of a wide range of substitutional atoms in the Pt(111) surface to attract a water molecule and to activate the formation of adsorbed $^{\bullet}$OH on them has for instance been calculated using molecular orbital (MO) theory [131]. A weakening of the Pt-CO bond strength can be brought about by electronic interactions between Pt and the alloying metal M; transfer of e^{-} d from M to Pt will result in the modification of Pt electronic properties [124].

The bifunctional mechanism can be seen as a mechanism in which the tasks are divided between the two metals. Platinum is in charge of methanol dehydrogenation, while the alloying metal (most likely ruthenium) should activate water and generate adsorbed hydroxyl radical at lower potentials than Pt. This mechanism can be described by Eqs. 2.49 to 2.52. As in methanol electrooxidation on Pt, a catalytic cycle can be drawn for methanol electrooxidation on a Pt/M bimetallic electrode (see Figure 2.14).

$$3Pt(H_2O) + CH_3OH \rightarrow Pt_3(CH_3OH)_{ads} + 3H_2O \qquad (2.49)$$

$$Pt_3(CH_3OH)_{ads} \rightarrow 2Pt + Pt(CO)_{ads} + 4H^+ + 4e^- \qquad (2.50)$$

$$M + H_2O \rightarrow M(^{\bullet}OH)_{ads} + H^+ + e^- \qquad (2.51)$$

$$Pt(CO)_{ads} + M(^{\bullet}OH)_{ads} \rightarrow Pt + M + CO_2 + H^+ + e^- \qquad (2.52)$$
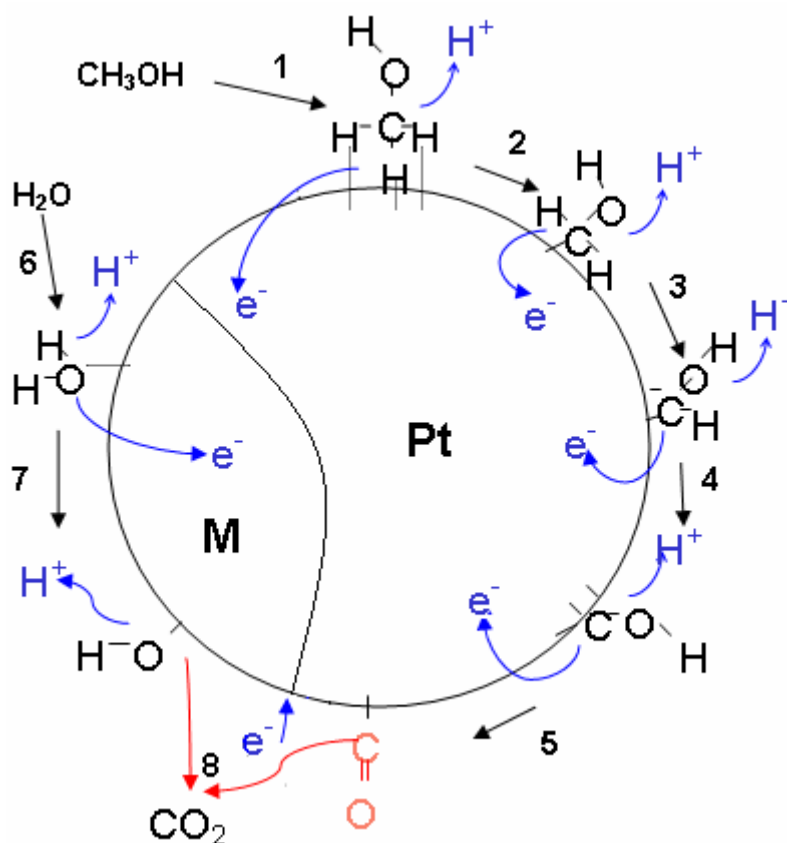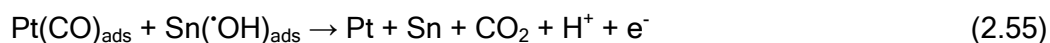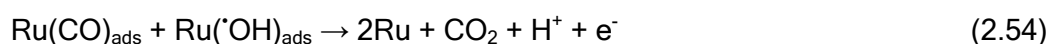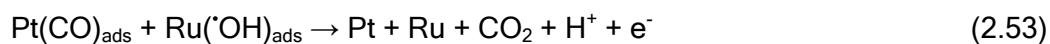
Figure 2.14: Catalytic cycle of methanol electrooxidation at a Pt/M bimetallic electrode. This cycle involves the following steps: adsorption (1) of one methanol molecule on three adjacent Pt sites, followed by the four successive, fast dehydrogenation steps (2-5) of adsorbed methanol leading to adsorbed CO at Pt. In parallel water activation and adsorption (6) of hydroxyl radicals at M sites take place and the surface reaction (7) between adsorbed CO (Pt) and $^\bullet$OH (M) finally yields free sites and CO_2 (8).

It can be seen that the dehydrogenation steps are identical on Pt and Pt/M surfaces. It must been pointed out that many O-adsorbing metals can produce negative effects, by inhibiting methanol adsorption, or many of them are not sufficiently stable under long-term use in acidic media. The only difference between the oxidation mechanisms on the two types of catalysts consists in the activation of water, which occurs on the alloying metal at lower potential than on Pt when an appropriate bimetallic surface is used. The surface reaction between adsorbed CO and OH depends on the nature of M and of its CO and/or OH adsorption abilities. For instance, it was seen that with Pt/Ru alloys, CO could be adsorbed on Pt as well as on Ru sites, with a strong preference for the Pt sites [168]. Therefore, on Pt/Ru the adsorbed CO can be oxidized following both Equations 2.53 and 2.54. To the contrary, only $^\bullet$OH will be adsorbed on the Sn sites of Pt/Sn alloys [143], and the only surface reaction that can occur and yield CO_2 as the final product is described by Equation 2.55:

$$Pt(CO)_{ads} + Ru(^{\bullet}OH)_{ads} \rightarrow Pt + Ru + CO_2 + H^+ + e^- \qquad (2.53)$$

$$Ru(CO)_{ads} + Ru(^{\bullet}OH)_{ads} \rightarrow 2Ru + CO_2 + H^+ + e^- \qquad (2.54)$$

$$Pt(CO)_{ads} + Sn(^{\bullet}OH)_{ads} \rightarrow Pt + Sn + CO_2 + H^+ + e^- \qquad (2.55)$$

According to these equations, it will be obvious that the different adsorbates should be attached to adjacent sites in order to allow oxidation and removal of adsorbed CO to occur. This can be a problem in the case of Pt/Sn alloys, since the adsorption of CO will not take place on Sn sites, which are solely covered by OH. Thus, the structure of the catalytic surface is of crucial importance for an alloy's capacity as an electrocatalyst for methanol oxidation, and a good dispersion of the two metals within the alloy surface is an important requirement.

An alternative explanation for the enhanced electrocatalytic behviour of Pt/Ru and Pt/Sn alloys is the so-called electronic effect, in which the substituting metal (either Ru or Sn) is assumed to reduce the strength of adsorption of CO on Pt. It has for instance been experimentally observed in the gas-phase adsorption of CO on Pt(111)-Sn [169, 170] that the Pt-CO bond strength was weakened in the presence of tin. Some experimental electrochemical results have also been presented in support of this mechanism [171-173]. A modification of the Pt electronic structure induced by Ru, and subsequent weakening of the Pt-CO bond strength on Pt/Ru alloys has been reported [174, 175]. It is an important question, in view of these observations, to determine the relative importance of a ligand effect versus a bifunctional mechanism. Quantum chemical methods are useful tools to study chemisorption and reactions on surfaces, and the adsorption properties of various Pt-based surfaces (adsorption energies of reactants or intermediates) have been studied theoretically in the cases of CO and methanol electrooxidation. It was concluded from such studies that, if both Ru and Sn effectively promote methanol and CO oxidation, their action modes are quite different. It could in fact be shown that the ligand effect plays some role in the oxidation of CO on Pt/Ru but is unimportant on Pt/Sn [176]. It was shown that ruthenium in the alloy catalyst modifies the electronic structure of platinum, thus reducing CO adsorption on Pt sites [177]. Still, the bifunctional mechanism cannot be neglected, and both effects contribute to the CO oxidation process on Pt/Ru, even if the dominating effect in a PEMFC is electronic [134]. It has been found by theoretical arguments while keeping in mind the need of three neighbouring Pt sites for alcohol adsorption determined that the optimum surface atom concentration of Ru was 50 % for CO oxidation, and 7-30 % for methanol oxidation. These theoretical findings are supported by experimental results. Alloying addition of tin and ruthenium are effective in promoting the oxidation of CO_{ads}, but acts differently: it was found that Pt/Sn and Pt/Ru promote the oxidation of two different types of CO_{ads} [178]. It was also seen

that the ternary system Pt/Ru/Sn was more efficient than the two binary ones, presumably due to a cooperation between the two alloying metals in the oxidation of the two types of CO_{ads} [178]. In methanol electrooxidation the enhancing effect of both the two metals was also evidenced [179]. It was seen, too, that the promoting effect of Sn was much more sensitive to the structure of the Pt substrate than the effect of Ru, and that the use of a high area substrate was preferable for better stability of Sn. It was postulated that this susceptibility of Sn could be at the origin of inconsistent literature results on Sn effects in methanol electrooxidation, which varied from significantly enhancing [130, 171] to negative [180], via moderate [136, 181].

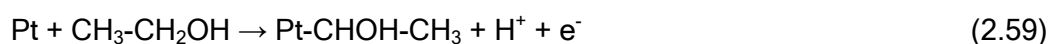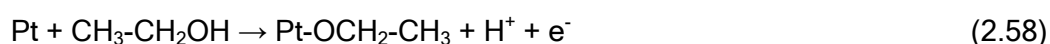### 6.4.2. Ethanol electrooxidation

The case of ethanol electrooxidation is rather more complicated, inasmuch as the complete reaction requires breaking of the molecule's C-C bond. It has also been studied quite thoroughly, since ethanol appears more promising as a fuel for DAFC than methanol. Special efforts were made to determine the reaction mechanisms and identify adsorbed intermediates by means of differential electrochemical mass spectrometry (DEMS), FTIR, electrochemical thermal desorption mass spectroscopy (ECTDMS), and chromatographic techniques (GC, HPLC). Generally, the overall electrooxidation of alcohols is accepted to follow Equation 2.56:
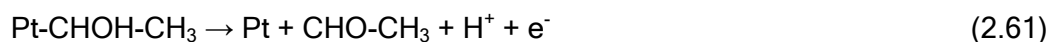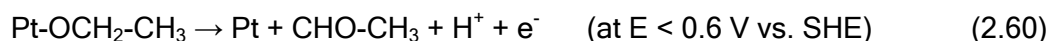
$$Pt + R\text{-}CH_2OH + H_2O \rightarrow Pt\text{-}R_{ads} + CO_2 + 5H^+ + 5e^- \qquad (2.56)$$
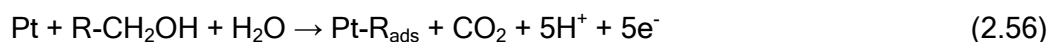
where the adsorbed intermediate species R_{ads} can be further oxidized to CO_2. Thus, it appears that the reaction mechanisms of alcohol electrooxidation on Pt always involve water or its adsorbed residue. Therefore, a good electrocatalyst must activate both alcohol adsorption and water dissociation. In the case of ethanol, the complete oxidation involves 12 electrons per molecule and can be described by Eq. 2.57:

$$C_2H_5OH + 3H_2O \rightarrow 2CO_2 + 12H^+ + 12e^- \qquad (2.57)$$

On pure platinum electrodes, the surface is rapidly poisoned by strongly adsorbed intermediates (CO) resulting from the dissociation of the molecule, as shown by infrared reflectance spectroscopy [182-184]. Other adsorbed species have also been identified, including reaction intermediates such as acetaldehyde or acetic acid, as well as some byproducts [183-185]. A detailed analysis of the reaction products has allowed a better understanding of the reaction mechanism of ethanol oxidation on Pt in acid medium. It involves parallel and consecutive oxidation reactions; ethanol can adsorb on Pt according to two modes (C-adsorbing or O-adsorbing) [183], as described by the following equations:

$$Pt + CH_3\text{-}CH_2OH \rightarrow Pt\text{-}OCH_2\text{-}CH_3 + H^+ + e^- \qquad (2.58)$$

$$Pt + CH_3\text{-}CH_2OH \rightarrow Pt\text{-}CHOH\text{-}CH_3 + H^+ + e^- \qquad (2.59)$$

which represents the initial steps of ethanol adsorption and oxidation. It was shown that acetaldehyde was formed at low potentials (E < 0.6 V vs. SHE) [184] while no acetic acid was detected in this potential range.

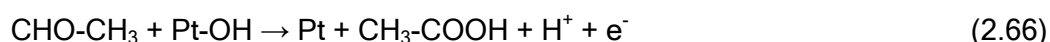$$Pt\text{-}OCH_2\text{-}CH_3 \rightarrow Pt + CHO\text{-}CH_3 + H^+ + e^- \quad \text{(at E < 0.6 V vs. SHE)} \quad (2.60)$$

$$Pt\text{-}CHOH\text{-}CH_3 \rightarrow Pt + CHO\text{-}CH_3 + H^+ + e^- \quad (2.61)$$

When acetaldehyde is formed, it can adsorb on Pt and forms a $Pt\text{-}CH_3\text{-}CO$ species according to Equation 2.62:

$$Pt + CHO\text{-}CH_3 \rightarrow Pt\text{-}CO\text{-}CH_3 + H^+ + e^- \quad \text{(at E < 0.4 V vs. SHE)} \quad (2.62)$$
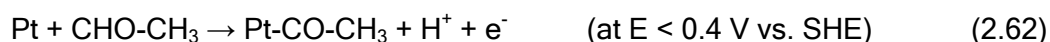
It was observed that CO residues exist on Pt at potentials as low as 0.3V vs. SHE; some traces of methane have also been observed at low potential values (E < 0.4 V vs. SHE) [183]. This can be explained by the following equations:

$$Pt\text{-}CO\text{-}CH_3 + Pt \rightarrow Pt\text{-}CO + Pt\text{-}CH_3 \quad \text{(at E > 0.3 V vs. SHE)} \quad (2.63)$$

$$Pt\text{-}CH_3 + Pt\text{-}H \rightarrow 2Pt + CH_4 \quad \text{(at E < 0.4 V vs. SHE)} \quad (2.64)$$

At potentials higher than 0.6 V vs. SHE, the dissociative adsorption of water can occur on Pt (Eq. 2.45), providing adsorbed hydroxyl radicals able to further oxidize the adsorption residues of ethanol. Then oxidation of adsorbed CO can take place according to Eq. 2.65. Acetaldehyde can also be oxidized following Eq. 2.66:

$$Pt\text{-}CO + Pt\text{-}OH \rightarrow 2Pt + CO_2 + H^+ + e^- \quad (2.65)$$

$$CHO\text{-}CH_3 + Pt\text{-}OH \rightarrow Pt + CH_3\text{-}COOH + H^+ + e^- \quad (2.66)$$

According to this mechanism, it is assumed that CO_2 is produced through chemisorbed intermediates while acetaldehyde is formed through weakly adsorbed ethanol. Again, the simultaneous presence of poisoning species and reaction intermediates requires the development of new electrocatalysts capable of breaking the C-C bond of the ethanol molecule and of oxidizing adsorbed CO at lower potentials. For this reason Pt/M alloys have been examined for the electrocatalysis of ethanol oxidation. Pt/Ru alloys, commonly considered to be the best electrocatalysts for methanol oxidation, have been tested as catalysts for ethanol oxidation. The same oxidation products have been identified on Pt/Ru as on Pt surfaces, and it was shown that Ru promotes the surface reaction between the chemisorbate and the oxidant via the bifunctional mechanism [186]. It has been argued, however, that Pt/Ru is not an appropriate electrocatalyst for ethanol electrooxidation; the formation of chemisorbed species from dissolved ethanol was indeed partially inhibited by the presence of Ru, favouring the oxidation pathway through weakly adsorbed intermediates, and thus the formation of acetaldehyde [187, 188]. Therefore, some alternative Pt/M electrocatalysts have been developed for complete ethanol oxidation. It was shown that Pt/Sn catalysts trapped in a polyaniline matrix exhibited higher catalytic activity toward ethanol oxidation than Pt/Ru [189]. Tin leads to increased current densities for

the electrooxidation of ethanol by depressing the poisoning phenomena during ethanol adsorption [190], and Pt/Sn electrocatalysts were found to be more selective toward the production of CO_2 than Pt [191]. The optimum Sn surface concentration is a very important question, since the concentration of surface oxygen-containing species, the lattice parameters, and the ohmic effects are directly related to this factor. A possible explanation for the enhanced activity of Pt/Sn as compared to Pt is the expanded lattice parameter favouring cleavage of the C-C bond [192]. Optimum Sn content can vary from 20 at. % [190] to 35-50 at. % [193, 194], depending on the authors. A mechanism for ethanol oxidation on Pt/Sn has also been proposed [195]. It was assumed that ethanol only adsorbs on Pt sites, so that the first steps (Eqs. 2.58 and 2.59) are the same on Pt/Sn as on Pt. Reactions. 2.58 to 2.63 would then occur at very low potentials, and with very rapid kinetics as compared to Pt. Once intermediates such as $Pt-CO-CH_3$ and Pt-CO are formed, they can be oxidized at potentials close to 0.3 V vs. SHE, because on tin OH species are formed at lower potentials. This explains also the higher efficiency of Pt/Sn in forming acetic acid as compared to Pt, since the OH species can in fact be used to oxidize adsorbed CO to CO_2 or $CO-CH_3$ to CH_3-COOH according to the bifunctional mechanism.

7. JUSTIFICATION OF THIS WORK

Prior to presenting the results obtained, and the theoretical model developed, the initial objectives of this thesis have to be clearly exposed. It can be seen from the above bibliographic part that the literature on alcohols oxidation at Pt-based electrode surfaces is very large, and that interest on this topic is not recent. The aim of this Chapter was not that of exhaustively reviewing the literature on this subject, but to rather giving a good overview of the major achievements and of the state of the art in the field. More particularly, there has been a strong interest in the development of new Pt-based catalyst for both methanol and ethanol electrooxidation, and it was shown that alloying Pt with other transition metals greatly enhance the catalytic activity of the surface. Among all Pt-M combinations tested, by large consensus Pt/Ru and Pt/Sn can be designated as the most efficient for the electrocatalysis of methanol and ethanol oxidation, respectively.

We propose within this thesis to synthesize and electrocatalytically characterize Pt-based nanocatalysts. Our aim was, not to find new types of catalyst but to use a relatively recent synthesis technique (*i.e.* the microemulsion technique) to prepare bimetallic or alloyed nanoparticles with controlled composition and high dispersion of the two metals, and determine the differences between the oxidation mechanisms on each particle type. It was a further aim to draw conclusions as to a possible

cooperation between metals in a microemulsion-synthesized ternary Pt/Ru/Sn catalyst.

Thus, no new systems were explored but we have focused on well-known catalytic surfaces and well-known fuels, *i.e.* Pt, Pt/Ru and Pt/Sn for the electrocatalysis of methanol and ethanol electrooxidation. These systems were mainly studied by means of electrochemical methods (cyclic voltammetry, chronoamperometry, impedance spectroscopy). For practical reasons, the particles were deposited on synthetic boron-doped diamond (BDD) electrodes. The choice of such a substrate was motivated by its outstanding properties of chemical inertness, low background current, the large potential window available between hydrogen and oxygen evolution, and high mechanical resistance to chemical or electrochemical attacks. The use of BDD as substrate for the study of supported particles and nanoparticles should be a good approach to the problems usually encountered with common substrates. It is well known, for instance, that Au substrates will undergo surface oxide formation. Moreover, electron transfer will occur from Au to Pt, modifying the electronic and catalytic properties of the Pt deposit. Other carbon-based substrate (glassy carbon, graphite) will also undergo surface oxides formation and corrosion. The work function of BDD is not well known, but it is expected that with this substrate electrode, it should be possible to study the oxidation of methanol and ethanol without any major interference.

8.   LIST OF SYMBOLS

Roman symbols

a	Ion activity	
A	Surface occupied by one mole	m^2
D	Adatoms flow	$mol\ m^{-1}\ s^{-1}$
e^-	Electron	
E	Potential vs. a reference	V
E^+	Cathode potential vs. a reference	V
E^-	Anode potential vs. a reference	V
F	Faraday's constant	$96500\ C\ mol^{-1}$
h	Nucleus height	m
i	Current	A
J	Nucleation rate	$mol\ m^{-2}\ s^{-1}$
k	Nucleation rate constant	$mol\ m^{-2}\ s^{-1}$
k_{com}	Rate of communication	$dm^3\ mol^{-1}\ s^{-1}$
M	Molar mass	$g\ mol^{-1}$

N_0	Number of possible nucleation sites	cm^{-2}
p	Pressure at the interface	Pa
Q	Electrical charge	C
r	Radius	m
R	Molar gas constant	8.314 J mol^{-1} K^{-1}
S	Real surface	m^2
S_0	Real surface normalisation factor	
t	Time	s
T	Temperature	K
W_e	Theoretical mass energy density	kWh kg^{-1}
z	Number of exchanged electrons	

Greek Symbols

ε_i	Free energy of incorporation	J m^{-2}
δ	Dirac function	
η	Overpotential	V
Θ	Fraction of active sites	
ρ	Density	g cm^{-3}
Γ	Hydrodynamic factor	
ω_0	Water-to-surfactant molar ratio	

Superscript

$\cdot$	Radical species
0	At standard conditions
®	Registered trade mark

Subscript

0	At the equilibrium
ad	Adatom
ads	Adsorbed
c	Critical
chem.	Chemisorbed
emf	Electromotive force
sol	In solution
st	Stationary state

9.   REFERENCES

[1]   Y. V. Pleskov, in: R. C. Alkire, D. M. Kolb (Eds.), *Advances in Electrochemical Science and Engineering*, Wiley-VCH, Weinheim (2002), p. 209.

[2]   S. Ferro, *J. Mater. Chem.* **12** (2002), 2843.

[3]   F. P. Bundy, H. T. Hall, H. M. Strong, R. H. Wentorf, *Nature* **176** (1955), 51.

[4]   B. V. Derjaguin, D. V. Fedoseev, V. M. Lukyanovich, B. V. Spitzin, V. A. Ryabov, A. V. Lavrentyev, *J. Cryst. Growth* **2** (1968), 380.

[5]   B. V. Derjaguin, B. V. Spitsyn, A. E. Gorodetsky, A. P. Zakharov, L. L. Bouilov, A. E. Aleksenko, *J. Cryst. Growth* **31** (1975), 44.

[6]   B. V. Spitsyn, L. L. Bouilov, B. V. Derjaguin, *J. Cryst. Growth* **52** (1981), 219.

[7]   S.-T. Lee, H. Y. Peng, X. T. Zhou, N. Wang, C. S. Lee, I. Bello, Y. Lifshitz, *Science* **287** (2000), 104.

[8]   M. Frenklach, S. Skokov, *J. Phys. Chem. B* **101** (1997), 3025.

[9]   F. Fontaine, E. Gheeraert, A. Deneuville, *Diamond Rel. Mater.* **5** (1996), 752.

[10]   I. Duo, A. Fujishima, Ch. Comninellis, *Electrochem. Comm.* **5** (2003), 695.

[11]   B. Marselli, J. Garcia-Gomez, P.-A. Michaud, M. A. Rodrigo, Ch. Comninellis, *J. Electrochem. Soc.* **150** (2003), D79.

[12]   J. Iniesta, P.-A. Michaud, M. Panizza, Ch. Comninellis, *Electrochem. Comm.* **3** (2001), 346.

[13]   M. Panizza, I. Duo, P.-A. Michaud, G. Cerisola, Ch. Comninellis, *Electrochem. Solid-State Lett.* **3** (2000), 550.

[14]   P.-A. Michaud, E. Mahé, W. Haenni, A. Perret, Ch. Comninellis, *Electrochem. Solid-State Lett.* **3** (2000), 77.

[15]   G. Fóti, D. Gandini, Ch. Comninellis, A. Perret, W. Haenni, *Electrochem. Solid-State Lett.* **2** (1999), 228.

[16]   D. Gandini, E. Mahé, P.-A. Michaud, W. Haenni, A. Perret, Ch. Comninellis, *J. Appl. Electrochem.* **30** (2000), 1345.

[17]   M. Panizza, P.-A. Michaud, G. Cerisola, Ch. Comninellis, *J. Electroanal. Chem.* **507** (2001), 206.

[18]   M. A. Rodrigo, P.-A. Michaud, I. Duo, M. Panizza, G. Cerisola, Ch. Comninellis, *J. Electrochem. Soc.* **148** (2001), D60.

[19]   L. Gherardini, P.-A. Michaud, M. Panizza, Ch. Comninellis, N. Vatistas, *J. Electrochem. Soc.* **148** (2001), D78.

[20]   A. J. Saterlay, S. J. Wilkins, K. B. Holt, J. S. Foord, R. G. Compton, F. Marken, *J. Electrochem. Soc.* **148** (2001), E66.

[21]   F. Marken, A. S. Bhambra, D.-H. Kim, R. J. Mortimer, S. J. Stott, *Electrochem. Comm.* **6** (2004), 1153.

[22]   K. J. McKenzie, F. Marken, *Electrochem. Solid-State Lett.* **5** (2002), E47.

[23]   K. J. McKenzie, D. Asogan, F. Marken, *Electrochem. Comm.* **4** (2002), 820.

[24]   I. Duo, Ch. Comninellis, S. Ferro, A. De Battisti, in: A. Wieckowski, E. R. Savinova, C. G. Vayenas (Eds.), *Catalysis and Electrocatalysis at Nanoparticle Surfaces*, Marcel Dekker, Inc., New York (2003), p. 877.

[25]   B. El Roustom, G. Fóti, Ch. Comninellis, *Electrochem. Comm.* **In Press**.

[26]   Y. Zhang, S. Asahina, S. Yoshihara, T. Shirakashi, *Electrochim. Acta* **48** (2003), 741.

[27]   Y. Zhang, V. Suryanarayanan, I. Nakazawa, S. Yoshihara, T. Shirakashi, *Electrochim. Acta* **49** (2004), 5235.

[28]   F. Montilla, E. Morallon, I. Duo, Ch. Comninellis, J. L. Vazquez, *Electrochim. Acta* **48** (2003), 3891.

[29]   G. Siné, Ch. Comninellis, *Electrochim. Acta* **50** (2005), 2249.

[30]   K. Tsujimoto, S. Mitani, T. Teraji, T. Ito, *Appl. Surf. Sci.* **237** (2004), 488.

[31]   O. Enea, B. Riedo, G. Dietler, *Nano Lett.* **2** (2002), 241.

[32]   J. Wang, G. M. Swain, *J. Electrochem. Soc.* **150** (2003), E24.

[33]   J. Wang, G. M. Swain, T. Tachinaba, K. Kobashi, *Electrochem. Solid-State Lett.* **3** (2000), 286.

[34]   J.-S. Gao, T. Arunagiri, J.-J. Chen, P. Goodwill, O. Chyan, J. Perez, D. Golden, *Chem. Mater.* **12** (2000), 3495.

[35]   P. Buffat, J.-P. Borel, *Phys. Rev. A* **13** (1976), 2287.

[36]   K. F. Peters, J. B. Cohen, Y.-W. Chung, *Phys. Rev. B* **57** (1998), 13430.

[37]   R. Rossetti, S. Nakahara, L. E. Brus, *J. Chem. Phys.* **79** (1983), 1086.

[38]   S. H. Choi, K. L. Wang, M. S. Leung, G. W. Stupian, N. Presser, B. A. Morgan, R. E. Robertson, M. Abraham, E. E. King, B. Tueling, S. W. Chung, J. R. Heath, S. L. Cho, J. B. Ketterson, *J. Vac. Sci. Technol. A* **18** (2000), 1326.

[39]   R. Grisel, K.-J. Weststrate, A. Gluhoi, B. E. Nieuwenhuys, *Gold Bull.* **35** (2002), 39.

[40]   G. C. Bond, *Gold Bull.* **34** (2001), 117.

[41]   T. Kobayashi, M. Haruta, H. Sano, M. Nakane, *Sensors Actuators* **13** (1988), 339.

[42]   T. Kobayashi, M. Haruta, S. Tsubota, H. Sano, B. Delmon, *Sensors Actuators B* **1** (1990), 222.

[43]   U. Heiz, W.-D. Schneider, in: K.-H. Meiwes-Broer (Ed.) *Metal Clusters at Surfaces. Structure, Quantum Properties, Physical Chemistry.*, Springer Verlag, Berlin (1999), p. 237.

[44] Y. Takasu, N. Ohashi, X.-G. Zhang, Y. Murakami, H. Minagawa, S. Sato, K. Yahikozawa, *Electrochim. Acta* **41** (1996), 2595.

[45] O. Savadogo, A. Essalik, *J. Electrochem. Soc.* **143** (1996), 1814.

[46] J. A. A. van den Tillaart, B. F. M. Kuster, G. B. Marin, *Catal. Lett.* **36** (1996), 31.

[47] T. Frelink, W. Visscher, J. A. R. van Veen, *J. Electroanal. Chem.* **382** (1995), 65.

[48] L. N. Lewis, *Chem. Rev.* **93** (1993), 2693.

[49] A. T. Bell, *Science* **299** (2003), 1688.

[50] G. Cao, *Nanostructures & Nanomaterials. Synthesis, Properties and Applications*, Imperial College Press, London (2004).

[51] K.-H. Meiwes-Broer (Ed.) *Metal Clusters at Surfaces - Structure, Quantum Properties, Physical Chemistry*, Springer-Verlag, Berlin (2000).

[52] A. Wieckowski, E. R. Savinova, C. G. Vayenas (Eds.), *Catalysis and Electrocatalysis at Nanoparticle Surfaces*, Marcel Dekker, Inc., New York (2003).

[53] S. Ye, K. Uosaki, in: A. J. Bard, M. Stratmann, E. Gileadi, M. Urbakh (Eds.), *Encylopedia of Electrochemistry Vol. 1: Thermodynamics and Electrified Interfaces*, Wiley-VCH, Weinheim (2001), p. 471.

[54] S. Nageswar, *Electrodeposition and Surface Treatment* **3** (1975), 417.

[55] D. M. Kolb, in: R. C. Alkire, D. M. Kolb (Eds.), *Advances in Electrochemical Science and Engineering*, Wiley-VCH, Weinheim (2002), p. 107.

[56] H.-F. Waibel, M. Kleinert, L. A. Kibler, D. M. Kolb, *Electrochimica Acta* **47** (2002), 1461.

[57] E. Mahé, *Etude de la formation et des propriétés électrochimiques locales de structures Métal1/Oxyde/Métal2*, PhD Thesis, Université Paris V Pierre et Marie Curie, Paris (1999).

[58] M. Paunovic, M. Schlesinger, in: M. Paunovic, M. Schlesinger (Eds.), *Fundamentals of Electrochemical Deposition*, John Wiley & Sons, Inc., New York (1998), p. 73.

[59] M. Fleischmann, H. R. Thirsk, *Electrochimica Acta* **2** (1960), 22.

[60] I. Markov, D. Kashchiev, *Journal of Crystal Growth* **13-14** (1972), 131.

[61] I. Markov, *Thin Solid Films* **35** (1976), 11.

[62] S. Fletcher, T. Lwin, *Electrochimica Acta* **28** (1983), 237.

[63] M. Paunovic, M. Schlesinger, in: M. Paunovic, M. Schlesinger (Eds.), *Fundamentals of Electrochemical Deposition*, John Wiley & Sons, Inc., New York (1998), p. 187.

[64]   I. Danielsson, B. Lindman, *Colloids Surf.* **3** (1981), 391.

[65]   J. Sjöblom, R. Lindberg, S. E. Friberg, *Adv. Colloid Interface Sci.* **65** (1996), 125.

[66]   T. P. Hoar, J. H. Schulman, *Nature* **152** (1943), 102.

[67]   J. H. Schulman, W. Stoeckenius, L. M. Prince, *J. Phys. Chem.* **63** (1959), 1677.

[68]   J. H. Schulman, D. P. Riley, *J. Colloid Sci* **3** (1948), 383.

[69]   D. F. Sears, J. H. Schulman, *J. Phys. Chem.* **68** (1964), 3529.

[70]   I. A. Zlochower, J. H. Schulman, *J. Colloid Interface Sci.* **24** (1967), 115.

[71]   P. A. Winsor, *Chem. Rev.* **68** (1968), 1.

[72]   H. L. Rosano, H. Schiff, J. H. Schulman, *J. Phys. Chem.* **66** (1962), 1928.

[73]   L. M. Prince, *J. Colloid Interface Sci.* **23** (1967), 165.

[74]   L. M. Prince, *J. Colloid Interface Sci.* **29** (1969), 216.

[75]   M. Boutonnet, J. Kizling, P. Stenius, *Colloids Surf.* **5** (1982), 209.

[76]   K. C. Song, J. H. Kim, *J. Colloid Interface Sci.* **212** (1999), 193.

[77]   N. Munshi, T. K. De, A. Maitra, *J. Colloid Interface Sci.* **190** (1997), 387.

[78]   I. Capek, *Adv. Colloid Interface Sci.* **110** (2004), 49.

[79]   H. Härelind Ingelsten, R. Bagwe, A. Palmqvist, M. Skoglundh, C. Svanberg, K. Holmberg, D. O. Shah, *J. Colloid Interface Sci.* **241** (2001), 104.

[80]   S. Qiu, J. Dong, G. Chen, *J. Colloid Interface Sci.* **216** (1999), 230.

[81]   C.-C. Wang, D.-H. Chen, T.-C. Huang, *Colloids Surf. A* **189** (2001), 145.

[82]   J. Solla-Gullón, A. Rodes, V. Montiel, A. Aldaz, J. Clavilier, *J. Electroanal. Chem.* **554-555** (2003), 273.

[83]   J. Solla-Gullón, F. J. Vidal-Iglesias, V. Montiel, A. Aldaz, *Electrochim. Acta* **49** (2004), 5079.

[84]   M.-L. Wu, D.-H. Chen, T.-C. Huang, *J. Colloid Interface Sci.* **243** (2001), 102.

[85]   M.-L. Wu, D.-H. Chen, T.-C. Huang, *Chem. Mater.* **13** (2001), 599.

[86]   H.-F. Eicke, P. E. Zinsli, *J. Colloid Interface Sci.* **65** (1978), 131.

[87]   R. Zana, J. Lang, in: S. E. Friberg, P. Bothorel (Eds.), *Microemulsion: Structure and Dynamics*, CRC Press, Boca Raton (1987), p. 153.

[88]   K. Holmberg, *J. Colloid Interface Sci.* **274** (2004), 355.

[89]   H.-f. Eicke, J. C. W. Shepherd, A. Steinemann, *J. Colloid Interface Sci.* **56** (1976), 168.

[90]   M. Fisher, W. Knoche, P. D. I. Fletcher, B. H. Robinson, *Colloid Polym. Sci* **258** (1980), 733.

[91]   M. P. Pileni, *Langmuir* **13** (1997), 3266.

[92]   M. P. Pileni, *Catal. Today* **58** (2000), 151.

[93]   M. P. Pileni, *Nature Mat.* **2** (2003), 145.

[94]   M. A. Lopez-Quintela, *Curr. Opinion Colloid Interface Sci.* **8** (2003), 137.

[95]   S. Quintillan, C. Tojo, M. C. Blanco, M. A. Lopez-Quintela, *Langmuir* **17** (2001), 7251.

[96]   C. Tojo, M. C. Blanco, M. A. Lopez-Quintela, *Langmuir* **13** (1997), 4527.

[97]   C. Tojo, M. C. Blanco, M. A. Lopez-Quintela, *J. Non-Cryst. Solids* **235-237** (1998), 688.

[98]   C. Tojo, M. C. Blanco, M. A. Lopez-Quintela, *Langmuir* **14** (1998), 6835.

[99]   Y. Li, C.-W. Park, *Langmuir* **15** (1999), 952.

[100]   M. P. Pileni, *Langmuir* **17** (2001), 7476.

[101]   I. Lisiecki, A. Filankembo, H. Sack-Kongehl, K. Weiss, M. P. Pileni, J. Urban, *Phys. Rev. B* **61** (2000), 4968.

[102]   I. Dekany, L. Nagy, L. Uri, Z. Kiraly, N. A. Kotov, J. H. Fendler, *Langmuir* **12** (1996), 3709.

[103]   J. Solla-Gullón, V. Montiel, A. Aldaz, J. Clavilier, *J. Electroanal. Chem.* **491** (2000), 69.

[104]   J. Solla-Gullón, V. Montiel, A. Aldaz, J. Clavilier, *J. Electrochem. Soc.* **150** (2003), E104.

[105]   A. S. Aricò, S. Srinivasan, V. Antonucci, *Fuel Cells* **1** (2001), 133.

[106]   A. Hamnett, in: W. Vielstich, H. A. Gasteiger, A. Lamm (Eds.), *Handbook of Fuel Cells - Fundamentals, Technology and Applications*, John Wiley & Sons, Ltd., New York (2003), p. 305.

[107]   C. Lamy, E. M. Belgsir, in: W. Vielstich, H. A. Gasteiger, A. Lamm (Eds.), *Handbook of Fuel Cells - Fundamentals, Technology and Applications*, John Wiley & Sons, Ltd., New York (2003), p. 323.

[108]   C. Lamy, E. M. Belgsir, J.-M. Léger, *J. Appl. Electrochem.* **31** (2001), 799.

[109]   M. Watanabe, S. Motoo, *J. Electroanal. Chem.* **60** (1975), 267.

[110]   T. Iwasita, X. Xinghua, *J. Electroanal. Chem.* **411** (1996), 95.

[111]   H. Angerstein-Kozlowska, B. E. Conway, W. B. A. Sharp, *Electroanal. Chem. Interfacial Electrochem.* **43** (1973), 9.

[112]   G. Jerkiewicz, G. Vatankhah, J. Lessard, M. P. Soriaga, Y.-S. Park, *Electrochim. Acta* **49** (2004), 1451.

[113]   B. E. Conway, *Progr. Surf. Sci.* **49** (1995), 331.

[114]   V. I. Birss, M. Chang, J. Segal, *J. Electroanal. Chem.* **355** (1993), 181.

[115]   D. A. Harrington, *J. Electroanal. Chem.* **420** (1997), 101.

[116]   M. E. Gamboa-Aldeco, E. Herrero, P. S. Zelenay, A. Wieckowski, *J. Electroanal. Chem.* **348** (1993), 451.

[117]   A. Kolics, A. Wieckowski, *J. Phys. Chem. B* **105** (2001), 2588.

[118]   K. Kinoshita, J. T. Lundquist, P. Stonehart, *J. Electroanal. Chem.* **48** (1973), 157.

[119]   A. Hamnett, in: A. Wieckowski (Ed.) *Interfacial Electrochemistry - Theory, Experiments, and Applications*, Marcel Dekker, Inc., New York (1999), p. 843.

[120]   W. C. Choi, J. D. Kim, S. I. Woo, *Catal. Today* **74** (2002), 235.

[121]   M. Gotz, H. Wendt, *Electrochim. Acta* **43** (1998), 3637.

[122]   Z. Jusys, T. J. Schmidt, L. Dubau, K. Lasch, L. Jorissen, J. Garche, R. J. Behm, *J. Power Sources* **105** (2002), 297.

[123]   K. L. Ley, R. Liu, C. Pu, Q. Fan, N. Leyarovska, C. Segre, E. S. Smotkin, *J. Electrochem. Soc.* **144** (1997), 1543.

[124]   K.-W. Park, J.-H. Choi, B.-K. Kwon, S.-A. Lee, Y.-E. Sung, H.-Y. Ha, S.-A. Hong, H. Kim, A. Wieckowski, *J. Phys. Chem. B* **106** (2002), 1869.

[125]   S. Motoo, M. Watanabe, *J. Electroanal. Chem.* **111** (1980), 261.

[126]   M. Watanabe, S. Motoo, *J. Electroanal. Chem.* **60** (1975), 259.

[127]   M. Watanabe, S. Motoo, *J. Electroanal. Chem.* **60** (1975), 275.

[128]   S. Motoo, M. Watanabe, *J. Electroanal. Chem.* **69** (1976), 429.

[129]   S. Motoo, M. Shibata, M. Watanabe, *J. Electroanal. Chem.* **110** (1980), 103.

[130]   M. Watanabe, Y. Furuuchi, S. Motoo, *J. Electroanal. Chem.* **191** (1985), 367.

[131]   A. B. Anderson, E. Grantsharova, S. Seong, *J. Electrochem. Soc.* **143** (1996), 2075.

[132]   J. O. m. Bockris, H. Wroblowa, *J. Electroanal. Chem.* **7** (1964), 428.

[133]   H. Binder, A. Köhling, G. Sandstede, in *From electrocatalysis to fuel cells*, Washington University Press (1972), p. 43.

[134]   P. Liu, J. K. Norskov, *Fuel Cells* **1** (2001), 192.

[135]   L. Dubau, C. Coutanceau, E. Garnier, J.-M. Léger, C. Lamy, *J. Appl. Electrochem.* **33** (2003), 419.

[136]   B. Bittins-Cattaneo, T. Iwasita, *J. Electroanal. Chem.* **238** (1987), 151.

[137]   P. N. Ross, K. Kinoshita, A. J. Scarpellino, P. Stonehart, *J. Electroanal. Chem.* **63** (1975), 97.

[138]   M. A. Quiroz, I. Gonzalez, Y. Meas, E. Lamy-Pitara, J. Barbier, *Electrochim. Acta* **32** (1987), 289.

[139]   V. B. Hughes, R. Miles, *J. Electroanal. Chem.* **145** (1983), 87.

[140]   B. D. McNicol, R. T. Short, *J. Electroanal. Chem.* **81** (1977), 249.

[141]   E. Ticanelli, J. G. Beery, M. T. Paffett, S. Gottesfeld, *J. Electroanal. Chem.* **258** (1989), 61.

[142] A. H. Haner, P. N. Ross Jr, U. Bardi, A. Atrei, *J. Vac. Sci. Technol. A* **10** (1992), 2718.

[143] T. E. Shubina, M. T. M. Koper, *Electrochim. Acta* **47** (2002), 3621.

[144] W. Vielstich, H. A. Gasteiger, A. Lamm (Eds.), *Handbook of Fuel Cells - Fundamentals, Technology and Applications*, John Wiley & Sons, Ltd., New York (2003).

[145] V. S. Bagotzky, Y. B. Vassilyev, *Electrochim. Acta* **12** (1967), 1323.

[146] N. A. Hampson, M. J. Willars, B. D. McNicol, *J. Power Sources* **4** (1979), 191.

[147] T. Iwasita, W. Vielstich, E. Santos, *J. Electroanal. Chem.* **229** (1987), 367.

[148] E. Herrero, K. Franaszczuk, A. Wieckowski, *J. Phys. Chem.* **98** (1994), 5074.

[149] K. D. Snell, A. G. Keenan, *Electrochim. Acta* **26** (1981), 1339.

[150] K. D. Snell, A. G. Keenan, *Electrochim. Acta* **27** (1982), 1683.

[151] J. Willsau, J. Heitbaum, *J. Electroanal. Chem.* **194** (1985), 27.

[152] B. Beden, M.-C. Morin, F. Hahn, C. Lamy, *J. Electroanal. Chem.* **229** (1987), 353.

[153] R. S. Goncalves, J.-M. Léger, C. Lamy, *Electrochim. Acta* **33** (1988), 1581.

[154] E. Pastor, S. González, A. J. Arvia, *J. Electroanal. Chem.* **395** (1995), 233.

[155] S.-G. Sun, Y. Lin, *Electrochim. Acta* **41** (1996), 693.

[156] I. d. A. Rodrigues, J. P. I. De Souza, E. Pastor, F. C. Nart, *Langmuir* **13** (1997), 6829.

[157] M. P. Hogarth, T. R. Ralph, *Platinum Metals Rev.* **46** (2002), 146.

[158] G.-Q. Lu, W. Chrzanowski, A. Wieckowski, *J. Phys. Chem. B* **104** (2000), 5566.

[159] B. Beden, C. Lamy, A. Bewick, K. Kunimatsu, *J. Electroanal. Chem.* **121** (1981), 343.

[160] X. H. Xia, T. Iwasita, F. Ge, W. Vielstich, *Electrochim. Acta* **41** (1996), 711.

[161] A. Peremans, A. Tadjeddine, *Chem. Phys. Lett.* **220** (1994), 481.

[162] F. Vidal, B. Busson, C. Six, O. Pluchery, A. Tadjeddine, *Surf. Sci.* **502-503** (2002), 485.

[163] F. Vidal, B. Busson, C. Six, A. Tadjeddine, L. Dreesen, C. Humbert, A. Peremans, P. Thiry, *J. Electroanal. Chem.* **563** (2004), 9.

[164] T. Iwasita, F. C. Nart, *J. Electroanal. Chem.* **317** (1991), 291.

[165] T. Iwasita, F. C. Nart, B. Lopez, W. Vielstich, *Electrochim. Acta* **37** (1992), 2361.

[166] J. Clavilier, C. Lamy, J. M. Leger, *J. Electroanal. Chem.* **125** (1981), 249.

[167] P. A. Christensen, A. Hamnett, J. Munk, G. L. Troughton, *J. Electroanal. Chem.* **370** (1994), 251.

[168] M. T. M. Koper, T. E. Shubina, R. A. van Santen, *J. Phys. Chem. B* **106** (2002), 686.

[169] M. T. Paffett, S. C. Gebhard, R. G. Windham, B. E. Koel, *J. Phys. Chem.* **94** (1990), 6831.

[170] C. Xu, B. E. Koel, *Surf. Sci.* **304** (1994), L505.

[171] M. M. P. Janssen, J. Moolhuysen, *Electrochim. Acta* **21** (1976), 861.

[172] M. M. P. Janssen, J. Moolhuysen, *J. Catal.* **46** (1977), 289.

[173] A. Wieckowski, *J. Electroanal. Chem.* **78** (1977), 229.

[174] C. Lu, C. Rice, R. I. Masel, P. K. Babu, P. Waszczuk, H. S. Kim, E. Oldfield, A. Wieckowski, *J. Phys. Chem. B* **106** (2002), 9581.

[175] D. Kardash, C. Korzeniewski, N. Markovic, *J. Electroanal. Chem.* **500** (2001), 518.

[176] Y. Ishikawa, M.-S. Liao, C. R. Cabrera, *Surf. Sci.* **463** (2000), 66.

[177] L. Giorgi, A. Pozio, C. Bracchini, R. Giorgi, S. Turtu, *J. Appl. Electrochem.* **31** (2001), 325.

[178] Y. Morimoto, E. B. Yeager, *J. Electroanal. Chem.* **441** (1998), 77.

[179] Y. Morimoto, E. B. Yeager, *J. Electroanal. Chem.* **444** (1998), 95.

[180] A. H. Haner, P. N. Ross, *J. Phys. Chem.* **95** (1991), 3740.

[181] T. Frelink, W. Visscher, J. A. R. van Veen, *Electrochim. Acta* **39** (1994), 1871.

[182] J. M. Perez, B. Beden, F. Hahn, A. Aldaz, C. Lamy, *J. Electroanal. Chem.* **262** (1989), 251.

[183] T. Iwasita, E. Pastor, *Electrochim. Acta* **39** (1994), 531.

[184] H. Hitmi, E. M. Belgsir, J. M. Léger, C. Lamy, R. O. Lezna, *Electrochim. Acta* **39** (1994), 407.

[185] S.-C. Chang, L.-W. H. Leung, M. J. Weaver, *J. Phys. Chem.* **94** (1990), 6013.

[186] N. Fujiwara, K. A. Friedrich, U. Stimming, *J. Electroanal. Chem.* **472** (1999), 120.

[187] V. M. Schmidt, R. Ianniello, E. Pastor, S. González, *J. Phys. Chem.* **100** (1996), 17901.

[188] R. Ianniello, V. M. Schmidt, J. L. Rodriguez, E. Pastor, *J. Electroanal. Chem.* **471** (1999), 167.

[189] C. T. Hable, M. S. Wrighton, *Langmuir* **9** (1993), 3284.

[190] F. Delime, J.-M. Léger, C. Lamy, *J. Appl. Electrochem.* **29** (1999), 1249.

[191] F. Vigier, C. Coutanceau, A. Perrard, E. M. Belgsir, C. Lamy, *J. Appl. Electrochem.* **34** (2004), 439.

[192] W. J. Zhou, S. Q. Song, W. Z. Li, Z. H. Zhou, G. Q. Sun, Q. Xin, S. Douvartzides, P. Tsiakaras, *J. Power Sources* **140** (2005), 50.

[193] W. Zhou, Z. Zhou, S. Song, W. Li, G. Sun, P. Tsiakaras, Q. Xin, *Appl. Catal. B* **46** (2003), 273.

[194] W. J. Zhou, S. Q. Song, W. Z. Li, G. Q. Sun, Q. Xin, S. Kontou, K. Poulianitis, P. Tsiakaras, *Solid State Ionics* **175** (2004), 797.

[195] F. Vigier, C. Coutanceau, F. Hahn, E. M. Belgsir, C. Lamy, *J. Electroanal. Chem.* **563** (2004), 81.

Chapter 3 Experimental Part

1. INTRODUCTION

In this chapter the materials (electrochemical cell, electrodes) and methods used in the present work are described. The experimental methods are of two main types, *i.e.* electrochemical and physical. First some information will be given the fabrication of BDD electrodes (performed at CSEM). The preparation methods of Pt-based nanoparticles (formulation of the microemulsions, parameters for electrodeposition) will be presented in detail. The electrochemical cell used here, the major electrochemical techniques (cyclic voltammetry, chronoamperometry and electrochemical impedance spectroscopy), and the information that can be extracted from such experiments will be described. Finally, essential details concerning the physical methods of investigation of particulate and bulk surfaces will be given.

2. PREPARATION OF BDD FILMS

BDD electrodes were synthesized by the hot-filament chemical vapour deposition technique (HF-CVD, see Chapter 2) on single crystal *p*-type Si <100> wafers (1-3 mΩ cm, Siltronix) substrates. These electrodes were purchased from CSEM (Swiss Center for Electronics and Microtechnology, Neuchâtel). The distance between the tungsten filament and the substrate was 20 mm. The filament temperature was between 2440 and 2560 °C, and that of the substrate was maintained at 830 °C. The reactive gas consisted in 1 % methane in hydrogen and contained 1 ppm of trimethylboron as the doping agent. The gas mixture was supplied to the reaction chamber at a flow rate of 5 L min^{-1}, which led to a diamond layer growth rate of 0.24 µm h^{-1}. The precursor gases are dissociated by thermal energy from the hot filament, resulting in the formation and diffusion of reactive species (mainly methyl radical) toward the substrate surface. A diamond film is then formed by absorption and coalescence.

The obtained diamond film thickness was about 1 µm with a resistivity in the range 10-30 mΩ cm. The doping level of boron expressed as B/C ratio was about 3500 ppm, which corresponds to a carrier concentration of 6.9×10^{20} atom cm^{-3}. The BDD films exhibit a randomly oriented polycrystalline surface, with crystallites size ranging from 200 to 800 nm approximately, as seen in Figure 3.1. In this work, diamond surface has been in general anodically pre-treated in 1 M H_2SO_4 at 10 mA cm^{-2} and room temperature for 30 min in order to eliminate most of the sp^2 and adsorbed hydrogen from the surface, according to our standard preparation procedure [1]. This procedure allows the obtaining of reproducible electrochemical

measurements and such treated BDD are the used substrates in this thesis. The aim was to take advantage of the well-known properties of BDD (wide potential window, chemical inertness...) [2, 3] to study the electrochemical behaviour of Pt-based nanoparticles without major interferences.
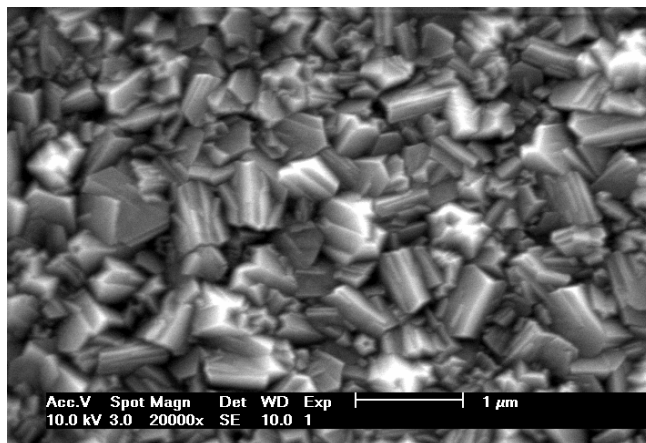

Figure 3.1: Typical SEM micrograph of the polycrystalline BDD surface.

3. PREPARATION OF PARTICLES AND NANOPARTICLES

3.1. Electrodeposition

Electrodeposition of Pt particles was performed in the conventional three-electrode cell presented below that was connected to computer-controlled Autolab PGstat30 potentiostat. A potential step, from a potential for which no deposition takes place to one for which Pt^{4+} ions are reduced was applied to BDD in a deaerated (saturated with N_2 gas) 2 mM H_2PtCl_6 + 1 M $HClO_4$ solution. The reduction reaction can be described by Equation 3.1:

$$PtCl_6^{2-} + 4e^- \rightarrow Pt + 6Cl^- \hspace{4cm} (3.1)$$

Typically the potential was stepped from 1 V to 0.02 V vs. SHE. The total amount of electrodeposited Pt as well as the size and surface density of deposits could be modulated adjusting the time of application of the reducing potential. Electrodeposition of Pt was also performed on Au nanoparticles decorating BDD, pre-deposited on diamond following a two-step method developed in our group [4]. The electrodeposition procedure was the same as on bare BDD. Such a BDD-Au/Pt composite electrode was realized in an attempt to combine the electrocatalytic properties of the particles of these two metals.

3.2. Microemulsion synthesis

Pt-based nanoparticles have also been synthesized using the microemulsion method [5]. A confined, nanosized reaction medium (the micelles) is provided where

the reduction of dissolved metallic precursors will take place. Using a water-in-oil (w/o: aqueous dispersion in a continuous oily phase) microemulsion as template, one can induce reduction in two ways: *(i)* mixing equal volumes of two microemulsions of identical formulations (implying identical size of micelles), the first containing the metal precursor and the second the reducing agent dissolved in the aqueous phases, or *(ii)* adding to a microemulsion containing the metal precursor a solid reducing agent that will diffuse into aqueous nanodroplets to produce reduction. These two ways are schematically illustrated in Figures 3.2 and 3.3, respectively.
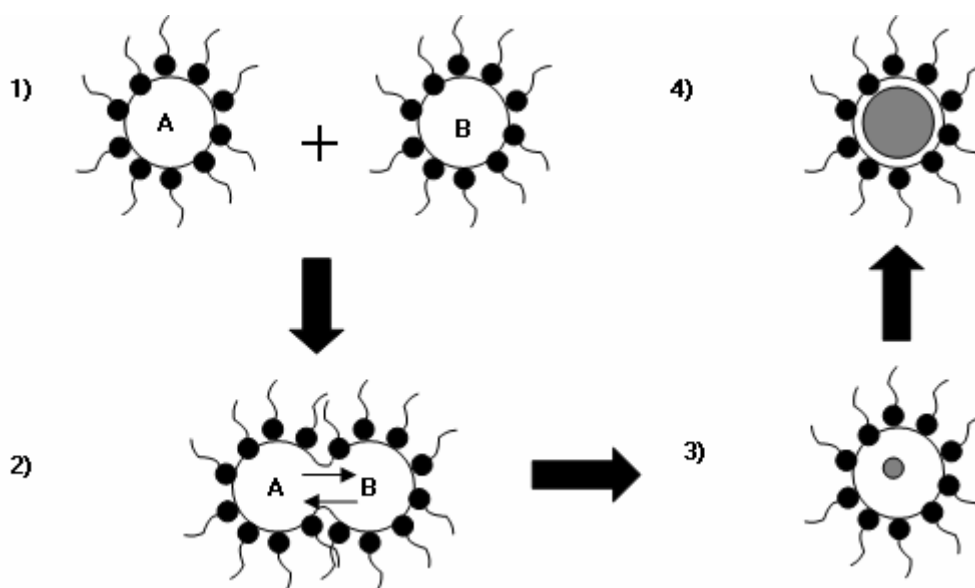
Figure 3.2: General scheme of synthesis of nanoparticles mixing two microemulsions. Steps of the process: **1)** mixing of the microemulsions, **2)** collision between aqueous nanodroplets, exchange of reactants and reaction, **3)** nucleation and **4)** growth of the particles in the inverse micelles. A = metallic precursors, B = reducing agent.
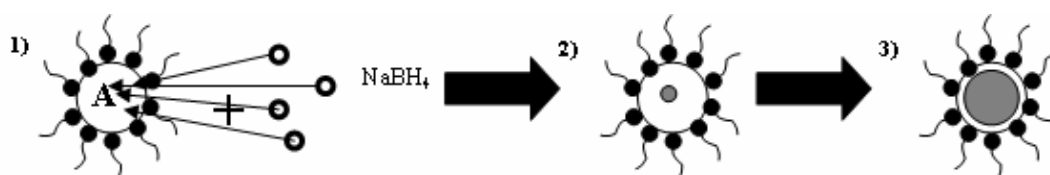
Figure 3.3: General scheme of synthesis of nanoparticles adding a solid reducing agent to a w/o microemulsion. Steps of the process: **1)** mixing of the microemulsion with solid NaBH$_4$, diffusion into the inverse micelles and reaction, **2)** nucleation and **3)** growth of the particles. A = metallic precursors.

The microemulsions used in this work were made of ultra-pure water (Millipore®), *n*-heptane (organic phase), and BRIJ®-30 (tetraethyleneglycol-monododecylether) as the surfactant. BRIJ®-30 was chosen as a non-ionic surfactant lacking sulphur groups that can strongly bind with Pt surfaces and alter their electrocatalytic properties. All microemulsions prepared for this work were identically formulated. The quantity of

surfactant represented 16.54 % by volume of the microemulsion, while the water-to-surfactant molar ratio (ω_0) was adjusted to a value of 3.8. The concentration of metal precursors (H_2PtCl_6, $RuCl_3$, $SnCl_2$) in the aqueous phase was 0.1 M. Bimetallic nanoparticles were synthesized by dissolving an appropriate mixture of metal precursors in the aqueous phase of the microemulsion. Hydrazine was the reducing agent when two microemulsions were mixed (synthesis of Pt nanoparticles), while sodium borohydride was used as the solid reducing agent in the synthesis of bimetallic nanoparticles. $NaBH_4$ was chosen for the synthesis of bimetallic particles, because it is a more powerful reducing agent than NH_2NH_2 producing nonpreferential co-reduction of the two salts dissolved in the aqueous phase of the microemulsion. The concentrations of the reducing agent were as follows: that of NH_2NH_2 in the aqueous phase of the second microemulsion was 2.5 M, while the quantity of solid $NaBH_4$ was that needed to yield a concentration of 1 M in the microemulsion aqueous phase. The reduction processes can be described by Equations 3.2 to 3.5:

$$H_2PtCl_6 + NH_2NH_2 \rightarrow Pt + 6HCl + N_2 \tag{3.2}$$

$$H_2PtCl_6 + NaBH_4 + 3H_2O \rightarrow Pt + H_3BO_3 + 5HCl + NaCl + 2H_2 \tag{3.3}$$

$$RuCl_3 + NaBH_4 + 3H_2O \rightarrow Ru + H_3BO_3 + 2HCl + NaCl + 5/2H_2 \tag{3.4}$$

$$SnCl_2 + NaBH_4 + 3H_2O \rightarrow Sn + H_3BO_3 + HCl + NaCl + 3H_2 \tag{3.5}$$
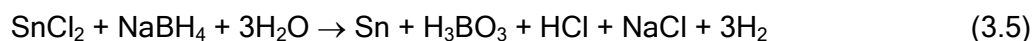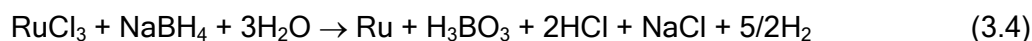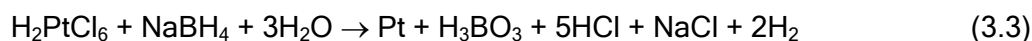
Preparatively, *n*-heptane and BRIJ®-30 were first mixed, then the aqueous phase containing the metal precursor(s) was slowly added while vigorously stirring the solution. This leads to a transparent, "homogeneous" solution, to which the reducing agent was added. The parameters for the synthesis of Pt and Pt-based nanoparticles are summarized in Table 3.1.

	Pt nanoparticles	Pt-based nanoparticles
Vol. % surfactant	16.54	16.54
Vol. % *n*-heptane	80.46	80.46
Vol. % H_2O	3	3
[metal ions]$_{aq}$ / M	0.1	0.1
[N_2H_4]$_{aq}$ / M	2.5	--
[N_2H_4]$_{aq}$/[metal ions]$_{aq}$	25	--
[$NaBH_4$]$_{aq}$ / M	--	1
[$NaBH_4$]$_{aq}$/[metal ions]$_{aq}$	--	10

Table 3.1: Experimental parameters for the synthesis of Pt-based nanoparticles by the microemulsion method.

4. ELECTROCHEMICAL CELL AND METHODS [6, 7]

4.1. Electrochemical cell

All electrochemical measurements were performed in a conventional three-electrode Teflon®-made cell (Figure 3.5) connected to a computer-controlled Autolab PGstat30 potentiostat. The working electrode was BDD or modified BDD (surface treated or supporting particles). The exposed area of diamond was 0.4 cm². The reference electrode was $Hg/Hg_2SO_4.K_2SO_4$ (sat.) with a Luggin capillary the end of which was brought close to the surface of the working electrode. The counter electrode was a Pt wire. All potentials are reported against the Standard Hydrogen Electrode (SHE). Solutions were made with ultra-pure water (Millipore®) and analytical grade reagents, and were saturated with nitrogen (Carbagas SA) prior to each experiment whenever Pt was involved in the measurement performed. Cyclic voltammetry and chronoamperometry measurements were controlled by GPES software, while impedance spectroscopy was carried out with the FRA computer program.
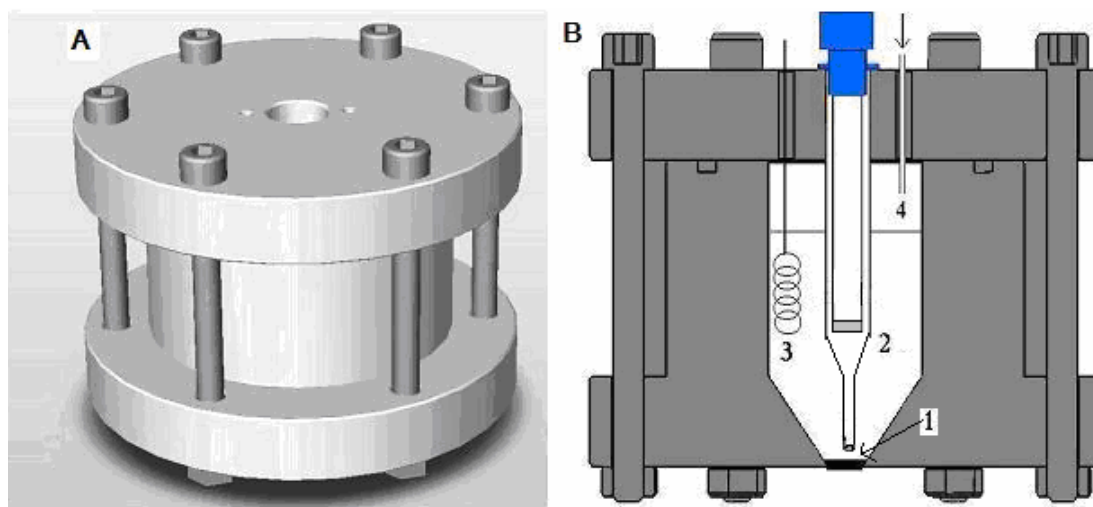
Figure 3.5: Electrochemical cell: (**A**) schematic view, (**B**) cross-section.
(**1**): working electrode, (**2**) reference electrode, (**3**) counter-electrode,(**4**) N_2 supply.

4.2. Electrochemical methods

Cyclic voltammetry (CV) is certainly the electrochemical technique most widely employed to gather information as to the surface state of the electrode under investigation as well as on interactions between an electrode and the electroactive species. The principle of CV consists in applying a linear variation of potential with time, cyclically at a given scan rate between two limits E_i and E_λ. The current response during this potential cycle is measured. The value of potential as a function

of time is given by Equations 3.6 and 3.7 for the reduction and oxidation sweeps, respectively:

$$E(t) = E_i - vt \tag{3.6}$$

$$E(t) = E_\lambda + vt \tag{3.7}$$

where E_i and E_λ are the potential limits (V vs. a reference electrode), v is the scan rate (V s^{-1}) and t is the time (s). Both the scan rate and the potential limits can be adjusted depending on the properties of the electrode and/or electroactive specie of interest.

In the electrochemical studies of Pt-based surfaces, CV can provide helpful information on the electrode's surface state, such as structure, degree of impurities or active surface area. A typical CV scan recorded in the anodic direction at a polycrystalline Pt surface in acid medium is shown in Figure 4.6. The peaks in this picture are labelled in their order of appearance with increasing potential. At cathodic potentials, reversible H_A and H_C peaks due to the adsorption and desorption of hydrogen on different crystallographic planes of the Pt surface are observed. At more anodic potentials, peaks O_A appear, which are indicative of the formation of different Pt oxides, and a plateau (broad region) that precedes O_2 evolution. In the reverse scan, Pt oxides are reduced in a unique and irreversible process (peak O_C) [8].
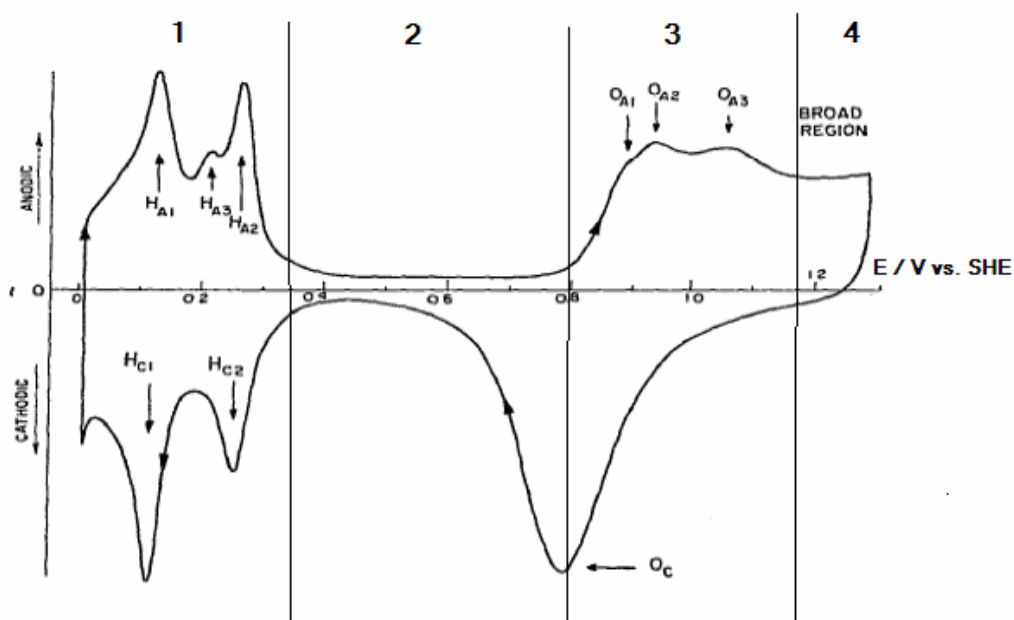
Figure 3.6: Typical CV profile of a polycrystalline Pt surface recorded in 0.5 M H_2SO_4 at 100 mV s^{-1} (adapted from [8]). Region 1 corresponds to H adsorption and desorption on different crystallographic planes of the Pt surface, region 2 corresponds to the double-layer region, region 3 corresponds to the formation of different Pt oxides and region 4 corresponds to the plateau of Pt oxides preceding O_2 evolution (not shown). In the reverse scan, all Pt oxides are reduced in a unique and irreversible process (peak O_C).

From the peaks in the picture shown in Figure 3.6, the "true" surface area of Pt can be calculated. Assuming a charge of 210 µC cm^{-2} (Q^0_H) for the adsorption-desorption of one hydrogen monolayer or 440 µC cm^{-2} (Q$^0_{ox}$) for the reduction of Pt oxides, the active surface area of Pt can be simply calculated using Equation 4.8:

$$S = \frac{Q}{Q^0} \tag{4.8}$$

where S is the Pt surface area (cm^2), and Q is the charge consumed for a given process (C). A similar treatment is possible in the case of gold surfaces, assuming a charge of 482 µC cm^{-2} for the reduction of Au oxides. CV was also used in the present work to estimate the electrocatalytic properties of a given surface: the onset potentials of oxidation or the specific molar currents are parameters that can serve to classify the efficiency of the different kinds of particles synthesized here. CV was also performed in solutions containing alcohols. A typical CV for methanol electrooxidation on Pt is shown in Figure 3.7; its unusual shape can be explained when looking at the different surface transitions that occur at Pt (see above), and from which it can be concluded with some simplification that methanol oxidation only occurs on Pt^0 surfaces when water is activated. Data describing the electrocatalytic properties of Pt and Pt-based surfaces, such as the maximum oxidation current density or the onset of oxidation, were extracted from these experiments.
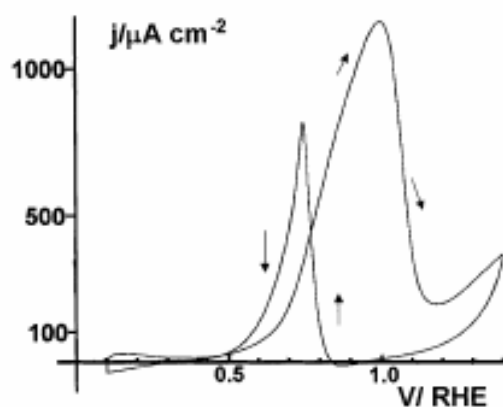

Figure 3.7: Typical CV for methanol oxidation at Pt particles electrodeposited on BDD. Recorded in 0.1 M CH$_3$OH + 0.5 M H$_2$SO$_4$ at 50 mV s^{-1} and 25°C [9].

Chronoamperometry (CA) typically represents the current response of a given system to a potential step leading from an equilibrium potential to a potential for which an oxido-reduction process occurs. The potential is imposed to the three-electrode setup while the current response is measured as a function of time. The electrocatalytic behaviour of BDD-supported Pt-based nanoparticles toward electrooxidation processes was also studied by CA. A typical CA curve for methanol oxidation at a Pt foil is shown in Figure 3.8. The current density decrease is due to

the accumulation of adsorbed intermediates on the surface, whose further oxidation to CO_2 is slow [10]. This implies that the tolerance of Pt-based surfaces to poisoning by adsorbed reaction intermediates could be followed by CA.
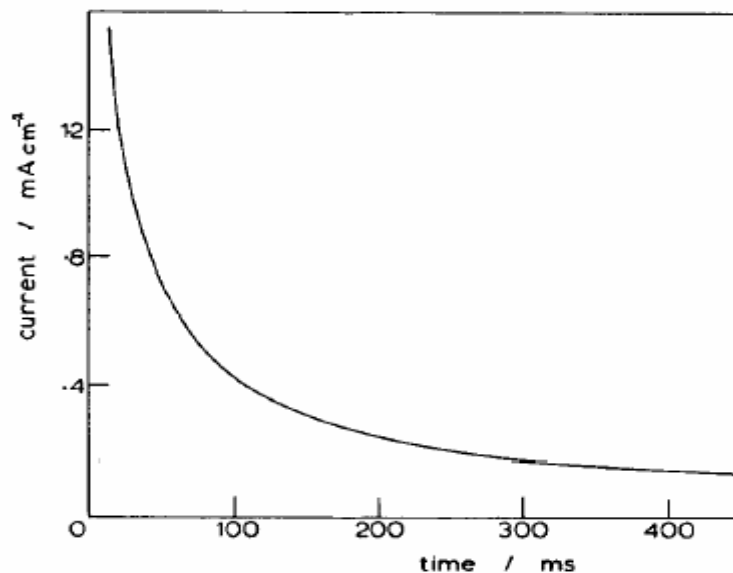

Figure 3.8: Typical current-time transient for methanol oxidation ata Pt foil at 60°C in 1 M CH_3OH + 1 M H_2SO_4 [11].

CA was the technique used to plate Pt from H_2PtCl_6 solutions. On the basis of the model developed by Scharifker and Hills [12], it was possible to plot the current-time transients for Pt electrodeposition on BDD in order to discriminate between the progressive (continuous formation of new nuclei with simultaneous growth of primary nuclei), and the instantaneous (formation and subsequent growth of primary nuclei) nucleation mechanisms.

Electrochemical impedance spectroscopy (EIS) consists, as well as CA and CV, in applying a potential perturbation to the system under investigation. However, in this case the potential excitation function is of sinusoidal type with frequency variation. With this technique, the kinetics of electrode reactions can be studied without the interference due to double-layer charging currents and ohmic drops in the experimental setup. For a sinusoidal excitation, the entrance function is given by:

$$\Delta x(t) = \Delta x \sin \omega t \tag{3.8}$$

and the exit function is:

$$\overline{\Delta x}(s) = H(s)\overline{\Delta x}(s) = \Delta x \frac{H(s)\omega}{s^2 + \omega^2} \tag{3.9}$$

where H is the transfer function of the system, defined as the ratio of the exit and entrance Laplace transforms, s is the parameter in Laplace coordinates and ω is the angular velocity or pulsation. Considering the complex nature of s, it will be

advantageous to discriminate the frequency domain, which depends on the angular velocity ω. Thus, the sinusoidal part of the exit function is given by:

$$\Delta y(t) = \Delta x |H(\omega)| (\sin\omega t + \varphi) \tag{3.10}$$

where |H(ω)| is the modulus of H(ω) defined as a function of real ReH(ω) and imaginary parts ImH(ω) of H(ω) as:

$$|H(\omega)| = \sqrt{\left[[ReH(\omega)]^2 + [ImH(\omega)]^2 \right]} \tag{3.11}$$

and ϕ is the argument defined as:

$$\phi = Arg[H(\omega)] = Arc\tan\left[\frac{ImH(\omega)}{ReH(\omega)} \right] \tag{3.12}$$

In an electrochemical system, the transfer function between potential (entrance function) and current (exit function) is the admittance, Y. In the frequency domain, admittance is given by:

$$\Delta\bar{I}(\omega) = Y(\omega)\Delta\bar{E}(\omega) \tag{3.13}$$

The transfer function between current (entrance) and potential (exit) is the impedance Z, which is the inverse of admittance. It is usual in electrochemistry to plot -ImZ(ω) as a function of ReZ(ω), in order to obtain so-called Nyquist diagrams. As an example, a typical Nyquist diagram for methanol oxidation on Pt is shown in Figure 3.9. The two successive loops can be explained by the fact that the rate-determining step (rds) of the process is the oxidation of adsorbed intermediates to give the final product (CO_2).
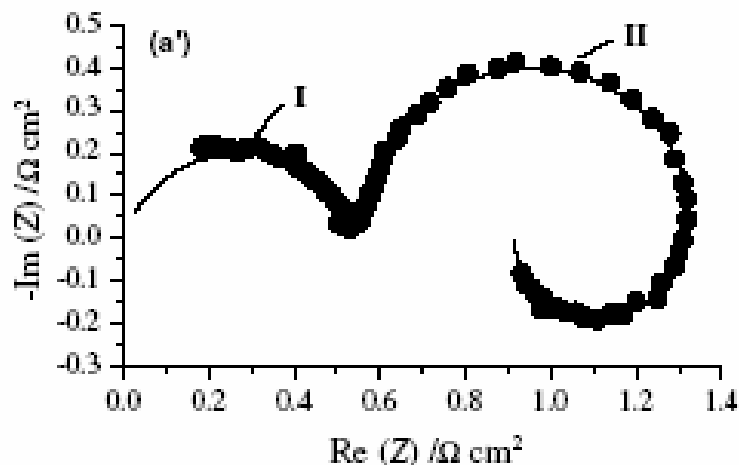

Figure 3.9: Typical Nyquist diagram obtained for methanol oxidation on Pt at 0.6 V and 60°C [13].

The profile of Nyquist diagrams can be rationalized in terms of equivalent circuits that take into account and quantify electrochemical steps of the process as well as

the electrolyte resistance, the charging of the double-layer or adsorption on the electrode surface. EIS was used in the present work to reveal differences in alcohols electrooxidation mechanisms on various Pt-based nanoparticulate catalytic surfaces.

5. PHYSICAL CHARACTERIZATION

5.1. Electronic Microscopies (TEM / SEM) [14, 15]

Electron Microscopy is based on the interactions that take place when an electron beam of high energy strikes a sample. Through a complex system of electromagnetic fields that work like lenses, the electrons are focussed on a certain region of the sample. The main difference between Transmission Electron Microscopy (TEM) and Scanning Electron Microscopy (SEM) is that in the former case electrons pass through the sample, whereas in the later case the electron probe scans the surface of the object under study. The reflected or transmitted electrons are used to produce high-magnification images of the sample.

The size of nanoparticles made by the microemulsion method, as well as their degree of agglomeration, were determined by TEM. A small droplet of the aqueous suspension of metallic particles was deposited onto an amorphous carbon-coated copper grid, and the excess water was removed before analysis in a Philips CM 300 Microscope that can operate with accelerating tensions up to 300 keV. EDX measurements were performed at the same time than TEM experiments (see Section 4.4 of this Chapter). While TEM images were recorded, EDX measurements were also made (see Section 5.4 of this Chapter). SEM was the employed technique for the direct observation of BDD surfaces (modified by electrochemical treatments or electrodeposited Pt particles). After its preparation, the sample was introduced into the vacuum chamber of a Philips XL 30 FEG Microscope, operating at a field emission of 1-30 kV, and then investigated. The TEM and SEM analyses were carried out at the Interdisciplinary Centre of Electron Microscopy (CIME), EPFL.

5.2. X-Ray Photoelectron Spectroscopy (XPS) [16]

This technique is based on the photoelectric effect. An incoming photon is absorbed in or near the surface of the solid under analysis; the energy of the photon is then transferred to an electron. If the energy of the photon is sufficiently high, the electron may leave the solid surface. The electron's kinetic energy after excitation is given by:

$$E_{kin} = h\nu - E_b(X) - \Phi_s \tag{3.14}$$

where $h\nu$ is the incoming photon's energy, $E_b(X)$ is the binding energy of an electron in state X, and Φ_s is the work function of the surface. However, the work function of

the sample Φ_s is different from that of the spectrometer Φ_{spect}, therefore, the kinetic energy inside the analyzer E'_{kin} is different from that immediately after the photoemission event E_{kin}. The quantity measured during a typical experiment is:

$$E'_{kin} = h\nu - E_b(X) - \Phi_{spect} \qquad\qquad (3.15)$$

where Φ_{spect} is the work function of the spectrometer. Considering that both the photon energy and the spectrometer work function are well-known, it becomes easy to calculate the initial electron state $E_b(X)$.

Using XPS, one can analyze solid samples, both qualitatively and quantitatively. Different oxidation states of a chemical element can be distinguished because of the shift to higher values of binding energies induced by the screening of the positive charge of the nucleus by the remaining valence electrons. Electronic transfers between the components of an alloy are also reflected in chemical shifts in the binding energies of a selected element (extraction work). It was possible from these shifts to see whether so-called electronic (ligand) effect is important for enhanced catalytic activity of a given surface. An example of chemical shifts of the XPS Pt*4f* peak observed at various Pt-based nanoparticles is shown in Figure 3.10. Lower binding energies of Pt arise due to transfer of e⁻ d from the alloying metal to Pt; this effect is more pronounced for Ni than for Ru, since Ni has a higher electronegativity difference relative to Pt. Such an electron transfer to Pt would result in the weakening of the Pt-CO bonds formed during methanol oxidation at Pt, and lead to a more facile removal of surface adsorbed intermediates [17].
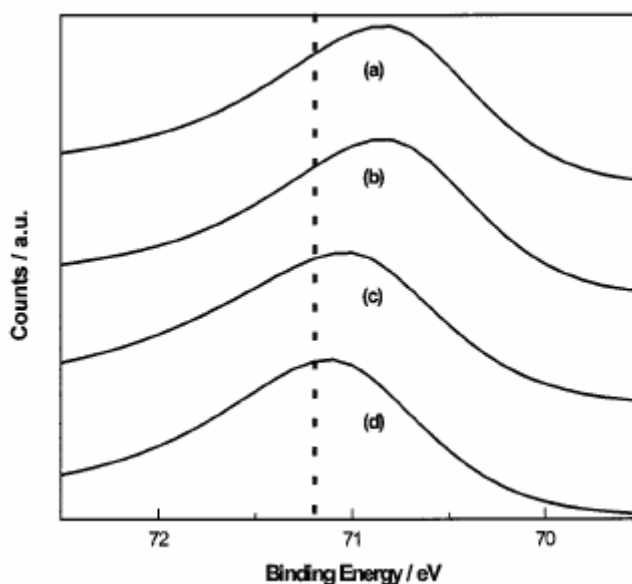

Figure 3.10: Pt*4f* peak shift of Pt-based nanoparticles; (a) Pt/Ni (1:1), (b) Pt/Ni (3:1), (c) Pt/Ru/Ni (5:4:1), and (d) Pt/Ru (1:1). Dotted vertical line: position of pure Pt [17].

In the present work, XPS was used to discriminate the oxidation states of metals in monometallic and bimetallic particles. It was also used as an elemental quantification method. A large droplet of the aqueous suspension of microemulsion-synthesized Pt nanoparticles was deposited on a BDD substrate and analysed after the excess water being dried under nitrogen atmosphere. For the Pt/Ru and Pt/Sn bimetallic nanoparticles, a gold substrate was used, since the Ru*3p* and C*1s* peaks are located at very similar values of binding energy (around 280 eV). Peaks of interest (C*1s*, Pt*4f*) within the different signals were deconvolved using the CasaXPS® computer software in order to discriminate between the different contributions of a single element.

For these measurements a Kratos Axis-Ultra spectrometer with monochromatic Al K_α X-ray source operated at 15 kV with a pass energy of 20 eV was used. A total area of 700×300 μm was investigated over a thickness of 50-100 Å. It should be realised that in the case of nanoparticles having a size between 2 and 5 nm, XPS cannot be considered as a superficial analysis technique. XPS measurements were conducted at the Laboratory of Chemical Metallurgy (IMX-LCM), EPFL.

5.3.   X-Ray Diffraction (XRD) [18]

This technique is based on the interactions between an incident electromagnetic radiation and atoms of the material. In the case of solid crystalline structures, the overlap of the different waves diffracted by successive atom layers can give rise to constructive and destructive interferences, depending on the interplanar distances of the network (d), on the wavelength of the used radiation (λ), and on the of incidence angle of incidence of the radiation on the surface of the solid (θ). All these parameters are related for a constructive interference by the Bragg's law (Eq. 3.16):

$$n\,\lambda = 2d\,\sin\theta \qquad\qquad\qquad (3.16)$$

Information about the crystalline structure of the material is available from XRD. Moreover, it is also possible to estimate the diameter of a particle (Scherrer's equation), analyzing the diffraction peaks bandwidth at half height. For XRD a large droplet of microemulsion-synthesized nanoparticles suspension was placed onto a BDD substrate. The excess water was completely removed under nitrogen atmosphere, and the sample was then analysed. The experimental apparatus used was a Siemens D500 Powder Diffractometer. Measurements were performed using the K_α Cu ray (1.54 Å) using slits of 1°/1°/1°/0.05° over the 5-90° range, a step of 0.04°, and a resolution of 4 sec/step. XRD measurements were carried out at the Laboratory of Ceramics (IMX-LC), EPFL.

5.4. Energy Dispersive X-Ray Spectroscopy (EDX) [19]

This analysis technique is based on the interactions that occur when a high-speed electronic beam hits the material under investigation. An electromagnetic radiation composed of X-Rays and visible light that is characteristic of each element is emitted. This emission can be used for qualitative and quantitative analysis of the samples. The atomic composition of bimetallic microemulsion-synthesized nanoparticles was determined by EDX during TEM. For EDX, an OXFORD system, model INCA, available at the Interdisciplinary Centre of Electron Microscopy (CIME), EPFL, was used.

5.5. Atomic absorption spectroscopy (AAS) [20]

AAS is a technique of elementary chemical analysis based on the absorption of light by atoms of an element present in a given sample when a beam of a certain wavelength irradiates it. Lamps emitting at a wavelength corresponding to the characteristic emission of a particular element being analyzed are used. With this technique the metallic elements could be analyzed quantitatively.

AAS was used to determine the platinum contents of different samples such as microemulsion-synthesized Pt-based nanoparticles or electrodeposited Pt on BDD. Metallic platinum was dissolved in a 8 M HCl solution containing traces of H_2O_2, (typically over a period of 6-8 h at 90 °C); this obtained solution was diluted ten more times in ultra-pure water prior its analysis. The equipment used for these measurements was a Shimadzu Model AA-6650 spectrophotometer.

6. REFERENCES

[1]   D. Gandini, E. Mahé, P.-A. Michaud, W. Haenni, A. Perret, Ch. Comninellis, *J. Appl. Electrochem.* **30** (2000), 1345.

[2]   Y. V. Pleskov, *Russ. Chem. Rev.* **68** (1999), 381.

[3]   Y. V. Pleskov, in: R. C. Alkire, D. M. Kolb (Eds.), *Advances in Electrochemical Science and Engineering*, Wiley-VCH, Weinheim (2002), p. 209.

[4]   B. El Roustom, G. Fóti, Ch. Comninellis, *Electrochem. Comm.* **7** (2005), 398.

[5]   M. Boutonnet, J. Kizling, P. Stenius, *Colloids Surf.* **5** (1982), 209.

[6]   A. J. Bard, L. R. Faulkner, *Electrochemical Methods - Fundamentals and Applications (2nd edition)*, John Wiley & Sons, Inc., New York (2001).

[7]   H. H. Girault, *Electrochimie physique et analytique*, PPUR, Lausanne (2001).

[8]   H. Angerstein-Kozlowska, B. E. Conway, W. B. A. Sharp, *Electroanal. Chem. Interfacial Electrochem.* **43** (1973), 9.

[9]   F. Montilla, E. Morallon, I. Duo, Ch. Comninellis, J. L. Vazquez, *Electrochim. Acta* **48** (2003), 3891.

[10]   A. Hamnett, in: A. Wieckowski (Ed.) *Interfacial Electrochemistry - Theory, Experiments, and Applications*, Marcel Dekker, Inc., New York (1999), p. 843.

[11]   N. A. Hampson, M. J. Willars, B. D. McNicol, *J. Power Sources* **4** (1979), 191.

[12]   B. Scharifker, G. Hills, *Electrochim. Acta* **28** (1983), 879.

[13]   J. Otomo, X. Li, T. Kobayashi, C.-j. Wen, H. Nagamoto, H. Takahashi, *J. Electroanal. Chem.* **573** (2004), 99.

[14]   T. G. Rochow, E. G. Rochow, *An Introduction to Microscopy by Means of Light, Electrons, X-Rays, or Ultrasound*, Plenum Press, New York (1978).

[15]   X.-F. Zhang, Z. Zhang (Eds.), *Progress in Transmission Electron Microscopy. Vol. 1: Concepts and Techniques*, Springer-Verlag, Heidelberg (1999).

[16]   T. A. Carlson (Ed.) *X-Ray Photoelectron Spectroscopy*, Dowden, Hutchinson & Ross, Inc., London (1978).

[17]   K.-W. Park, J.-H. Choi, B.-K. Kwon, S.-A. Lee, Y.-E. Sung, H.-Y. Ha, S.-A. Hong, H. Kim, A. Wieckowski, *J. Phys. Chem. B* **106** (2002), 1869.

[18]   B. E. Warren, *X-Ray Diffraction*, Addison-Wesley Publishing Company, Reading (1969).

[19]   G. Svehla (Ed.) *Energy Dispersive X-Ray Fluorescence Analysis*, PWN, Warsaw (1989).

[20]   M. Slavin, *Atomic Absorption Spectoscopy*, Wiley, New York (1978).

Chapter 4 RESULTS: Electrodeposition of Pt Particles on BDD and BDD-Au Modified Electrodes. Use in Alcohols Electrooxidation

1. INTRODUCTION

The study of small metallic particles has gained considerable attention during the last few years due to the outstanding properties of this class of material compared to those of bulk materials [1] and has covered fields as different as optics, magnetism, or electronics. In catalysis and electrocatalysis, Pt particles have certainly been the most studied ones due to their potential use in the Direct Alcohol Fuel Cell Technology [2-5]. Gold nanoparticles have also shown surprisingly high catalytic activity for CO oxidation [6, 7] or oxygen reduction [8, 9], whereas bulk gold has been for a long time considered as a poor chemisorber and catalyst.

Metal nanoparticles can be synthesized using a wide variety of techniques and methods. Among them electrodeposition is certainly the easier one to be carried out for electrochemists, and consequently this method has been largely theoretically and experimentally studied [10-13]. Electrochemical deposition has been used for the realization of metallic films and particles of various natures on various types of substrates. For instance the electrodeposition of Pt on glassy carbon [14] or tungsten [15] has been experimentally studied. Studies of the electrodeposition of other metals, such as molybdenum [16], mercury [17], or alloys [18] have also been reported. Moreover the development of new powerful tools such as the Scanning Tunnelling Microscope (STM) has allowed the observation of the first stages of this process [19-21]. Due to its outstanding properties of chemical inertness, mechanical resistance or wide potential window available between oxygen and hydrogen evolution [22, 23] the synthetic boron-doped diamond (BDD) electrode has been also used as substrate electrode for metal electrodeposition. The electrodeposition on BDD of several metals including silver [24], iridium oxide [25], lead [26] or platinum [27, 28] has been investigated using electrochemical techniques and AFM (Atomic Force Microscopy). It has been found that, for electrodeposited Pt particles on BDD [28], the deposit was stable and the response of the composite electrode could be attributed solely to the supported particles. Such BDD-Pt composite electrode was also successfully used for the electrocatalysis of methanol electrooxidation.

During this Chapter of the thesis a new method for the co-deposition of Au and Pt particles on BDD electrode is presented. The interest of having both Pt and Au deposited onto the same substrate comes from the extraordinary catalytic activity of gold nanoparticles for CO oxidation [6, 7], that is well-known as the major poisoning

adsorbed species during methanol electrooxidation on Pt [29]. However there are very few studies on the simultaneous use of Pt and Au electrocatalysts. It has been shown that Au ad-atoms deposited on a Pt surface had the same electrocatalytic properties than a Au/Pt alloy [30] and Pt/Au electrodes have been used for the electrooxidation of phenol in acid medium [31]. It has also been shown that the simultaneous use of graphite-based platinum electrodes and metal oxide supported gold nanoparticles is a promising solution for the search of anode catalysts for methanol electrooxidation in alkaline medium [32]. Our preparation method of Au/Pt co-deposits on BDD involves two steps: *(i)* deposition of stable Au nanoparticles on the diamond substrate by heat treatment of a sputtered gold film on BDD [33] and *(ii)* electrodeposition of additional Pt particles from a hexachloroplatinic ions solution, leading to co-deposited Au and Pt particles on diamond. Preliminary heating tests of the co-deposit have also been conducted to prepare a Au/Pt alloy in which the two metals should be more closely related. The aim was to allow most efficient surface migration of adsorbed CO from methanol dehydrogenation from Pt sites (where they are produced) to Au sites (where they can be easily removed). The electrodeposition of Pt was performed both on Au pre-modified and bare BDD substrates. In both cases the deposition mechanism was determined by chronoamperometry and the deposits physically characterized by SEM and XPS. Moreover the electrocatalytic activity of the three types of deposits on diamond (Pt, Au/Pt and calcinated Au/Pt) toward methanol and ethanol electrooxidation was evaluated by cyclic voltammetry.

2. EXPERIMENTAL

The BDD electrodes used here were purchased by CSEM (Centre Suisse d'Electronique et Microtechnique, Neuchâtel) and were synthesised by the hot filament chemical vapour deposition technique (HF-CVD) on single crystal p-type Si <100> wafers (1-3 mΩcm, Siltronix). The doping level of boron expressed as B/C ratio was about 3500 ppm. The obtained diamond film thickness was about 1 μm with a resistivity in the range 10-30 mΩcm. This as-grown BDD contains some graphitic (sp^2) phase and is hydrogen terminated. Anodic polarization of diamond (10 mA cm^{-2} in 1 M H_2SO_4 at 25 °C during 30 min) eliminates most of the sp^2 and adsorbed hydrogen from the surface, and is our standard procedure to obtain reproducible electrochemical measurements [34].

Electrodeposition of Pt on BDD was performed applying a potential step from a potential value for which no deposition occurs to a value for which Pt^{4+} ions are reduced to Pt^0, to a 2 mM H_2PtCl_6 in 1 M $HClO_4$ solution that was previously saturated with nitrogen gas. The reduction reaction occurred following Equation 4.1:

$$PtCl_6^{2-} + 4e^- \rightarrow Pt + 6Cl^- \tag{4.1}$$

For this purpose the three-electrode cell presented in Chapter 3 was used, with BDD as working electrode (exposed surface of diamond: 0.4 cm^2), Hg/Hg$_2$SO$_4$.K$_2$SO$_4$(sat.) as reference and a platinum wire as counter electrode. The electrodeposition process was followed by means of chronoamperometry (CA), and all other types of electrochemical measurements presented during this Chapter were done using the same set-up. All solutions were made with ultra-pure (Millipore$^®$) water using analytical grade reactants without further purification.

Electrodeposition of Pt on BDD modified by Au nanoparticles (BDD-Au) was performed by the same way as on bare BDD. Deposition of Au nanoparticles on BDD was realised using a two-step preparation method developed in our group [33]. A gold film was firstly deposited on diamond by short-time (6 to 12s) sputtering in an inert atmosphere, and then heated at 600°C in order to yield stable Au nanoparticles of diameter in the 10-15 nm range. The BDD-Au composite electrode was used as working electrode in the set-up described above. The resulting BDD-Au/Pt electrode was then used directly or after an additional heating treatment (400°C for 1 h in air) realized as an attempt to yield an alloy between the two metals.

Both the BDD-Pt and BDD-Au/Pt electrode were electrochemically and physically characterized by X-ray Photoelectron Spectroscopy (XPS) and Scanning Electron Microscopy (SEM), using the methods and set-ups described in Chapter 3. The Pt*4f* doublet in XPS spectra was deconvolved using the CasaXPS$^®$ software to evaluate the electronic interaction between the two metals. Electrochemical measurements were performed as described above; all potentials reported here are plotted with respect to the Standard Hydrogen Electrode (SHE). All solutions were made in ultra-pure water (Millipore$^®$) using analytical grade reactants without further purification and were saturated with nitrogen gas prior to each experiment.

3. RESULTS AND DISCUSSION

3.1. Electrodeposition of Pt on BDD electrode

3.1.1. Deposition mechanism and physical characterization

Electrodeposition of Pt on BDD was carried out in a 2mM H$_2$PtCl$_6$ + 1 M HClO$_4$ solution, stepping the potential from a value for which no deposition occurs (typically 1 V vs. SHE) to a value for which reduction and deposition of Pt^{4+} ions take place (0.02 V vs. SHE). The amount of electrodeposited Pt was monitored by the integrated charge of the I-t electrodeposition curve, assuming in first approximation that side reactions (incomplete reduction of Pt^{4+}, hydrogen evolution on deposited Pt...) can be

neglected. A typical current-time transient for the electrodeposition of Pt particles on a BDD electrode is shown in Figure 4.1. This chronoamperometric curve is very closed to the theoretical one for electrochemical deposition [10] and can be divided into 4 successive time intervals as illustrated on Fig. 4.1. At the beginning of the first time interval (zone I in Fig. 4.1), a sharp increase followed by a current decay is observed, that corresponds to the double-layer charging current and the initial nucleation process. Free growth of independent nuclei for deposition or formation of new nucleation sites without overlapping effects explain the current increase of the second interval time (zone II of Fig. 4.1). During the third interval time (zone III in Fig. 4.1), the growth of independent nuclei and nuclei overlap can simultaneously occur; the current increases up to a maximum (j_m on Fig. 4.1) for which nuclei overlapping happens. Finally during the fourth interval time (zone IV in Fig. 4.1), the current decreases due to the overlapping of the diffusion zones of different nuclei and the coalescence of the growing centres. From the time t_m corresponding to j_m, the current decreases due to the decrease in the surface area of deposited platinum particles, and it can then be considered that a change from hemispherical to linear mass transfer diffusion occurs because of particles size increase.
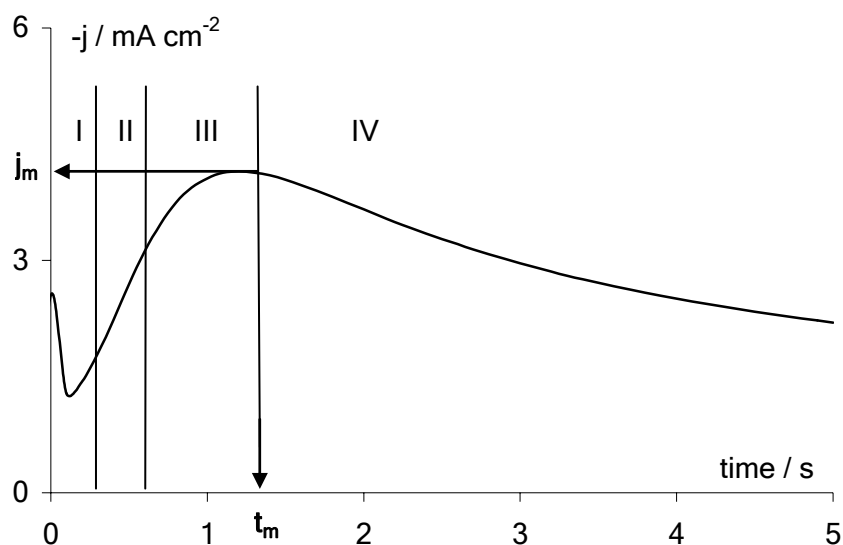
Figure 4.1: Chronoamperometric curve of the electrodeposition of Pt on a BDD electrode. Potential step from +1 to +0.02 V vs. SHE in 2 mM H_2PtCl_6 + 1 M $HClO_4$ solution at T = 25 °C. The different time intervals during the deposition process are marked (zones I-IV) as well as the maximum current density (j_m) and the corresponding maximum time (t_m).

In the domain of free growing of nuclei (zone II) the I-t curve can be plotted in order to yield linear $j^{1/2}$ vs. t plots. This indicates a 3D-nucleation process of hemispherical nucleus with diffusion control [10]. On the basis of this behaviour,

Scharifker and Hills [35] have developed a theoretical model that allows the determination of the nucleation mode between the instantaneous or progressive mechanisms. In the instantaneous nucleation mechanism, all the nuclei are rapidly created during the first stages of the process and their number remains constant all along the growth. In the progressive nucleation mechanism, new nuclei are continuously formed during the whole deposition process because the nucleation rate is low. At the same time, the primary nuclei growth takes place. Figure 4.2 shows the experimental I-t curve plotted in reduced variables (curve a) as well as those relative to the two mechanisms (curve b and curve c for progressive and nucleation mechanisms, respectively). It can be seen on Fig. 4.2 that the experimental curve is in better accordance with those for a progressive nucleation mechanism. Similar results have also been obtained for the electrodeposition of platinum on graphite [20].
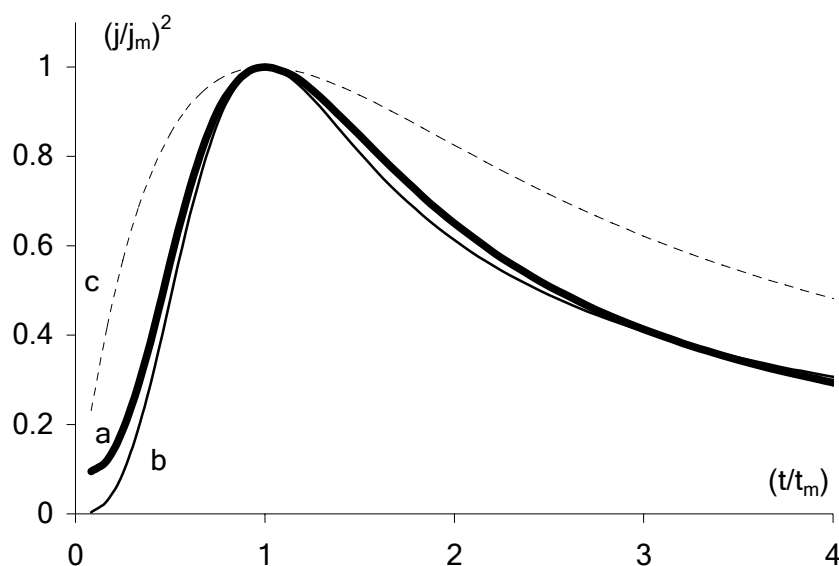
Figure 4.2: I-t response of Pt electrodeposition on BDD plotted in reduced variables. Experimental values (a), theoretical data for progressive (b) and instantaneous (c) nucleation [35].

Figure 4.3 shows SEM micrographs, at two different magnification scales, of a BDD-Pt electrode prepared by a potential step from 1 to 0.02 V vs. SHE in a 2 mM H_2PtCl_6 + 1 M $HClO_4$ solution during 5 s (see Figure 4.4). Well-spherical and isolated Pt particles can be observed on these pictures, with a very large size domain that covers in this case the 40-700 nm range. This is indicative of continuous formation of new nuclei during the deposition process and is in agreement with the progressive mechanism of nucleation of Pt on BDD determined from Fig. 4.2.
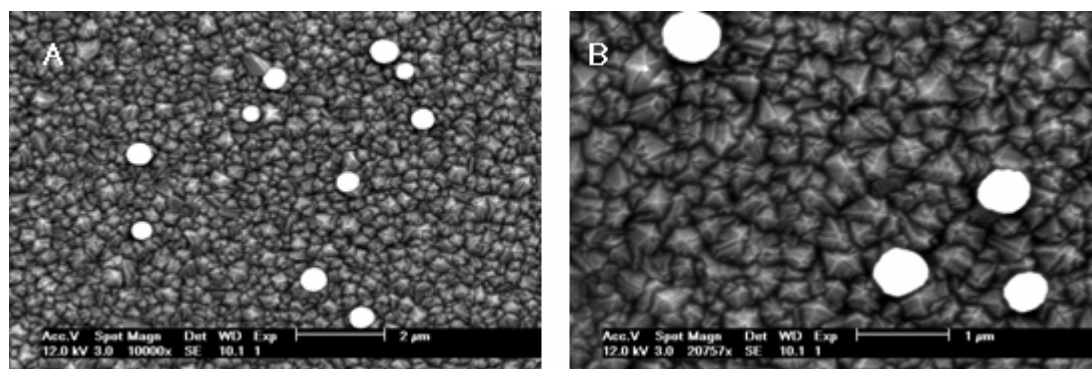
Figure 4.3: SEM micrographs at two different magnification scales of a BDD-Pt electrode prepared by electrodeposition with a single potential step from 1 to 0.02 V vs. SHE in a 2 mM H_2PtCl_6 + 1 M $HClO_4$ solution (see Fig. 4.4).
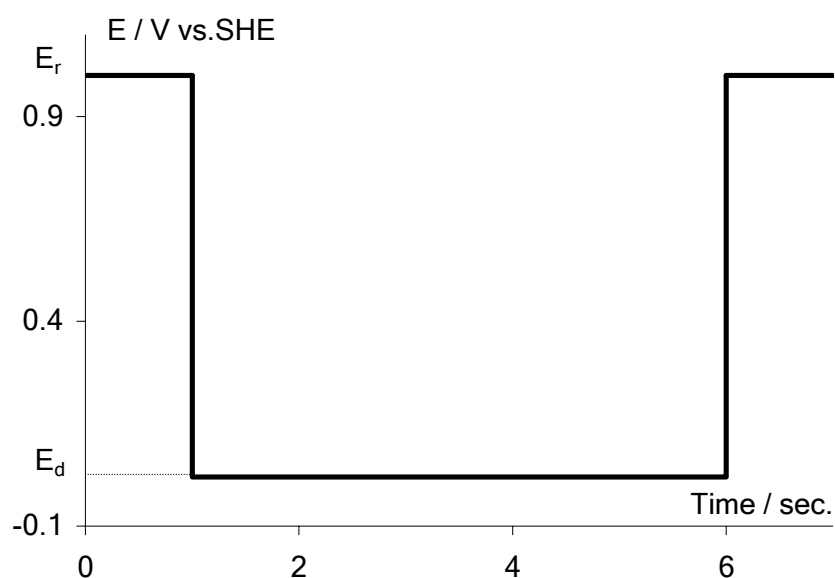

Figure 4.4: Potential-time sequence usually followed for the deposition of Pt particles on BDD in a mono-step sequence. Deposition solution: deaerated 2 mM H_2PtCl_6 + 1 M $HClO_4$. E_d = deposition potential, E_r = relaxation potential.

It is possible to control to a certain extent the obtained size of electrodeposited Pt particles. Adjusting the deposition time and potential or performing electrodeposition following a multi-step deposition procedure (application of a reduction potential followed by a relaxation potential, and repetition of the sequence) allows obtaining smaller particles. Figure 4.5 shows SEM micrographs of Pt particles deposited on a BDD electrode using the following multi-step procedure: one pulse of 1 sec. at 0.02 V vs. SHE, followed by four pulses of 0.5 sec. each at the same potential, with all the deposition pulses separated by relaxation steps of 10 sec. at 1 V vs. SHE (see Figure 4.6). This multi-step procedure was applied to a 2 mM H_2PtCl_6 + 1 M $HClO_4$ solution. It can be seen on these images that the size of such electrodeposited particles is limited to the 30-100 nm size range. However this is again a quite large size domain that does not allow the use of the "nanoparticle" term. Such broad size distribution

has already been reported [27] and has been explained by the BDD surface non-homogeneity (presence of non-diamond impurities).
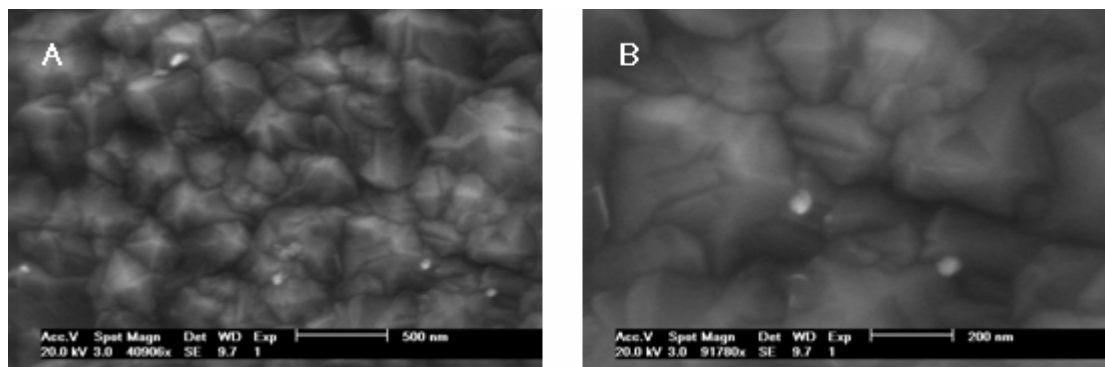

Figure 4.5: SEM micrographs at two different magnification scales of Pt particles electrodeposited on BDD according to multi-step deposition procedure. Application of one pulse of 1 sec. at 0.02 V vs. SHE, followed by four pulses of 0.5 sec. each at the same potential, with all the deposition pulses separated by relaxation steps of 10 sec. at 1 V vs. SHE, in a H_2PtCl_6 2 mM + $HClO_4$ 1 M solution (see Fig. 4.6).
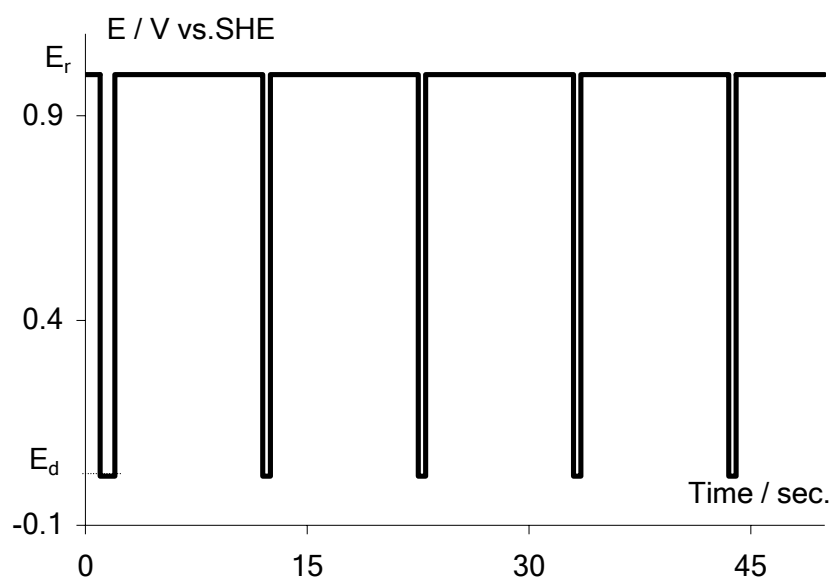
Figure 4.6: Potential-time sequence usually followed for the deposition of Pt particles on BDD in a multi-step sequence. Deposition solution: deaerated 2 mM H_2PtCl_6 + 1 M $HClO_4$. E_d = deposition potential, E_r = relaxation potential.

Electrodeposited Pt particles have also been characterized by XPS. Figure 4.7 shows the XPS survey of the BDD-Pt electrode made by a one-step electrodeposition procedure. Besides the main C *1s* (280 eV), due to the diamond substrate, and O *1s* (532 eV) peaks, due to interaction with atmospheric oxygen, the signal of Pt*4f* is clearly observable at approximately 70 eV and confirms the presence of Pt on the BDD surface. The contribution of Si*2p* is caused by the underlying substrate. Atomic quantification of elements has revealed that Pt is present on the surface in small quantities (around 1.5 at. %).
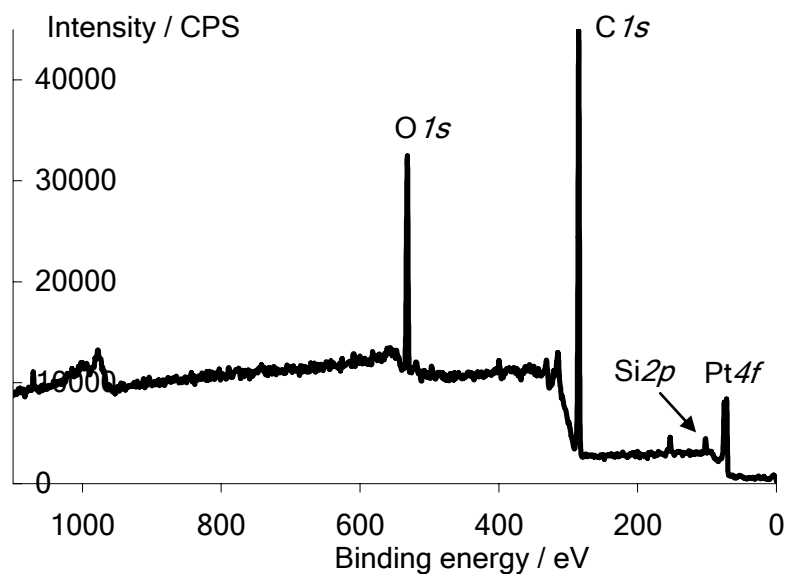
Figure 4.7: XPS survey of a BDD-Pt electrode made by one-step electrodeposition (from 1 to 0.02 V vs. SHE during 5 sec. in 2 mM H_2PtCl_6 + 1 M $HClO_4$ solution).
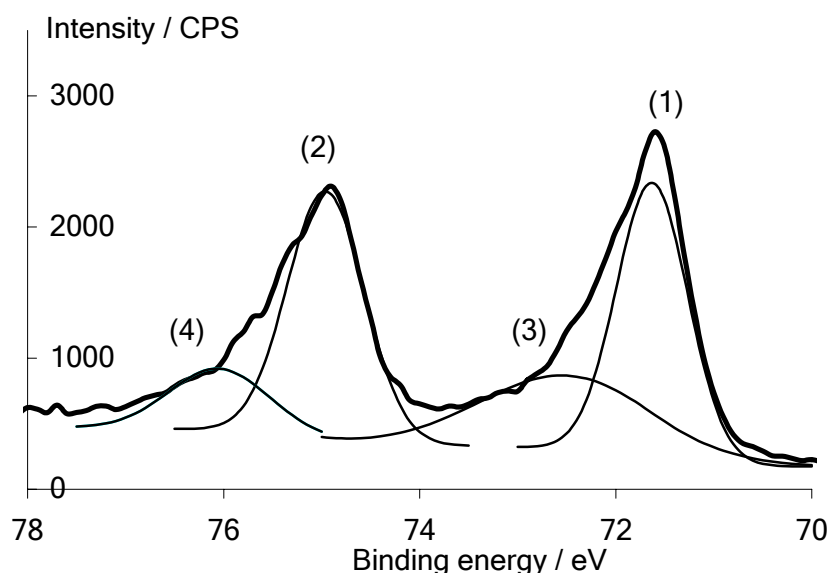

Figure 4.8: Deconvolved XPS Pt*4f* doublet of a BDD-Pt electrode made by one-step electrodeposition (from 1 to 0.02 V vs. SHE during 5 sec. in a 2 mM H_2PtCl_6 + 1 M $HClO_4$ solution).

Moreover, the Pt*4f* doublet of electrodeposited Pt particles on BDD has been deconvolved determine their chemical and oxidation state, using the CasaXPS® computer software (see Figure 4.8). It can be seen that the Pt*4f* signal is composed of four different contributions (peaks 1 to 4 on Fig. 4.8). Peaks 1 and 2 can be attributed to Pt$4f_{7/2}$ and Pt$4f_{5/2}$ lines of metallic Pt (Pt^0), respectively, whereas peaks 3 and 4 can be ascribed to Pt$4f_{7/2}$ and Pt$4f_{5/2}$ lines of Pt^{II} from PtO or Pt(OH)$_2$ [36]. The ratio between metallic and oxidized (+II) forms of Pt was about 3:1. The presence of oxygenated Pt can be due to interaction with the solvent during electrodeposition

and/or with atmospheric oxygen during storage of the BDD-Pt electrode before the measurement was done.

3.1.2. Electrochemical and electrocatalytic characterization

A typical CV of Pt particles electrodeposited on BDD following the procedure described above is shown in Figure 4.9. This voltammogram exhibit the characteristic feature of Pt, *i.e.* two distinctive H adsorption-desorption peaks between 0.05 and 0.35 V followed by a fine double-layer region corresponding to metallic Pt. Further potential cycling inducing the formation of Pt oxides (broad plateau) was not performed here in order to avoid surface rearrangement [37] and aggregation of particles [38]. The electrochemical response of this BDD-Pt composite electrode can solely be attributed to the deposited Pt particles, even at very low Pt loadings, due to the low background current and chemical inertness of diamond. This justifies the choice of BDD as substrate for the electrochemical characterization of nanoparticles.
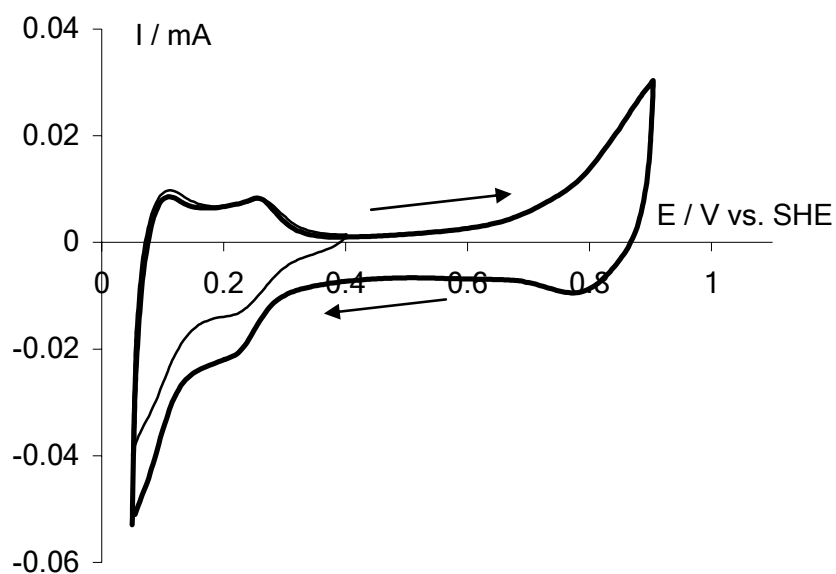
Figure 4.9: CV of electrodeposited Pt particles on BDD electrode. Recorded in 1 M $HClO_4$ at 50 mV s^{-1} and 25°C. Parameters for electrodeposition: potential step of 5 sec. from 1 to 0.02 V vs. SHE in 1 M $HClO_4$ + 2 mM H_2PtCl_6 solution.

The behaviour of electrodeposited Pt particles has also been investigated toward methanol and ethanol electrooxidation. Figures 4.10 and 4.11 show the CV for methanol and ethanol electrooxidation on electrodeposited Pt particles on BDD, respectively. The measured currents are normalized in terms of specific molar currents (A mol$^{-1}_{met}$) that can be defined as follows:

$$j \text{ (A mol}^{-1}_{met}) = S \text{ (cm}^2 \text{ mol}^{-1}_{met}) \times J \text{ (A cm}^{-2})$$ (4.2)

where S represents a geometric effect (nanosizing) and J an electronic effect (catalysis). These CV exhibit the characteristic features of alcohols oxidation on Pt, *i.e.* two well-defined oxidation peaks occurring during the forward and the reverse scans. This unusual shape is due to the surface transitions that occur on Pt when the potential is cycled. Indeed methanol dehydrogenation takes place on Pt at potential as low as 0.05 V vs. SHE. However at this potential value water is not activated and therefore Pt is readily poisoned by reaction intermediates (CO) that block the surface, explaining the flat current feature in this potential region. As soon as water is activated, the current increases due to surface reaction between adsorbed CO and ˙OH that yields the final product CO_2. The following current decrease is caused by formation of Pt oxides; the surface is not capable of MeOH adsorption. During the reverse scan, Pt oxides are firstly reduced and therefore the current can increase again. Finally the water is not activated, explaining the new current decrease and the formation of the second oxidation peak. The CV of methanol electrooxidation at electrodeposited Pt particles on BDD also exhibits some remarkable features that must be commented. First, it can be noticed that the reverse scan oxidation peak is located at a lower potential value ($\Delta E_p \approx 0.06$ V) than the forward scan one (see Fig. 4.10). It indicates that the two successive CO oxidation processes are not exactly of same nature and it can reasonably be postulated that the oxygenated species involved in CO removal is not the same. However the beginning of the forward scan peak and the end of the reverse scan one are located exactly at the same potential values, sign that the Pt surface is in the same state before any oxidative CO removal and after the occurrence of the two CO oxidation processes (Fig. 4.10). It can therefore be assumed that the adsorbed intermediate (poison) is of same nature, whatever is the potential scanning direction, as soon as the potential is not sufficient to allow water dissociation. Finally it can be noticed that, at potential values below water activation (*i.e.* approximately between 0.05-0.5 V vs. SHE), the measured specific molar current is slightly negative. This can be due to impurities adsorbed at the Pt nanoparticles surface coming from the electrodeposition medium.

A similar mechanism should theoretically be considered in the case of ethanol electrooxidation. However this case is much more complicated as it implies the activation of the breaking of the C-C bond. It can be said that the difference in the specific molar currents of the two alcohols electrooxidation on Pt is due to the inability of Pt to promote the C-C bond scission. If a complete methanol electrooxidation of methanol (yielding to CO_2) is considered, six electrons have to be released per methanol molecule oxidized. It is then possible to consider also that ethanol electrooxidation is stopped at C_2 intermediate species that only needs the release of

two electrons per molecule formed. Acetic acid and acetaldehyde are species corresponding to these requirements that have been identified as intermediate in ethanol electrooxidation [39]. It is therefore possible that ethanol electrooxidation could be stopped at these stages. However there is no evidence that the electrooxidation of MeOH on Pt is complete.
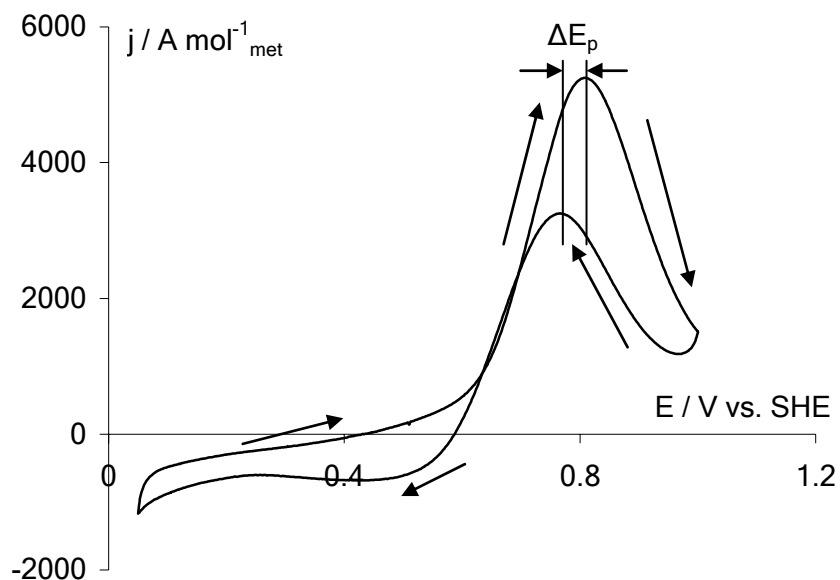

Figure 4.10: CV of MeOH electrooxidation on electrodeposited Pt particles on BDD. Recorded in 1 M $HClO_4$ + 0.1 M CH_3OH at 20 mV s^{-1} and 25°C. One-step electrodeposition (1 to 0.02 V vs. SHE in 1 M $HClO_4$ + 2 mM H_2PtCl_6 during 5 sec.).
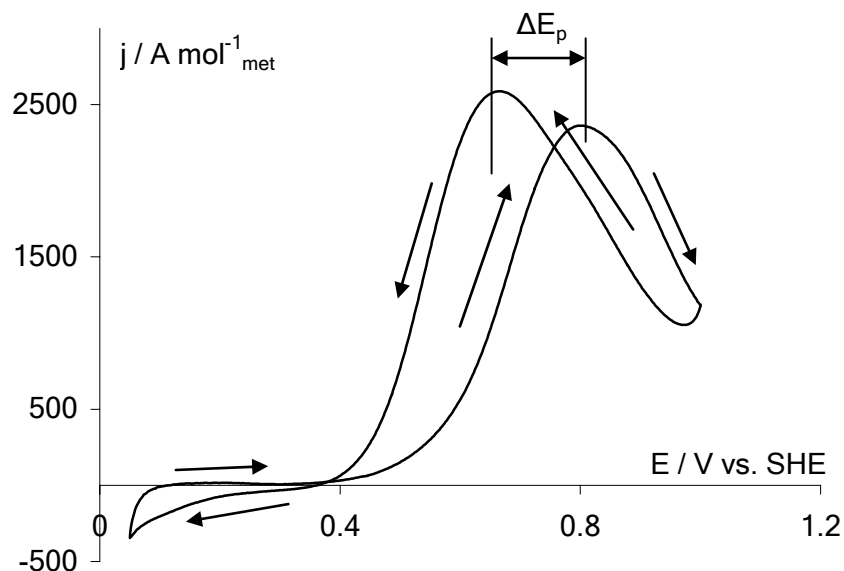
Figure 4.11: CV of EtOH electrooxidation on electrodeposited Pt particles on BDD electrode. Recorded in 1 M $HClO_4$ + 0.1 M CH_3CH_2OH at 20 mV s^{-1} and 25°C. One-step electrodeposition (1 to 0.02 V vs. SHE in 1 M $HClO_4$ + 2 mM H_2PtCl_6 5 sec.).

The other main differences between the CV of EtOH electrooxidation and that of MeOH electrooxidation are the relative positions and intensities of the two oxidation peaks. The difference between reverse and forward peak positions is larger in the case of ethanol electrooxidation ($\Delta E_p \approx 0.15$ V) and the reverse scan peak is of higher intensity than the forward scan one. Moreover the current decrease that follows the reverse scan peak is located at potential 0.15 V lower than the current increase that precedes the forward scan peak. This indicates that the two surface oxidation steps are not exactly of same nature and certainly not involve the same oxygenated species. It indicates also that the catalytic surface is not in the same state in the forward and in the reverse scans. As the potential window was limited in order to avoid surface rearrangements and aggregation of particles, it can reasonably be supposed that a change in the nature of adsorbed intermediates at Pt depending on the potential scanning direction could be at the origin of such differences between the two ethanolic oxidation peaks.

3.2. Electrodeposition of Pt on BDD-Au modified electrode

3.2.1. Deposition mechanism and physical characterization

Electrodeposition of Pt particles has also been carried out on Au nanoparticles pre-modifying a BDD substrate. The aim was to combine the advantages of the two types of particles for the catalysis of methanol and ethanol electrooxidation. Gold nanoparticles exhibit indeed a surprisingly high catalytic activity for CO oxidation even at low temperature [6, 7], whereas bulk gold has always been considered as a poor chemisorber and catalyst. As CO is well-known to be the major contaminant that blocks the Pt active surface in methanol oxidation, the combination of Pt particles on one hand and Au particles on the other hand could be a solution to avoid or at least limit the CO poisoning issue encountered with usual DAFC catalysts. Moreover it has also been tried to heat the Au/Pt deposit in order to realize an alloy. The aim was to realize a structure in which the two metals would be closely related in order to facilitate surface migration of adsorbed CO from Pt sites (where they are generated) to Au sites (where they can be easily oxidized) by increasing the Au/Pt interface. Finally it must be pointed out that only preliminary results on this topic are presented within this thesis; numerous parameters such as relative amounts of the two metals or duration of the heat treatment step performed after Pt electrodeposition have not been optimized yet.

Gold was deposited on diamond by sputtering technique in inert atmosphere at room temperature. A direct current (dc) mode with a discharge of 330 V was applied under an argon pressure of 10^{-2} mbar. Under these conditions the deposition rate

was 0.09 nm s^{-1} on a smooth surface, as determined by profilometric measurement (Alphastep Model 500) of the film thickness on smooth silicon samples processed simultaneously. This finding is in very good agreement with the mass deposition rate of 0.17 μg s^{-1} per 1 cm^2 geometrical surface area obtained by atomic absorption analysis (Shimadzu Model AA-6650) after complete dissolution of the gold deposits in *aqua regia* at 80°C during 30 min. The gold deposit was then heated at 600°C in air in order to yield stable nanoparticles on the diamond substrate [33]. Control over the size of the obtained particles was achieved monitoring the duration of the sputtering step; a sputtering time of 20 sec. led to nanoparticles of diameter included in the 15-20 nm range with a gold loading of 3.7 μg cm^{-2}, as it can be seen in Figure 4.12.A. Increasing the sputtering time results in an increase of both the particles size and density, as it can be observed on Figs. 4.12.B and 4.12.C that show BDD-Au composite electrode surfaces made with sputtering times of 40 and 50 sec., respectively. These sputtering conditions correspond to gold loadings on the diamond substrate of 7.4 and 9.25 μg cm^{-2}, respectively. During all the following sections experiments have been performed using short-time (20 sec., 3.7 μg cm^{-2}) sputtered BDD-Au electrodes and the deposited amount of gold on BDD have been determined according to the sputtering conditions listed above. Specific molar currents reported during the next sections of this Chapter have been calculated taking into account the gold loading on the diamond electrode in addition of the deposited platinum.
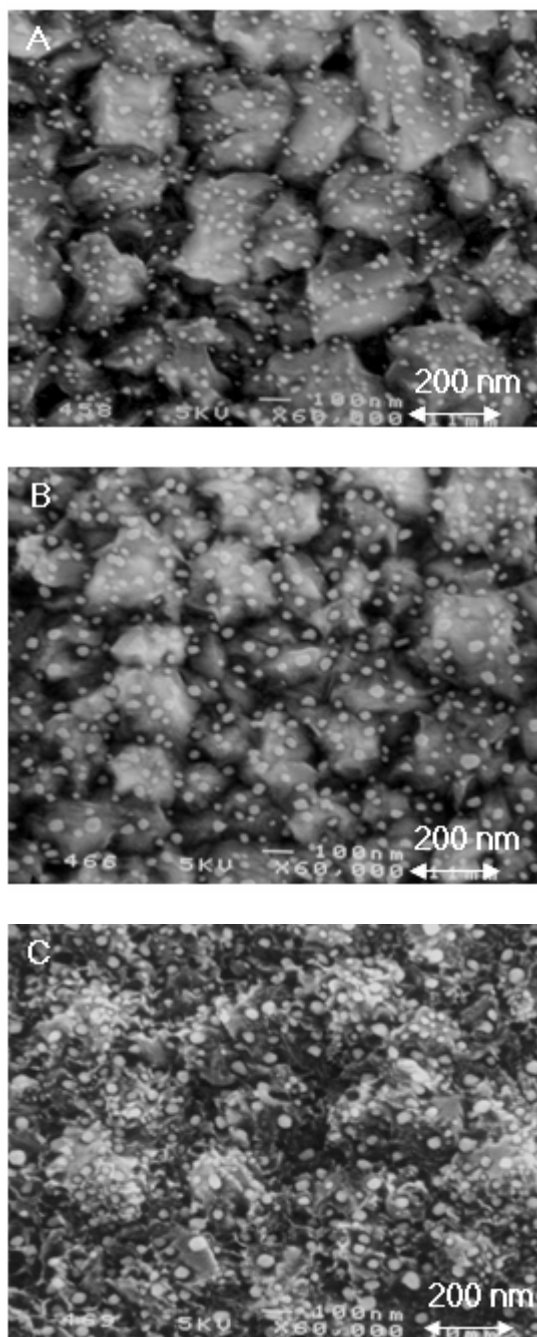
Figure 4.12: SEM micrographs of thermally decomposed Au nanoparticles on BDD electrode. A continuous Au film is deposited on diamond by sputtering (dc mode, discharge of 330 V under 10^{-2} mbar argon pressure at room temperature) for 20 (**A**), 40 (**B**) and 50 sec. (**C**), and then heated in air at 600°C for 1 hour. These sputtering conditions correspond to gold loading of 3.7 (**A**), 7.4 (**B**) and 9.25 μg cm^{-2} (**C**).

The BDD-Au composite electrode has been electrochemically characterized by means of CV in the supporting electrolyte. Figure 4.13 shows the CV, recorded in 1 M $HClO_4$ at 50 mV s^{-1}, of a BDD-Au electrode. As it was the case for electrodeposited Pt particles on BDD (see Fig. 4.9), the response of the BDD-Au composite electrode can solely be attributed to the supported gold particles. The well-known Au oxides reduction peak, located around 1 V vs. SHE is clearly distinguishable on the BDD-Au

composite electrode electrochemical signal and is stable over repetitive potential cycling [33], indicating that particles are firmly attached to the diamond surface.
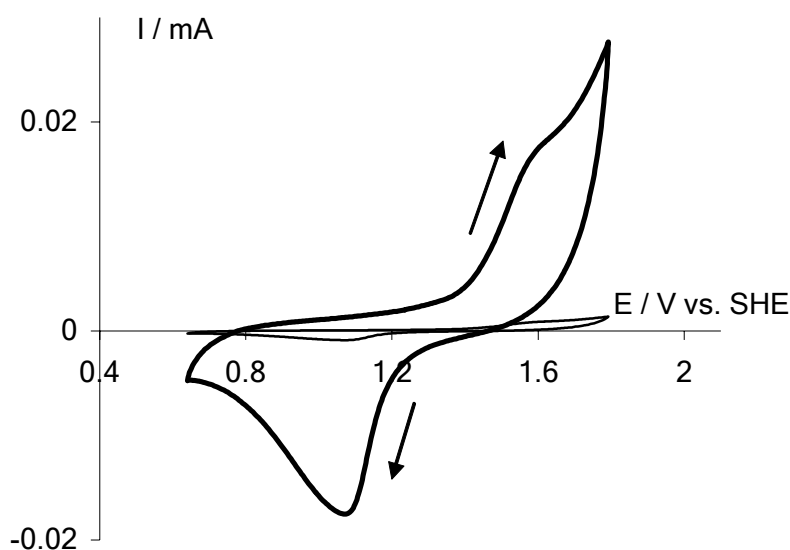

Figure 4.13: CV of thermally decomposed Au nanoparticles deposited on BDD (thick solid line). Recorded in 1 M HClO4 at 50 mV s^{-1} and 25°C. Parameters for sputtering: dc mode, discharge of 330 V under 10^{-2} mbar argon pressure at room temperature for 20 sec., followed by calcination at 600°C in air for 1 h. For comparison the CV of a bare BDD electrode (thin solid line) is added to the picture.

The electrodeposition of Pt particles has also been performed on this BDD-Au composite electrode and the process was investigated by means of chronoamperometry. Figure 4.14 shows a typical current-time transient for the electrodeposition of Pt on a BDD-Au composite electrode. Conditions for Pt electrodeposition on BDD-Au were the same than those for Pt electrodeposition on bare BDD, *i.e.* a potential step from 1 to 0.02 V vs. SHE was applied during 5 seconds to a deaerated 1 M HClO$_4$ + 2 mM H$_2$PtCl$_6$ solution. The main difference between this curve and those for Pt electrodeposition on bare BDD is that the initial sharp current increase followed by a current decay due to double-layer charging and initial nucleation process are not observed here (see Fig. 4.1). However the same following steps (*i.e.* free growth of independent nuclei, nuclei overlap and overlapping of diffusion zones) can be observed in both cases.

In this case also the Scharifker-Hills model for electronucleation [35] could be applied. Figure 4.15 shows experimental I-t curve plotted in reduced variables (curve a) together with curves relative to the two theoretical mechanisms (curve b and c for progressive and nucleation mechanisms, respectively). It can be seen on Fig 4.13 that the experimental curve is in better accordance with those relative to a progressive nucleation mechanism, as it was also determined for Pt electrodeposition

91

on bare BDD (see Fig. 4.2). It can therefore be postulated that Au nanoparticles pre-modifying the diamond surface act like preferential nucleation sites, thus playing a similar role than non-diamond impurities on the bare BDD electrode surface [27].
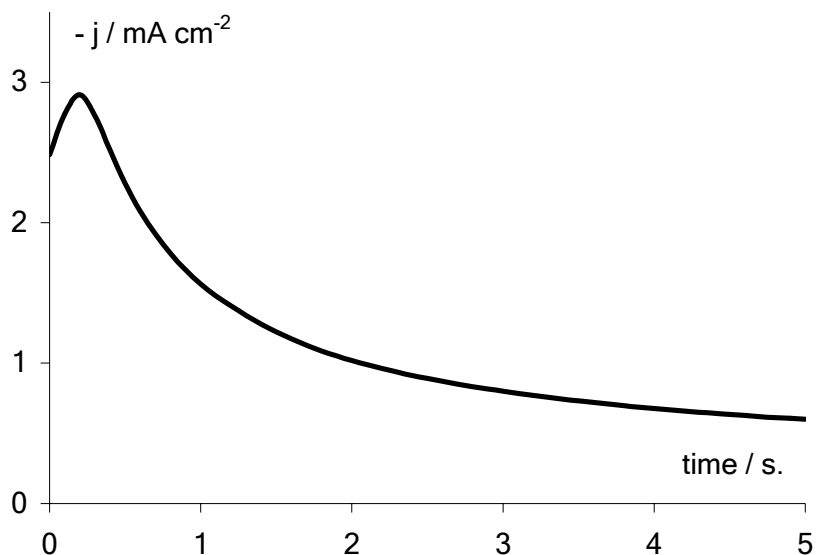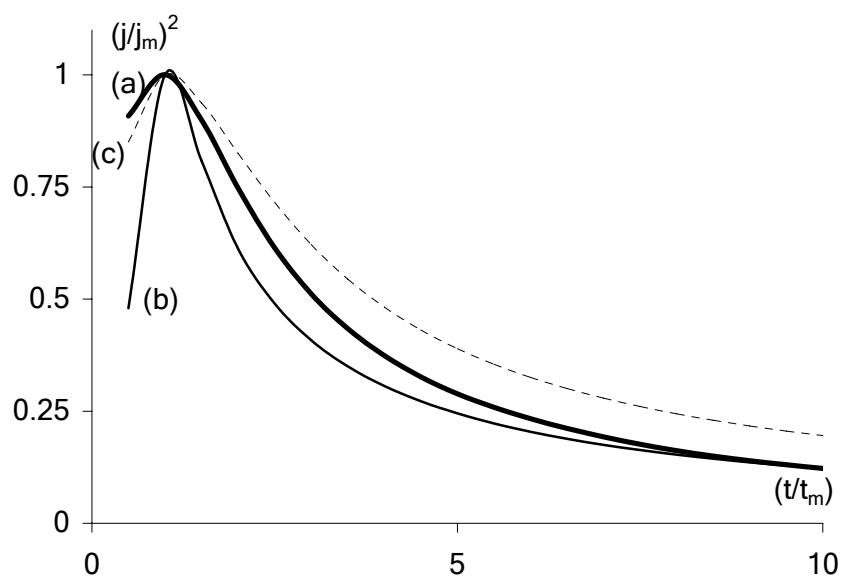

Figure 4.14: Chronoamperometric curve of the electrodeposition of Pt on a BDD-Au electrode. Potential step from +1 to +0.02 V vs. SHE in 2 mM H_2PtCl_6 + 1 M $HClO_4$ solution at T = 25 °C. Parameters for sputtering: dc mode, discharge of 330 V under 10^{-2} mbar argon pressure at room temperature for 20 sec., followed by calcination at 600°C in air for 1 h.

Figure 4.15: I-t response of Pt electrodeposition on BDD-Au plotted in reduced variables. (a) Experimental values. (b) Theoretical data for progressive nucleation [35]. (c) Theoretical data for instantaneous nucleation [35]. Parameters for sputtering: dc mode, discharge of 330 V under 10^{-2} mbar argon pressure at room temperature for 20 sec., followed by calcination at 600°C in air for 1 h.

The morphology of this new type of BDD-Au/Pt electrode was investigated by SEM. A typical SEM micrograph of this kind of modified diamond surface with two types of particles is shown in Figure 4.16. Conditions for the realization of the BDD-Au/Pt electrode were those already mentioned for sputtering (primary Au particles deposition) and electrodeposition (additional Pt particles deposition). It can be seen on the image of Fig. 4.16 that some particle aggregates are present on the diamond surface, indicating that Pt particles should preferentially be deposited near Au particles. Larger particles than those present on the BDD-Au electrode, presumably resulting from Pt electrodeposition (up to 100 nm in diameter), can also be observed on this picture. However there is no absolute evidence on the respective locations of Au and Pt nanoparticles on the surface as chemical analysis of objects of this scale was not possible with the SEM apparatus resolution.
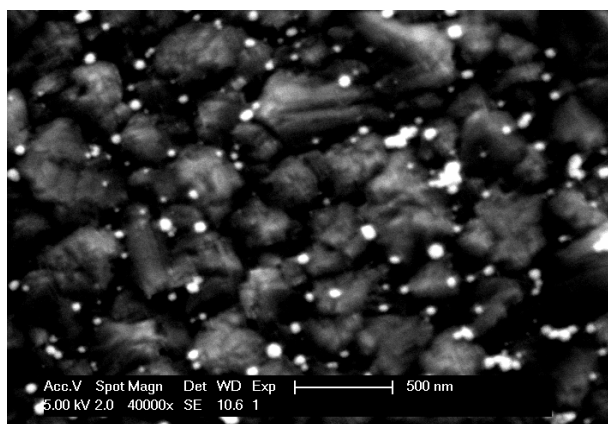

Figure 4.16: SEM micrograph of a BDD-Au/Pt electrode.

XPS analyses have been conducted on BDD-Au/Pt composite electrode. Figure 4.17 shows the XPS survey of such an electrode. Contributions of both the two metals (Au$4f$ doublet at 80-90 eV and Pt$4f$ doublet at 70-80 eV) are observable on Fig. 4.17, confirming the presence of both Au and Pt particles on the diamond surface. Therefore the surface that will be used for further electrocatalytic applications is really a bimetallic one. However these analyses only give poor insights on the structure of the deposit. The whole depth of particles is indeed investigated by XPS. Consequently the relative location of the two metals particles, or the existence of eventual complex structure (core-shell or onion-like for instance) are information that are not accessible. Finally the two peaks attributed to the contributions of C $1s$ (280-290 eV) and O $1s$ (530-540 eV) are due to the underlying diamond substrate and interactions with atmospheric oxygen, respectively.
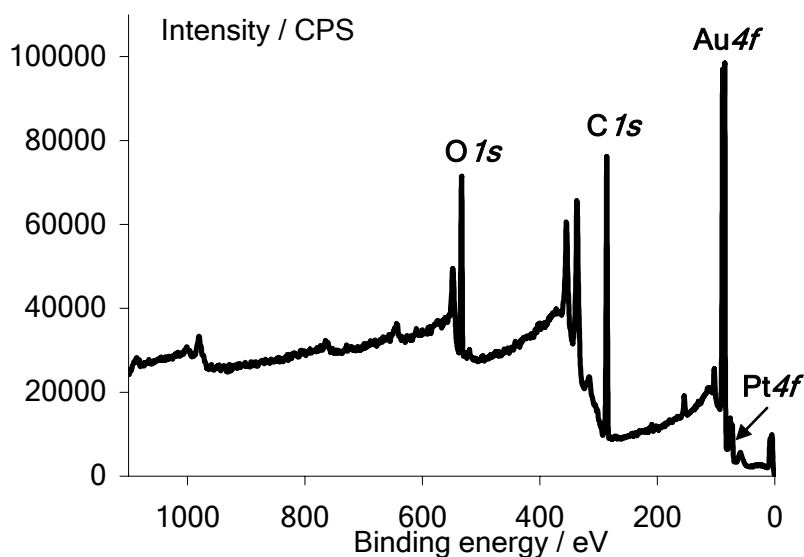
Figure 4.17: XPS survey spectrum of a BDD-Au/Pt electrode.

The CasaXPS® software was used to perform the deconvolution of the Pt4f and Au4f signals in order to determine the respective oxidation states of these two metals. Deconvolved XPS doublets of Pt*4f* and Au*4f* in BDD-Au/Pt composite electrodes are shown in Figures 4.18 and 4.19, respectively. The Pt*4f* signal is composed of four main contributions (peaks 1 to 4 on Fig. 4.18), as it has already been observed in the case of electrodeposited Pt particles on bare BDD (see Fig. 4.8). Peaks 1 and 2 can be attributed to Pt*4f$_{7/2}$* and Pt*4f$_{5/2}$* lines of metallic Pt (Pt^0), respectively, whereas peaks 3 and 4 can be attributed to Pt*4f$_{7/2}$* and Pt*4f$_{5/2}$* lines of Pt^{II} present for instance in PtO or Pt(OH)$_2$ [36]. The ratio between metallic and oxidized (+II) forms of Pt was about 3:1 and was similar to those observed for Pt electrodeposited on bare BDD. The presence of oxygenated Pt can be due to interaction with the solvent during electrodeposition and/or with atmospheric oxygen during storage of the BDD-Au/Pt electrode before the measurement was done. On the contrary the Au*4f* doublet is only composed of two well-defined Gaussian peaks (peaks 1 and 2 on Fig. 4.19). These peaks can be attributed to Au*4f$_{7/2}$* (peak 1) and Au*4f$_{5/2}$* (peak 2) contributions [40], and there is no other contributions. The displacement of binding energies from the table values relative to bulk gold is due to the small size of Au particles [41].
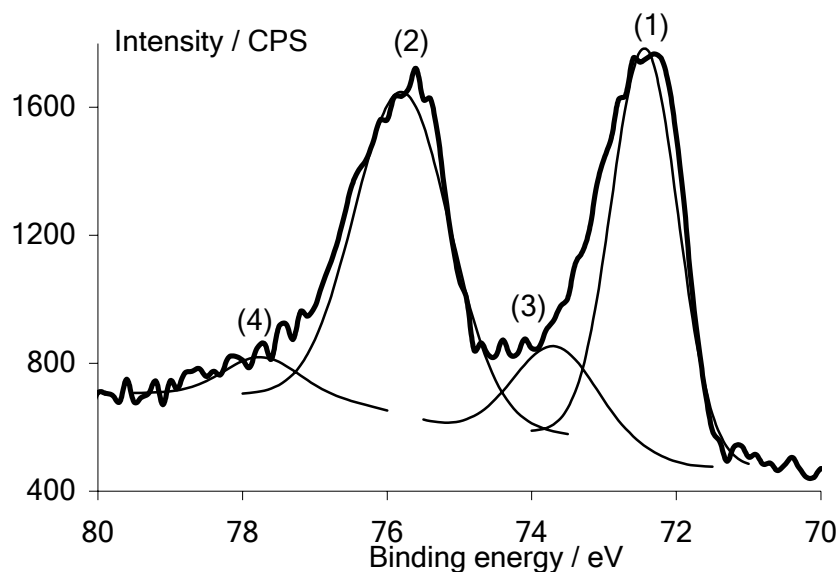
Figure 4.18: XPS deconvolved Pt*4f* doublet of a BDD-Au/Pt electrode.
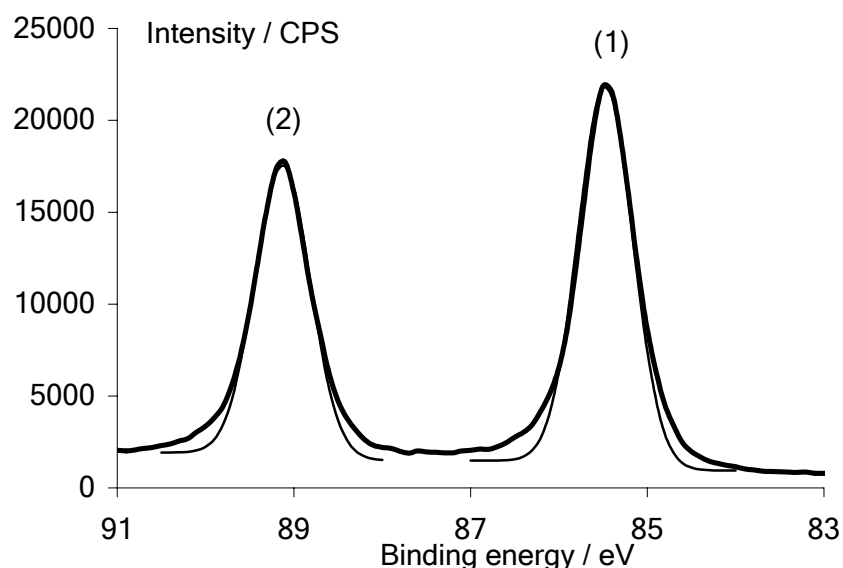

Figure 4.19: XPS deconvolved Au*4f* doublet of a BDD-Au/Pt electrode.

3.2.2. Electrochemical and electrocatalytic characterization

The BDD-Au/Pt composite electrode has also been electrochemically characterized by means of CV measurements conducted both with and without the presence of electroactive species to be oxidized. Figure 4.20 shows the CV of Au/Pt particles deposited on BDD, both calcinated (400°C in air for 1 h) and non-calcinated, in pure supporting electrolyte (1 M $HClO_4$). The two reduction peaks of metal oxides are clearly visible and distinguishable on the CV of the non-calcinated BDD-Au/Pt electrode (thick solid line in Fig. 4.20). The reduction of Au oxides occurs at ≈ 1.1 V vs. SHE and that of Pt oxides at ≈ 0.6 V. This is indicative of the presence of the two

metals on the diamond substrate, and that both the two metals are accessible to the electrolyte so that the deposit is certainly composed of Au particles deposited together with Pt particles. Similar profile of CV of Au/Pt surface has ever been observed in sulphuric acid [42]. Calcination of the deposit at 400°C for 1 h yields to a decrease in the reduction peak area of Pt oxides whereas the reduction peak area of Au oxides remains almost constant. Moreover the reduction peak of Au oxides is slightly shifted to lower potential values whereas the Pt oxides reduction peak position is not changed. It seems that calcination results in the exaltation of the Au character of the BDD-Au/Pt electrode, certainly due to surface segregation and coverage of Pt particles by Au leading to some kind of core-shell structure. Therefore the calcinated composite electrode can certainly be considered as a surface Au-rich one whereas the non-calcinated may be regarded as a surface Pt-rich one. This view is reinforced by the increase in O_2 evolution overpotential evolution that is induced by calcination. The melting point of small (less than 50 nm) gold particles is indeed around 400°C [43] whereas those for Pt particles of the same size is around 900°C; this can explain the fact that gold can cover more or less completely the Pt deposit depending on the calcination conditions.
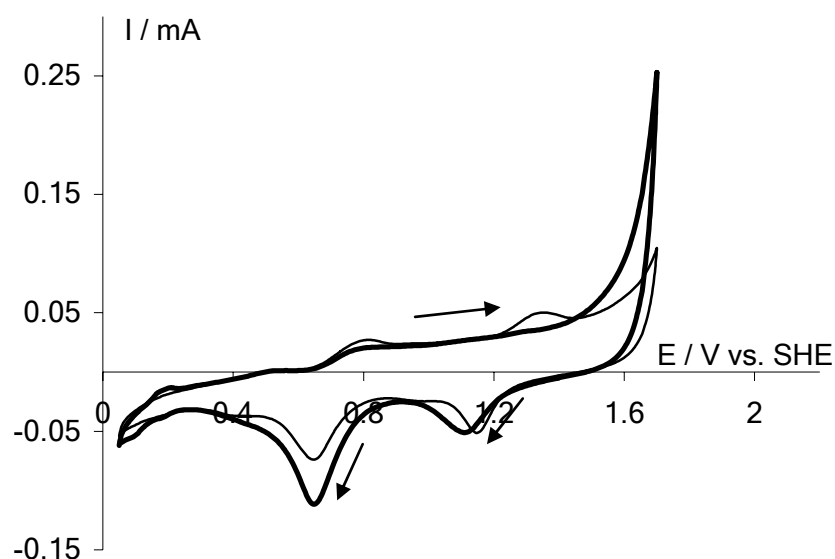

Figure 4.20: CV of Au/Pt (thick solid line) and calcinated Au/Pt (1 h in air at 400°C, thin solid line) particles deposited on BDD. Recorded in 1 M $HClO_4$ at 50 mV s^{-1} and 25°C. Parameters for sputtering: dc mode, discharge of 330 V under 10^{-2} mbar argon pressure at room temperature for 20 sec., followed by calcination at 600°C in air for 1 h. Parameters for electrodeposition: potential step of 5 sec. from 1 to 0.02 V vs. SHE in 1 M $HClO_4$ + 2 mM H_2PtCl_6 solution.

The behaviour of both calcinated and non-calcinated BDD-Au/Pt electrodes toward methanol and ethanol electrooxidation has also been investigated. Figures

4.21 and 4.22 show the CV recorded on the two types of bimetallic deposits on BDD toward the electrooxidation of methanol and ethanol, respectively. Specific molar currents are plotted here with respect to the total amount of deposited metals (*i.e.* platinum plus gold) deduced from integration of current-time transients (Pt) and sputtering conditions (Au). On both the two figures the CV relative to alcohol electrooxidation on calcinated deposit is represented by thick lines. It can be seen on these pictures that the specific molar oxidation currents for non-calcinated Au/Pt deposit are lower than those observed for electrodeposited Pt alone; however the normalisations are taking into account the gold deposit that is not effective for alcohols dehydrogenation at room temperature. Neglecting Au particles deposited on BDD and considering Pt as the only metal present on diamond leads to specific molar currents comparable to those observed in Figs. 4.10 and 4.11. This indicates that the gold deposit only has poor influence on the intrinsic activity of Pt when the two types of metallic particles are only co-deposited on the diamond substrate, especially in the case of methanol electrooxidation. The shape of the CV of ethanol electrooxidation is indeed strongly affected by the addition of Au to Pt since the occurrence of the reverse scan oxidation peak can only be supposed as it is of very low intensity compare to the forward scan one. It can be supposed that the presence of Au at the surface considerably hinders the oxidation and/or adsorption processes that would normally occur at a pure Pt surface during the reverse potential scan. We have also attempted to realize a structure (alloy or other) in which the two metals would be more closely related in order to take advantage of both the remarkable electrocatalytic properties of both Pt and Au nanoparticles. However the calcination carried out under our preliminary conditions dramatically decreases the electrocatalytic activity of the deposit both toward methanol and ethanol electrooxidation. Moreover the characteristic features of alcohols oxidation at Pt have disappeared and only one oxidation peak can be observed in both cases. This is certainly due to the fact that Pt oxides are more difficult to reduce and hence no oxidation event is possible during the reverse potential scan.
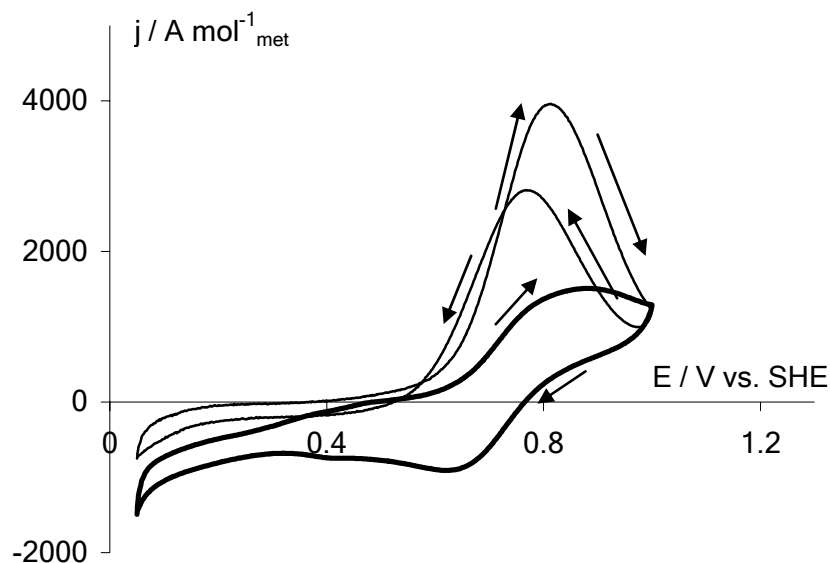
Figure 4.21: CV of MeOH electrooxidation on Au/Pt particles (thin solid line) and calcinated Au/Pt (thick solid line) deposited on BDD. Recorded in 1 M HClO$_4$ + 0.1 M CH$_3$OH at 20 mV s^{-1} and 25°C. Parameters for sputtering: dc mode, discharge of 330 V under 10^{-2} mbar argon pressure at room temperature for 20 sec., followed by calcination at 600°C in air for 1 h. Parameters for electrodeposition: potential step of 5 sec. from 1 to 0.02 V vs. SHE in 1 M HClO$_4$ + 2 mM H$_2$PtCl$_6$ solution.
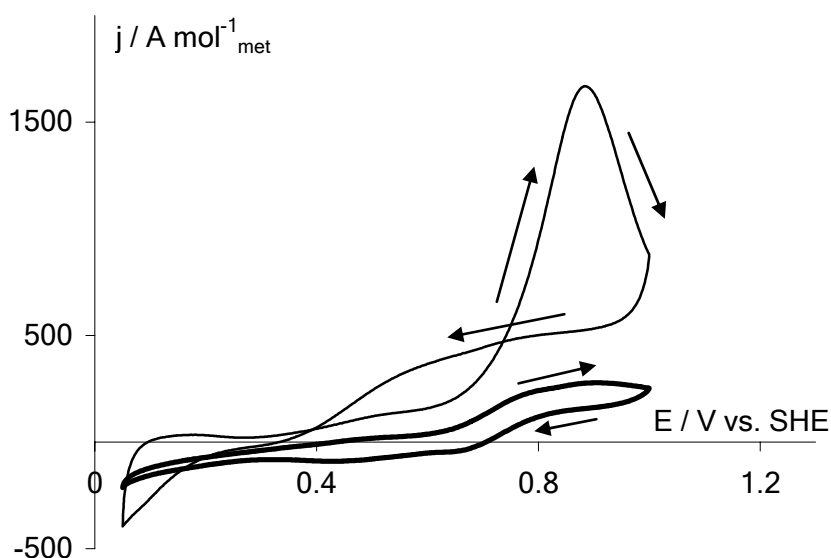

Figure 4.22: CV of EtOH electrooxidation on Au/Pt particles (thin solid line) and calcinated Au/Pt (thick solid line) deposited on BDD. Recorded in 1 M HClO$_4$ + 0.1 M CH$_3$CH$_2$OH at 20 mV s^{-1} and 25°C. Parameters for sputtering: dc mode, discharge of 330 V under 10^{-2} mbar argon pressure at room temperature for 20 sec., followed by calcination at 600°C in air for 1 h. Parameters for electrodeposition: potential step of 5 sec. from 1 to 0.02 V vs. SHE in 1 M HClO$_4$ + 2 mM H$_2$PtCl$_6$ solution.

From the above results it can be postulated that such heat treatment results in melting of gold nanoparticles that cover the Pt deposit leading to a core-shell

structure in which the core would be composed of Pt. Consequently the surface capable of alcohol dissociative adsorption decreases and the electrocatalytic activity is decreased concomitantly. Heat treatment using other conditions could be a solution to realize a more efficient Au/Pt bimetallic surface for electrocatalysis of methanol or ethanol electrooxidation. Requirements for such surface would be to preserve its adsorption properties and to allow fast and effective migration of adsorbed CO from Pt sites to Au sites where it can be easily oxidized. In particular the use of a temperature for which both the two metals melt (at least 900°C) should be tested in the next future. However the changes that the diamond substrate can undergo under such conditions (in particular surface oxide formation) must also be taken into account as they could greatly influence the behaviour of the supported particles (metal-support interactions).

4. CONCLUSIONS

During this Chapter of the thesis, Pt particles have been electrodeposited on the BDD electrode, both bare and pre-modified by thermally deposited Au nanoparticles. The mechanism of deposition and physical nature of the deposits on the two types of substrate have been investigated using electrochemical methods, electron microscopy (SEM) and XPS. Moreover the electrocatalytic activity of such BDD-Pt and BDD-Au/Pt composite electrodes have been evaluated toward both methanol and ethanol electrooxidation.

It has been shown that, whatever the substrate used was, Pt electronucleation occurred following a progressive mechanism during which new nuclei are continuously formed simultaneously than growth of primary nuclei. It can be supposed that pre-deposited Au nanoparticles on BDD act like non-diamond C sp^2 impurities present on diamond, *i.e.* as preferential nucleation sites. Electrodeposited Pt particles exhibited a very large size distribution (40-700 nm in diameter) that does not allow the use of the term "nanoparticles" and are mainly in the metallic state both on bare BDD and BDD-Au electrodes. Finally the electrocatalytic activity of Pt and Au-Pt deposits toward methanol and ethanol electrooxidation has been estimated by CV. The difference in activities toward the electrooxidation of these two alcohols was attributed to the inability of both Pt and Au/Pt to promote the scission of the C-C bond of ethanol. Moreover it has been observed that, if Au nanoparticles are neglected in specific molar currents calculations, the activities of the two kinds of composite electrodes were absolutely comparable. This is indicative that Au does not play any role on the electrocatalytic behaviour of Pt and that surface migration of adsorbed CO

(produced from methanol electrooxidation for instance) from Pt sites to Au sites does not occur efficiently when the two metals are just co-deposited.

As gold nanoparticles have exhibited extremely high catalytic activity toward CO oxidation even at low temperature, some attempts were done in order to realize a Au/Pt alloy, or at least a structure in which the two metals would be more closely related. For this purpose the BDD-Au/Pt has been calcinated at 400°C in air for 1 h as a preliminary test. It has been observed by CV that such a treatment exalted the Au character of the deposit detrimentally to the Pt character. As a consequence the electrocatalytic activity of the calcinated surface has also decreased. It is suspected that under the used conditions gold nanoparticles melt and cover the platinum deposit, leading to a core-shell structure and thus impeaching the dehydrogenation steps in alcohol electrooxidation. A solution should be to use a temperature for which both the two metals melt in order to realize a more homogeneous surface. Nevertheless other conditions such as the relative quantities of Pt and Au or the heating time have also to be optimized in order to realize a better Au/Pt alloy catalyst suitable for electrocatalysis of alcohol electrooxidation. Moreover the size of the obtained Pt nanoparticles was not sufficiently low and the size distribution was too large to really take advantage of any size effect. Therefore another synthesis technique of Pt nanoparticles that fulfil these requirements is needed and the next Chapter will deal with the synthesis and characterization of microemulsion-synthesized Pt nanoparticles deposited on BDD.

5. REFERENCES

[1]   G. Cao, *Nanostructures & Nanomaterials. Synthesis, Properties and Applications*, Imperial College Press, London (2004).

[2]   R. Parsons, T. VanderNoot, *J. Electroanal. Chem.* **257** (1988), 9.

[3]   S. Wasmus, A. Kuver, *J. Electroanal. Chem.* **461** (1999), 14.

[4]   A. S. Aricò, S. Srinivasan, V. Antonucci, *Fuel Cells* **1** (2001), 133.

[5]   C. Lamy, A. Lima, V. LeRhun, F. Delime, C. Coutanceau, J.-M. Léger, *J. Power Sources* **105** (2002), 283.

[6]   T. Kobayashi, M. Haruta, H. Sano, M. Nakane, *Sensors Actuators* **13** (1988), 339.

[7]   T. Kobayashi, M. Haruta, S. Tsubota, H. Sano, B. Delmon, *Sensors Actuators B* **1** (1990), 222.

[8]   M. S. El-Deab, T. Ohsaka, *Electrochem. Comm.* **4** (2002), 288.

[9]   M. S. El-Deab, T. Ohsaka, *Electrochim. Acta* **47** (2002), 4255.

[10] M. Paunovic, M. Schlesinger, *Fundamentals of Electrochemical Deposition*, John Wiley & Sons, Inc., New York (1998).

[11] S. Nageswar, *Electrodeposition Surf. Treat.* **3** (1975), 417.

[12] I. Markov, *Thin Solid Films* **35** (1976), 11.

[13] I. Markov, E. Stoycheva, *Thin Solid Films* **35** (1976), 21.

[14] P. Allongue, E. Souteyrand, *J. Electroanal. Chem.* **286** (1990), 217.

[15] A. Kelaidopoulou, G. Kokkinidis, A. Milchev, *J. Electroanal. Chem.* **444** (1998), 195.

[16] M. P. Zach, K. H. Ng, R. M. Penner, *Science* **290** (2000), 2120.

[17] D. R. Salinas, E. O. Cobo, S. G. Garcia, J. B. Bessone, *J. Electroanal. Chem.* **470** (1999), 120.

[18] M. Paunovic, M. Schlesinger, in: *Fundamentals of Electrochemical Deposition*, John Wiley & Sons, Inc., New York (1998), p. 187.

[19] R. T. Potzschke, C. A. Gervasi, S. Vinzelberg, G. Staikov, W. J. Lorenz, *Electrochim. Acta* **40** (1995), 1469.

[20] F. Gloaguen, J. M. Léger, C. Lamy, A. Marmann, U. Stimming, R. Vogel, *Electrochim. Acta* **44** (1999), 1805.

[21] H.-F. Waibel, M. Kleinert, L. A. Kibler, D. M. Kolb, *Electrochim. Acta* **47** (2002), 1461.

[22] Y. V. Pleskov, *Russ. Chem. Rev.* **68** (1999), 381.

[23] Y. V. Pleskov, in: R. C. Alkire, D. M. Kolb (Eds.), *Advances in Electrochemical Science and Engineering*, Wiley-VCH, Weinheim (2002), p. 209.

[24] M. E. Hyde, R. M. J. Jacobs, R. G. Compton, *J. Electroanal. Chem.* **562** (2004), 61.

[25] C. Terashima, T. N. Rao, B. V. Sarada, N. Spataru, A. Fujishima, *J. Electroanal. Chem.* **544** (2003), 65.

[26] M. E. Hyde, R. Jacobs, R. G. Compton, *J. Phys. Chem. B* **106** (2002), 11075.

[27] O. Enea, B. Riedo, G. Dietler, *Nano Lett.* **2** (2002), 241.

[28] F. Montilla, E. Morallon, I. Duo, Ch. Comninellis, J. L. Vazquez, *Electrochim. Acta* **48** (2003), 3891.

[29] A. Hamnett, in: A. Wieckowski (Ed.) *Interfacial Electrochemistry - Theory, Experiments, and Applications*, Marcel Dekker, Inc., New York (1999), p. 843.

[30] M. Watanabe, S. Motoo, *J. Electroanal. Chem.* **60** (1975), 259.

[31] P. I. Iotov, S. V. Kalcheva, *J. Electroanal. Chem.* **442** (1998), 19.

[32] P. C. Biswas, Y. Nodasaka, M. Enyo, M. Haruta, *J. Electroanal. Chem.* **381** (1995), 167.

[33] B. El Roustom, G. Fóti, Ch. Comninellis, *Electrochem. Comm.* **7** (2005), 398.

[34]   D. Gandini, E. Mahé, P.-A. Michaud, W. Haenni, A. Perret, Ch. Comninellis, *J. Appl. Electrochem.* **30** (2000), 1345.

[35]   B. Scharifker, G. Hills, *Electrochim. Acta* **28** (1983), 879.

[36]   J. S. Hammond, N. Winograd, *J. Electroanal. Chem.* **78** (1977), 55.

[37]   J. Clavilier, D. Armand, *J. Electroanal. Chem.* **199** (1986), 187.

[38]   Y. Takasu, Y. Fujii, K. Yasuda, Y. Iwanaga, Y. Matsuda, *Electrochim. Acta* **34** (1989), 453.

[39]   J. M. Perez, B. Beden, F. Hahn, A. Aldaz, C. Lamy, *J. Electroanal. Chem.* **262** (1989), 251.

[40]   K. Juodkazis, J. Juodkazyte, V. Jasulaitiene, A. Lukinskas, B. Sebeka, *Electrochem. Comm.* **2** (2000), 503.

[41]   D. M. Cox, B. Kessler, P. Fayet, W. Eberhardt, Z. Fu, D. Sondericher, R. Sherwood, A. Kaldor, *Nanostructured Mater.* **1** (1992), 161.

[42]   H. Moller, P. C. Pistorius, *J. Electroanal. Chem.* **570** (2004), 243.

[43]   P. Buffat, J.-P. Borel, *Phys. Rev. A* **13** (1976), 2287.

Chapter 5   RESULTS: Deposition of Microemulsion-Synthesized Pt Nanoparticles on BDD Electrodes for Alcohols Electrooxidation.   Activation   by   Electrogenerated Hydroxyl Radicals

1. INTRODUCTION

Since a few decades there is a growing interest in the study of supported catalyst nanoparticles (Pt, Ru, IrO_2, RuO_2) due to the different and sometimes novel properties of the later compared to those of bulk materials. Special attention was focused on Pt nanoparticles due to their applicability for the Direct Alcohol Fuel Cell (DAFC) technology [1, 2]. However, the complete oxidation of methanol to carbon dioxide passes through several adsorbed intermediates [3] and CO poisoning that blocks methanol adsorption onto reactive sites dramatically decreases the catalyst activity [4]. Alloying Pt with other transition metals (Ru, Sn, Mo, W or Ni) enhances CO tolerance of pure Pt, but the reasons are still under debate. Two approaches are currently privileged: the so-called bifunctional mechanism [5], during which Pt adsorbs methanol and the other metal dissociates water molecules at lower overpotentials than Pt, and the electronic effect, in which the Pt-CO bond is weakened by the modification of Pt electronic properties induced by the presence of the alloying metal [6]. On the other hand, the necessity of alloying metals instead of just mixing them is now an open question [7].

Special requirements in electrocatalysis consist in obtaining monodispersed nanoparticles, ideally in the 1-5 nm range, with well-defined compositions. These requirements are not simple to satisfy with electrodeposition, especially on an inhomogeneous electrode surface such as BDD [8, 9] (see Chapter 4 of this manuscript). The microemulsion method is well-known, since the first work of Boutonnet *et al.* [10], to be an efficient and simple way to prepare metallic particles in the nanometer scale with narrow size distribution. A water-in-oil (w/o) microemulsion is a thermodynamically stable, optically transparent and isotropic dispersion of aqueous nanodroplets coated by a layer of surfactant in a continuous oily phase [11]. This method has been successfully used for the synthesis of nanomaterials like pure metals [10, 12], alloys [13-15] or metal oxides [16]. However, the surfactant layer that limits the particles growth to the droplet dimensions becomes a problem for their electrochemical and electrocatalytic characterization. Cleaning of such particles thus appears as a major challenge in order to allow their electrochemical study. Electrochemical aging or activation (*i.e.* potential sweep between typically 0 and 1.3-1.5 V vs. SHE) has been used to clean Pt surfaces but it implies surface

rearrangements or recombination [17], and aggregation in the case of particles [18]. Recently, a cleaning procedure that includes CO adsorption and stripping has been successfully used for the decontamination of Pt-based nanoparticles prepared in microemulsion systems [19, 20].

In this Chapter, results about the deposition and activation of microemulsion-synthesized Pt nanoparticles on BDD are presented. The choice of the BDD electrode as substrate for Pt nanoparticles can be justified by the inert character of its surface, its very low background current and its large electrochemical window available [21]. Moreover, the use of BDD as substrate can be a good approach to solve the problems of corrosion (Glassy Carbon) or oxide formation (Au and Ti substrates) encountered with usual substrates, problems that can result in the modification of the catalytic activity of the deposited particles (metal-support interactions). Diamond electrodes have thus been used as substrate for the deposition of particles as different as mercury and silver [22], lead dioxide [23], ruthenium oxides [24, 25], gold [26, 27], and Pt [8, 9, 28]. A new synthesis method of Pt particles was used during this Chapter because electrodeposition only led to large Pt particles with broad size distribution that cannot be considered strictly as nano-objects (see Chapter 4). As already stated, this Chapter is centred on the deposition on BDD and activation of pure Pt nanoparticles by electrogenerated hydroxyl radicals. It was indeed shown in a recent paper from our laboratory [29] that free and highly reactive hydroxyl radicals are produced on BDD electrodes by water discharge at high overpotentials (> 2.3 V vs. SHE). These electrogenerated hydroxyl radicals at the BDD surface participate in the oxidation of the residual surfactant layer present on the Pt nanoparticles, resulting in a clean surface. Furthermore in order to avoid detachment of Pt nanoparticles during this treatment, we have also considered the use of a Nafion® film to mechanically stabilize these ones, following a similar way than Swain *et al.* who entrapped their particles in an additional diamond layer [30-32].

2. EXPERIMENTAL

2.1. Nanoparticles synthesis

Platinum nanoparticles were obtained by reduction of H_2PtCl_6 with hydrazine in a w/o microemulsion of water / tetraethyleneglycol-monododecylether (BRIJ® 30) / n-heptane, following Equation 5.1:

$$H_2PtCl_6 + NH_2NH_2 \rightarrow Pt + 6HCl + N_2 \quad\quad\quad\quad (5.1)$$

BRIJ® 30 has been chosen as surfactant because this non-ionic tensioactive will not interact as strongly as other ones, such as SDS (sodiumdodecylsulfate) for instance, with the Pt surface. Therefore BRIJ® 30 would be more easily eliminated

than other surfactants. The microemulsions were prepared using ultra-pure water (Millipore® system). BRIJ® 30 and n-heptane were purchased from Fluka and Riedel-de-Haën, respectively, and were used as received. The reactants (Fluka, analytical grade) were dissolved into the aqueous phases of two different microemulsions that had the same composition and water-to-surfactant molar ratio ($\omega_0 = 3.8$). The quantity of surfactant represented 16.54 % of the volume of the microemulsion, and the concentrations of H_2PtCl_6 and hydrazine in the aqueous phases were 0.1 and 2.5 M, respectively. From a practical point of view, n-heptane and BRIJ® 30 were first mixed. Then the aqueous phase was slowly added and the solution was vigorously stirred. This results in a transparent, homogeneous and pale yellow (Pt microemulsion) solution. The parameters used for the synthesis of Pt nanoparticles are summarized in Table 5.1.

	Pt nanoparticles
Vol. % surfactant	16.54
Vol. % n-heptane	80.46
Vol. % H_2O	3
$[PtCl_6^{2-}]_{aq}$ / M	0.1
$[N_2H_4]_{aq}$ / M	2.5
$[N_2H_4]_{aq}/[PtCl_6^{2-}]_{aq}$	25

Table 5.1: Experimental parameters for the synthesis of Pt nanoparticles using the microemulsion method.

The synthesis of particles was realized mixing equal volumes of the two microemulsions. The general scheme of Pt nanoparticles synthesis mixing two microemulsions is presented in Figure 5.1. It involves the following steps: (**1**) mixing of the two microemulsions, (**2**) formation of metastable dimers due to Brownian motion and exchange of reactants, (**3**) nucleation and (**4**) growth of the particles into the interior of the inverse micelles. Growth of the particles was finally stopped by the surfactant layer that stabilises the aqueous dispersion, and hence is limited to the inverse micelles dimensions.
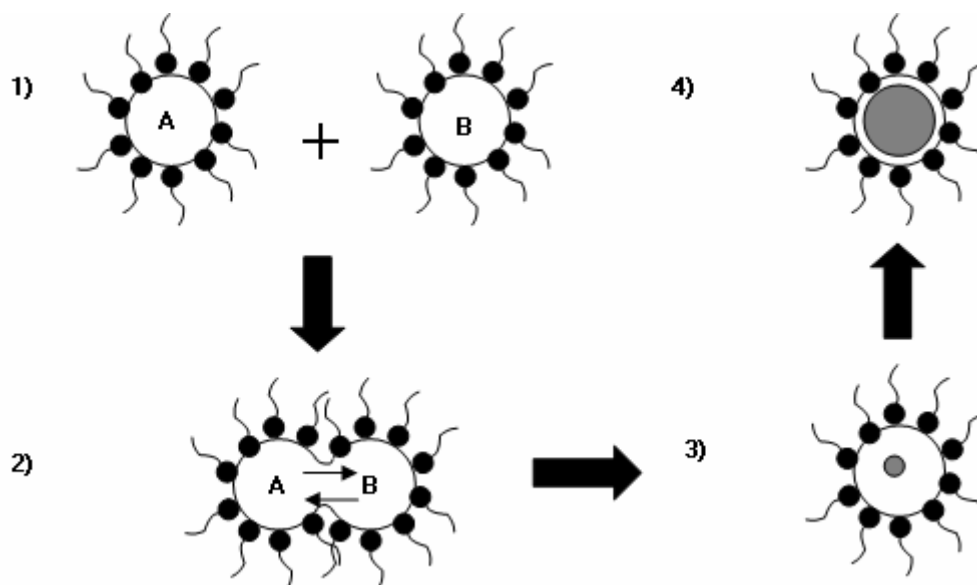
Figure 5.1: General scheme of synthesis of Pt nanoparticles mixing two microemulsions. Steps of the process: **1)** mixing of the microemulsions, **2)** collision between aqueous nanodroplets, exchange of reactants and reaction, **3)** nucleation and **4)** growth of the particles in the inverse micelles. A = H_2PtCl_6(aq.), B =N_2H_4(aq.), aqueous nanodroplets dispersed in n-heptane and stabilized by a BRIJ®-30 layer.

After complete reduction, that needs only a few minutes to take place and is evidenced by colour change to dark black (typical colour of metallic particles), acetone was added to the solution to cause phase separation and precipitation of the particles. This precipitate was rinsed several times with acetone and ultra-pure water, and then centrifuged for a few minutes to eliminate most of the surfactant. Finally particles were put in a small volume of ultra-pure water as a suspension, and the Pt content in this suspension was determined by Atomic Absorption Spectrometry (AAS).

2.2.   BDD-Pt electrode preparation

Boron-doped diamond electrodes were purchased by CSEM (Centre Suisse d'Electronique et Microtechnique, Neuchâtel). BDD films were synthesised by the hot filament chemical vapour deposition technique (HF-CVD) on single crystal p-type Si <100> wafers (1-3 mΩcm, Siltronix). The doping level of boron expressed as B/C ratio was about 3500 ppm. The obtained diamond film thickness was about 1 μm with a resistivity in the range 10-30 mΩcm. This as-grown BDD contains some graphitic (sp^2) phase and is hydrogen terminated. Activation of BDD by anodic polarization (10 mA cm^{-2} in 1 M H_2SO_4 at 25 °C during 30 min) eliminates most of the sp^2 and adsorbed hydrogen from the surface, and is necessary to obtain reproducible electrochemical measurements [33].

Platinum nanoparticles were deposited onto the BDD substrate putting a droplet (5 µl) of the suspension onto diamond. The excess water was dried under nitrogen atmosphere. The BDD-Pt-Nafion® electrode was realized adding 5 µl of a commercial solution of Nafion® (5 wt % in aliphatic alcohols, Aldrich), diluted ten more times in pure ethanol, to the BDD-Pt electrode. The excess alcohol was also removed under nitrogen atmosphere. The BDD-Pt or BDD-Pt-Nafion® electrode was then transferred to the electrochemical cell.

2.3. Measurements

Electrochemical measurements were conducted using the conventional three-electrode cell described in Chapter 3, with BDD-supported Pt nanoparticles as working electrode (exposed area of diamond: 0.4 cm^2), Hg/Hg$_2$SO$_4$.K$_2$SO$_4$(sat.) as reference and a platinum wire as counter electrode. All potentials reported here are plotted with respect to the Standard Hydrogen Electrode (SHE). All solutions were made in ultra-pure (Millipore® system) water using analytical grade reactants without further purification. Before any experiment the solution was saturated with nitrogen gas and measurements were conducted under a nitrogen atmosphere.

Physical characterization of particles was conducted by means of TEM, XPS and XRD, using the methods and apparatus described in Chapter 3. For TEM analysis, a small droplet of the particles suspension was put on an amorphous carbon-coated copper grid; the excess water was then removed and the grid placed in the vacuum chamber of the microscope in order to be analyzed. Both XRD and XPS measurements of particles were carried out with particles deposited on a BDD substrate. Deconvolution of the Pt*4f* XPS peak of particles was performed using the CasaXPS® computer program.

3. RESULTS AND DISCUSSION

3.1. Pt nanoparticles characterization

3.1.1. Physical characterization

Pt particles size has been investigated by Transmission Electronic Microscopy (TEM). A TEM micrograph of microemulsion-synthesized Pt nanoparticles, as well as the size distribution established according to such measurements on more than 100 single particles, is presented in Figure 5.2. It can be seen on this picture that Pt particles are present on the grid as isolated spherical units of diameter include in the 2-5 nm range with narrow distribution. This domain corresponds well with the commonly accepted definition of a nano-object in catalysis. Moreover a mean

diameter of 2.43 nm has been determined for pure Pt microemulsion-synthesized nanoparticles on the basis of TEM measurements.
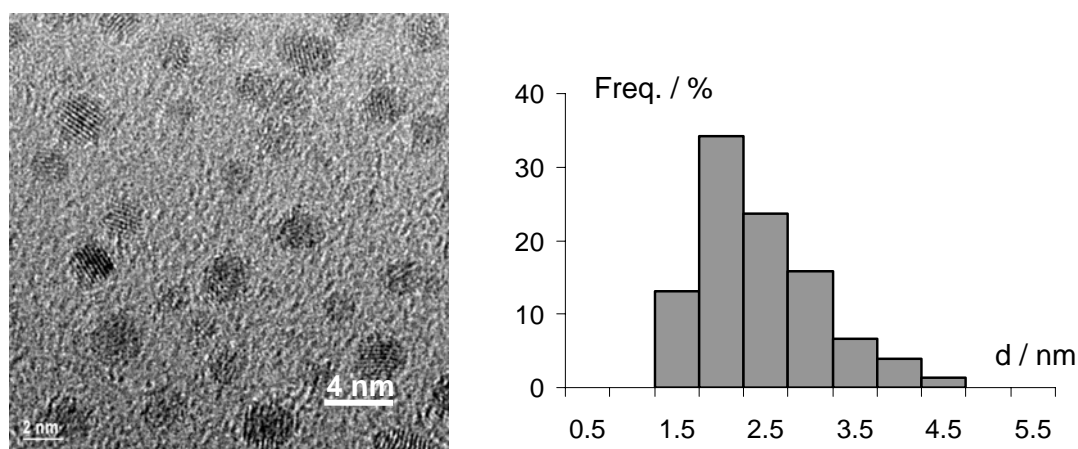

Figure 5.2: TEM micrograph and size distribution of microemulsion-synthesized Pt nanoparticles.

The XRD spectrum of BDD-supported Pt nanoparticles is shown in Figure 5.3. It exhibits the typical bands associated with the face-centred cubic (fcc) structure of Pt and others that can be attributed to the diamond substrate. Peaks associated with Pt structure are listed on Fig. 5.3. Other peaks can be attributed to the (111) and (220) planes of diamond (44° and 75.3°), and to the (400) plane of silicium (70°) [34].
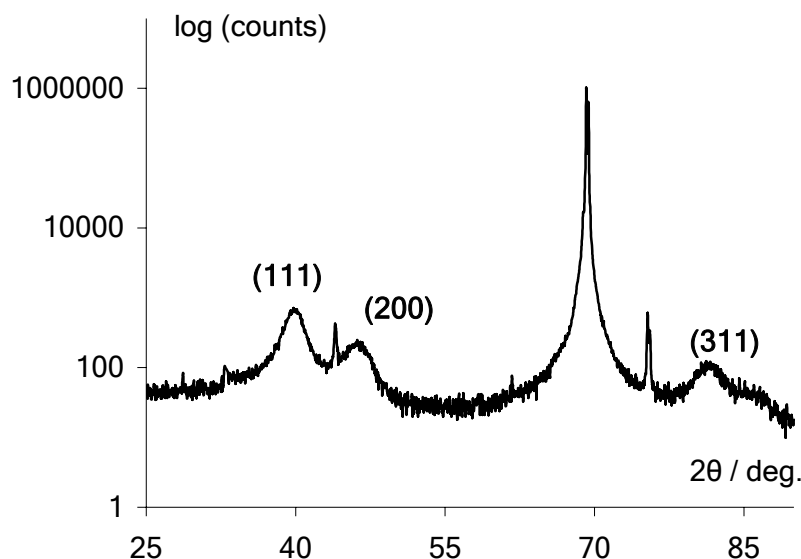
Figure 5.3: XRD pattern of BDD-supported Pt nanoparticles.

As the (220) peak of Pt (located at 67.3°) is here completely hidden by the (400) Si peak, the (111) reflection of metallic Pt (located near 40°) was taken into account to estimate the crystallite size using the Debye-Scherrer formula [35]:

$$d = \frac{0.91\lambda_{CuK\alpha}}{Bcos\theta} \qquad\qquad (5.2)$$

where d is the average diameter of the crystallites, λ the CuKα X-radiation wavelength, B the excess line width (in radians) and θ the Bragg angle. Based on this analysis the average diameter of particles has been found to be closed to 2.3 nm. This value is quite closed to that obtained by TEM; however it is difficult to affirm that XRD is more precise than TEM in this case because of the peaks broadening that is often encountered in XRD of nanoparticles [36].

XPS analyses have also been conducted on BDD-supported Pt nanoparticles in order to determine the contribution of the different oxidation states of the metal. The complete survey and the deconvoluted Pt*4f* doublet of the BDD-Pt XPS spectrum are shown in Figures 5.4 and 5.5, respectively. The predominant C *1s* peak, located at approximately 284 eV is due to the BDD substrate and the O *1s* peak at 532 eV mainly comes from interactions with atmospheric oxygen. Platinum is only present at the diamond surface as traces (less than 1 atomic percent) because only a few µl of Pt suspension was added to the BDD substrate in a similar way than it was done for electrochemical studies.
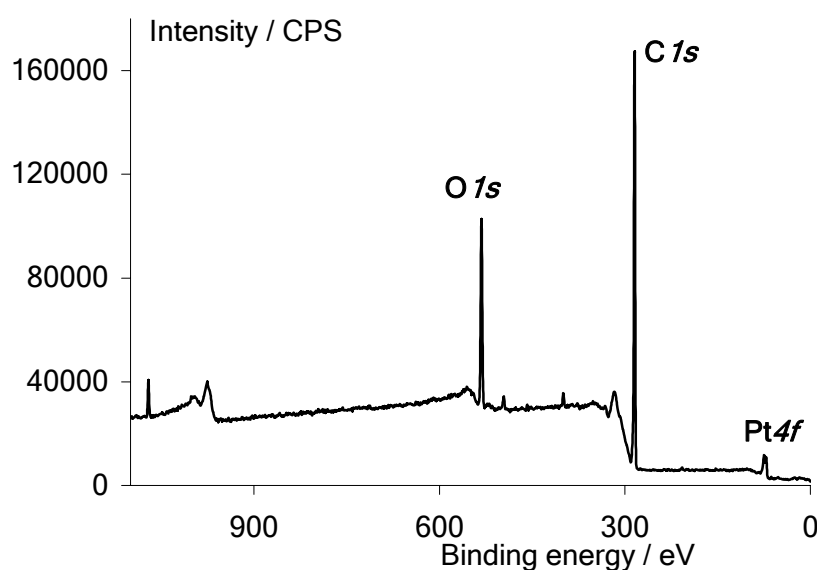

Figure 5.4: XPS spectrum of BDD-supported Pt nanoparticles.

The Pt*4f* doublet, located at 70-78 eV, has been deconvolved using the CasaXPS® software in order to discriminate the different contributions of this signal. The result of this deconvolution is shown in Figure 5.5. Four different peaks contribute to the observed signal; peaks (1) and (2) can be attributed to Pt*4f*$_{7/2}$ and Pt*4f*$_{5/2}$ lines of metallic Pt (Pt^0), respectively, whereas peaks (3) and (4) can be attributed to Pt*4f*$_{7/2}$ and Pt*4f*$_{5/2}$ lines of Pt^{II} present for instance in PtO or Pt(OH)$_2$ [37].

The ratio between metallic and oxidized (+II) forms of Pt was about 3:1. This important proportion in Pt^{II} species can be explained by the fact that samples were stocked in air sometimes during several days before the measurement was done. It must be noticed that particles used for electrochemical tests should have higher Pt^0 contents as they were freshly taken from the aqueous suspension before their use, and immediately putted under nitrogen atmosphere.
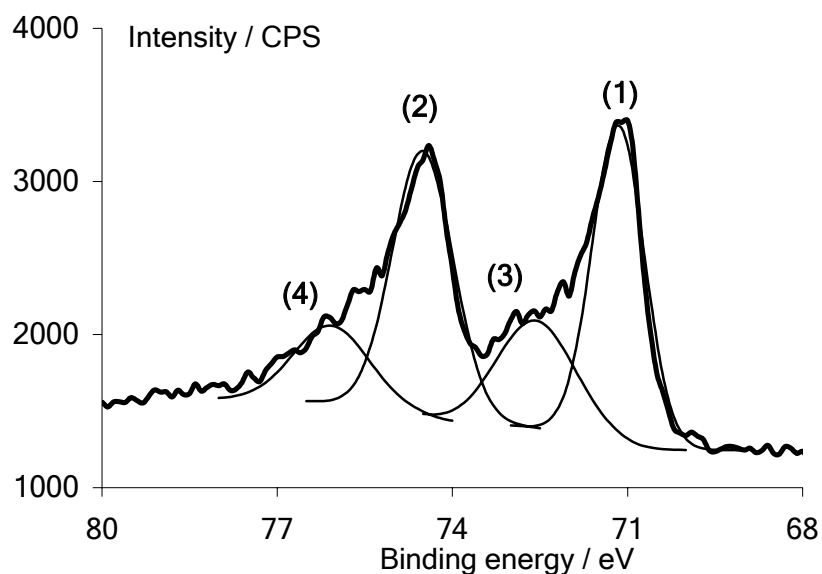

Figure 5.5: Deconvolved XPS Pt*4f* doublet of BDD-supported Pt nanoparticles.

3.1.2. Electrochemical characterization

Microemulsion-synthesized Pt nanoparticles were electrochemically characterized when deposited on a BDD electrode that was used as substrate. For this purpose, a known volume of the Pt nanoparticles aqueous suspension was deposited onto the diamond plate and the excess water was then remove under nitrogen atmosphere. This composite BDD-Pt electrode was then used in electrochemical experiments. Figure 5.6 shows the influence of successive additions of Pt suspension on the CV response of the BDD-Pt electrode, recorded in 1 M $HClO4$ solution at a scan rate of 50 mV s^{-1}. It can be seen on the voltammograms presented in Fig. 5.6 that the increase in deposited amount of Pt does not modify the shape of the obtained voltammograms. Moreover, there is a linear relationship between the volume of Pt suspension added to the diamond substrate and the charge associated with the H adsorption-desorption processes on Pt, as shown in Figure 5.7. This indicates that the electrochemical response is directly proportional to the deposited amount of particles. This linear relationship between the charge and the volume of suspension is also the sign that, from a practical point of view, the way in

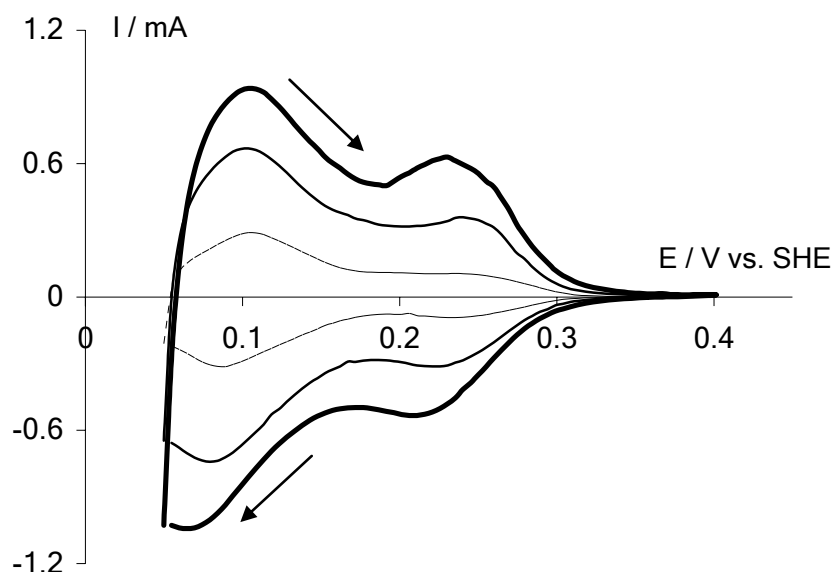which particles are taken from the suspension and deposited on the substrate is suitable and reproducible.

Figure 5.6: CV of a BDD-Pt electrode, recorded in 1 M $HClO_4$ at 50 mV s^{-1} and 25°C, with increasing amounts of deposited Pt particles. Volumes of Pt suspension added to the substrate: 5 (thin dashed line), 10 (thin solid line) and 15 µl (thick solid line).
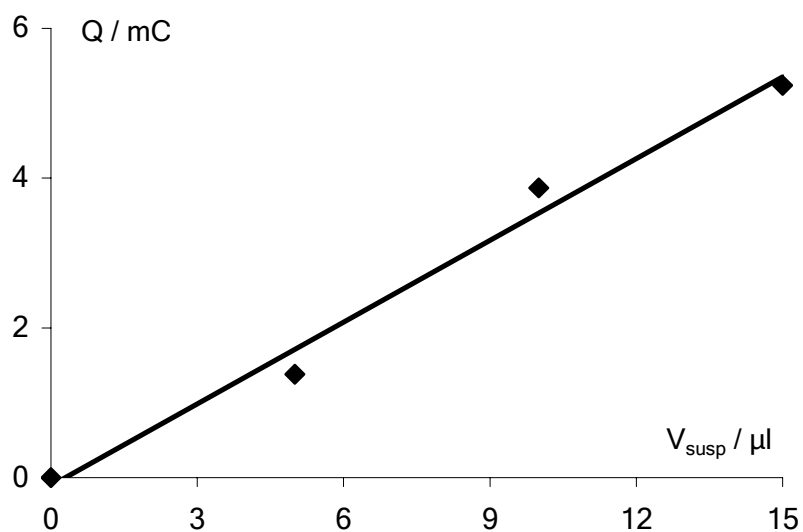

Figure 5.7: Linear relationship between the volume of Pt nanoparticles suspension added to the diamond substrate and the measured charge in the H adsorption-desorption region on Pt. Measurements done in 1 M $HClO_4$ at v = 50 mV s^{-1}.

The behaviour of this BDD-Pt composite electrode has also been tested toward methanol and ethanol electrooxidation processes, that are reactions, as already stated in the Introduction, of crucial interest for the development of the Direct Alcohol Fuel Cell (DAFC) technology. Typical CV of both methanol and ethanol electrooxidation on a BDD-Pt electrode are shown together in Figure 5.8.
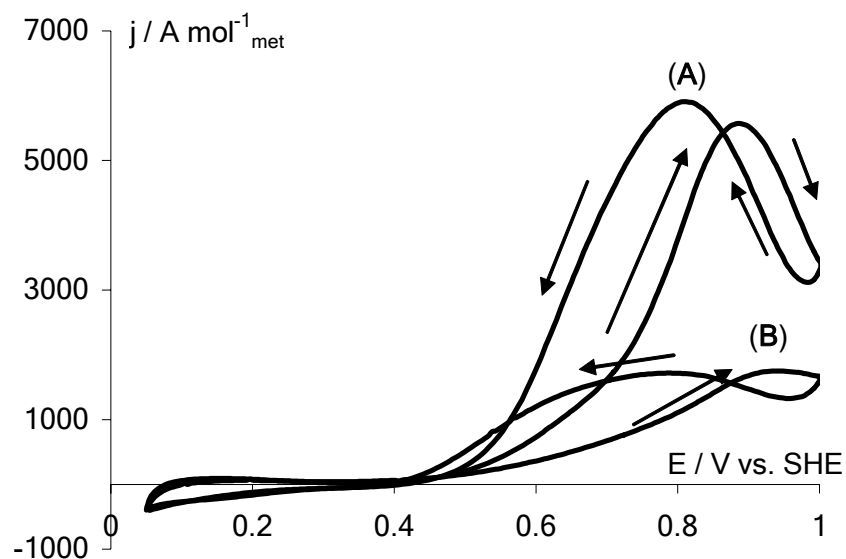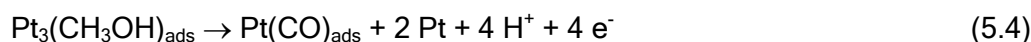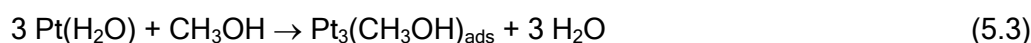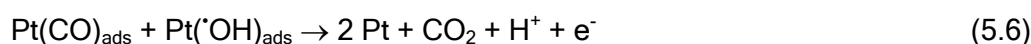
Figure 5.8: CV for the electrooxidation of MeOH (**A**) and EtOH (**B**) on Pt nanoparticles deposited on a BDD electrode. $HClO_4$ 1 M + Alcohol 0.1 M, v = 20 mV s^{-1} at T = 25°C:

The specific molar currents displayed in Fig 5.8 have been plotted with respect to the total molar amount of metal deposited on BDD, on the basis of Pt contents in the aqueous suspension determined by AAS (data not shown) and with the knowledge of the deposited volume of this Pt suspension on the diamond substrate. These voltammograms exhibit the characteristic features of methanol and ethanol electrooxidation on Pt, *i.e.* two well-defined oxidation peaks that occur during the forward (first peak) and the reverse scans (second peak). The CV of methanol electrooxidation can for instance be described as a sequence of multiple and complex physicochemical phenomena [38]. At very low overpotentials (0.05 V vs. SHE), methanol easily adsorbs on Pt, adsorption that is followed by alcohol dehydrogenation (during a fast process) as described in Equations 5.3 and 5.4:

$$3\ Pt(H_2O) + CH_3OH \rightarrow Pt_3(CH_3OH)_{ads} + 3\ H_2O \tag{5.3}$$

$$Pt_3(CH_3OH)_{ads} \rightarrow Pt(CO)_{ads} + 2\ Pt + 4\ H^+ + 4\ e^- \tag{5.4}$$

As a consequence, carbon monoxide (CO) blocks the Pt active sites, explaining the flat feature of CV of Fig. 5.8 between 0.05 and 0.45 V approximately. CO removal needs oxidation by hydroxyl radicals generated from water discharge on Pt. However, water dissociation does not occur on Pt at potentials below 0.4 V. When this potential is attained, the following sequence can take place (reactions 5.5 and 5.6):

$$Pt + H_2O \rightarrow Pt(^\bullet OH)_{ads} + H^+ + e^- \tag{5.5}$$

$$Pt(CO)_{ads} + Pt(^\bullet OH)_{ads} \rightarrow 2\ Pt + CO_2 + H^+ + e^- \tag{5.6}$$

This explains the current increase after 0.45 V: Pt can readsorb and reoxidize methanol. The current decrease after 0.9 V vs. SHE can be related to the Pt surface

transitions: cycling the potential in acidic media up to 1 V and higher values leads to the formation of Pt oxides. Consequently there is no Pt free for water discharge and the current decreases. During the reverse scan of potential, Pt oxides are reduced, so water discharge and methanol complete oxidation can take place again. Finally the current decreases again due to CO poisoning of the surface when the potential is not sufficiently high to allow water dissociation. The reverse scan oxidation peak is of higher intensity than the forward scan one and located at less positive potential, indicating that the CO removal process are not exactly the same in the forward and reverse potential scans.

A similar mechanism should be theoretically expected in the case of ethanol electrooxidation; however ethanol complete electrooxidation is a much more complicated case as it needs the breaking of the C-C bond. On platinum this reaction first yields to several adsorbed intermediates, namely acetaldehyde and acetic acid that have been identified by means of Fourier Transform Infra-Red Spectroscopy (FTIR) [39, 40]. The breaking of the C-C bond of these adsorbates is one of the key problems in ethanol-feed DAFC. A good electrocatalyst for the complete oxidation of ethanol is indeed defined as an activator of the C-C bond breaking [41]. Thus it can reasonably be postulated that the observed difference in activity of Pt particles towards the oxidation of methanol and ethanol is due to the inability of pure Pt to promote the breaking of the ethanol C-C bond. This incomplete oxidation would lead to acetaldehyde and/or acetic acid that only need 2 electrons per molecule of adsorbate formed. This explains the fact that on Fig. 5.8, activity of Pt is three times more important towards methanol electrooxidation, and that the oxidation current peaks are located at approximately 0.9 (forward scan) and 0.75 V vs. SHE (reverse scan) for methanol oxidation, and at 0.95 (forward) and 0.8 V (reverse) for ethanol oxidation.

3.2.   Nafion®-assisted activation by electrogenerated ˙OH radicals

At this point it was desired to introduce some novelty in this work. Consequently it was decided to use one of the well-known properties of the diamond electrode, *i.e.* the ability to produce from water discharge at high potentials (> 2.5 V vs. SHE) free and highly reactive hydroxyl radicals [29]. This process can be described according to reaction 5.7:

$$H_2O \rightarrow {}^{\bullet}OH + H^+ + e^- \hspace{4cm} (5.7)$$

The aim was to use these hydroxyl radicals in order to clean the nanoparticles from the residual surfactant that can coat the catalytic surface. Although the microemulsion method permits the synthesis of nanoparticles with narrow size

distribution, the surfactant used in the formulation of the microemulsion can indeed still coat the particles surface and thus remains a problem for their electrochemical and electrocatalytic characterization. Some procedures, that include adsorption and stripping of CO, have recently been proposed to clean Pt and Pt-based alloys nanoparticles synthesized via the microemulsion route [15, 19, 20].

Electrogenerated hydroxyl radicals on BDD are not of same nature than those produced on Pt (see reaction 5.5); $^{\bullet}$OH produced on BDD are free and highly reactive radicals. It has also been showed that they are involved in oxidation of organics on BDD. It was expected that these radicals could be used to activate the Pt deposits. Considering also the high potentials needed in order to produce these radicals, it was imagined to mechanically stabilize the Pt nanoparticles by an additional Nafion$^{®}$ layer. Swain and coworkers have followed a similar way, performing an additional CVD procedure after their Pt particles being deposited on diamond [30-32]. Here, 5 µl of a commercial solution of Nafion$^{®}$ (5 wt % in aliphatic alcohols, Aldrich), diluted ten more times in pure ethanol, have just been deposited onto the BDD-Pt electrode. It was also expected that coverage by this proton-exchange membrane will induce lower loss of nanoparticles activity than that can be suspected from coverage with diamond. The excess alcohol was then removed by drying under nitrogen atmosphere and by CV in the supporting electrolyte. A schematic view of the BDD-Pt-Nafion$^{®}$ composite electrode is given in Figure 5.9.
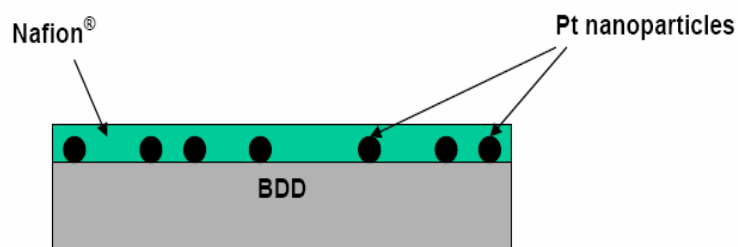

Figure 5.9: Schematic representation of the BDD-Pt-Nafion$^{®}$ electrode.

This composite electrode has been tested electrochemically, first in pure supporting electrolyte. CV of the BDD-Pt-Nafion$^{®}$ electrode, recorded in 1 M HClO$_4$ at 20 mV s^{-1} are shown in Figure 5.10 and compared to those obtained for a non-coated BDD-Pt electrode. It can be seen on CV of Fig 5.10 that the signal of the coated electrode represents approximately 70 % of that of the non-coated one, due to some surface blocking of active sites by the polymer film. However the profile of CV is similar for the two electrode types, indicating that the surface state of particles is not altered by the Nafion$^{®}$ layer. The large ethanol stripping peak, only observed during the first cycle of potential around 0.65 V vs. SHE, also indicates elimination of the

114

solvent from the initial Nafion® solution. Similar observations were made in the case of alcohols electrooxidation (Figure 5.11): the presence of the coating polymer layer does not influence the oxidation peaks shapes and positions but only their intensities.
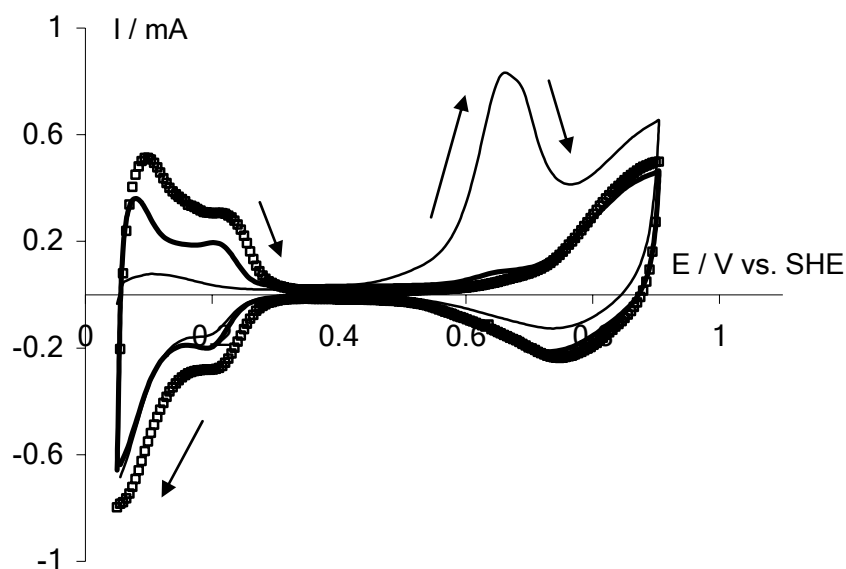

Figure 5.10: CV of microemulsion-synthesized Pt nanoparticles deposited on BDD before (open squares) and after the addition of the Nafion® solution (thin line: 1st scan; thick line: 5th scan).HClO$_4$ 1 M, v = 20 mV s^{-1} at T = 25°C.
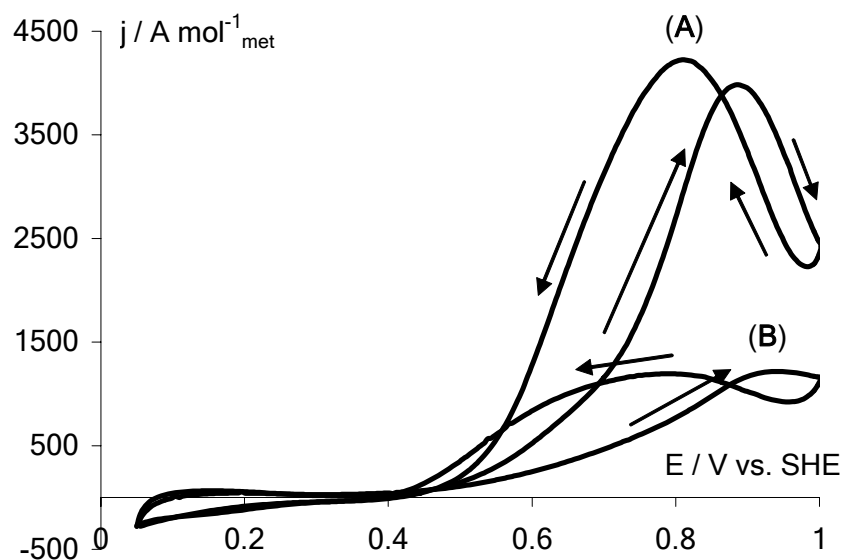

Figure 5.11: Typical CV for the electrooxidation of MeOH (**A**) and EtOH (**B**) on Pt nanoparticles coated by a Nafion® layer deposited on a BDD electrode. HClO$_4$ 1 M + Alcohol 0.1 M, v = 20 mV s^{-1} at T = 25°C:

In spite of this lack of activity caused by the polymer overlayer, it has been considered to test the behaviour of both the coated and the non-coated electrodes under potential conditions for which free, highly reactive hydroxyl radicals are

produced on BDD. For this purpose, a potentiostatic pre-treatment (2.5 V vs. SHE) was applied to the electrode for a given time in a 1 M HClO$_4$ solution; then the potential was cycled and the charge associated with the H adsorption-desorption processes on Pt determined. Figure 5.12 and 5.13 show the evolution of this normalized charge as a function of activation time.
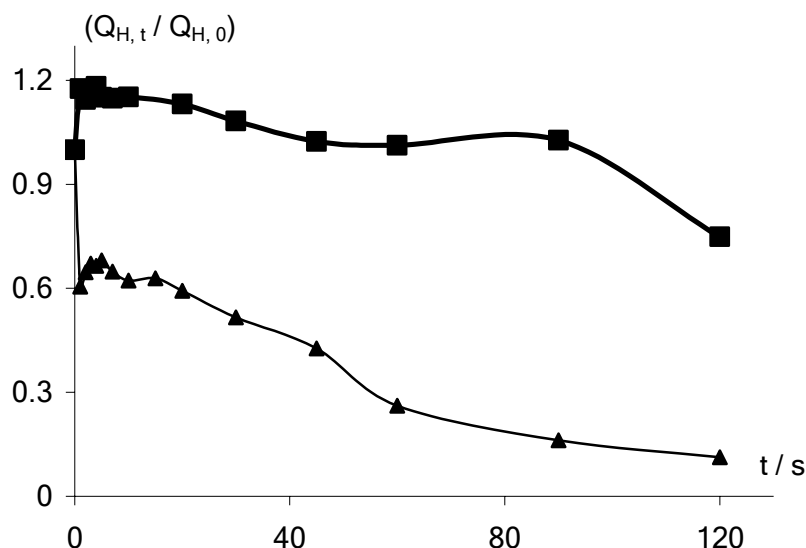

Figure 5.12: Evolution of the normalized charge in the H adsorption-desorption region of Pt on a BDD-Pt (thin line with triangle markers) and a BDD-Pt-Nafion$^{®}$ (thick line with square markers) electrode as a function of activation time at 2.5 V vs. SHE. Scan rate of 50 mV s^{-1} in 1 M HClO$_4$ at 25°C.
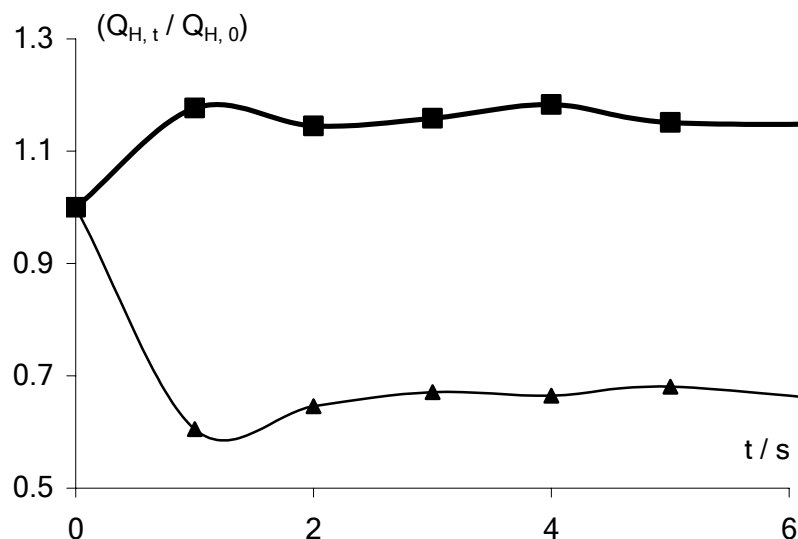

Figure 5.13: Zoom on the 0-5 seconds domain of Figure 5.12.

It can be seen on Fig. 5.12 that the charge diminishes for the two electrodes at long activation times. However this decrease is less pronounced in the case of the coated electrode, indicating that the Nafion$^{®}$ overlayer effectively stabilizes the

deposited nanoparticles. Moreover, a zoom on the 0-5 s interval activation time is given in Figure 5.13. It can be clearly seen that the two electrodes do not behave similarly within this domain. Whereas the charge of the non-coated electrode decreases as soon as the activation treatment is applied, it can be observed for the coated electrode the charge increases during the first seconds of treatment. This indicates that activation by electrogenerated hydroxyl radicals leads to additional cleaning of the particles surface from the residual surfactant. Moreover an optimum activation time, for which the charge reaches a maximum, of approximately 3 seconds can be defined. The CV of Figure 5.14, in which are shown CV of a BDD-Pt-Nafion® electrode before and after application of the activation procedure, give rise to the hypothesis that activation by electrogenerated hydroxyl radicals effectively cleans the particles. Indeed the CV of the activated electrode exhibit better-defined peaks of higher intensities than the non-activated one, indicating a cleaner surface.
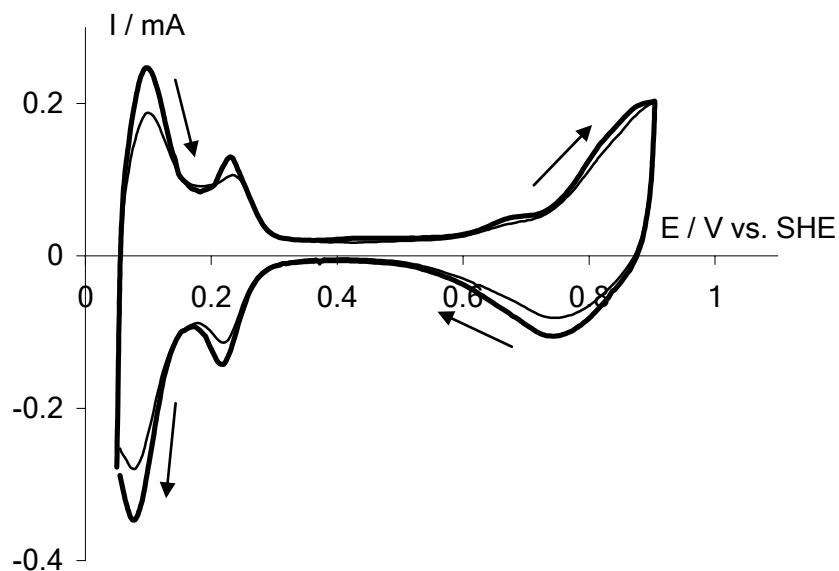

Figure 5.14: CV of a BDD-Pt-Nafion® electrode before activation (thin line) and after 3 sec. (thick line) of activation at 2.5 V vs. SHE. Scan rate of 50 mV s^{-1} in 1 M HClO$_4$ at 25°C.

Similar activation procedures have also been conducted in the presence of alcohols (methanol and ethanol). In this case after the activation treatment (2.5 V vs. SHE) was applied, a CV experiment was ran in the presence of the alcohol to be oxidized and the specific molar oxidation currents were measured. The evolution of the normalized specific molar current of the forward scan methanol oxidation peak with the activation time is shown in Figure 5.15 for a BDD-Pt and a BDD-Pt-Nafion® electrode. For clarity the evolution of the reverse scan oxidation peak is omitted here but the same evolution tendency, with lower levels of increase, was also observed.
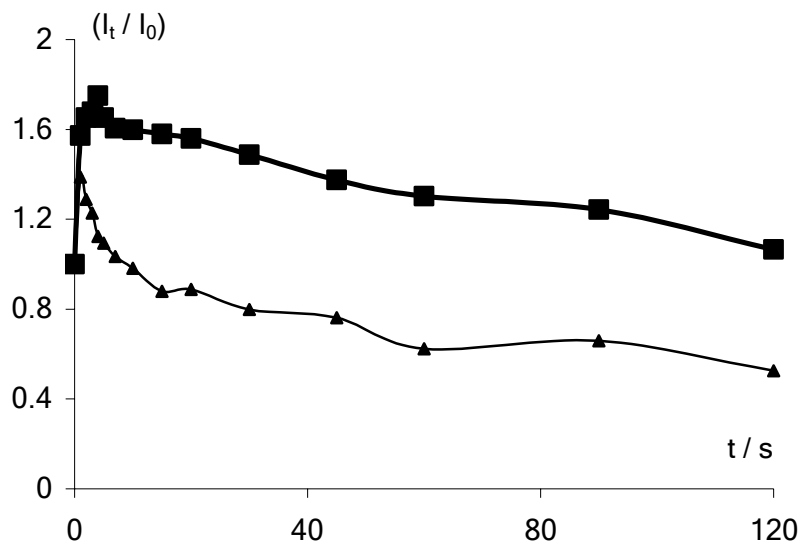
Figure 5.15: Evolution of the normalized oxidation current (1st oxidation peak) charge in the H adsorption-desorption region of Pt on a BDD-Pt (thin line with triangle markers) and a BDD-Pt-Nafion® (thick line with square markers) electrode as a function of activation time at 2.5 V vs. SHE. Scan rate of 20 mV s^{-1} in 1 M HClO$_4$ + 0.1 M MeOH at 25°C.
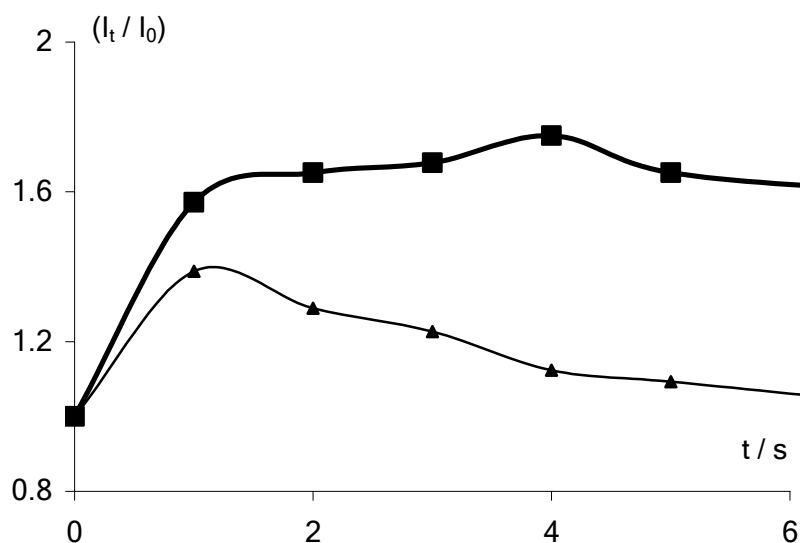

Figure 5.16: Zoom on the 0-5 seconds domain of Figure 5.15.

Without Nafion®, the curve of methanol oxidation (thin line with triangle markers in Fig. 5.15) begins with a strong increase followed by a continuous decrease. As soon as the polymer is added to the Pt deposit (thick line with square markers in Fig. 5.15), the initial increase of activity is of higher importance and the subsequent decrease at more long time is limited. Initial enhancement of catalytic activity can be due to assistance of oxidation by hydroxyl radicals when the polymer is absent, and by combination of this process with additional cleaning of the particles when Nafion® is present. The final decrease in activity can be related to the loss of catalytic material.

Zooming on the 0-5 sec. region allows the definition of an optimum activation time of the order of 4 seconds (see Figure 5.16).

CV of a BDD-Pt-Nafion® recorded in 1 M HClO$_4$ + 0.1 M CH$_3$OH at 20 mV s^{-1} before (thin line) and after activation (4 seconds at 2.5 V vs. SHE) are shown in Figure 5.17. It can be seen that the onset of forward scan oxidation peak is shifted to less positive potentials by the activation procedure whereas the reverse scan oxidation peak position remained unchanged. It can also be noticed that after activation, the forward scan peak intensity is more important than that of the reverse scan. Such behaviour can be explained by participation of electrogenerated ˙OH radicals in the methanol oxidation process itself, by spillover onto the Pt surface. This may explain both the increase in oxidation current and the shift in peak position. The oxidation peak recorded during the reverse scan is of lower intensity than the first one, certainly due to the fact that all the electrogenerated free hydroxyl radicals were consumed during the forward scan. The response during the reverse scan is only due to the Pt deposit and assistance of the oxidation process by ˙OH radicals may not occur. Nevertheless the catalyst surface is more active than it was before activation.
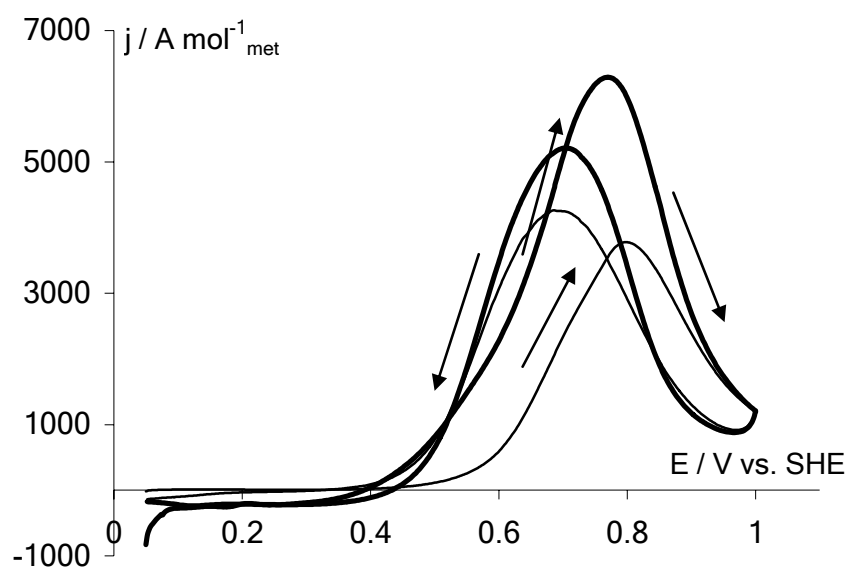
Figure 5.17: CV of a BDD-Pt-Nafion® electrode after 0 (thin line) and 3 sec. (thick line) of activation at 2.5 V vs. SHE. Scan rate of 20 mV s^{-1} in 1 M HClO$_4$ + MeOH 0.1 M at 25°C.

Similar behaviour has also been observed in the case activation of BDD-Pt and BDD-Pt-Nafion® electrodes in the presence of ethanol (data not shown), both in terms of curves profiles and activity enhancement levels. This seems to indicate that activation of the Pt deposits by electrogenerated ˙OH radicals does not activate the breaking of the C-C bond of ethanol.

119

4. CONCLUSIONS

The synthesis of Pt nanoparticles via the microemulsion method allows the formation of true nanoparticles (*i.e.* 2-5 nm in mean diameter) with narrow size distribution. XRD measurements have confirmed that such particles are well in the nano-range, and it has been shown by XPS that they are mainly in the metallic (Pt^0) state. Nanoparticles deposition on a BDD substrate electrode can be performed in a simple and reproducible way, putting a known volume (a few µl) of the aqueous Pt suspension on diamond and evaporating the solvent under nitrogen atmosphere. This BDD-Pt composite electrode has been tested in the electrooxidation of methanol and ethanol. The specific molar current is 3 times lower in the case of ethanol electrooxidation, due to Pt inability to promote the scission of the ethanol C-C bond.

However it is possible that some surfactant molecules, inherent from the synthesis mode, still adhere on the particles surface and therefore affect their electrocatalytic activity. One of the main properties of the BDD electrode, *i.e.* electrogeneration at high potentials of free and highly reactive hydroxyl radicals from water discharge, was used to clean the obtained nanoparticles. Electrogenerated hydroxyl radicals on BDD are not of same nature than those produced by potential cycling on Pt; it has indeed been shown that they are involved in organics oxidation processes on BDD. Considering also the high potentials required for hydroxyl radicals electrogeneration, a composite BDD-Pt-Nafion® electrode was realized, adding a Nafion® layer on top of the Pt deposit. Under potential conditions of hydroxyl radicals production, the BDD-Pt-Nafion® is more stable than the non-coated one as shown by the evolution of the charge in the H adsorption-desorption region on Pt with the time of anodic activation (2.5 V vs. SHE). Moreover, an increase in charge can be observed at the beginning of the activation process on the coated electrode, due to additional cleaning of residual surfactant from the surface. Enhancement of catalytic activity towards methanol and ethanol electrooxidation processes was also observed, and attributed both to additional cleaning of the catalyst surface and ˙OH spillover onto Pt. Hydroxyl radicals may participate in the methanol oxidation process itself.

Although microemulsion-synthesized Pt nanoparticles were shown to be efficient both for methanol and ethanol electrooxidation, it is well-known that the catalytic sites are readily poisoned by adsorbed reaction intermediates. As a consequence there are no Pt sites available for further alcohol dehydrogenation and the activity of the surface is decreased dramatically. It is also well-known that a solution can be to realize a mixture or an alloy between Pt and a second transition metal. Among all the tested alloying metals, Ru have the higher effect on methanol oxidation; it is now commonly accepted that Pt/Ru catalysts exhibit the best electrocatalytic activity

toward methanol electrooxidation. Therefore the next Chapter will deal with the synthesis and the characterization of bimetallic Pt/Ru nanoparticles deposited on the BDD electrode. Electrocatalytic activity of such particles will be evaluated not only for methanol electrooxidation, but also for ethanol electrooxidation.

5. REFERENCES

[1]   A. Hamnett, in: W. Vielstich, H. A. Gasteiger, A. Lamm (Eds.), *Handbook of Fuel Cells - Fundamentals, Technology and Applications*, John Wiley & Sons, Ltd., New York (2003), p. 305.

[2]   C. Lamy, E. M. Belgsir, in: W. Vielstich, H. A. Gasteiger, A. Lamm (Eds.), *Handbook of Fuel Cells - Fundamentals, Technology and Applications*, John Wiley & Sons, Ltd., New York (2003), p. 323.

[3]   T. Iwasita, W. Vielstich, E. Santos, *J. Electroanal. Chem.* **229** (1987), 367.

[4]   P. Waszczuk, A. Wieckowski, P. Zelenay, S. Gottesfeld, C. Coutanceau, J.-M. Léger, C. Lamy, *J. Electroanal. Chem.* **511** (2001), 55.

[5]   M. Watanabe, S. Motoo, *J. Electroanal. Chem.* **60** (1975), 267.

[6]   K.-W. Park, J.-H. Choi, B.-K. Kwon, S.-A. Lee, Y.-E. Sung, H.-Y. Ha, S.-A. Hong, H. Kim, A. Wieckowski, *J. Phys. Chem. B* **106** (2002), 1869.

[7]   L. Dubau, F. Hahn, C. Coutanceau, J.-M. Léger, C. Lamy, *J. Electroanal. Chem.* **554-555** (2003), 407.

[8]   O. Enea, B. Riedo, G. Dietler, *Nano Lett.* **2** (2002), 241.

[9]   F. Montilla, E. Morallon, I. Duo, Ch. Comninellis, J. L. Vazquez, *Electrochim. Acta* **48** (2003), 3891.

[10]   M. Boutonnet, J. Kizling, P. Stenius, *Colloids Surf.* **5** (1982), 209.

[11]   I. Danielsson, B. Lindman, *Colloids Surf.* **3** (1981), 391.

[12]   J. Rymes, G. Ehret, L. Hilaire, M. Boutonnet, K. Jiratova, *Catal. Today* **75** (2002), 297.

[13]   M.-L. Wu, D.-H. Chen, T.-C. Huang, *J. Colloid Interface Sci.* **243** (2001), 102.

[14]   M.-L. Wu, D.-H. Chen, T.-C. Huang, *Chem. Mater.* **13** (2001), 599.

[15]   J. Solla-Gullón, V. Montiel, A. Aldaz, J. Clavilier, *Electrochem. Comm.* **4** (2002), 716.

[16]   K. C. Song, J. H. Kim, *Powder Technol.* **107** (2000), 268.

[17]   J. Clavilier, D. Armand, *J. Electroanal. Chem.* **199** (1986), 187.

[18]   Y. Takasu, Y. Fujii, K. Yasuda, Y. Iwanaga, Y. Matsuda, *Electrochim. Acta* **34** (1989), 453.

[19]   J. Solla-Gullón, V. Montiel, A. Aldaz, J. Clavilier, *J. Electroanal. Chem.* **491** (2000), 69.

[20]   J. Solla-Gullón, V. Montiel, A. Aldaz, J. Clavilier, *J. Electrochem. Soc.* **150** (2003), E104.

[21]   Y. V. Pleskov, in: R. C. Alkire, D. M. Kolb (Eds.), *Advances in Electrochemical Science and Engineering*, Wiley-VCH, Weinheim (2002), p. 209.

[22]   N. Vinokur, B. Miller, Y. Avyigal, R. Kalish, *J. Electrochem. Soc.* **146** (1999), 125.

[23]   A. J. Saterlay, S. J. Wilkins, K. B. Holt, J. S. Foord, R. G. Compton, F. Marken, *J. Electrochem. Soc.* **148** (2001), E66.

[24]   S. Ferro, A. De Battisti, *J. Phys. Chem. B* **106** (2002), 2249.

[25]   K. J. McKenzie, F. Marken, *Electrochem. Solid-State Lett.* **5** (2002), E47.

[26]   Y. Zhang, S. Asahina, S. Yoshibira, T. Shirakashi, *Electrochimica Acta* **48** (2003), 741.

[27]   B. El Roustom, G. Fóti, Ch. Comninellis, *Electrochem. Comm.* **7** (2005), 398.

[28]   G. Siné, Ch. Comninellis, *Electrochim. Acta* **50** (2005), 2249.

[29]   B. Marselli, J. Garcia-Gomez, P.-A. Michaud, M. A. Rodrigo, Ch. Comninellis, *J. Electrochem. Soc.* **150** (2003), D79.

[30]   J. Wang, G. M. Swain, T. Tachinaba, K. Kobashi, *Electrochem. Solid-State Lett.* **3** (2000), 286.

[31]   J. Wang, G. M. Swain, *J. Electrochem. Soc.* **150** (2003), E24.

[32]   J. Wang, G. M. Swain, *Electrochem. Solid-State Lett.* **5** (2002), E4.

[33]   D. Gandini, E. Mahé, P.-A. Michaud, W. Haenni, A. Perret, C. Comninellis, *J. Appl. Electrochem.* **30** (2000), 1345.

[34]   M. Pandey, R. D'Cunha, A. K. Tyagi, *J. Alloys Compounds* **333** (2002), 260.

[35]   R. Vijayalakshmi, S. Kapoor, S. K. Kulshreshtha, *Solid State Sci.* **4** (2002), 489.

[36]   B. E. Warren, *X-Ray Diffraction*, Addison-Wesley Publishing Company, Reading (1969).

[37]   J. S. Hammond, N. Winograd, *J. Electroanal. Chem.* **78** (1977), 55.

[38]   M. P. Hogarth, T. R. Ralph, *Platinum Metals Rev.* **46** (2002), 146.

[39]   B. Beden, M.-C. Morin, F. Hahn, C. Lamy, *J. Electroanal. Chem.* **229** (1987), 353.

[40]   J. M. Perez, B. Beden, F. Hahn, A. Aldaz, C. Lamy, *J. Electroanal. Chem.* **262** (1989), 251.

[41]   F. Vigier, C. Coutanceau, F. Hahn, E. M. Belgsir, C. Lamy, *J. Electroanal. Chem.* **563** (2004), 81.

Chapter 6 RESULTS: Deposition of Microemulsion-Synthesized Pt/Ru Nanoparticles on BDD Electrodes for Alcohols Electrooxidation

1. INTRODUCTION

Supported catalyst nanoparticles have attracted during the last few decades an increasing interest, due to the different and sometimes novel properties of these materials compared to those of bulk ones [1]. The potential applications of nanoparticles cover fields as different as magnetism, optics, or electronics. More specifically in catalysis gold nanoparticles have shown an extraordinary catalytic activity [2, 3], the most spectacular example being certainly the catalysis of CO oxidation even at low temperature [4, 5]. Special attention was also focused on Pt nanoparticles due to their applicability to the Direct Alcohol Fuel Cell (DAFC) technology [6, 7], mainly fed with methanol or ethanol. However in the case of methanol electrooxidation on Pt the surface is readily and rapidly poisoned by strongly adsorbed reaction intermediates (CO) that block the catalytic sites and impeach further alcohol adsorption steps [8]. These adsorbed CO need, to be removed from the surface, to be oxidized by hydroxyl radicals coming from water activation, but it requires high overpotentials on Pt (at least 0.5 V vs. SHE whereas methanol dehydrogenation occur at 0.05 V). Special efforts were consequently made to circumvent this limitation and lowering of the overpotential necessary to water activation was possible adding a second metal to Pt. In a series of papers Watanabe and Motoo have systematically studied the influence of various metallic ad-atoms on the electrocatalytic activity of Pt toward the electrooxidation of methanol [9, 10], CO [11-14] or formic acid [15]. It is now commonly accepted [16-18] that Pt/Ru surfaces are the most efficient ones for catalysis of methanol electrooxidation. Consequently numerous papers in literature are devoted to the synthesis, characterization and electrocatalytic performance of Pt/Ru catalytic surfaces. However the synthesis methods, including for instance electrodeposition [19], carbonyl metal complexes [20] or impregnation-reduction method [17], are so various that it is difficult to compare the results obtained by different groups. In many cases the synthesis of alloys was desired; nevertheless the question of the necessity of alloying the two metals together instead of just obtaining a mixture is now under debate [16].
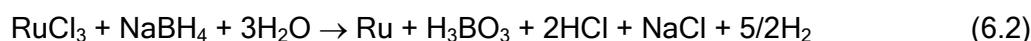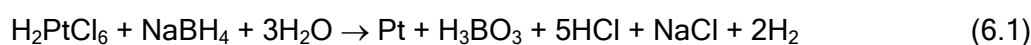
In the present Chapter, results relative to the synthesis, characterization (physical and electrochemical) and electrocatalytic performance toward both methanol and ethanol electrooxidation of microemulsion-synthesized Pt/Ru nanoparticles are presented. The microemulsion method is indeed well-known, since the first work of

Boutonnet et al. [21], to be an efficient and simple way to prepare metallic nanoparticles with narrow size distribution. A water-in-oil (w/o) microemulsion is a thermodynamically stable, optically transparent dispersion of aqueous nanodroplets, stabilized by a surfactant layer, in a continuous oily phase [22]. A microemulsion provides compartmentalized nanoreactors (the inverse micelles) in which a chemical reaction, for instance the reduction of a metallic precursor, can take place. This method has been successfully used for the synthesis of metallic nanoparticles including metals [23-26], metal oxides [27] or alloys [28-30]. Electrochemical and electrocatalytic characterization of the particles have been performed when deposited on a BDD substrate, that has been chosen due to its remarkable properties of chemical inertness, low background current and mechanical resistance to chemical and electrochemical attacks [31]. Due to these properties the BDD electrode has been used for the study of supported particles [26, 32, 33], avoiding the problems that can be encountered with common substrates (corrosion, oxide formation...). Physical characterization has been performed by means of TEM, XRD, EDX and XPS measurements and electrochemical and electrocatalytic characterizations using cyclic and linear sweep voltammetries, chronoamperometry and impedance spectroscopy.

2. EXPERIMENTAL

2.1. Nanoparticles synthesis

Platinum/Ruthenium nanoparticles were obtained by reduction of a mixture of H_2PtCl_6 (Fluka) and $RuCl_3$ (Riedel-de-Haën) with sodium borohydride in a w/o microemulsion of water / tetraethyleneglycol-monododecylether (BRIJ$^{®}$ 30) / n-heptane, following Equations 6.1 and 6.2:

$$H_2PtCl_6 + NaBH_4 + 3H_2O \rightarrow Pt + H_3BO_3 + 5HCl + NaCl + 2H_2 \qquad (6.1)$$

$$RuCl_3 + NaBH_4 + 3H_2O \rightarrow Ru + H_3BO_3 + 2HCl + NaCl + 5/2H_2 \qquad (6.2)$$

This method of synthesis was chosen instead of the mixing of two microemulsions presented in Chapter 5 because $NaBH_4$ is a more powerful reducing agent that will avoid competition between reactions 6.1 and 6.2 and allow the formation of true bimetallic particles. The microemulsions were prepared using ultra-pure water (Millipore$^{®}$ system). BRIJ$^{®}$ 30 and n-heptane were purchased from Fluka and Riedel-de-Haën, respectively, and were used as received. The metallic precursors were dissolved into the aqueous phase of one microemulsion that has a water-to-surfactant molar ratio (ω_0) fixed at 3.8. The quantity of surfactant represented 16.54 % of the volume of the microemulsion, and the aqueous phase was constituted of

mixtures of 0.1 M solutions of the metallic salts. Relative amounts of the precursors solutions were adjusted depending on the alloy final composition that was desired. During this part of the thesis, Pt/Ru bimetallic particles of 80, 60, 50, 40, and 20 atomic percent in Pt were synthesized, in addition of pure Pt and Ru particles. From a practical point of view, the surfactant and n-heptane were first mixed. Then the aqueous phase was slowly added and the solution vigorously stirred. This results in a transparent, homogeneous solution which colour changes from pale yellow to dark brown increasing Ru content. The conditions for the synthesis of the Pt/Ru particles by the microemulsion method are summarized in Table 6.1.

	Pt/Ru nanoparticles
Vol. % surfactant	16.54
Vol. % n-heptane	80.46
Vol. % H_2O	3
$[PtCl_6^{2-}]_{aq}$ / M	0.1
$[RuCl_3]_{aq}$ / M	0.1
$[NaBH_4]_{aq}$ / M	1
$[NaBH_4]_{aq}/[metal\ ions]_{aq}$	10

Table 6.1: Experimental parameters for the synthesis of Pt/Ru nanoparticles using the microemulsion method.

The synthesis was realised adding to the microemulsion the amount of solid sodium borohydride necessary to yield a concentration of 1 M of $NaBH_4$ in the aqueous phase. The general scheme of nanoparticles synthesis adding a solid reducing agent to a microemulsion is shown in Figure 6.1. It involves the following steps: (**1**) mixing of the microemulsion with the solid reducing agent that diffuses into the inverse micelles to react with the metallic precursors, (**2**) nucleation and (**3**) growth of the particles into the interior of the inverse micelles. Growth of the particles was finally stopped by the surfactant layer that stabilises the aqueous dispersion.
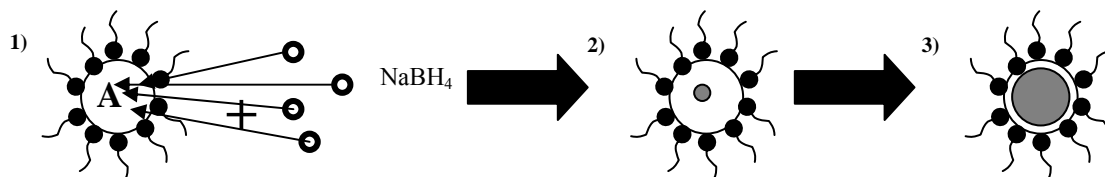

Figure 6.1: General scheme for the synthesis of Pt/Ru particles adding a solid reducing agent to a microemulsion. Steps of the process: **1)** mixing of the microemulsion with solid $NaBH_4$, diffusion into the inverse micelles and reaction, **2)** nucleation and **3)** growth of the particles. A = H_2PtCl_6 + $RuCl_3$(aq.) in appropriate ratios, aqueous droplets dispersed in n-heptane and stabilized by a BRIJ®-30 layer.

After complete reduction, that needs only a few minutes to take place and is evidenced by colour change to dark black and gas release, acetone was added to the solution to cause phase separation and precipitation of the particles. The precipitate was rinsed several times with acetone and ultra-pure water, and then centrifuged for a few minutes to eliminate most of the surfactant. Finally particles were put in a small volume of ultra-pure water as a suspension. The Pt contents of this final aqueous suspension were determined using AAS.

2.2.   BDD-Pt/Ru electrode preparation

BDD films were synthesised by the hot filament chemical vapour deposition technique (HF-CVD) on single crystal p-type Si <100> wafers (1-3 mΩcm, Siltronix). The doping level of boron expressed as B/C ratio was about 3500 ppm. The obtained diamond film thickness was about 1 μm with a resistivity in the range 10-30 mΩcm. This as-grown BDD contains some graphitic (sp^2) phase and is hydrogen terminated. Activation of BDD by anodic polarization (10 mA cm^{-2} in 1 M H_2SO_4 at 25 °C during 30 min) eliminates most of the sp^2 and adsorbed hydrogen from the surface, and is necessary to obtain reproducible electrochemical measurements [34].

Pt/Ru nanoparticles were deposited onto the BDD substrate putting a droplet (5 μl) of the suspension onto diamond. The excess water was dried under nitrogen atmosphere. The BDD-Pt/Ru electrode was then transferred to the electrochemical cell for measurements.

2.3.   Measurements

Electrochemical measurements were conducted using the conventional three-electrode cell described in Chapter 3, with BDD-supported Pt nanoparticles as working electrode (exposed area of diamond: 0.4 cm^2), Hg/Hg$_2$SO$_4$.K$_2$SO$_4$(sat.) as reference and a platinum wire as counter electrode. All potentials reported here are plotted with respect to the Standard Hydrogen Electrode (SHE). All solutions were made in ultra-pure (Millipore$^®$ system) water using analytical grade reactants without further purification. Before any experiment the solution was saturated with nitrogen gas and measurements were conducted under a nitrogen atmosphere.

Physical characterization of the particles was conducted by means of TEM, XPS and XRD, using the methods and apparatus described in Chapter 3. For TEM analysis, a small droplet of the particles suspension was put on an amorphous carbon-coated copper grid; the excess water was then removed and the grid placed in the vacuum chamber of the microscope in order to be analyzed. XRD measurements of particles were carried out with particles deposited on a BDD

substrate, whereas XPS analyses were performed using a gold substrate due to the proximity of the C $1s$ and Ru$3d$ peaks (closed to 280 eV). Deconvolution of the peaks of interest in XPS spectra (Pt$4f$ and Ru$3p$) was done using the CasaXPS® computer program.

3. RESULTS AND DISCUSSION

3.1. Pt/Ru nanoparticles characterization

Several different types of bimetallic Pt/Ru particles have been synthesized via the microemulsion method, adjusting the ratio of metallic precursors dissolved in the aqueous phase of the initial microemulsion. The following particles, labelled according to their theoretical atomic contents, have been synthesized: $Pt_{80}Ru_{20}$, $Pt_{60}Ru_{40}$, $Pt_{50}Ru_{50}$, $Pt_{40}Ru_{60}$, $Pt_{20}Ru_{80}$, plus pure Pt and pure Ru. All these particles have been characterized by TEM. Figure 6.2 shows as representative examples TEM micrographs of Pt (Fig. 6.2.A), $Pt_{50}Ru_{50}$ (6.2.B) and Ru nanoparticles (6.2.C). It can be seen on these pictures that particles are present on the copper grid as small, isolated and well-spherical units, of diameter in the 2-5 nm range that corresponds well with the definition of a nano-object in electrocatalysis.

Moreover the size distributions of all the synthesized Pt/Ru nanoparticles were established on the basis of TEM measurements on more than 100 individual particles in each case. It can be seen on Figure 6.3 that size distributions of all types of nanoparticles have similar shape and covers approximately the same size domain. The small fluctuations between the size distributions of different nanoparticles most likely come from fluctuations in the experimental realization of the microemulsions. The fact that the composition of the mixture of metallic salts in the aqueous phase of the microemulsion (at constant total concentration) does not seem to influence the size of the obtained nanoparticles indicates the suitability of this synthesis technique. It is also the sign that the key parameter for controlling the size of microemulsion-synthesized nanoparticles is the formulation of the starting microemulsion and more particularly an accurate value of ω_0 must be chose.
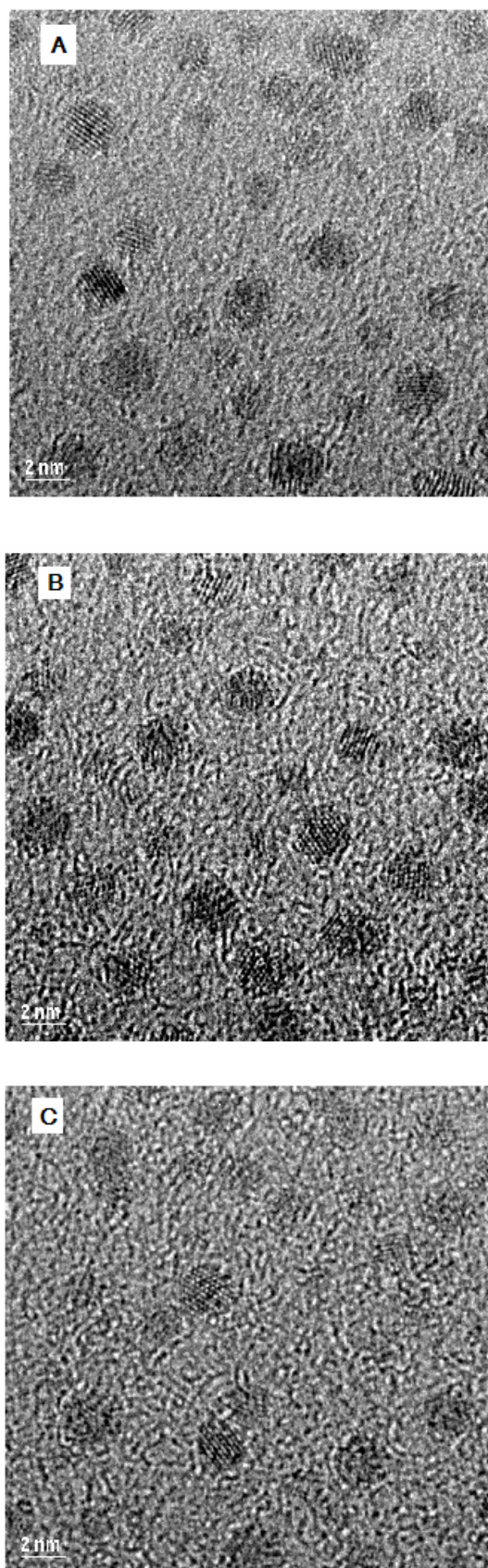
Figure 6.2: TEM micrographs of Pt (**A**), $Pt_{50}Ru_{50}$ (**B**) and Ru (**C**) nanoparticles synthesized via the microemulsion method.
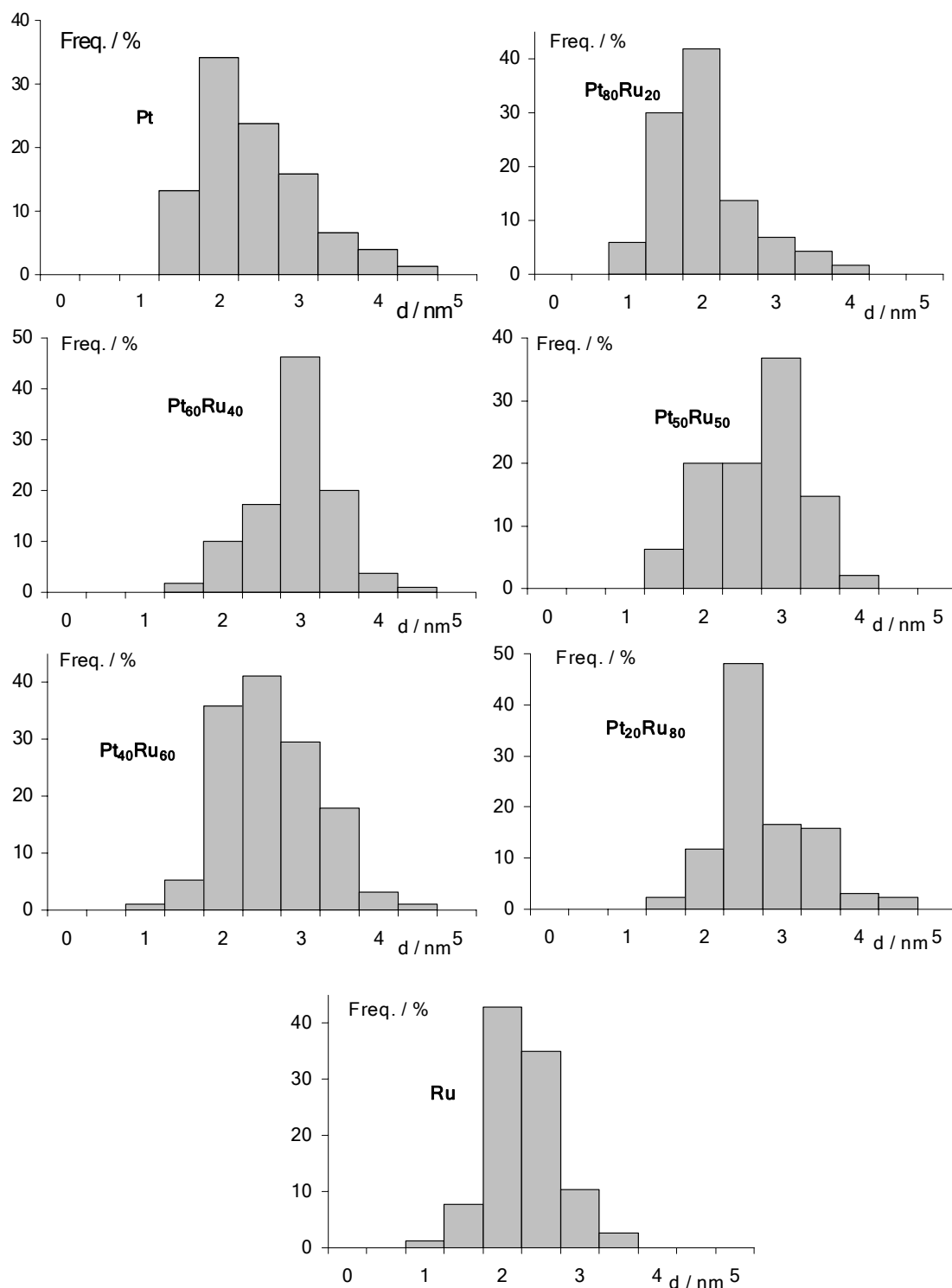
Figure 6.3: Size distributions of microemulsion-synthesized Pt/Ru nanoparticles determined by TEM.

The XRD diffractogramms of all the synthesized Pt/Ru nanoparticles, deposited on BDD, are shown in Figure 6.4. Peaks ascribable to the typical fcc (face-centred cubic) Pt structure are listed on curve a of Fig. 6.4. The other main peaks observable on spectra of Fig. 6.4 can be attributed to the (111) and (220) planes of diamond (44° and 75.3°), and to the (400) plane of silicium (70°) [35]. The shift to higher angle

values and widening of Pt peaks with increasing the Ru contents in the sample can also been observed. They can be more clearly seen in Figure 6.5, which shows the XRD patterns of Pt, $Pt_{80}Ru_{20}$ and $Pt_{50}Ru_{50}$ nanoparticles deposited on BDD in the region of (111) and (200) reflections. The bands displacement indicates a decrease in the sample lattice parameter and is characteristic of a Pt/Ru alloy formation [36].
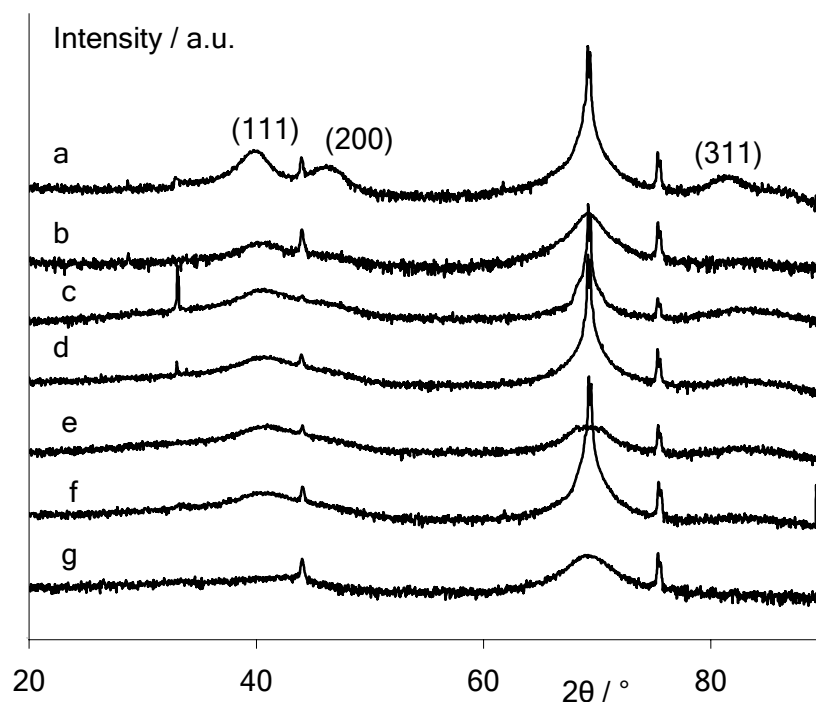

Figure 6.4: XRD spectra of microemulsion-synthesized Pt/Ru nanoparticles deposited on BDD. (a): Pt, (b): $Pt_{80}Ru_{20}$, (c) $Pt_{60}Ru_{40}$, (d): $Pt_{50}Ru_{50}$, (e): $Pt_{40}Ru_{60}$, (f): $Pt_{20}Ru_{80}$, and (g): Ru nanoparticles.
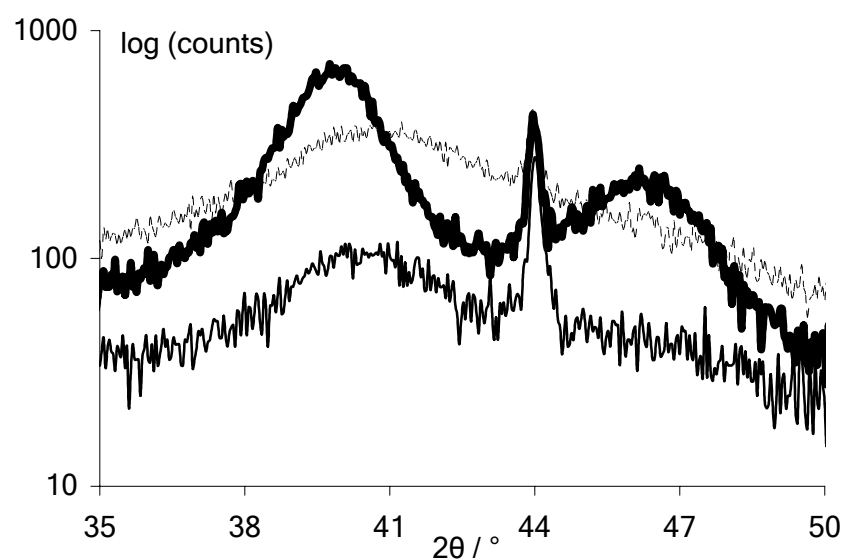
Figure 6.5: XRD patterns of microemulsion-synthesized Pt (thick solid line), $Pt_{80}Ru_{20}$ (thin solid line) and $Pt_{50}Ru_{50}$ (thin dashed line) nanoparticles deposited on BDD.

130

It can be observed on Figures 6.4 and 6.5 that a gradual loss of crystallinity occurs when the Ru content in particles is increased. In the case of Ru there is no distinguishable crystalline band. Loss of crystallinity can be attributed to the presence of increasing amounts of Ru in the amorphous state. The results obtained by XRD indicate that, in addition of the formation of an alloy between Pt and Ru evidenced by bands displacement, it may exist regions where Ru is not alloyed with Pt but only present in its amorphous state [36]. The lattice parameter for the different nanoparticles has also been calculated for a fcc structure using the Vegard's law:

$$a_{fcc} = \frac{\sqrt{2}\lambda_{CuK\alpha}}{\sin\theta_{max}} \qquad (6.3)$$

The evolution of the lattice parameter with the nanoparticles composition is given in Figure 6.6. The relation between the lattice parameter and the Ru contents in the nanoparticles is almost linear; a similar behaviour has ever been reported by Gasteiger and co-workers [37] and this formula has already been used for the calculation of the massic composition of Pt/Ru samples [36].
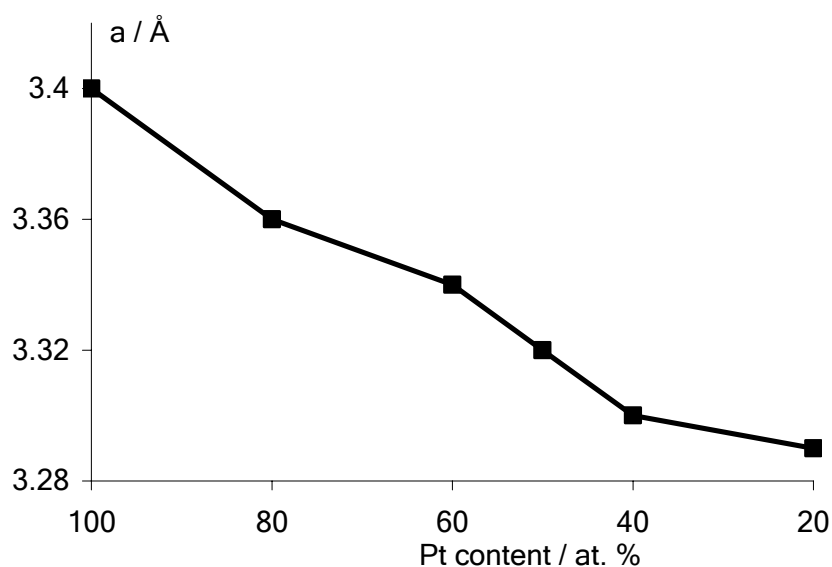

Figure 6.6: Lattice parameter of microemulsion-synthesized Pt/Ru nanoparticles deduced from XRD.

In addition of the bands displacement, bands widening was also observed. This is related to a decrease in the particles diameter. The mean diameter of particles was determined by XRD and the obtained values were compared to those obtained by TEM (see Figure 6.7). As the (220) peak of Pt (located at 67.3°) is completely hidden by the (400) Si peak, the (111) reflection of metallic Pt (located near 40°) was taken into account to estimate the crystallite size using the Debye-Scherrer formula [38]:

$$d = \frac{0.91\lambda_{CuK\alpha}}{Bcos\theta} \qquad\qquad (7.4)$$

where d is the crystallites average diameter, λ the CuKα X-radiation wavelength, B the excess line width (in radians) and θ the Bragg angle. However the diameters deduced from XRD must be used with precautions: the quality decrease in signals, due to the samples loss of crystallinity, can dramatically influence the calculations of both the lattice parameter and the diameter, especially for Ru-rich samples. As already stated, the fluctuations observed in diameters deduced from TEM may be linked to some fluctuations in the experimental realization of the microemulsions and concomitant fluctuations in the ω_0 value, rather than to an influence of the microemulsion aqueous phase composition. It has indeed been reported that the key factor that governs the size of the w/o microemulsion aqueous cores, and therefore the size of the obtained particles, was the water-to-surfactant molar ratio [25].
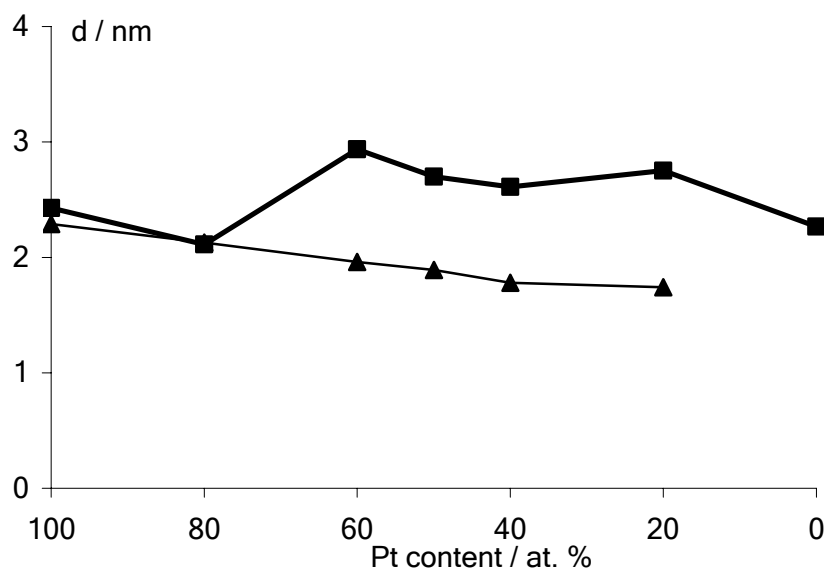

Figure 6.7: Mean diameter of microemulsion-synthesized Pt/Ru nanoparticles determined by TEM (thick line with square markers) and XRD measurements (thin line with triangle markers).

XPS analyses have also been conducted on microemulsion-synthesized Pt/Ru nanoparticles. In this case a gold substrate was used rather than BDD. The reason for a such a change is that the XPS signals of C *1s* and Ru*3p* are very close one of the other (around 280 eV), and that the use of a diamond substrate will inevitably induce a very strong C *1s* signal that will completely hide the Ru*3p* contribution. As a typical example the XPS survey of $Pt_{50}Ru_{50}$ nanoparticles supported on gold is shown in Figure 6.8. Besides the main Au*4f* (substrate) and O *1s* peaks (interaction with atmospheric oxygen), the contributions of Pt*4f* (around 70-75 eV) and Ru*3p* (near 280 eV) are clearly observable. XPS was also used as an atomic quantification tool.

Atomic quantification results by XPS and EDX analyses (performed during TEM measurements) are presented in Table 6.2 and compared to those expected from the feeding mixtures of metallic salts in the microemulsions aqueous phases. The atomic compositions of Pt/Ru nanoparticles deduced from both XPS and EDX were very close to the expected values. This indicates that the microemulsion method permits the synthesis of bimetallic nanoparticles of finely controlled composition.
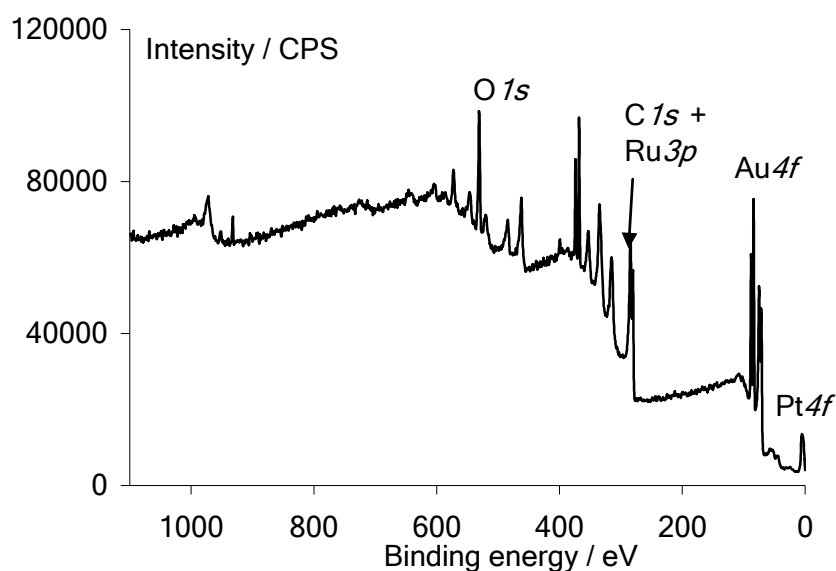

Figure 6.8: XPS survey spectrum of $Pt_{50}Ru_{50}$ nanoparticles deposited on a gold.

Nominal Pt content / at. %	XPS Pt content / at. %	EDX Pt content / at. %
100	100	100
80	78.9	84
60	58	61.7
50	50	53.6
40	39.9	36.8
20	21.7	16.5
0	0	0

Table 6.2: Atomic composition of bimetallic microemulsion-synthesized Pt/Ru nanoparticles determined by means of XPS and EDX.

The obtained XPS spectra of Pt/Ru nanoparticles were further analyzed and the Pt$4f$ and Ru$3p$ contributions of all signals were deconvolved using the CasaXPS® software. As typical examples the deconvolved Pt$4f$ and Ru$3p$ signals of $Pt_{50}Ru_{50}$ nanoparticles are shown in Figure 6.9 and 6.10, respectively. The Pt signal is composed of four main contributions: peaks (1) and (2) are due to Pt$4f_{7/2}$ and Pt$4f_{5/2}$ lines of metallic Pt (Pt^0), respectively, whereas peaks (3) and (4) are ascribable to

Pt$4f_{7/2}$ and Pt$4f_{5/2}$ lines of Pt^{II} present in PtO or Pt(OH)$_2$ [39]. The ratio between metallic and oxidized forms of Pt was about 4:1 for all the nanoparticles. The signal of Ru$3p$ was much more complicated to treat due to the proximity of the C$1s$ signal. However the existence of two doublets, located around 280 and 283.3 eV, was observed in all samples. These peaks have been assigned to the presence of metallic Ru and/or species with low oxidation state (peaks 1 and 2), and to species with an oxidation state of +IV (peaks 3 and 4) [40, 41]. The relative composition between the different oxidation states was 65-70 % for low oxidation states and 30-35 % for Ru(IV) species.

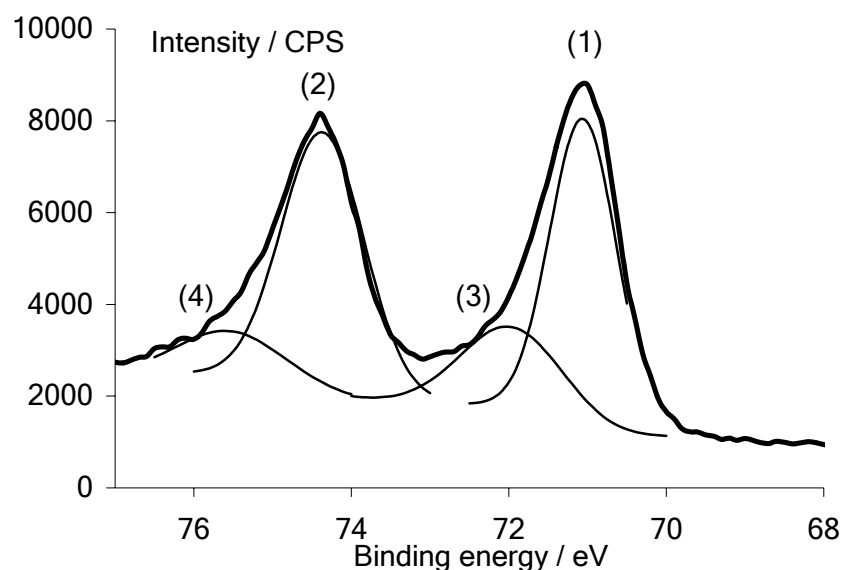**Figure 6.9**: Deconvolved XPS Pt$4f$ signal of microemulsion-synthesized Pt$_{50}$Ru$_{50}$ nanoparticles deposited on Au substrate.
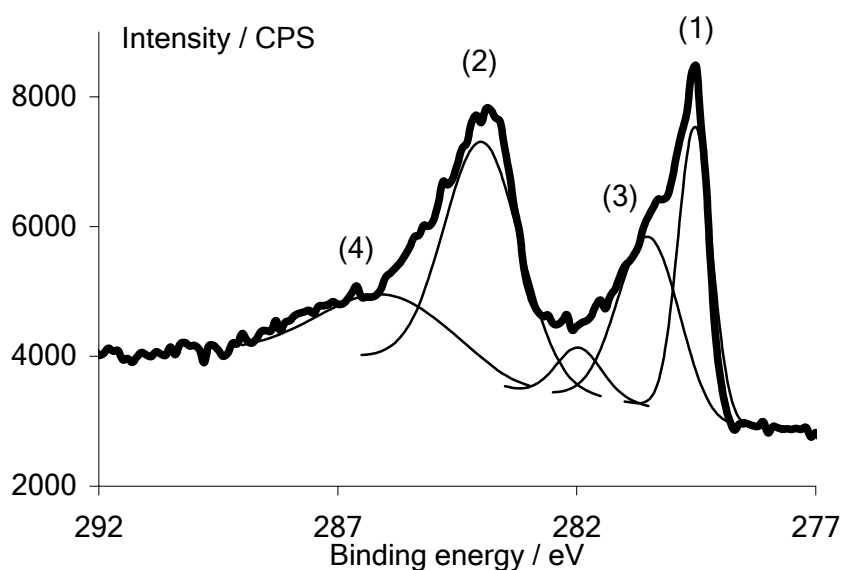

Figure 6.10: Deconvolved XPS Ru$3p$ signal of microemulsion-synthesized Pt$_{50}$Ru$_{50}$ nanoparticles deposited on Au substrate.

Another important information that can be extracted from XPS measurements is the estimation of the modification of Pt electronic properties induced by the presence of the alloying metal. The chemical shift of the $Pt4f_{7/2}$ line in all Pt/Ru samples is illustrated in Figure 6.11. It can be seen from Fig. 6.11 that the XPS $Pt4f$ signal in alloys is shifted to lower values of binding energy. The shift is in all cases of the order of 0.1-0.2 eV. This is indicative of e⁻ d transfer from the alloying metal (Ru) to Pt [42], and therefore of a modification of Pt work function. As a result the strength of the Pt-CO bond formed after methanol dehydrogenation would be weakened and therefore the poisoning intermediates would be more easily eliminated; this is the principle of the so-called electronic effect. However the observed shift is quite low due to the weak difference of electronegativities between Pt and Ru. Therefore an increase in the electrocatalytic activity of Pt/Ru surfaces compared to Pt ones, as it has already been reported, could not solely been attributed to this electronic effect. Nevertheless the electronic effect should play an effective role due to the formation of true alloys as shown by XRD.
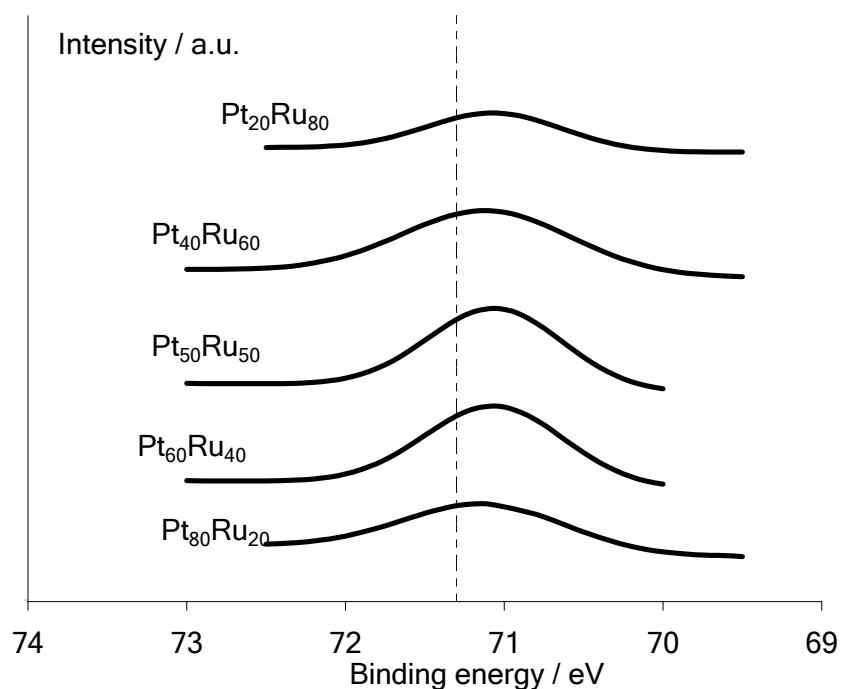

Figure 6.11: Chemical shift of the XPS $Pt4f_{7/2}$ (Pt^0) line of bimetallic microemulsion-synthesized Pt/Ru nanoparticles deposited on Au substrate. The dashed vertical line represents the position of the signal in pure Pt nanoparticles.

Obviously, in the case of analysis of objects of dimensions as low as 2-5 nm, XPS can no longer been considered as a surface investigation tool. Information extracted from XPS analyses concern the whole nanoparticle, including its bulk. Cyclic voltammetry appears to be a convenient way to circumvent these limitations. CV of BDD-supported Pt/Ru nanoparticles recorded at 50 mV s⁻¹ 1 M $HClO_4$ solution are

135

shown in Figure 6.12. The continuous transition between the shapes of pure Pt and pure Ru signals is clearly observable when the Ru content is increased in the samples. The region of H adsorption-desorption on Pt is worse and worse-defined as Ru content is increased. Whereas two very small waves can still be observed for $Pt_{80}Ru_{20}$ nanoparticles only one bump ascribable to H adsorption-desorption processes on Pt, is present on the CV recorded for Pt/Ru nanoparticles with lower Pt contents (down to 40 at. %). Finally the CV obtained for $Pt_{20}Ru_{80}$ and pure Ru nanoparticles deposited on BDD do not exhibit any feature that can be attributed to hydrogen adsorption and desorption processes. Moreover the double-layer region is increased with the Ru content. As this double-layer region corresponds to the potential region of water activation this is certainly due to the ability of Ru to activate water at lower potentials than Pt. Moreover the low value of the double-layer capacitance observed in the case of pure Pt nanoparticles is indicative of low contribution of the support electrode; this justifies the choice of BDD for this use. This transition indicates that the surface moves gradually from a dominant Pt surface character to a dominant Ru surface character. This is also a good indication of the kind of surface that would be more suitable for electrocatalysis of alcohols (methanol and ethanol) oxidation. As Pt is the only metal, at least at room temperature, capable of methanol dehydrogenation, Pt/Ru surfaces with a marked Pt surface character should be more efficient in the electrocatalysis of methanol oxidation for instance. In the case of these microemulsion-synthesized Pt/Ru nanoparticles, $Pt_{80}Ru_{20}$, $Pt_{60}Ru_{40}$ and eventually $Pt_{50}Ru_{50}$ surfaces seem to be the most promising ones for this purpose. It must also be pointed out that the limit of the scanning potential window in the anodic direction of BDD-supported Pt/Ru nanoparticles was fixed at 0.8-0.9 V vs. SHE. This was done to avoid Ru oxidation and dissolution from the nanoparticles surface and Pt oxides formation that can result in surface reorganization [43] and aggregation of particles [44]. Moreover using this potential range the amplitude of the CV signals was maintained upon repetitive cycles, indicating stability of the deposit on the diamond substrate.
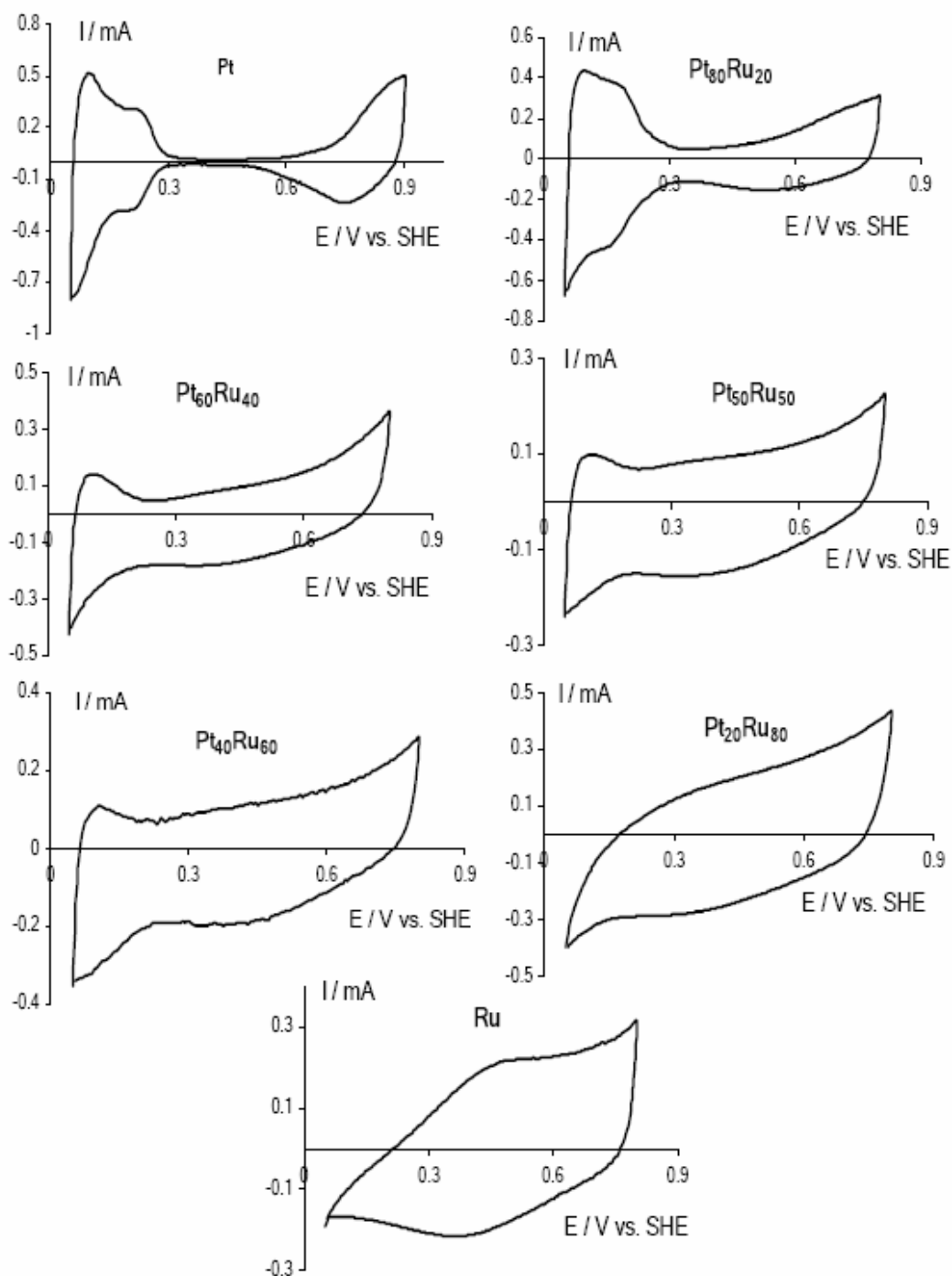
Figure 6.12: CV of microemulsion-synthesized Pt/Ru nanoparticles deposited on BDD. Recorded in 1 M $HClO_4$ at a scan rate of 50 mV s^{-1}, T = 25°C.

In order to summarize this characterization part, it can be said that the microemulsion method allows the formation of Pt/Ru particles of controlled composition and size. It was indeed shown by TEM and XRD that these particles are really in the nano-size domain (mean diameter around 3 nm for all the synthesized nanoparticles), thus allowing the use of nanomaterials unique properties in

electrocatalysis. The similar size distributions obtained for all the samples indicate that the microemulsion method permits a fine control of the obtained particles size. The small differences between size distributions can most likely be attributed to small fluctuations in the practical preparation of the starting microemulsions leading in small modifications of the water-to-surfactant molar ratios. There is no evidence that the composition of the aqueous phase of the microemulsion influences the size of the obtained nanoparticles. Moreover the effectiveness of Pt/Ru alloy formation was evidenced analyzing the displacement of the XRD bands attributed to Pt and demonstrating that the lattice parameter of the samples followed the Vegard's law. The mean diameters calculated from XRD were in the same range than those deduced from TEM. It was also shown by XPS and EDX that the composition of all samples was very close to the theoretical ones (deduced from the ratios of metallic salts introduced in the aqueous phases of the initial microemulsion), demonstrating the suitability of the method for the synthesis of bimetallic particles of controlled composition. XPS has also shown that Pt in all samples is mainly metallic (ratio between metallic and oxidized (+II) Pt around 4:1). However it must be pointed out that samples were stored during several days in air before the measurements were done and that particles taken directly from the suspensions were certainly less oxidized. Most interestingly, a very low chemical shift of the XPS Pt$4f$ signal to lower values of binding energies (0.1-0.2 eV of difference) was observed in Pt/Ru alloys compared to Pt. Such a low chemical shift can be attributed to the low difference between the electronegativities of the two elements and allows making the assumption that an eventual enhanced electrocatalytic activity of Pt/Ru surfaces may be due to a combination between the bifunctional mechanism and a ligand effect. The CV recorded in pure supporting electrolyte gave more insights on the surface state of the particles than XPS that will explore the whole depth of objects of typically 3 nm in diameter. It was observed that Pt-rich particles presented the most marked Pt surface character, and it has been postulated that these particles may be more efficient for electrocatalysis of methanol and ethanol electrooxidation as they should be more capable to perform the alcohol dehydrogenation steps.

3.2. Electrocatalytic characterization

The electrocatalytic activity of microemulsion-synthesized Pt/Ru nanoparticles has been tested toward reactions of interest for the Direct Alcohol Fuel Cell (DAFC) technology. For this purpose the electrooxidation of methanol and ethanol have been chosen since these alcohols appear to be the most promising ones for this technology. Electrocatalytic characterization of BDD-supported nanoparticles has

been carried out by means of cyclic voltammetry (CV), chronoamperometry (CA), and electrochemical impedance spectroscopy (EIS).

Figure 6.13 shows CV of methanol and ethanol electrooxidation on BDD-supported microemulsion-synthesized Pt nanoparticles. The current is normalized with respect to the total amount of deposited metal, determined on the basis of Pt titration in the aqueous suspension by AAS and XPS determination of the atomic composition of particles. As already stated in Chapter 5 of this manuscript, the difference in activity toward the electrooxidation of the two alcohols is due to the inability of Pt to promote the ethanol molecule C-C bond scission. This implies that ethanol electrooxidation on Pt yields C_2 species (acetaldehyde and acetic acid have been identified by FTIR [45]) that cannot undergo further oxidation. Therefore the activation of the C-C bond breaking in ethanol-feed DAFC has been a major challenge during the last few years [7, 46, 47]. One other remarkable feature is that the section between the forward and reverse scan is located at the same potential for the two alcohols (around 0.85 V). This indicates that at this point Pt is in the same surface state in the forward and in the reverse scans and that the nature of the electroactive species under investigation does not play any role on it.

Figure 6.13: CV of MeOH (**A**) and EtOH (**B**) electrooxidation on BDD-supported microemulsion-synthesized Pt nanoparticles. Recorded in 1 M $HClO_4$ + 0.1 M Alcohol at 20 mV s^{-1} and 25°C.

Similar experiments have also been conducted on the different microemulsion-synthesized Pt/Ru nanoparticles deposited on BDD. Figure 6.14 shows, as a typical example, the CV for both methanol and ethanol electrooxidation at $Pt_{50}Ru_{50}$ nanoparticles deposited on BDD. The potential domain under investigation is more

restricted in the case of Pt/Ru nanoparticles than for Pt in order to avoid Ru oxidation and dissolution. Figure 6.15 summarizes the evolution of the specific molar current measured by CV both for methanol and ethanol electrooxidation as a function of the composition of the deposited particles. For simplicity the particles are here labelled according to their respective nominal compositions whereas specific molar currents were calculated with respect to the total amount of deposited metal (Pt and Ru) according to the atomic compositions determined by XPS. As a general tendency it can be observed, for both the two processes considered here, that the specific molar oxidation current decreases with decreasing the Pt content in the nanoparticles. This is because, at least at room temperature, Pt is the only metal capable of performing alcohols dehydrogenation. One of the roles of Ru is to promote water activation at lower potentials than Pt, according to the bifunctional mechanism that can be summarized within Equations 6.5 to 6.8:

$$3\ Pt(H_2O) + CH_3OH \rightarrow Pt_3(CH_3OH)_{ads} + 3\ H_2O \tag{6.5}$$

$$Pt_3(CH_3OH)_{ads} \rightarrow Pt(CO)_{ads} + 2\ Pt + 4\ H^+ + 4\ e^- \tag{6.6}$$

$$Ru + H_2O \rightarrow Ru(^{\cdot}OH)_{ads} + H^+ + e^- \tag{6.7}$$

$$Pt(CO)_{ads} + Ru(^{\cdot}OH)_{ads} \rightarrow Pt + Ru + CO_2 + H^+ + e^- \tag{6.8}$$
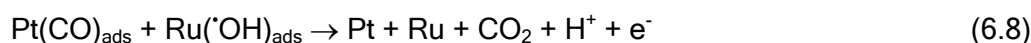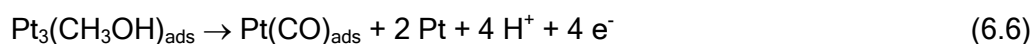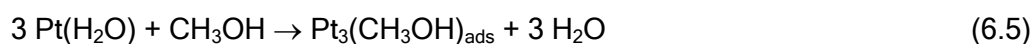
Therefore it seems obvious that decreasing the surface Pt content will decrease the adsorption abilities of the particles, thus decreasing its electrocatalytic activity. It must be pointed out also than the CV recorded on pure Ru in the presence of methanol or ethanol does not differ from those recorded in the pure supporting electrolyte, confirming that no electrooxidation of alcohols occurs on Ru (data not shown). Interestingly, the section between reverse and forward scan is still in the case of both methanol and ethanol electrooxidation on Pt/Ru nanoparticles located at approximately the same potential values (around 0.6 V for all samples, see for instance Fig. 6.14). The lowering of this section potential compared to that observed at Pt is an indication of water activation at lower potential at Pt/Ru than at Pt, and thus of occurrence of the bifunctional mechanism.
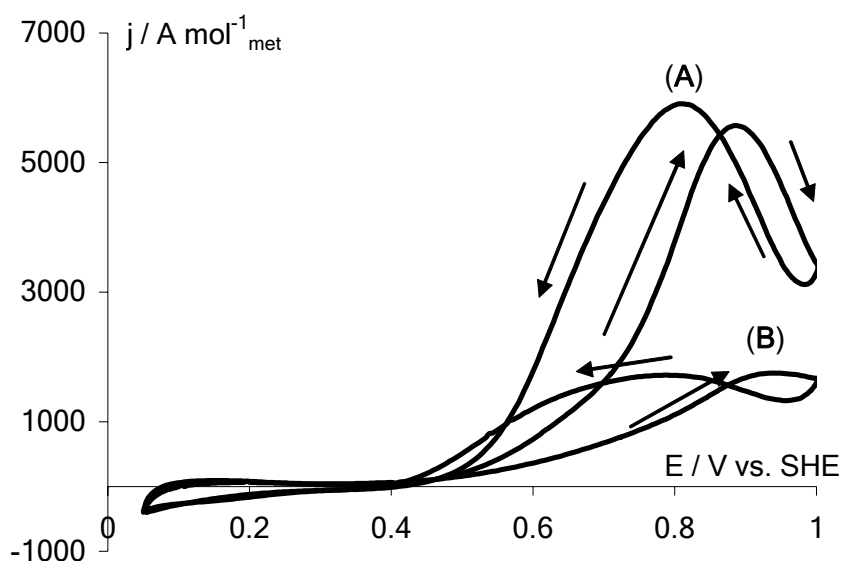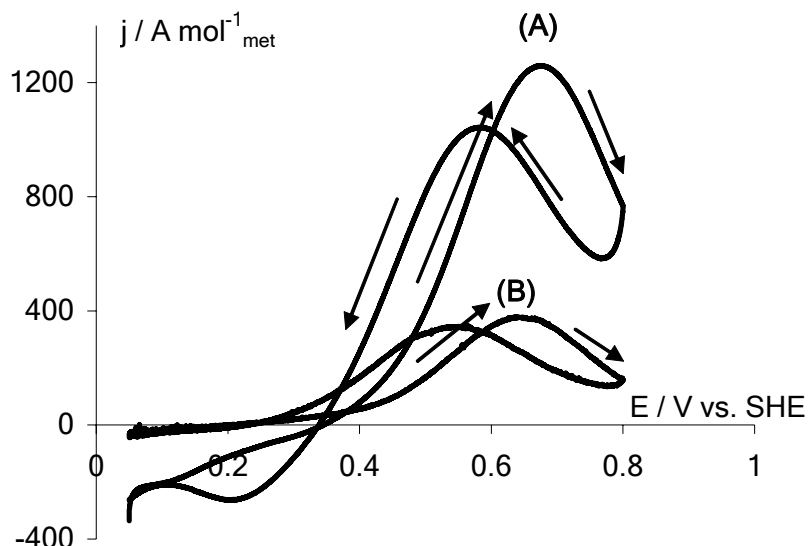
Figure 6.14: CV of MeOH (**A**) and EtOH (**B**) electrooxidation on BDD-supported microemulsion-synthesized $Pt_{50}Ru_{50}$ nanoparticles. Recorded in 1 M $HClO_4$ + 0.1 M Alcohol at 20 mV s^{-1} and 25°C.
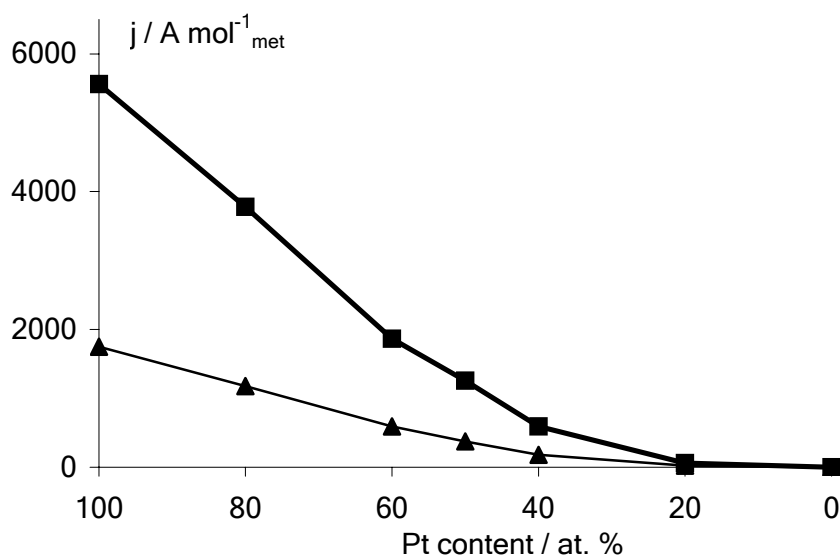

Figure 6.15: Evolution of the specific molar oxidation current (forward scan) for the electrooxidation of MeOH (thick line with square markers) and EtOH (thin line with triangle markers) on BDD-supported microemulsion-synthesized Pt/Ru nanoparticles. Recorded by CV in 1 M $HClO_4$ + 0.1 M Alcohol at 20 mV s^{-1} and 25°C.

The beneficial effect of Ru addition to Pt in catalysis of alcohols electrooxidation appears clearly in Figure 6.16. This figure shows linear sweep voltammograms recorded at 1mV s^{-1} in a 1 M $HClO_4$ + 0.1 M CH_3OH solution on Pt and $Pt_{80}Ru_{20}$ nanoparticles deposited on BDD. It can be seen on this figure that the onset of methanol electrooxidation is appreciably shifted to lower potential values on the bimetallic nanoparticles (from approximately 0.52 V to 0.43 V at a specific molar current of 50 A mol$^{-1}_{met}$). This is because, according to the bifunctional mechanism

141

[10], Ru allows water activation at lower potentials than Pt. Consequently the surface reaction between adsorbed CO (mainly on Pt) and adsorbed ˙OH (mainly on Ru) can take place earlier on the Pt/Ru surface. Pt sites are then free for further dehydrogenation and the current can increase. For clarity only the linear sweep voltammograms for Pt and $Pt_{80}Ru_{20}$ are shown in Fig. 6.16, but similar trends were observed in the case of other synthesized Pt/Ru nanoparticles. Similar observations could also be done in the case of ethanol electrooxidation (data not shown).
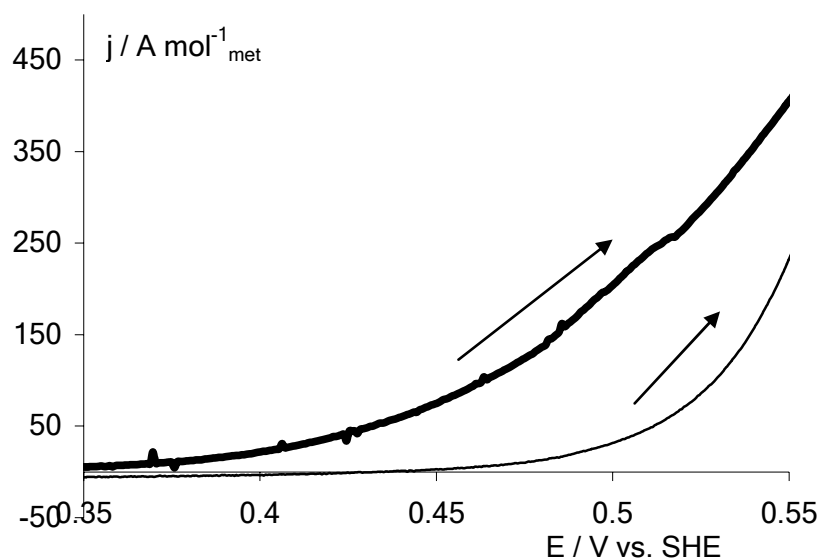

Figure 6.16: Polarization curves and onset of MeOH electrooxidation on microemulsion-synthesized Pt (thin line) and $Pt_{80}Ru_{20}$ (thick line) nanoparticles deposited on BDD. Recorded in 1 M $HClO_4$ + 0.1 M CH_3OH at 1 mV s^{-1} and 25°C.

Another appreciable illustration of the beneficial effect of Ru addition to Pt for catalysis of methanol electrooxidation is given by the current-time transients recorded in methanol solutions. Figures 6.17 and 6.18 show current-time transients for methanol electrooxidation recorded on BDD-supported Pt and $Pt_{80}Ru_{20}$ nanoparticles in a 1 M $HClO_4$ + 0.1 M CH_3OH solution at constant potentials of 0.4 V and 0.6 V vs. SHE, respectively. Such potentials were chosen because at the former potential water dissociation is not activated on pure Pt surface and at the latter one water dissociation is activated either on Pt and Pt/Ru surfaces. It can be seen firstly that, whatever the potential and the surface are, all the j-t curves exhibit similar profiles, *i.e.* strong initial specific molar current decay followed by a plateau. This type of profile has already been observed and attributed to fast adsorption of intermediates blocking the catalytic surface sites [8]. Similar profiles were also observed in the case of ethanol electrooxidation (data not shown) and attributed to the increasing surface coverage with partially oxidized intermediates [48].

However some differences are observable in the j-t curves of MeOH electrooxidation on Pt and $Pt_{80}Ru_{20}$ surfaces depending on the applied potential. At 0.6 V vs. SHE (Fig. 6.18), water dissociation is activated on Pt and therefore free Pt catalytic sites are available for methanol dehydrogenation. As this step is, at least at room temperature, only possible on Pt sites the initial specific molar oxidation current is quite larger on pure Pt nanoparticles than on bimetallic ones. The specific molar current then falls dramatically on Pt as a consequence of surface poisoning. The current decrease is far less pronounced on the $Pt_{80}Ru_{20}$ nanoparticles, indicating higher poison (mainly CO) tolerance of this type of surface. Moreover, as Ru promotes water dissociation at lower potentials than Pt, the surface reaction between adsorbed CO and oxygenated species may take place with faster kinetics. Therefore extended electrocatalytic activity can be achieved on Pt/Ru. At lower potential values (E = 0.4 V vs. SHE, Fig. 6.17) the initial specific molar oxidation current is of the same order of magnitude both on Pt and $Pt_{80}Ru_{20}$, and then falls rapidly. In this case water dissociation is not activated on pure Pt so that the surface reaction between adsorbed CO and hydroxyl radicals cannot take place whereas the role of Ru, according to the bifunctional mechanism, is to promote water dissociation at lower potentials than Pt. The surface reaction can take place earlier and with faster kinetics, and therefore the initial specific molar current is increased on Pt/Ru. In this case also current decrease is less pronounced on the bimetallic surface and a higher specific molar oxidation current is reached at the end of experiment on $Pt_{80}Ru_{20}$ nanoparticles.

Figure 6.17: Chronoamperometric curve at 0.4 V vs. SHE for the electrooxidation of MeOH on BDD-supported microemulsion-synthesized Pt (thin line) and $Pt_{80}Ru_{20}$ (thick line) nanoparticles. Recorded in 1 M $HClO_4$ + 0.1 M CH_3OH at 25°C. **Inset:** zoom on the 0-10 s time domain.
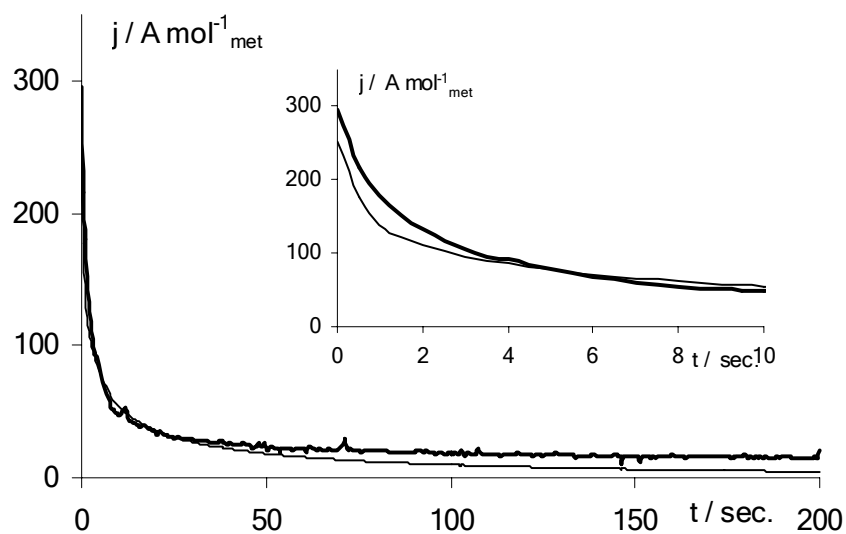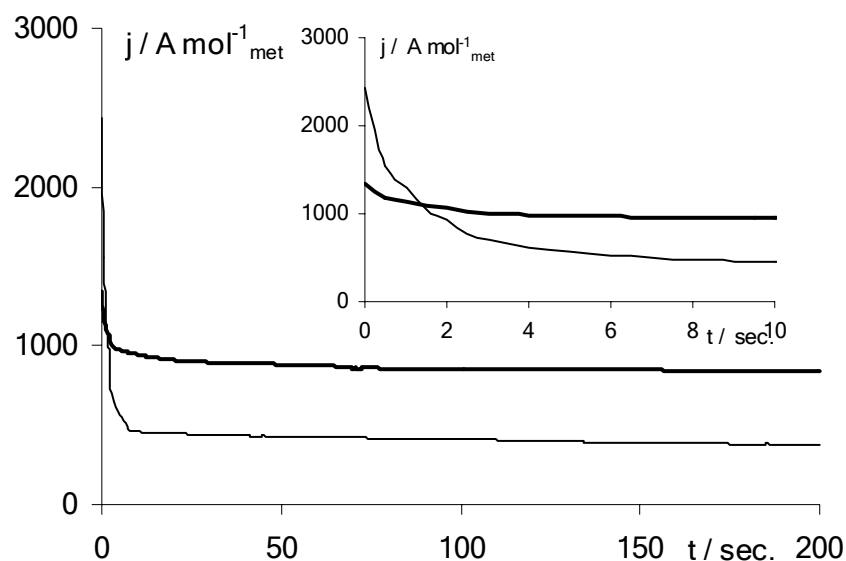

Figure 6.18: Chronoamperometric curve at 0.6 V vs. SHE for the electrooxidation of MeOH on BDD-supported microemulsion-synthesized Pt (thin line) and $Pt_{80}Ru_{20}$ (thick line) nanoparticles. Recorded in 1 M $HClO_4$ + 0.1 M CH_3OH at 25°C. **Inset:** zoom on the 0-10 s time domain.

Figures 6.19 and 6.20 summarize the results obtained for electrooxidation of methanol and ethanol, respectively, at constant potentials of 0.4, 0.5 and 0.6 V vs. SHE. On these figures are reported the measured values of specific molar oxidation currents at the end of conducted experiments (200 sec.), time for which all curves attained a current plateau. It can be seen from these two figures that, whatever the

applied potential and the used fuel are, the evolution of the "steady state" specific molar oxidation current vs. the Pt particles content exhibit similar profiles; the most active nanoparticles within those that have been synthesized are $Pt_{80}Ru_{20}$, and Pt-rich nanoparticles ($Pt_{80}Ru_{20}$ and $Pt_{60}Ru_{40}$) are more efficient than Pt. The activity then decreases with decreasing the Pt content in particles. These results are in good agreement with others from literature [29]. The reason for such behaviour is that only Pt is capable of performing the alcohol dehydrogenation steps at room temperature. It is possible to consider that the observed activities for all the synthesized particles result from the balance between alcohol adsorption ability on one hand and CO tolerance due to occurrence of both the bifunctional mechanism and the electronic effect on the other hand. According to the largely accepted mechanism of methanol electrooxidation on Pt [49], three Pt sites are necessary to adsorb one methanol molecule. Obviously with decreasing the Pt contents in Pt/Ru nanoparticles, the probability for the methanol molecule to find three neighbouring Pt sites will decreases concomitantly. Even if Ru plays an important role in the activity of Pt/Ru surfaces providing oxygenated species from water dissociation at lower potential than Pt itself, it can also hinder the adsorption of the alcohol on the surface thus dramatically lowering the activity of Pt-poor bimetallic surfaces at room temperature.

Figure 6.19: Specific molar current for MeOH electrooxidation on BDD-supported microemulsion-synthesized Pt/Ru nanoparticles. Recorded in 1 M $HClO_4$ + 0.1 M CH_3OH at 25°C at constant potentials of 0.4 (thin dashed line with cross markers), 0.5 (thin solid line with triangle markers) and 0.6 V vs. SHE (thick solid line with square markers) after 200 sec of electrolysis.

Finally, it can also been observed comparing Figs 6.19 and 6.20 that the ratio between methanol and ethanol specific molar oxidation currents on Pt/Ru surfaces is

in all cases about 3 for a given composition and applied potential. If it is supposed that the electrooxidation of MeOH on Pt and Pt/Ru nanoparticles is complete and leads to CO_2, it can be considered that 6 e$^-$ have been exchanged per methanol molecule consumed. Considering also that ethanol electrooxidation is complete and yields CO_2 as final product, the total number of exchanged electrons per ethanol molecule consumed would be 12 and therefore the expected specific molar oxidation currents for ethanol electrooxidation should be the double than those relative to methanol electrooxidation. As the specific molar oxidation currents, for all the synthesized Pt/Ru nanoparticles, for ethanol electrooxidation represent approximately the third than those for methanol electrooxidation, it can be concluded that the ethanol C-C bond has not been broken even partially on Pt/Ru nanoparticles, and that ethanol electrooxidation probably leads to C_2 intermediates, such as acetaldehyde or acetic acid, that cannot been further oxidized [45]. It must be pointed out also that there is no evidence that methanol electrooxidation effectively yields CO_2 as final product in this case; however it seems obvious that the scission of the C-C bond in ethanol is not activated on Pt/Ru nanoparticles. Consequently Pt/Ru cannot be regarded as a good electrocatalyst for ethanol oxidation.
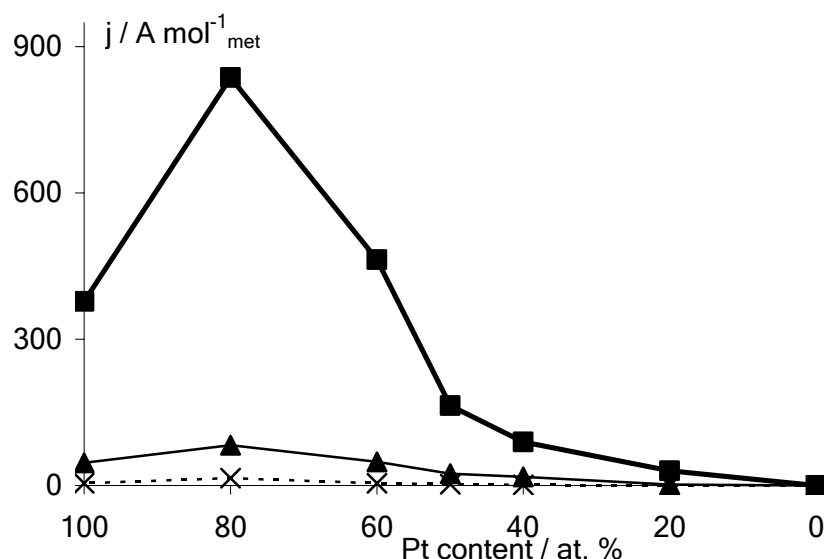

Figure 6.20: Specific molar current for EtOH electrooxidation on BDD-supported microemulsion-synthesized Pt/Ru nanoparticles. Recorded in 1 M $HClO_4$ + 0.1 M CH_3CH_2OH at 25°C at constant potentials of 0.4 (thin dashed line with cross markers), 0.5 (thin solid line with triangle markers) and 0.6 V vs. SHE (thick solid line with square markers) after 200 sec of electrolysis.

In order to further investigate both methanol and ethanol electrooxidation processes on microemulsion-synthesized Pt/Ru nanoparticles, electrochemical impedance spectroscopy (EIS) measurements have been carried out. EIS

146

experiments have been performed at potentials of 0.4 and 0.6 V vs. SHE (before and after water activation on pure Pt) both on Pt and Pt-rich ($Pt_{80}Ru_{20}$) nanoparticles, using potential modulations of 10 mV with a frequency range comprised between 100 kHz and 0.01 Hz. The aim was to obtain additional evidences of the applied potential and catalytic surface influences on the oxidation process. Figures 6.21 and 6.22 show the Nyquist plots for MeOH electrooxidation on Pt and $Pt_{80}Ru_{20}$ nanoparticles deposited on BDD at 0.4 and 0.6 V vs. SHE, respectively. The Nyquist plots recorded on Pt at 0.4 V (Fig. 6.21) exhibits a well-defined open semi-spherical shape whereas that recorded on $Pt_{80}Ru_{20}$ (inset of Fig. 6.21) exhibit the beginning of a terminal induction loop. This induction loop is also present on both the two Nyquist plots on those recorded at 0.6 V on the two different types of nanoparticles (see Fig. 6.22). Such shapes of Nyquist plots for the electrooxidation of methanol on Pt [50] and Pt/Ru [51] surfaces have already been observed in literature.

The large impedance arc for MeOH electrooxidation at 0.4 V is indicative of a slow reaction rate. It can be assumed that the slow kinetics is caused by surface poisoning by reaction intermediates (mainly CO_{ads}) that are strongly adsorbed on Pt active sites and consequently block continuous dehydrogenation of methanol. At this same potential, the diameter of the impedance arc at high frequencies is largely lower and the inductive loop appears at low frequencies on the signal recorded on $Pt_{80}Ru_{20}$. Increasing the potential up to 0.6 V (potential for which water is activated both on Pt and $Pt_{80}Ru_{20}$ nanoparticles) the diameters of the impedance arcs decrease importantly, indicating that charge-transfer resistance for methanol oxidation becomes smaller. Moreover the presence of inductive loops can be observed on both the two signals (see Fig. 6.22) and the low frequency intersect of impedance with x-axis (polarization resistance: $R_{\omega \rightarrow 0}$) also decreases when the potential increases, indicating that the overall methanol oxidation rate is faster [52]. The "pseudo-inductive" behaviour means that the current signal follows a voltage perturbation with a phase delay [53] and is generally associated with consecutive heterogeneous reactions involving adsorbed intermediates [54, 55]. This pseudo-inductive behaviour was firstly observed during corrosion tests; it was caused by pitting in the protection layer and subsequent corrosion of the metal within the holes of the protection layer. The occurrence of pseudo-inductive behaviour in the case of methanol electrooxidation can be explained similarly than the corrosion phenomenon; initially the reaction sites are covered with an adsorbed CO layer generated from methanol dehydrogenation (in analogy with the protective layer in corrosion). When the potential increases some of the weakly adsorbed CO are oxidized, producing holes in the adsorbed CO layer (similarly than the beginning of pitting). Therefore the

subsequent methanol oxidation can take place within these holes, just like the corrosion of metal in the holes of the protective layer. Consequently the Nyquist plots shape changes with increasing potential can be ascribed to the beginning of water activation that results in surface reaction between adsorbed CO and hydroxyl radicals to yield free Pt sites for further methanol adsorption. Observation of the pseudo-inductive behaviour on $Pt_{80}Ru_{20}$ at lower potentials than on pure Pt indicates that water activation occurs earlier on the alloyed nanoparticles; this can explain also the smaller values of charge-transfer resistance to methanol oxidation observed at 0.4 V on BDD-supported $Pt_{80}Ru_{20}$ nanoparticles. Moreover it must be pointed out that an electronic effect could reasonably be expected as Pt/Ru nanoparticles are alloyed ones. A weakened Pt-CO bond can also be partially at the origin of the faster kinetics for the surface reaction between CO_{ads} and oxygenated species. However, it can also be observed that when the potential is increased (0.6 V), the charge-transfer resistance to methanol oxidation becomes smaller for pure Pt nanoparticles. This indicates that, as soon as water is activated on a given surface, the alcohol adsorption properties of this surface dominate in its electrocatalytic behaviour, whereas before water activation on pure Pt the lower adsorption properties of $Pt_{80}Ru_{20}$ are counter-balanced by both the electronic effect and the bifunctional mechanism. These phenomena are not of sufficiently high importance to ensure superior activity of the alloyed surface when the surface reaction between adsorbed CO and oxygenated species can take place with appreciable kinetics on Pt. It has also be pointed out in literature that the change of shapes of the Nyquist plots as a function of the applied potential could be ascribed to involvement of adsorbed oxygenated species [56]. These observations are also in good agreement with those from CV and linear sweep voltammetry (see Figs. 6.15 and 6.16, respectively).

Figure 6.21: EIS Nyquist plot of MeOH electrooxidation on Pt (triangle markers) and $Pt_{80}Ru_{20}$ (square markers) at 0.4 V vs. SHE. Recorded in 1 M $HClO_4$ + 0.1 M CH_3OH at 25°C. **Inset**: Nyquist plot for MeOH electrooxidation on $Pt_{80}Ru_{20}$ nanoparticles.

Figure 6.22: EIS Nyquist plot of MeOH electrooxidation on Pt (triangle markers) and $Pt_{80}Ru_{20}$ (square markers) at 0.6 V vs. SHE. Recorded in 1 M $HClO_4$ + 0.1 M CH_3OH at 25°C.

Impedance measurements have also been conducted in the presence of ethanol. Figures 6.23 and 6.24 show the Nyquist plots of EtOH electrooxidation on Pt and $Pt_{80}Ru_{20}$ nanoparticles deposited on BDD at 0.4 and 0.6 V vs. SHE, respectively. It seems that both the two Nyquist plots recorded at 0.4 V (Fig. 6.23) exhibit a well-defined semi-spherical shape; however the mass transfer resistance is so high for EtOH electrooxidation on pure Pt that the semi-circle is not closed. Nyquist plots

recorded at 0.6 V (Fig. 6.24) exhibit quite different shapes. If that recorded on Pt nanoparticles is a semi-circle terminated by an inductive loop, that recorded on $Pt_{80}Ru_{20}$ can be seen as two successive semi-circles, the second one being terminated also by an inductive loop. It can be seen that, at a given potential and surface, the value of charge-transfer resistance is higher in the case of ethanol electrooxidation than for methanol electrooxidation. This indicates that methanol oxidation rate is faster than ethanol electrooxidation whatever the surface and the applied potential are; this is also in good agreement with the observed values of respective specific molar oxidation currents from CV measurements (see Fig. 6.15). However comparisons with literature data are difficult as publications dealing with impedance spectroscopy of ethanol oxidation are rare. Nevertheless an analogy can be made with the electrooxidation of 2-propanol on Pt [57]. It was suggested in this article that the use of 2-propanol in fuel cell was limited by the slow reaction rate and surface poisoning by acetone (reaction intermediate). Therefore it can be postulated here that slow kinetics and high resistances observed here in the case of ethanol electrooxidation are caused by strong adsorption of reaction intermediates (acetic acid and acetaldehyde) and that the problem of the C-C bond breaking necessary for the complete oxidation to CO_2 is still present both on Pt and $Pt_{80}Ru_{20}$ nanoparticles. This is in good agreement with results previously presented within this Chapter, from which it was concluded that the issue of the C-C bond breaking of the ethanol molecule still remains. Therefore it must be said again that Pt/Ru are not appropriate electrocatalysts of ethanol oxidation.
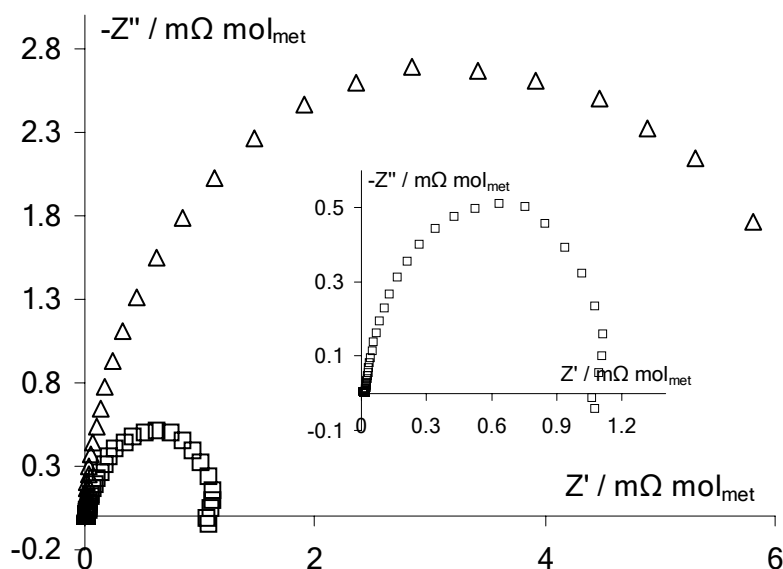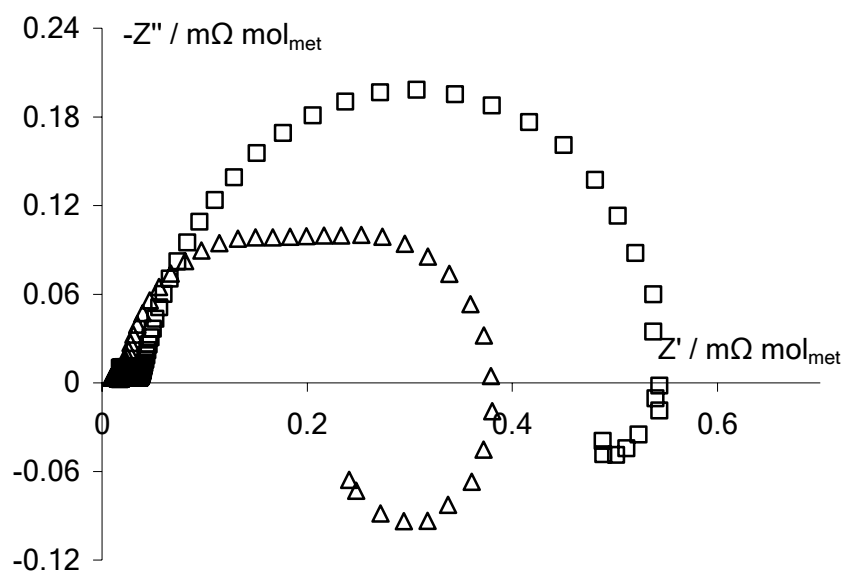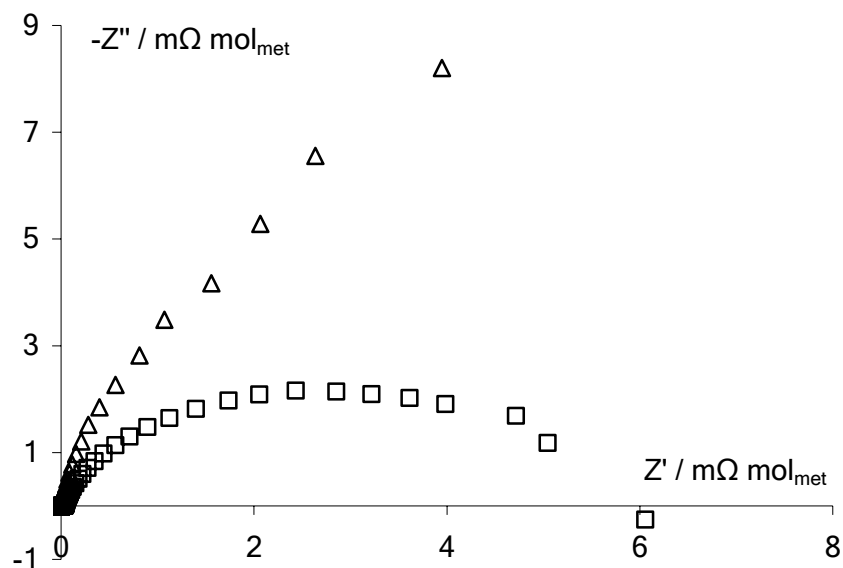
Figure 6.23: EIS Nyquist plot of EtOH electrooxidation on Pt (triangle markers) and $Pt_{80}Ru_{20}$ (square markers) at 0.4 V vs. SHE. Recorded in 1 M $HClO_4$ + 0.1 M CH_3CH_2OH at 25°C.
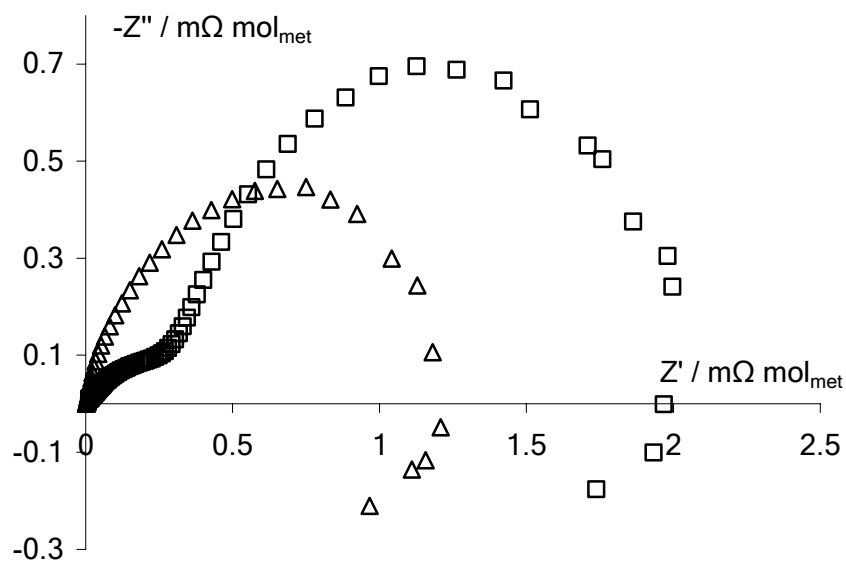
Figure 6.24: EIS Nyquist plot of EtOH electrooxidation on Pt (triangle markers), and $Pt_{80}Ru_{20}$ (square markers) at 0.6 V vs. SHE. Recorded in 1 M $HClO_4$ + 0.1 M CH_3CH_2OH at 25°C.

4. CONCLUSIONS

During this Chapter Pt/Ru nanoparticles of different compositions, synthesized following the microemulsion route, have been deposited on the BDD electrode for their electrochemical and electrocatalytic characterization. Physical characterization techniques have also been used for the study of such particles. It has been chosen to mix Pt and Ru salts in the starting microemulsions because alloys and other

bimetallic structures combining these two metals are commonly accepted in literature as the best electrocatalysts for methanol electrooxidation.

It was shown by TEM that particles were of spherical shape, with very little aggregation observable on the microscope grid and that their diameter is limited to the 2-5 nm size domain. Size distributions of the different samples were all similar and quite narrow; the observed size distributions for nanoparticles reflected those for inverse micelles in the initial microemulsions. The narrow size distributions indicate that the microemulsion method allows fine particles size control. XRD measurements have shown that Pt/Ru alloys are formed and have confirmed the order of magnitude of the diameter deduced by TEM. Atomic quantification of elements present in particles have been performed by XPS and EDX; the results obtained using both the two methods have shown that the compositions of particles are in all the cases quite close to the nominal ones (*i.e.* the ratio between metallic precursors that was initially introduced in the microemulsion). Moreover it was shown that Pt in particles was mainly metallic; the detected Pt^{II} species were presumably formed by interactions with atmospheric oxygen. Finally XPS was used to estimate an eventual "electronic effect" on Pt due to the presence of Ru; the chemical shifts of the Pt*4f* doublet to lower values of binding energies was attributed to an electronic transfer from Ru to Pt that can lead to the modification of Pt properties and weakening of the Pt-CO bond. However, due to the low values of displacements, the ligand effect could not certainly be considered as the sole origin of an eventual enhancement of the electrocatalytic activity of Pt/Ru nanoparticles.

CV recorded on BDD-supported Pt/Ru nanoparticles in pure supporting electrolyte have shown the gradual loss of Pt surface character when the Ru content is increased in the particles. More particularly the peaks attributed to H adsorption-desorption processes on Pt became worse-defined until no peaks can be attributed to these phenomena for Ru and Ru-rich nanoparticles. Such measurements gave also an idea about what would be the more appropriate surfaces for catalysis of methanol and ethanol electrooxidation. CV performed in the presence of alcohols have confirmed the results obtained in the electrolyte; the surfaces with a marked Pt surface character exhibited the higher specific molar oxidation currents both for methanol and ethanol electrooxidation, Pt being the most efficient surface. Furthermore the specific molar oxidation currents obtained in the case of ethanol electrooxidation were always lower than those for methanol electrooxidation, indicating that the C-C bond scission remains not activated onto this type of surface. However, the well-known beneficial effect of Ru addition to Pt was clearly observable in chronoamperometric and linear sweep (at slow scan rate) analyses. It was shown

by these purposes that, using bimetallic Pt-rich nanoparticles, the onset of methanol electrooxidation was appreciably shifted to lower potentials and that the tolerance to surface poisoning was greatly enhanced with a maintained activity under constant oxidative potential conditions. Further investigations on both methanol and ethanol electrooxidation processes on Pt and $Pt_{80}Ru_{20}$ nanoparticles were conducted using EIS. It was shown that the pseudo-inductive behaviour, sign of surface reaction between adsorbed CO and oxygenated species, began at lower potential on Pt/Ru than on pure Pt. It was also deduced that the electrocatalytic behaviour depends on the applied potential; as soon as water activation takes place on Pt the adsorption properties of particles are the dominating factor.

In order to summarize it can be said that the microemulsion method efficiently leads to the formation of Pt/Ru alloys nanoparticles of controlled composition and size. The Pt-rich bimetallic surfaces exhibit the better electrocatalytic activity and the higher tolerance to CO poisoning. It seemed that these effects could be attributed to the combination of the bifunctional mechanism, *i.e.* water activation on Ru at lower potentials than on Pt and of the electronic effect, *i.e.* weakening of the Pt-CO bond strength. Thus the surface reaction between adsorbed CO and oxygenated species to yield CO_2 can take place with faster kinetics. However it seems also that the issue of the C-C bond breaking in ethanol electrooxidation was not solved using Pt/Ru nanoparticles. Therefore, regarding the advantages of ethanol compared to methanol (lower toxicity, production from biomass, higher theoretical mass energy density), a new type of catalytic surface is needed for this application that is of important interest. Among all bimetallic Pt-based catalytic surfaces tested for the catalysis of ethanol electrooxidation it was shown that Pt/Sn was the most efficient one. Therefore the next Chapter will deal with the synthesis and characterization of microemulsion-synthesized Pt/Sn nanoparticles. The evaluation of their electrocatalytic activity will be more focused on the case of ethanol electrooxidation.

5. REFERENCES

[1] G. Cao, *Nanostructures & Nanomaterials. Synthesis, Properties and Applications*, Imperial College Press, London (2004).

[2] G. C. Bond, *Gold Bull.* **34** (2001), 117.

[3] R. Grisel, K.-J. Weststrate, A. Gluhoi, B. E. Nieuwenhuys, *Gold Bull.* **35** (2002), 39.

[4] T. Kobayashi, M. Haruta, H. Sano, M. Nakane, *Sensors Actuators* **13** (1988), 339.

[5]   T. Kobayashi, M. Haruta, S. Tsubota, H. Sano, B. Delmon, *Sensors Actuators B* **1** (1990), 222.

[6]   A. Hamnett, in: W. Vielstich, H. A. Gasteiger, A. Lamm (Eds.), *Handbook of Fuel Cells - Fundamentals, Technology and Applications*, John Wiley & Sons, Ltd., New York (2003), p. 305.

[7]   C. Lamy, E. M. Belgsir, in: W. Vielstich, H. A. Gasteiger, A. Lamm (Eds.), *Handbook of Fuel Cells - Fundamentals, Technology and Applications*, John Wiley & Sons, Ltd., New York (2003), p. 323.

[8]   A. Hamnett, in: A. Wieckowski (Ed.) *Interfacial Electrochemistry - Theory, Experiments, and Applications*, Marcel Dekker, Inc., New York (1999), p. 843.

[9]   M. Watanabe, S. Motoo, *J. Electroanal. Chem.* **60** (1975), 259.

[10]   M. Watanabe, S. Motoo, *J. Electroanal. Chem.* **60** (1975), 267.

[11]   M. Watanabe, S. Motoo, *J. Electroanal. Chem.* **60** (1975), 275.

[12]   S. Motoo, M. Shibata, M. Watanabe, *J. Electroanal. Chem.* **110** (1980), 103.

[13]   S. Motoo, M. Watanabe, *J. Electroanal. Chem.* **111** (1980), 261.

[14]   M. Watanabe, M. Shibata, S. Motoo, *J. Electroanal. Chem.* **187** (1985), 161.

[15]   S. Motoo, M. Watanabe, *J. Electroanal. Chem.* **98** (1979), 203.

[16]   L. Dubau, F. Hahn, C. Coutanceau, J.-M. Léger, C. Lamy, *J. Electroanal. Chem.* **554-555** (2003), 407.

[17]   N. Fujiwara, K. Yasuda, T. Ioroi, Z. Siroma, Y. Miyazaki, *Electrochim. Acta* **47** (2002), 4079.

[18]   Z. Jusys, J. Kaiser, R. J. Behm, *Electrochim. Acta* **47** (2002), 3693.

[19]   F. Richarz, B. Wohlmann, U. Vogel, H. Hoffschulz, K. Wandelt, *Surf. Sci.* **335** (1995), 361.

[20]   A. J. Dickinson, L. P. L. Carrette, J. A. Collins, K. A. Friedrich, U. Stimming, *Electrochim. Acta* **47** (2002), 3733.

[21]   M. Boutonnet, J. Kizling, P. Stenius, *Colloids Surf.* **5** (1982), 209.

[22]   I. Danielsson, B. Lindman, *Colloids Surf.* **3** (1981), 391.

[23]   J. Solla-Gullón, V. Montiel, A. Aldaz, J. Clavilier, *J. Electroanal. Chem.* **491** (2000), 69.

[24]   H. Härelind Ingelsten, R. Bagwe, A. Palmqvist, M. Skoglundh, C. Svanberg, K. Holmberg, D. O. Shah, *J. Colloid Interface Sci.* **241** (2001), 104.

[25]   I. Capek, *Adv. Colloid Interface Sci.* **110** (2004), 49.

[26]   G. Siné, Ch. Comninellis, *Electrochim. Acta* **50** (2005), 2249.

[27]   K. C. Song, J. H. Kim, *J. Colloid Interface Sci.* **212** (1999), 193.

[28]   J. Solla-Gullón, A. Rodes, V. Montiel, A. Aldaz, J. Clavilier, *J. Electroanal. Chem.* **554-555** (2003), 273.

[29]   J. Solla-Gullón, F. J. Vidal-Iglesias, V. Montiel, A. Aldaz, *Electrochim. Acta* **49** (2004), 5079.

[30]   M.-L. Wu, D.-H. Chen, T.-C. Huang, *Chem. Mater.* **13** (2001), 599.

[31]   Y. V. Pleskov, *Russ. Chem. Rev.* **68** (1999), 381.

[32]   B. El Roustom, G. Fóti, Ch. Comninellis, *Electrochem. Comm.* **7** (2005), 398.

[33]   F. Montilla, E. Morallon, I. Duo, Ch. Comninellis, J. L. Vazquez, *Electrochim. Acta* **48** (2003), 3891.

[34]   D. Gandini, E. Mahé, P.-A. Michaud, W. Haenni, A. Perret, Ch. Comninellis, *J. Appl. Electrochem.* **30** (2000), 1345.

[35]   M. Pandey, R. D'Cunha, A. K. Tyagi, *J. Alloys Compounds* **333** (2002), 260.

[36]   A. S. Aricò, P. L. Antonucci, E. Modica, V. Baglio, H. Kim, V. Antonucci, *Electrochim. Acta* **47** (2002), 3723.

[37]   H. A. Gasteiger, P. N. Ross Jr, E. J. Cairns, *J. Surf. Sci.* **67** (1993), 293.

[38]   R. Vijayalakshmi, S. Kapoor, S. K. Kulshreshtha, *Solid State Sci.* **4** (2002), 489.

[39]   J. S. Hammond, N. Winograd, *J. Electroanal. Chem.* **78** (1977), 55.

[40]   J. B. Goodenough, R. Manoharan, A. K. Shukla, K. V. Ramesh, *Chem. Mater.* **1** (1989), 391.

[41]   A. S. Aricò, P. Creti, H. Kim, R. Mantenga, N. Giordano, V. Antonucci, *J. Electrochem. Soc.* **143** (1996), 3950.

[42]   K.-W. Park, J.-H. Choi, B.-K. Kwon, S.-A. Lee, Y.-E. Sung, H.-Y. Ha, S.-A. Hong, H. Kim, A. Wieckowski, *J. Phys. Chem. B* **106** (2002), 1869.

[43]   J. Clavilier, D. Armand, *J. Electroanal. Chem.* **199** (1986), 187.

[44]   Y. Takasu, Y. Fujii, K. Yasuda, Y. Iwanaga, Y. Matsuda, *Electrochim. Acta* **34** (1989), 453.

[45]   J. M. Perez, B. Beden, F. Hahn, A. Aldaz, C. Lamy, *J. Electroanal. Chem.* **262** (1989), 251.

[46]   X. H. Xia, H.-D. Liess, T. Iwasita, *J. Electroanal. Chem.* **437** (1997), 233.

[47]   D. Cao, S. H. Bergens, *J. Power Sources* **124** (2003), 12.

[48]   T. Iwasita, E. Pastor, *Electrochim. Acta* **39** (1994), 531.

[49]   M. P. Hogarth, T. R. Ralph, *Platinum Metals Rev.* **46** (2002), 146.

[50]   R. E. Melnick, G. T. R. Palmore, *J. Phys. Chem. B* **105** (2001), 1012.

[51]   G. Wu, L. Li, B.-Q. Xu, *Electrochim. Acta* **50** (2004), 1.

[52]   I. M. Hsing, X. Wang, Y.-J. Leng, *J. Electrochem. Soc.* **149** (2002), A615.

[53]   Y.-J. Leng, X. Wang, I. M. Hsing, *J. Electroanal. Chem.* **528** (2002), 145.

[54]   R. D. Armstrong, M. Henderson, *J. Electroanal. Chem.* **39** (1972), 81.

[55]   D. A. Harrington, B. E. Conway, *Electrochim. Acta* **32** (1987), 1703.

[56]   R. E. Melnick, G. T. R. Palmore, *J. Phys. Chem. B* **105** (2001), 9449.

[57]   J. Otomo, X. Li, T. Kobayashi, C.-j. Wen, H. Nagamoto, H. Takahashi, *J. Electroanal. Chem.* **573** (2004), 99.

Chapter 7 RESULTS: Deposition of Microemulsion-Synthesized Pt/Sn Nanoparticles on BDD Electrodes for Alcohols Electrooxidation

1. INTRODUCTION

The development of new catalysts for fuel cells applications is currently a very active research field. For the Direct Alcohol Fuel Cell (DAFC), mainly fed with methanol or ethanol [1, 2], special efforts are still realized in the design of new anode catalysts. For this purpose Pt is the most efficient known catalyst; however its use is severely limited by the cost of the metal and surface poisoning that occurs during alcohols electrooxidation and blocks the catalytic surface [3]. In order to circumvent these limitations several routes are simultaneously followed: *(i)* the use of nanoparticulate materials, both to take advantage of the unique properties of nanomaterials [4] and to improve catalyst dispersion, and *(ii)* alloying Pt with another transition metal. Alloying Pt with a second metal indeed enhances the electrocatalytic activity of Pt but the reasons for such an effect are still under debate. Two approaches are currently privileged: *(i)* the so-called "bifunctional mechanism" [5] in which the second metal activates water at lower potentials that can do Pt, providing adsorbed oxygen-containing species that will react at the surface with adsorbed CO, and *(ii)* the "electronic effect" in which the Pt-CO bond is weakened by the modification of Pt electronic properties induced by the alloying metal. The most current view is that the promoting effect of alloying may involve a combination of these two effects [6]. Moreover the necessity of synthesizing a Pt-based alloy rather than a mixture between the two metals is now an open question [7].

Among all the tested bimetallic combinations, it is now well accepted that Pt/Ru is the best choice for the electrocatalysis of methanol electrooxidation [8-10]. Nevertheless electrocatalysis of ethanol electrooxidation is probably of greater interest regarding this fuel advantages compared to those of methanol (lower toxicity, production from biomass, higher theoretical mass energy density). The problem is that the complete electrooxidation of ethanol on Pt proceeds via the formation of C_2 intermediate adsorbates and needs the activation of the breaking of the C-C bond [11]. For this particular use it is now well accepted that Pt/Sn surfaces are the most appropriate catalysts. However the reasons for enhanced electrocatalytic activity of Pt/Sn toward ethanol oxidation are still unclear and results from literature can be opposite [12-16] depending on the catalyst synthesis method and working conditions.
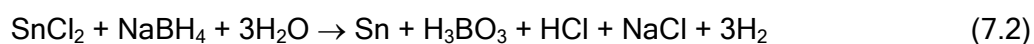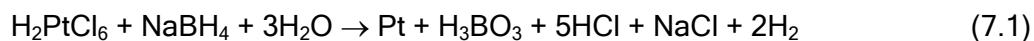
In the present Chapter, results relative to the synthesis of Pt/Sn bimetallic nanoparticles via the microemulsion route, their characterization (both physical and

electrochemical) and electrocatalytic performance toward both methanol and ethanol electrooxidation are presented. The microemulsion method is indeed well-known, since the first work of Boutonnet et al. [17], to be an efficient and simple way to prepare metal and metallic nanoparticles with narrow size distribution. A microemulsion provides compartmentalized nanoreactors (the inverse micelles) in which a chemical reaction, for instance the reduction of a metallic precursor, can take place. This method has been successfully used for the synthesis of metallic nanoparticles including metals [18-21], metal oxides [22] or alloys [23-25]. However, the synthesis of Pt/Sn nanoparticles using the microemulsion method has not been reported yet to the best of our knowledge. Particles electrochemical and electrocatalytic characterization have been performed once deposited on a BDD substrate, that has been chosen due to its remarkable properties of chemical inertness, low background current and mechanical resistance to chemical and electrochemical attacks [26]. Due to these properties the BDD electrode has used for the study of supported particles [21, 27, 28], avoiding the problems encountered with other common substrates (corrosion, oxide formation...). Physical characterization has been performed by means of TEM, XRD, EDX and XPS measurements and electrochemical and electrocatalytic characterizations using cyclic and linear sweep voltammetries, chronoamperometry and impedance spectroscopy.

2. EXPERIMENTAL

2.1. Nanoparticles synthesis

Platinum/Tin nanoparticles were obtained by reduction of a mixture of H_2PtCl_6 (Fluka) and $SnCl_2$ (Riedel-de-Haën) with sodium borohydride in a w/o microemulsion of water / tetraethyleneglycol-monododecylether (BRIJ$^{®}$ 30) / n-heptane, following Equations 7.1 and 7.2:

$$H_2PtCl_6 + NaBH_4 + 3H_2O \rightarrow Pt + H_3BO_3 + 5HCl + NaCl + 2H_2 \qquad (7.1)$$
$$SnCl_2 + NaBH_4 + 3H_2O \rightarrow Sn + H_3BO_3 + HCl + NaCl + 3H_2 \qquad (7.2)$$

As in the case of Pt/Ru nanoparticles (Chapter 6) it has been chosen to perform the reduction using solid sodium borohydride rather than hydrazine dissolved in a w/o microemulsion of same formulation because sodium borohydride is a more powerful reducing agent that will avoid competition between reactions 7.1 and 7.2 and yield true bimetallic particles. The microemulsions were prepared using ultra-pure water (Millipore$^{®}$). BRIJ$^{®}$ 30 and n-heptane were purchased from Fluka and Riedel-de-Haën, respectively, and used as received. The metallic precursors were dissolved into the aqueous phase of one microemulsion that has a water-to-surfactant molar

ratio (ω_0) of 3.8. The surfactant represented 16.54 % of the volume of the microemulsion, and the aqueous phase was constituted of mixtures of 0.1 M solutions of the metallic salts. Relative amounts of the precursors solutions were adjusted depending on the desired particle final composition. Pt/Sn bimetallic particles of 80, 60, 50, 40, and 20 atomic percents in Pt were synthesized, in addition of Pt particles. From a practical point of view, the surfactant and n-heptane were first mixed. Then the aqueous phase was slowly added and the solution vigorously stirred. This results in a transparent, homogeneous solution which colour changes from pale yellow to dark brown increasing Sn content. Conditions for the synthesis of the Pt/Sn particles by the microemulsion method are summarized in Table 7.1.

	Pt/Sn nanoparticles
Vol. % surfactant	16.54
Vol. % n-heptane	80.46
Vol. % H_2O	3
$[PtCl_6^{2-}]_{aq}$ / M	0.1
$[SnCl_2]_{aq}$ / M	0.1
$[NaBH_4]_{aq}$ / M	1
$[NaBH_4]_{aq}/[metal\ ions]_{aq}$	10

Table 7.1: Experimental parameters for the synthesis of Pt/Sn nanoparticles using the microemulsion method.

The synthesis was realised adding to the microemulsion the amount of solid $NaBH_4$ necessary to yield a concentration of 1 M in the aqueous phase. The general scheme of Pt/Sn nanoparticles synthesis is presented in Figure 7.1. It involves the following steps: (**1**) mixing of the microemulsion with the solid reducing agent that diffuses into the inverse micelles to react with the metallic precursors, (**2**) nucleation and (**3**) growth of the particles into the interior of the inverse micelles. Growth of the particles was stopped by the surfactant layer that stabilises the aqueous dispersion.

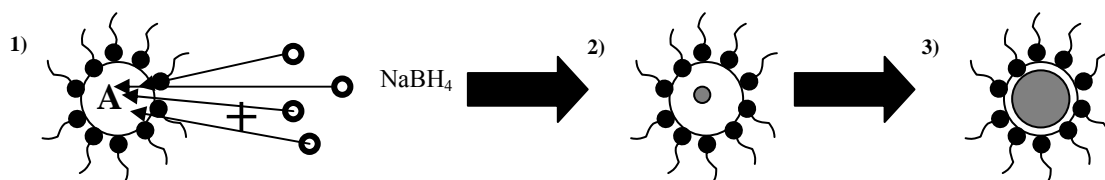**Figure 7.1**: General scheme for the synthesis of Pt/Sn particles adding a solid reducing agent to a microemulsion. Steps of the process: **1)** mixing of the microemulsion with solid $NaBH_4$, diffusion into the inverse micelles and reaction, **2)** nucleation and **3)** growth of the particles. A = H_2PtCl_6 + $SnCl_2$(aq.) in appropriate ratios, aqueous droplets dispersed in n-heptane and stabilized by a BRIJ®-30 layer.

After complete reduction, that needs only a few minutes and is evidenced by colour change to dark black, acetone was added to the solution to cause phase separation and precipitation of the particles. The precipitate was rinsed several times with acetone and ultra-pure water, and then centrifuged for a few minutes to eliminate most of the surfactant. Finally particles were put in a small volume of ultra-pure water as a suspension. The Pt contents of this final aqueous suspension were determined using AAS.

2.2. BDD-Pt/Sn electrode preparation

BDD films were synthesised by the hot filament chemical vapour deposition technique (HF-CVD) on single crystal p-type Si <100> wafers (1-3 mΩcm, Siltronix). The doping level of boron expressed as B/C ratio was about 3500 ppm. The obtained diamond film thickness was about 1 µm with a resistivity in the range 10-30 mΩcm. This as-grown BDD contains some graphitic (sp^2) phase and is hydrogen terminated. Activation of BDD by anodic polarization (10 mA cm^{-2} in 1 M H_2SO_4 at 25 °C during 30 min) eliminates most of the sp^2 and adsorbed hydrogen from the surface, and is necessary to obtain reproducible electrochemical measurements [29]. Pt/Sn nanoparticles were deposited onto the BDD substrate putting a droplet (5 µl) of the suspension onto diamond. The excess water was dried under nitrogen atmosphere. The BDD-Pt/Sn electrode was then transferred to the electrochemical cell for measurements.

2.3. Measurements

Electrochemical measurements were conducted using the conventional three-electrode cell described in Chapter 3, with BDD-supported Pt nanoparticles as working electrode (exposed area of diamond: 0.4 cm^2), Hg/Hg_2SO_4.K_2SO_4(sat.) as reference and a platinum wire as counter electrode. All potentials reported here are plotted with respect to the Standard Hydrogen Electrode (SHE). All solutions were made in ultra-pure (Millipore® system) water using analytical grade reactants without further purification. Before any experiment the solution was saturated with nitrogen gas and measurements were conducted under a nitrogen atmosphere.

Physical characterization of particles was conducted by means of TEM, XPS and XRD, using the methods and apparatus described in Chapter 3. For TEM analysis, a small droplet of the particles suspension was put on an amorphous carbon-coated copper grid; the excess water was then removed and the grid placed in the vacuum chamber of the microscope in order to be analyzed. XRD measurements of particles were carried out with particles deposited on a BDD substrate, whereas XPS analyses

were performed using a gold substrate. Deconvolution of the peaks of interest in XPS spectra (Pt$4f$ and Sn$3d$) was done using the CasaXPS® computer program.

3. RESULTS AND DISCUSSION

3.1. Pt/Sn nanoparticles characterization

Several different types of bimetallic Pt/Sn particles have been synthesized via the microemulsion method, adjusting the ratio of metallic precursors dissolved in the initial microemulsion aqueous phase. The following particles, labelled according to their theoretical atomic contents, have been synthesized: $Pt_{80}Sn_{20}$, $Pt_{60}Sn_{40}$, $Pt_{50}Sn_{50}$, $Pt_{40}Sn_{60}$, $Pt_{20}Sn_{80}$, and Pt. All these particles have been characterized by TEM. The synthesis of pure Sn particles could not be achieved, either mixing a $SnCl_2$ microemulsion with solid sodium borohydride or with a hydrazine microemulsion. It has been claimed by certain authors that Pt microcrystals catalyse the decomposition of $NaBH_4$ [30] so that the presence of Pt is certainly necessary to perform the co-reduction of Sn. Figure 7.2 shows as representative examples TEM micrographs of Pt (Fig. 7.2.A), $Pt_{60}Sn_{40}$ (7.2.B) and $Pt_{20}Ru_{80}$ nanoparticles (7.2.C). It can be seen on these pictures that particles are present on the copper grid as small isolated and well-spherical units, of diameter in the 2-5 nm range that corresponds well of the definition of a nano-object in electrocatalysis.

Moreover, the size distributions of all the synthesized Pt/Ru nanoparticles have been established on the basis of TEM measurements on more than 100 individual particles in each case. The size distributions of all the synthesized Pt/Sn nanoparticles are presented in Figure 7.3. It can be seen on Fig. 7.3 that all size distributions are quite close one of the others; all synthesized Pt/Sn nanoparticles exhibit quite narrow distribution with diameter included approximately between 1.5 and 4.5 nm. The low broadness of size distributions reflects the non-homogeneity of inverse micelles in the starting microemulsions due to small probable experimental fluctuations in their preparation; however the similarities between size distributions are indicative of the repeatability of the synthesis procedure. Moreover it is the sign that the composition of the aqueous phase does not influence the size of the obtained nanoparticles. The key parameter in the size control of the nanoparticles prepared following the microemulsion route is the value of the water-to-surfactant molar ratio (ω_0), and hence fine control of microemulsion-synthesized nanoparticles size can be achieved using a correctly formulated microemulsion template.
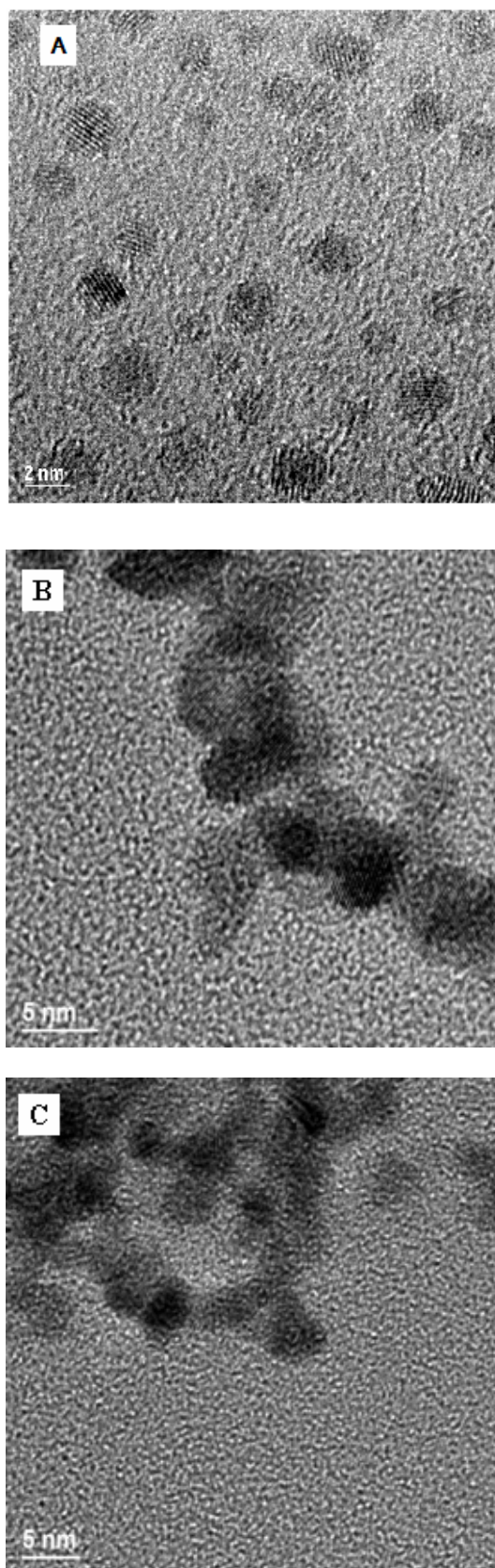
Figure 7.2: TEM micrographs of Pt (**A**), $Pt_{60}Sn_{40}$ (**B**) and $Pt_{20}Sn_{80}$ (**C**) nanoparticles synthesized via the microemulsion method.
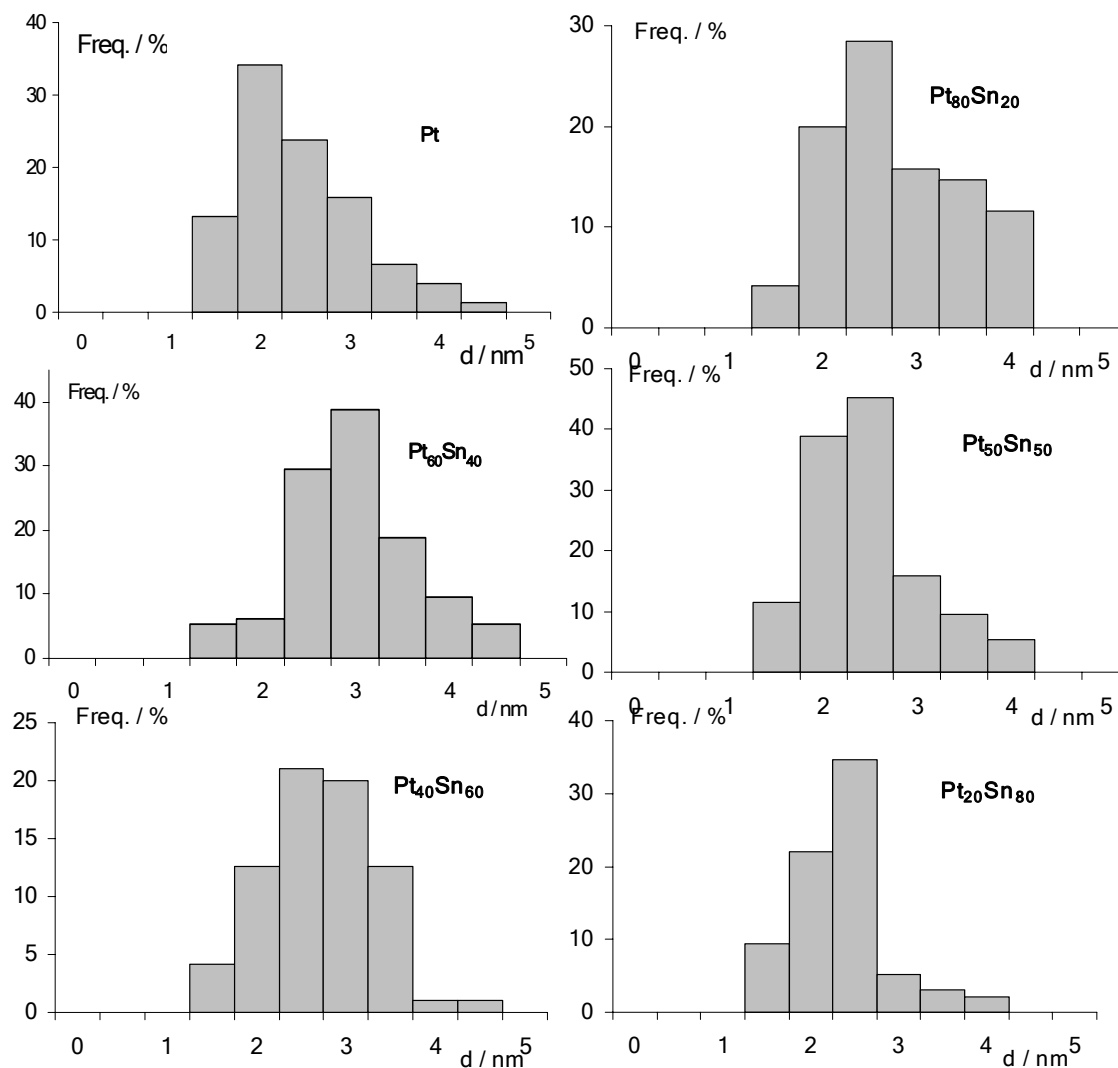
Figure 7.3: Size distributions of microemulsion-synthesized Pt/Sn nanoparticles determined by TEM.

The crystalline structure of microemulsion-synthesized Pt/Sn nanoparticles has been investigated by XRD. Figure 7.4 shows the XRD patterns of all the synthesized Pt/Sn particles deposited on a BDD substrate. The peaks ascribable to the typical Pt fcc structure are listed on Fig. 7.4. The other main peaks observable on spectra presented in Fig. 7.4 can be attributed to the (111) and (220) planes of diamond (44° and 75.3°), to the (400) plane of silicium (70°) [31], and to the (101), (200), (112), (211) (202) and (213) planes of Sn (located at 2θ values of 33.1, 56.5, 61.8, 66, 66.5 and 86.7°, respectively) [32]. The (220) contribution of Sn is completely hidden by the (400) Si signal. It can be seen on Fig. 7.4 that the signal ascribed to Pt is not altered by the gradual addition of Sn in the particles; both (111) and (200) bands of Pt are well-defined and discernable on all the spectra. This indicates that there is no loss of crystallinity in the Pt lattice and that two different crystalline phases coexist in the

particles. Consequently it should be considered that in the case of Pt/Sn, the microemulsion route leads to bimetallic nanoparticles rather than true alloys. Pt/Sn particles are certainly composed of separated crystalline islands of Pt on one hand and Sn on the other hand.
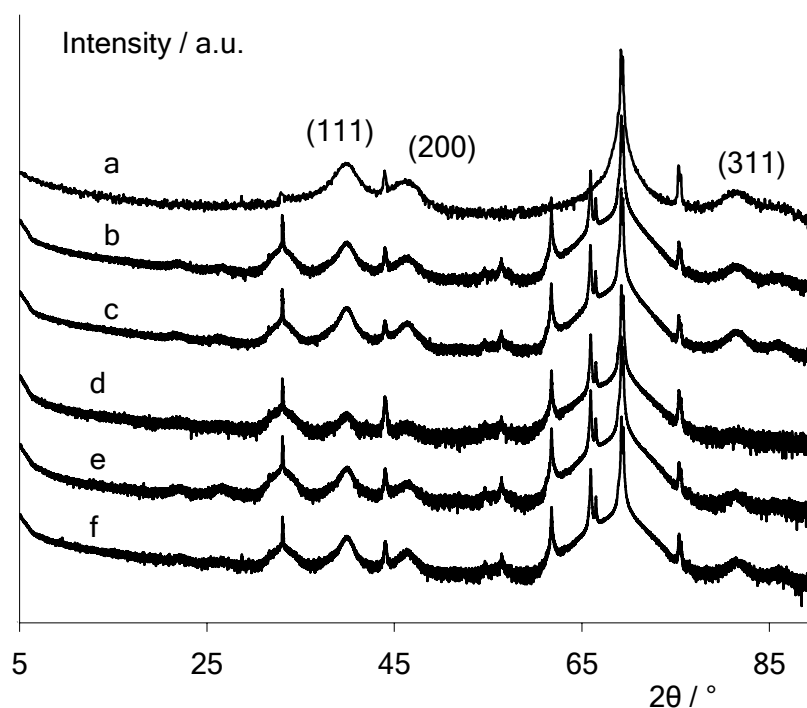

Figure 7.4: XRD spectra of microemulsion-synthesized Pt/Sn nanoparticles deposited on BDD; (a): Pt, (b): $Pt_{80}Sn_{20}$, (c): $Pt_{60}Sn_{40}$, (d): $Pt_{50}Sn_{50}$, (e): $Pt_{40}Sn_{60}$ and (f): $Pt_{20}Sn_{80}$ nanoparticles.

The effectiveness of alloy synthesis was also checked regarding the band displacements of Pt (111) and Pt (200) XRD reflections. Figure 7.5 shows, as typical examples, the positions of these reflection bands in Pt, $Pt_{80}Sn_{20}$ and $Pt_{50}Sn_{50}$ nanoparticles deposited on BDD. It can be seen on this picture that no band displacement can be observed for both contributions. These band displacements have been attributed to alloy formation in the case of Pt/Ru surfaces [33]. Therefore the absence of displacement indicates that bimetallic nanoparticles are synthesized rather than true alloys. This is also in good agreement with hypotheses of conservation of Pt crystallinity and coexistence of two distinct crystalline phases in the samples, made from Fig. 7.4. The existence of a bimetallic surface rather than an alloy does not make the determination of the lattice parameter (Vegard's law) and of the mean diameter of the synthesized nanoparticles consistent. However, the question of the necessity of alloying metals instead of just mixing them is now under debate [7] so that the fact that Pt/Sn nanoparticles are not true alloys seems not to be a limitation to their use as electrocatalysts. Finally it must be said that an electronic

effect between Sn and Pt would not be expected to be effective (or at least with a low magnitude compared to the bifunctional mechanism) due to the unalloyed nature of particles.
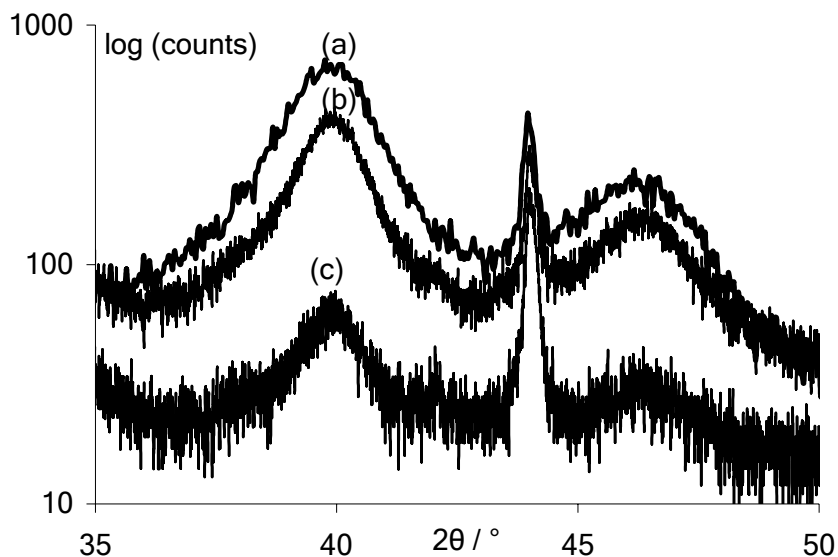

Figure 7.5: XRD patterns of microemulsion-synthesized Pt (a), $Pt_{80}Sn_{20}$ (b) and $Pt_{50}Sn_{50}$ (c) nanoparticles deposited on BDD.

The mean diameter of all the synthesized Pt/Sn bimetallic nanoparticles has consequently been determined only on the basis of TEM measurements. Figure 7.6 shows the mean diameter of Pt/Sn nanoparticles, based on measurements carried out on more than one hundred particles in each case, as a function of the Pt atomic content in the samples. For all the synthesized samples the mean diameter of nanoparticles is included in the 2-3 nm size range. Fluctuations between diameters of different types of particles may be attributed to little variations in the experimental conditions of synthesis, *i.e.* in some little differences in the practical formulation of the starting microemulsions that can influence the molar water-to-surfactant ratio (ω_0) and therefore the size of the aqueous nanodroplets dispersed in the organic phase. Fig. 7.6 does not give any evidence of influence of the aqueous phase composition (ratio of metallic salts introduced in the initial microemulsions) on the size of the resulting nanoparticles; this supports the view that the key parameter in the control of particles size is the control of ω_0.
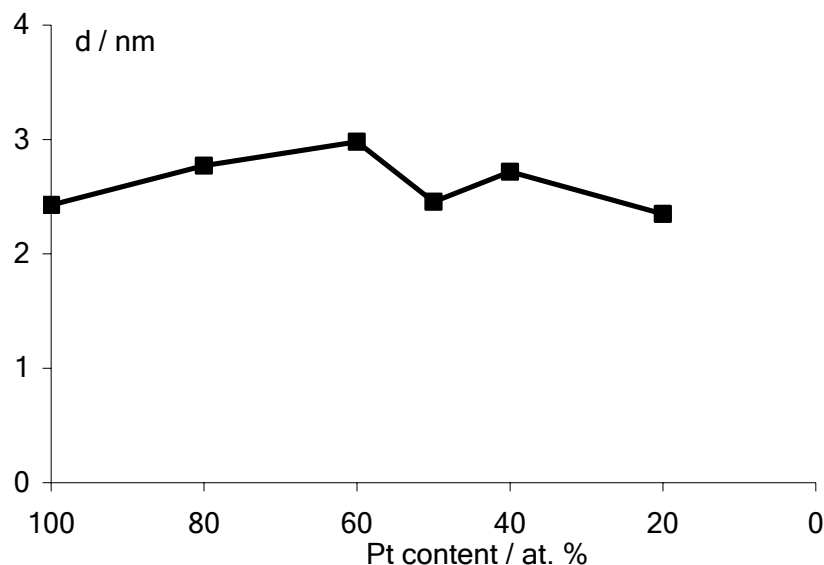
Figure 7.6: Mean diameter of microemulsion-synthesized Pt/Sn nanoparticles determined by means of TEM measurements.

Pt/Sn nanoparticles have also been physically characterized by XPS. Figure 7.7 shows as a typical example the XPS survey spectrum of $Pt_{50}Sn_{50}$ nanoparticles supported on a gold substrate. The presence of both Pt$4f$ (70-80 eV) and Sn$3d$ (485-500 eV) contributions can be observed on this spectrum. Peaks due to O $1s$ and C $1s$ can be ascribed to interactions with atmospheric species and the presence of some remaining surfactant, respectively, whereas Au$4f$ peak is caused by the substrate. XPS has also been used as an atomic quantification tool in order to determine if particles compositions correspond to nominal ones (*i.e.* ratios that were introduced in the aqueous phases of the starting microemulsions). Such quantitative analysis has also been conducted by EDX measurements performed during TEM analysis. Both XPS and EDX quantitative analysis results are reported in Table 7.2. It can be seen from this table that, for all the synthesized Pt/Sn particles, the determined compositions by both these two experimental techniques are in good agreement with theoretical ones, indicating the suitability of this synthesis method for obtaining Pt/Sn particles of controlled compositions. For simplicity, all particles are labelled during the next sections according to their nominal compositions, whereas all specific molar currents calculations have been performed with respect to the compositions determined experimentally by XPS.
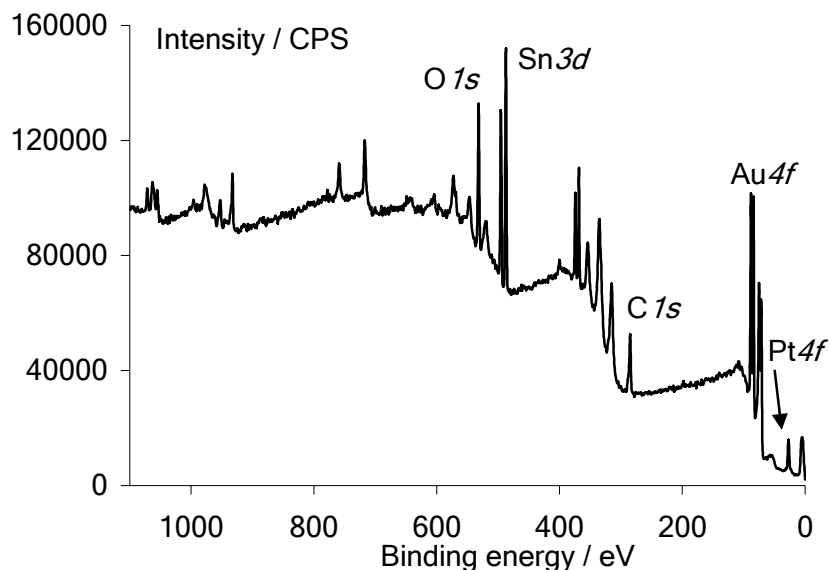
Figure 7.7: XPS survey spectrum of $Pt_{50}Sn_{50}$ nanoparticles deposited on a gold substrate.

Nominal Pt content / at. %	XPS Pt content / at. %	EDX Pt content / at. %
100	100	100
80	83.2	77.4
60	63.9	59.2
50	53.6	54.6
40	42.8	38.7
20	23.8	17.6

Table 7.2: Atomic composition of bimetallic microemulsion-synthesized Pt/Sn nanoparticles determined by means of XPS and EDX.

The XPS Pt$4f$ and Sn$3d$ doublets have also been deconvolved using the CasaXPS® software to determine the metals oxidation states in particles. Figures 7.8 and 7.9 show the deconvolved signals of Pt$4f$ and Sn$3d$ contributions, respectively, of $Pt_{50}Sn_{50}$ nanoparticles deposited onto a gold substrate. The Pt$4f$ signals is composed by four individual peaks; peaks (1) and (2) can be attributed to Pt$4f_{7/2}$ and Pt$4f_{5/2}$ lines of metallic Pt (Pt^0), respectively, whereas peaks (3) and (4) can be attributed to Pt$4f_{7/2}$ and Pt$4f_{5/2}$ lines of Pt^{II} present for instance in PtO or Pt(OH)$_2$ [34]. The ratio between metallic (0) and oxidized (+II) forms of Pt was about 4:1 for all the synthesized nanoparticles. The Sn$3d$ signal exhibits two well-defined isolated peaks; peak (1) located at approximately 487 eV can be attributed to the Sn$3d_{5/2}$ contribution and peak (2) at 496 eV to the Sn$3d_{3/2}$ contribution of Sn^{II} [35, 36]. It must be pointed out that discrimination between signals of Sn^{II} and Sn^{IV} is often difficult to carry out.

167

However it seems obvious in this case that Sn is present in particles in an oxidized form.
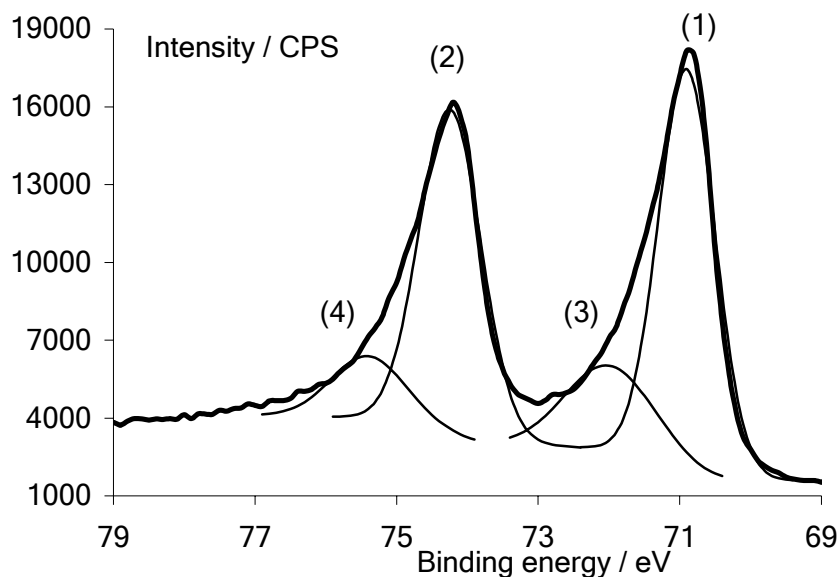

Figure 7.8: Deconvolved XPS Pt*4f* signal of microemulsion-synthesized $Pt_{50}Sn_{50}$ nanoparticles deposited on Au substrate.
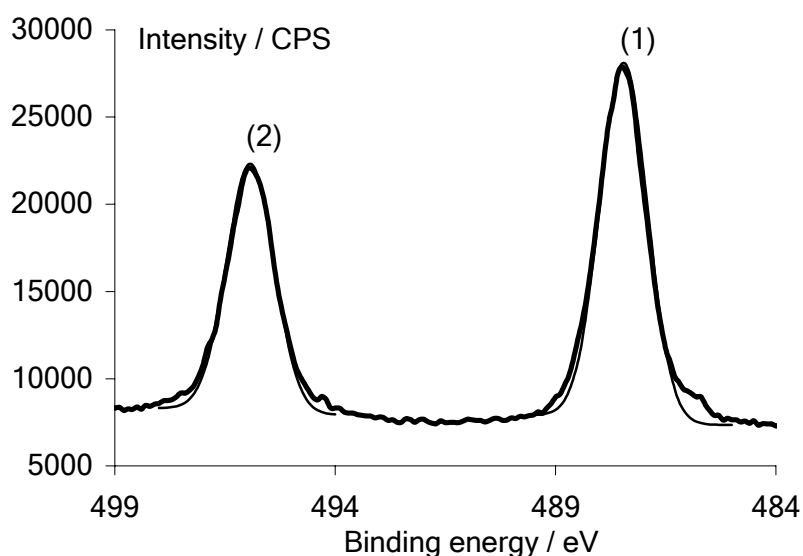
Figure 7.9: Deconvolved XPS Sn*3d* signal of microemulsion-synthesized $Pt_{50}Sn_{50}$ nanoparticles deposited on Au substrate.

XPS analysis was also used in order to evidence some electronic interactions between the two metals in the particles. For this purpose the position of the Pt*4f$_{7/2}$* (Pt^0) line in the different Pt/Sn nanoparticles was compared (see Figure 7.10) to that observed for Pt. It can be seen from Fig. 7.10 that this line is shifted to lower values of binding energies in bimetallic particles compared to that of pure Pt. This is indicative of e$^-$ d transfer from Sn to Pt [37], due to the difference of

electronegativities between the two metals (χPt = 2.2, χSn = 1.8). The larger chemical shift observed in the case of these Pt/Sn bimetallic nanoparticles than in the case of Pt/Ru alloys nanoparticles (see Fig. 6.11) can be attributed to the larger difference in electronegativities between Pt and Sn than between Pt and Ru (χRu = 2.2). Such an electron transfer is of great importance because it modifies the Pt work function and induces weakening of the Pt-CO bond, being at the origin of the so-called electronic effect. The electronic effect is a possible reason for enhanced electrocatalytic activity of bimetallic surfaces compared to Pt. Therefore a possible enhancement in electrocatalytic activity of Pt/Sn nanoparticles compared to pure Pt could be ascribed to the combination of the bifunctional mechanism and the ligand effect. It can also been observed that the higher the Sn content in the sample, the higher the XPS chemical shift and therefore the higher the electronic effect of Sn on Pt. However it must be pointed out that Pt/Sn nanoparticles are not true alloys so that the electronic transfer certainly only concerns Pt and Sn atoms that are located at the interface between islands of the two metals. Therefore the electronic effect would certainly be of lower importance than the cooperative effect. However the magnitude of this electronic effect (if any) would greatly be dependant on the "degree of mixture" between the two metals, *i.e.* on the dispersion of the two metals.

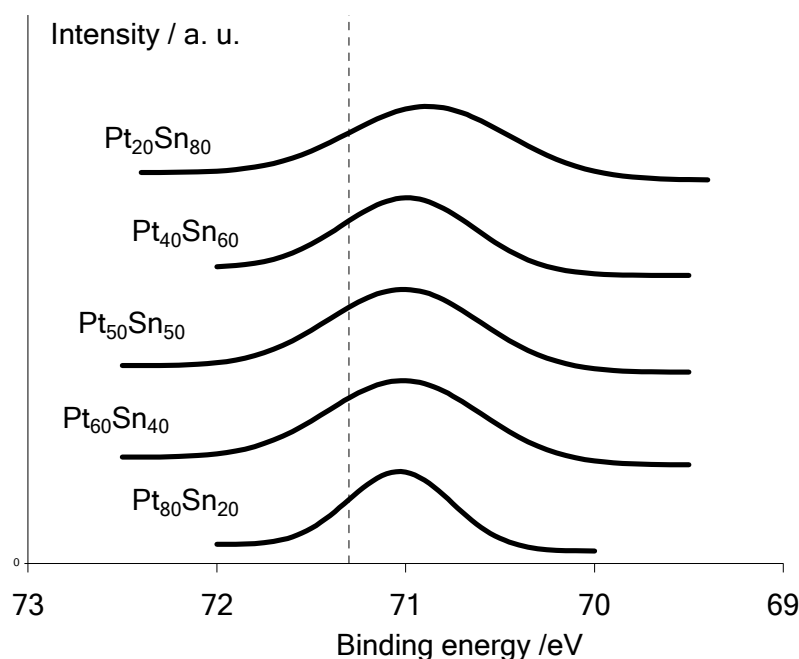**Figure 7.10**: Chemical shift of the XPS Pt$4f_{7/2}$ line of bimetallic microemulsion-synthesized Pt/Sn nanoparticles deposited on Au substrate. The vertical dashed line represents the position of the Pt$4f_{7/2}$ line of pure Pt nanoparticles.

Obviously in the case of analysis of objects of dimensions as low as 3 nm, XPS can no longer be considered as a surface analysis tool as all the depth of the sample will be probed. Therefore XPS gives in this case information about the whole volume of nanoparticles and not only on their surface. CV thus appears to be a more powerful method for investigating the surface state of Pt/Sn nanoparticles. Moreover the use of BDD as substrate electrode allows avoiding most of the problems that can be encountered with common substrates (oxides formation, surface corrosion...). Figure 7.11 shows the CV of all the synthesized Pt/Sn bimetallic nanoparticles deposited on BDD, recorded in 1 M $HClO_4$ at a scan rate of 50 mV s^{-1} and room temperature. As it has been observed in the case of Pt/Ru nanoparticles deposited on BDD (see Chapter 6), increasing the amount of the second metal in the bimetallic nanoparticles results in the decrease of the Pt character of the surface. It can indeed be seen on the CV presented in Fig. 7.11 that the higher the Sn content in the bimetallic particles, the lower the peaks resolution in the H adsorption-desorption region on Pt. Two distinct waves are still discernable for $Pt_{80}Sn_{20}$ nanoparticles, whereas as soon as the Pt content is decreased to 60 at. % only one small bump can be observed. Another remarkable trend is that the current in the double-layer region is increased as soon as Sn is added to Pt. The low double-layer capacitance observed for pure Pt nanoparticles is also indicative of low contribution of the substrate electrode, thus justifying the choice of BDD for the electrochemical study of supported particles. As this double-layer region corresponds to the potential domain for which water can be activated this means that water activation can take place at lower potential values on bimetallic Pt/Sn surfaces than on pure Pt. The shapes of these CV allow assumptions on the more efficient electrocatalysts for methanol and ethanol oxidation. As Pt is the only metal capable of alcohol dehydrogenation, $Pt_{80}Sn_{20}$ nanoparticles seem to be the most promising ones for these applications. It must be also pointed out that the electronic effect of Sn on Pt evidenced in Fig. 7.10 can play a role and that the electrocatalytic activity of given nanoparticles may depend on the balance between adsorption properties on one hand, and electronic interactions and cooperative effect between the two metals on the other hand. It is also important to note that potential limits in the anodic direction were chosen in order to avoid Pt oxides formation and the concomitant aggregation of particles [38], surface reorganization [39] or dissolution of the second metal. Finally it must be pointed out that, within the fixed potential limits used here, the amplitude of the different CV remained constant, indicating stability of the deposited nanoparticles on the diamond substrate.
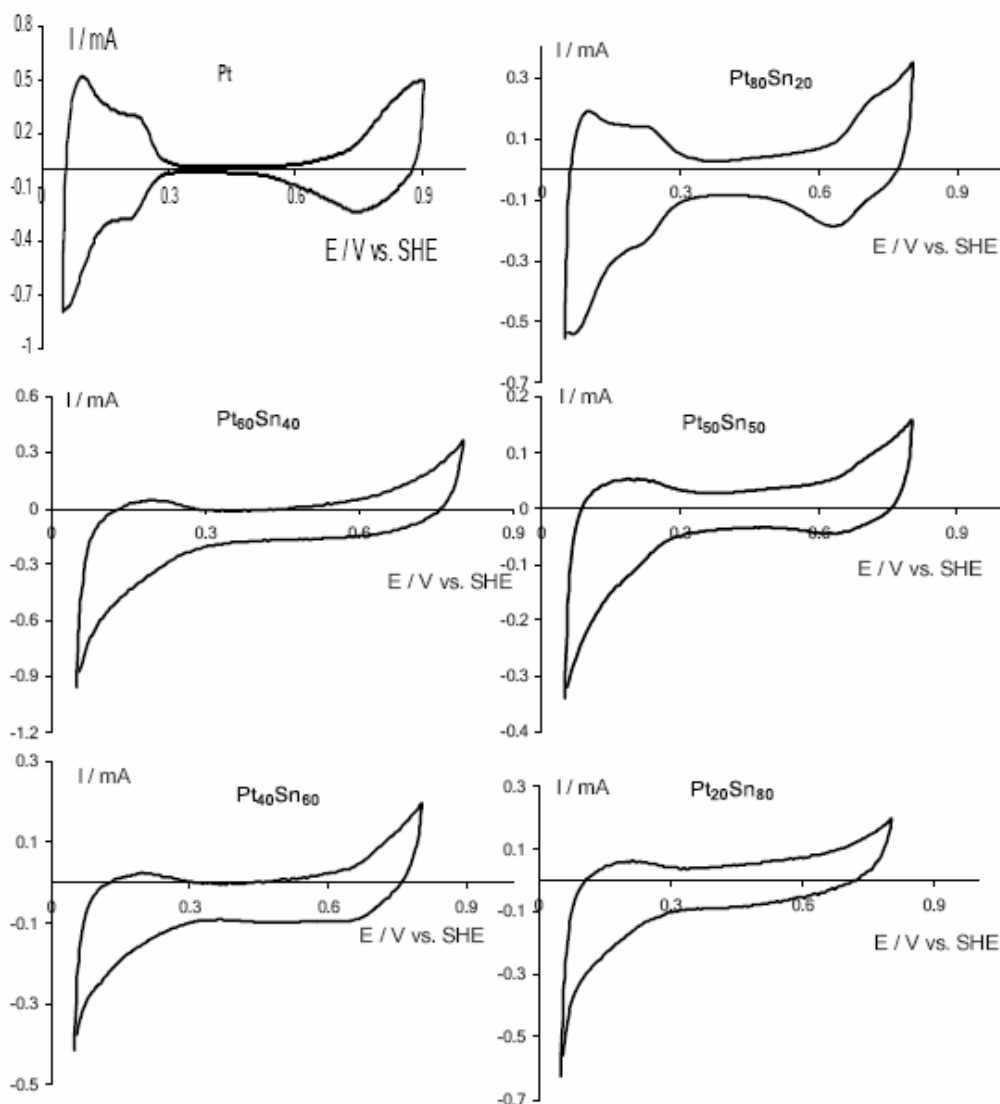
Figure 7.11: CV of microemulsion-synthesized Pt/Sn nanoparticles deposited on BDD. Recorded in 1 M $HClO_4$ at a scan rate of 50 mV s^{-1}, T = 25°C.

In order to summarize this characterization part, it can be said that the microemulsion method effectively leads to Pt/Sn nanoparticles of controlled composition and of diameter around 2-3 nm with narrow size distribution. It has been shown by XRD measurements that bimetallic Pt/Sn particles were formed rather than true alloys as it was the case for Pt/Ru particles (see Chapter 6). It was also shown by means of XPS that the presence of Sn in the particles induced a large chemical shift of the Pt*4f* doublet position to lower values of binding energies. This can be attributed to an electronic transfer from Sn to Pt that modifies Pt electronic properties (work function) and implies weakening of the Pt-CO bond. The larger values of chemical shifts observed in the case of Pt/Sn nanoparticles than for Pt/Ru nanoparticles could be ascribed to the larger difference in electronegativity between

Pt and Sn than between Pt and Ru. However electrochemical characterization of the particles is more informative on the surface state of objects of dimensions as low as 3 nm in diameter than XPS that will explore the whole depth of particles. CV of all the synthesized BDD-supported Pt/Sn nanoparticles were recorded in pure supporting electrolyte (HClO$_4$ 1 M). It was observed on these voltammograms that, as in the case of Pt/Ru nanoparticles, the increase of the second metal content results in the lowering of the quality of the H adsorption-desorption features of pure Pt. This is indicative of gradual decrease of Pt from the surface and continuous transition of particles from Pt character to Sn character as Sn is increased in the nanoparticles.

3.2.   Electrocatalytic characterization

The bimetallic Pt/Sn nanoparticles synthesized have also been electrocatalytically characterized. For this purpose the same electrochemical set-up than those described in preceding Chapters was used. Measurements were conducted at room temperature in deaerated (saturated with N$_2$) solutions of 1 M HClO$_4$ + 0.1 M alcohol made from analytical grade products. The Pt content in the different Pt/Sn nanoparticles suspensions was determined by AAS. The specific molar currents calculated here are plotted with respect to the total amount of deposited metals on the diamond substrate deduced from both AAS experiments and elemental quantification obtained from XPS. However for simplicity Pt/Sn nanoparticles are labelled according to their theoretical compositions.

Figure 7.12 presents the CV for methanol and ethanol electrooxidation on Pt nanoparticles deposited on BDD. These CV exhibit the characteristic features of methanol and ethanol electrooxidation on Pt, *i.e.* two well-defined oxidation peaks, one occurring in the forward scan and the second one during the reverse scan. This is due to the Pt surface transitions that occur during potential cycling. At potential as low as 0.05 V vs. SHE, methanol is readily dehydrogenated on metallic Pt; consequently the surface is blocked by adsorbed intermediated (mainly CO in the case of methanol) and the specific molar current is very low. At approximately 0.4-0.5 V water is activated and therefore surface reaction between adsorbed CO and $^\cdot$OH can take place; Pt sites are again available for further dehydrogenation steps and the specific molar current increases. After Pt oxides formation, the specific molar current decreases leading to the first peak because Pt oxides are not capable of alcohol adsorption. During the reverse scan Pt oxides are reduced into metallic Pt that can dehydrogenate again. Finally the specific molar current decreases again due to surface poisoning as soon as water is not activated. As already stated during Chapters 5 and 6 of this thesis, the difference in activities toward methanol and

ethanol electrooxidation is due to the inability of Pt to promote the ethanol molecule C-C bond scission. Therefore the finding of catalyst that activates the C-C bond breaking has been one of the major challenges for the development of DAFC fed with ethanol [40-42] or 2-propanol [43, 44] for instance.
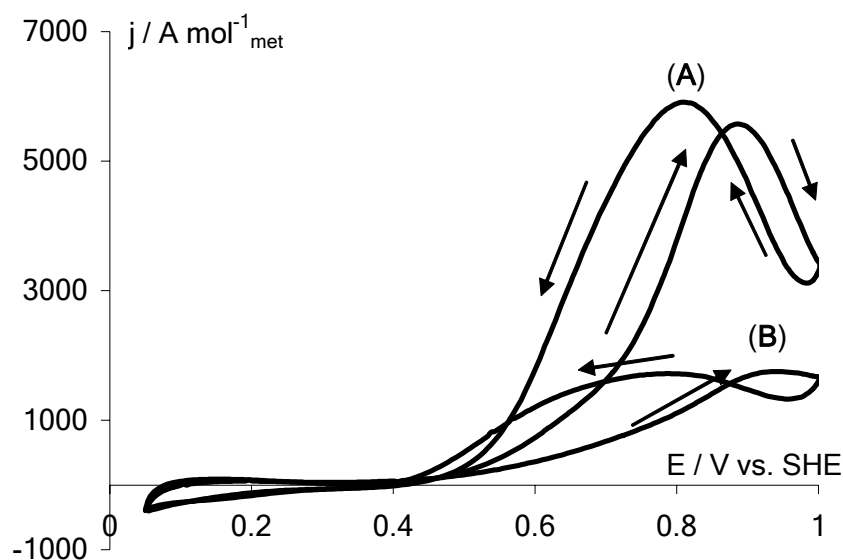

Figure 7.12: CV of MeOH (**A**) and EtOH (**B**) electrooxidation on BDD-supported microemulsion-synthesized Pt nanoparticles. Recorded in 1 M $HClO_4$ + 0.1 M Alcohol at 20 mV s^{-1} and 25°C.

Similar experiments have also been conducted on all the synthesized Pt/Sn nanoparticles. Figure 7.13 shows, as a typical example, the CV of methanol and ethanol electrooxidation at microemulsion-synthesized $Pt_{40}Sn_{60}$ nanoparticles. These CV also exhibit the characteristic features of alcohol electrooxidation at Pt-based surfaces, *i.e.* the two well-defined oxidation peaks are clearly observable. The section between these two oxidation peaks is in this case also located at the same potential value (around 0.75 V) whatever the used fuel is. Lowering of this section potential is indicative of occurrence of the bifunctional mechanism and activation of water at lower potentials. However the most noticeable characteristic of these CV is certainly the fact that the specific molar oxidation current is higher in the case of ethanol electrooxidation than for methanol electrooxidation. This is certainly due to activation (at least partial) of the ethanol C-C bond breaking by Pt/Sn electrocatalysts.
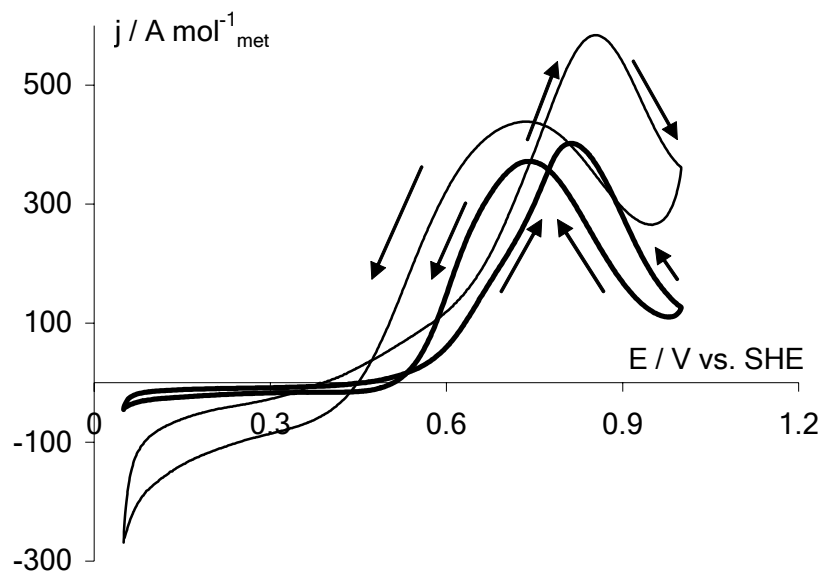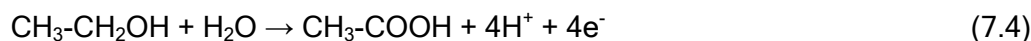
Figure 7.13: CV of MeOH (thick line) and EtOH (thin line) electrooxidation on BDD-supported microemulsion-synthesized $Pt_{40}Sn_{60}$ nanoparticles. Recorded in 1 M $HClO_4$ + 0.1 M Alcohol at 20 mV s^{-1} and 25°C.

Figure 7.14 summarizes the specific molar oxidation currents obtained both for methanol and ethanol electrooxidation on Pt/Sn bimetallic nanoparticles deposited on BDD electrodes. This figure is very interesting in the sense that it can be observed that the curve for ethanol electrooxidation crosses that one relative to methanol electrooxidation as soon as Sn is added to the surface. The values of specific molar oxidation currents are then maintained at higher levels in the case of ethanol electrooxidation. It means that, on these Pt/Sn surfaces, the number of exchanged electrons during oxidation is more important for ethanol electrooxidation. Regarding the ratio between specific molar oxidation currents of the two alcohols and if a complete methanol oxidation (leading to CO_2 as the final product with 6 electrons exchanged) is supposed, it implies that, depending on the nanoparticles used, up to 12 electrons can be released during ethanol electrooxidation (case of $Pt_{80}Sn_{20}$). This value corresponds to the complete oxidation of ethanol to CO_2 and therefore it can be postulated that the use of such surfaces allows the activation of the C-C bond scission. However results on this topic available in literature are quite controversial and still under debate (see for instance ref. [12-16, 45]). Moreover there is no evidence here that methanol electrooxidation is effectively complete and yields CO_2 as final product. Another tendency that can be deduced from Fig. 7.14 is the decrease in the specific molar current for both methanol and ethanol electrooxidation with decreasing the Pt content in nanoparticles. This is because Pt is the only metal capable of alcohols dehydrogenation at room temperature. It seems obvious that decreasing the Pt content in particles will decrease concomitantly the density of Pt

sites available for adsorption. Therefore the surface adsorption properties will be altered. However in the case of ethanol electrooxidation these lower adsorption properties with higher Sn contents are counterbalanced by the apparent effect of tin addition on the activation of the C-C bond scission. Finally these results confirm those obtained for the electrochemical characterization of BDD-supported Pt/Sn nanoparticles shown in Fig. 7.11: the most efficient nanoparticles are the ones that have exhibited a marked Pt surface character in pure supporting electrolyte. As the specific molar current is higher for surfaces with the lower ligand effect but the higher adsorption properties (*i.e.* $Pt_{80}Sn_{20}$ nanoparticles), it seems that the limiting step is here the alcohol adsorption on the surface. It was indeed shown in Fig. 7.10 that the higher the Sn content in nanoparticles, the higher the chemical shift of XPS Pt*4f* signal and hence the higher the electronic effect. Regarding the first results obtained on ethanol electrooxidation on Pt/Sn nanoparticles and the advantages of using this fuel rather than methanol in DAFC (lower toxicity, higher theoretical mass energy density and production from the biomass), this section will be more centred on the electrocatalysis of ethanol electrooxidation. As the aliphatic chain of ethanol contains two carbons the electrooxidation of ethanol on Pt is a quite more complicated case than methanol electrooxidation. Nevertheless of ethanol electrooxidation mechanism in acidic medium on Pt is now quite well-established on the basis of reaction products analyses (by means of GC, HPLC, DEMS or FTIR) [13, 46, 47]. The overall ethanol electrooxidation reaction on Pt is given by Equation 7.3:

$$C_2H_5OH + 3\ H_2O \rightarrow 2\ CO_2 + 12H^+ + 12e^- \qquad (7.3)$$
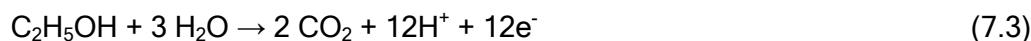
This global equation involves parallel and consecutive oxidation reactions:

$$CH_3\text{-}CH_2OH + H_2O \rightarrow CH_3\text{-}COOH + 4H^+ + 4e^- \qquad (7.4)$$

$$CH_3\text{-}CH_2OH \rightarrow CH_3\text{-}CHO + 2H^+ + 2e^- \qquad (7.5)$$

Reaction 7.4 occurs mainly at higher electrode potentials ($E \geq 0.8$ V vs. SHE) for which water is activated to form oxygenated species at the Pt surface whereas reaction 7.5 occurs mainly at lower potential values ($E \leq 0.6$ V vs. SHE). At intermediate potentials ($0.6 \leq E \leq 0.8$ V) water discharge occurs:

$$Pt + H_2O \rightarrow Pt\text{-}OH_{ads} + H^+ + e^- \qquad (7.6)$$

so that the oxidation of adsorbed CH_3-CHO may produce acetic acid as illustrated in Equation 7.7:

$$(CH_3\text{-}CHO)_{ads} + Pt\text{-}OH_{ads} \rightarrow CH_3\text{-}COOH + Pt + H^+ + e^- \qquad (7.7)$$
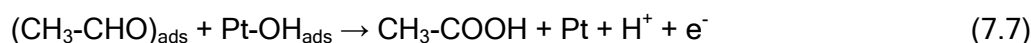
Further oxidation to CO_2 is difficult at room temperature on pure Pt; however the presence of both CO, CO_2 and methane determined experimentally [41, 48, 49] at low potentials ($E \leq 0.4$ V vs. SHE) can be explained by the following sequence of reactions:

$$Pt + CH_3CHO \rightarrow Pt\text{-}(CO\text{-}CH_3)_{ads} + H^+ + e^- \qquad (7.8)$$

$$Pt + Pt\text{-}(CO\text{-}CH_3)_{ads} \rightarrow Pt\text{-}(CO)_{ads} + Pt\text{-}(CH_3)_{ads} \qquad (7.9)$$

$$Pt + H_2O \rightarrow Pt\text{-}H_{ads} + Pt\text{-}OH_{ads} \qquad (7.10)$$

$$Pt\text{-}(CH_3)_{ads} + Pt\text{-}H_{ads} \rightarrow 2\,Pt + CH_4 \qquad (7.11)$$

$$Pt\text{-}(CO)_{ads} + Pt\text{-}OH_{ads} \rightarrow 2\,Pt + CO_2 + H^+ + e^- \qquad (7.12)$$
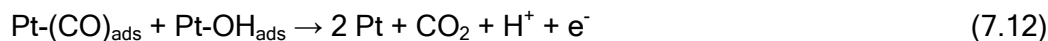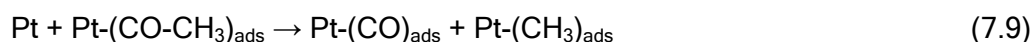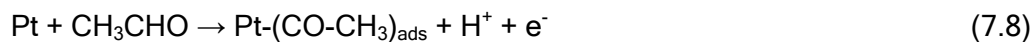
One of the great challenges here would be to elucidate the action mode of the Pt/Sn catalysts and to determine if the mechanism involves the direct scission of the molecule C-C bond when it is adsorbed on the surface or if it involves the formation of C_2 intermediates that can be further oxidized more efficiently and rapidly on Pt/Sn. The determination of the relative importance of the bifunctional mechanism on one hand and the electronic effect (if any) on the other hand would be of great importance for this purpose. Attention will be focused in this case on Pt-rich surfaces and mainly on $Pt_{80}Sn_{20}$ nanoparticles as they have shown the best performance for ethanol electrooxidation, due to their higher alcohol adsorption properties at room temperature.
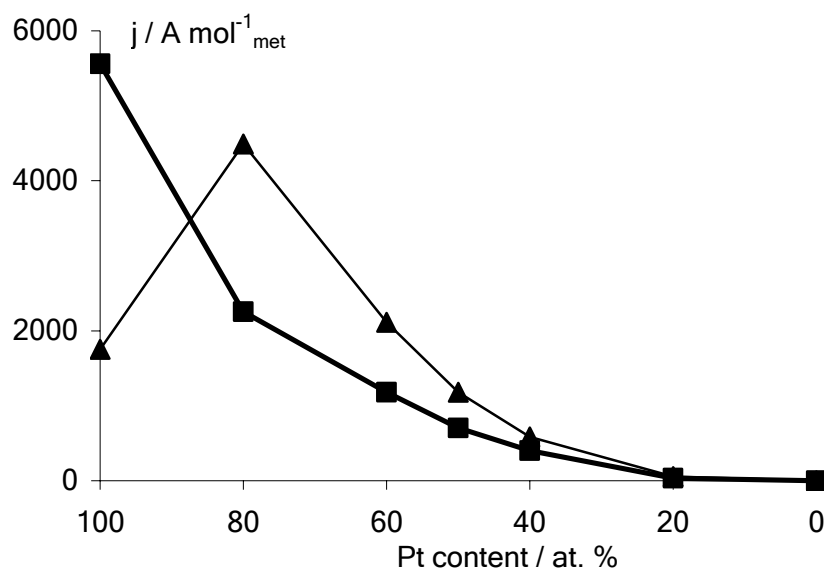
Figure 7.14: Evolution of the specific molar current for the electrooxidation of MeOH (thick line with square markers) and EtOH (thin line with triangle markers) on BDD-supported microemulsion-synthesized Pt/Sn nanoparticles. Recorded by CV in 1 M $HClO_4$ + 0.1 M Alcohol at 20 mV s^{-1} and 25°C.

Another evidence of electrocatalysis of ethanol electrooxidation by BDD-supported Pt/Sn nanoparticles is given by Figure 7.15, which shows polarization curves recorded at 1 mV s^{-1} and room temperature in 1 M $HClO_4$ + 0.1 M EtOH solution. It can be clearly seen on this picture that the onset of ethanol electrooxidation is largely shifted to lower potential values on the bimetallic surface.

176

For instance to reach an specific molar current of 200 A mol$^{-1}_{met}$ a potential of 0.6 V is necessary at Pt whereas a value of 0.4 V is sufficient at Pt$_{80}$Sn$_{20}$ nanoparticles. The lowering of the onset of ethanol electrooxidation can certainly be most likely attributed to the bifunctional mechanism. The observed current increase needs the availability of free adsorption sites (Pt) that can be generated from surface reaction between adsorbed hydroxyl radicals from water dissociation and adsorbed intermediates that poison the surface. The relative starting potentials of current increases on Pt and Pt$_{80}$Sn$_{20}$ nanoparticles thus indicates that water activation takes place earlier on the bimetallic surface than on pure Pt and illustrates the role of Sn in Pt/Sn nanoparticles. This is also in good agreement with CV of Fig. 7.11 in which the increase of the double-layer capacitance with increasing the Sn content in particles was evidenced and related to water activation feasible at lower potentials on this type of surfaces.
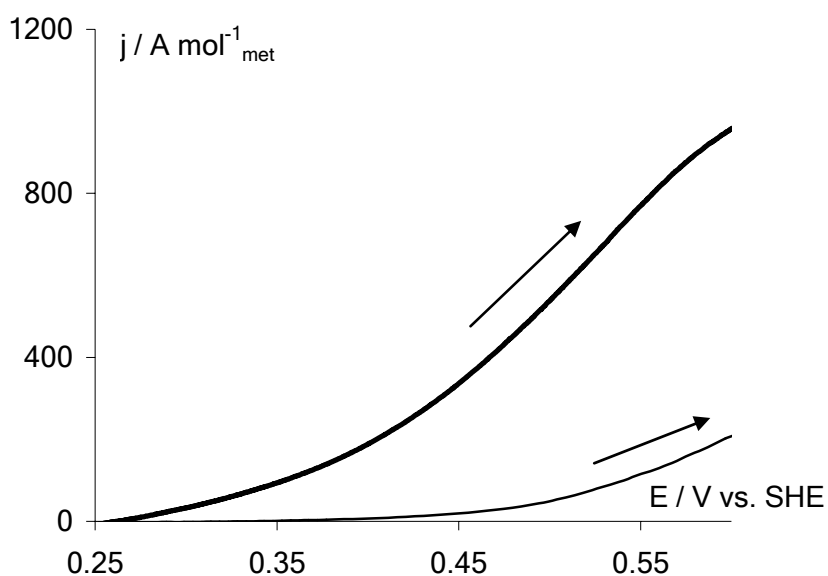
Figure 7.15: Polarization curves and onset of EtOH electrooxidation on microemulsion-synthesized Pt (thin line) and Pt$_{80}$Sn$_{20}$ (thick line) nanoparticles deposited on BDD. Recorded in 1 M HClO$_4$ + 0.1 M EtOH at 1 mV s^{-1} and 25°C.

Figures 7.16 and 7.17 show the current-transient curves for ethanol electrooxidation on Pt and Pt$_{80}$Sn$_{20}$ nanoparticles deposited on BDD and recorded at constant potentials of 0.4 and 0.6 V vs. SHE, respectively. These potentials have been chosen because they correspond to values located before and after water activation on Pt. The j-t curves shown in both Figs. 7.16 and 7.17 exhibit the same type of profile, *i.e.* an initial and fast current decay followed by a current plateau. Similar profiles have ever been observed in the case of methanol electrooxidation on Pt and explained by fast surface poisoning by adsorbed intermediates [3]. In the case of ethanol electrooxidation such profile was attributed to a great extent to the

increasing surface coverage with partially oxidized intermediates [16, 41]. Whatever the applied potential is, the initial specific molar current is higher on the bimetallic surface than on Pt. On the contrary when Pt/Ru nanoparticles were used for methanol electrooxidation at constant potential it was observed that the initial specific molar current was higher on the bimetallic surface only before water activation on Pt (see Chapter 6). This indicates that the bifunctional mechanism is certainly not solely responsible for enhanced electrocatalytic activity of Pt/Sn toward ethanol electrooxidation. When water is activated on Pt the initial specific molar oxidation current is higher on $Pt_{80}Sn_{20}$ nanoparticles (Fig. 7.17); this can be attributed to the effect of Sn on Pt that presumably allows the activation of the C-C bond scission (eventually partially) in the ethanol molecule. Activation of the ethanol C-C bond scission by Sn addition can have several origins and this property is quite controversial in literature. Explanations such as a forced stretching of the ethanol C-C bond due to incorporation of Sn atoms with high a lattice parameter [11] or existence of a specific, weakly bonded Pt-CO state at Pt/Sn [50] have been proposed. The electrocatalytic behaviour of Pt/Sn surfaces greatly depends on its preparation mode. The dispersion of the two metals at the surface is of crucial importance as it has been shown by Density Functional Theory (DFT) calculations that oxygenated species coming from water dissociation are exclusively adsorbed on Sn sites [50]. Therefore the surface reaction between the poison and oxygenated species requires, to be carried out efficiently, high mobility of adsorbates or important interface between the two metals. It can reasonably be postulated that a good dispersion of the two metals at the nanoparticles surface can be one of the origins of the apparent activation of the C-C bond breaking using microemulsion-synthesized Pt/Sn electrocatalysts. The bimetallic surface is also more tolerant to poisoning than Pt; the value of the specific molar current at the plateau is indeed always higher in the case of $Pt_{80}Sn_{20}$ nanoparticles. Moreover the initial current decay is less pronounced and abrupt for the bimetallic nanoparticles than for pure Pt, indicating that the Pt/Sn surface is less sensitive to surface poisoning by adsorbed intermediates that are hence more efficiently removed. This effect can be related to the bifunctional mechanism; therefore the global enhanced and extended electrocatalytic activity of $Pt_{80}Sn_{20}$ toward ethanol electrooxidation (compared to Pt) can be considered as the result of the combination of a ligand effect and bifunctional mechanism. However the probable ligand effect induced by Sn addition to Pt is certainly not of same nature than those induced by Ru as it seems that this metal does not influence the activation of the C-C bond breaking.
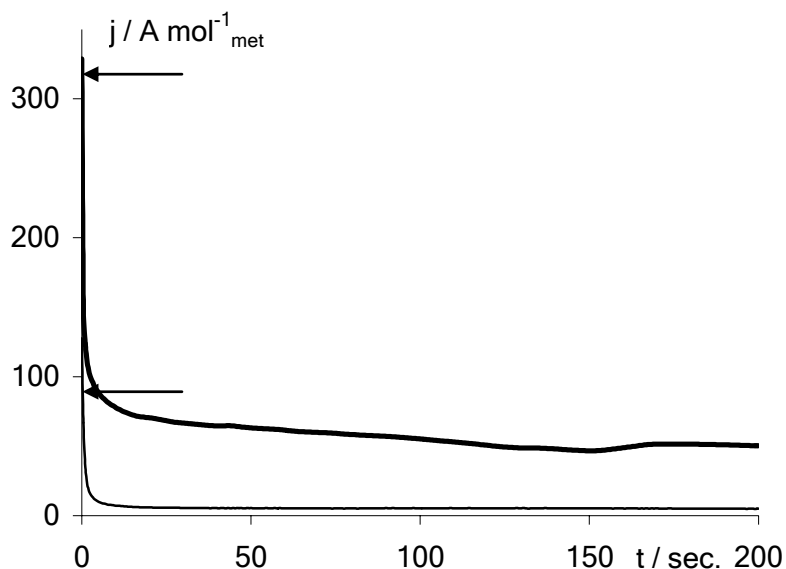
Figure 7.16: Chronoamperometric curve at 0.4 V vs. SHE for the electrooxidation of EtOH on BDD-supported microemulsion-synthesized Pt (thin line) and $Pt_{80}Sn_{20}$ (thick line) nanoparticles. Recorded in 1 M $HClO_4$ + 0.1 M CH_3CH_2OH at 25°C. Specific molar currents at t = 0 are marked by arrows.
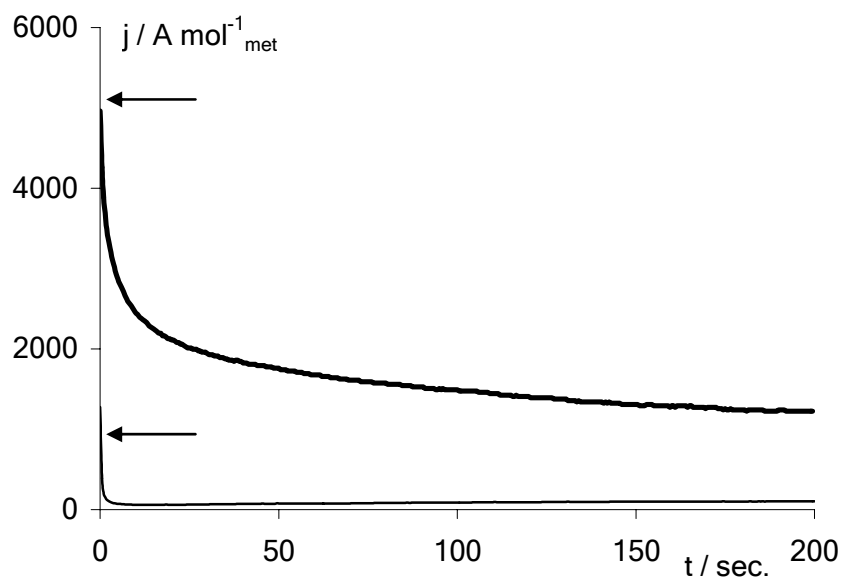
Figure 7.17: Chronoamperometric curve at 0.6 V vs. SHE for the electrooxidation of EtOH on BDD-supported microemulsion-synthesized Pt (thin line) and $Pt_{80}Sn_{20}$ (thick line) nanoparticles. Recorded in 1 M $HClO_4$ + 0.1 M CH_3CH_2OH at 25°C. Specific molar currents at t = 0 are marked by arrows.

Figures 7.18 and 7.19 summarize the values of the specific molar currents (after 200 sec. of electrolysis) measured for experiments similar to those presented in Figs. 7.16 and 7.17. Results relative to methanol and ethanol electrooxidation are presented in Figures 7.18 and 7.19, respectively, and have been conducted at selected constant potentials (0.4, 0.5 and 0.6 V vs. SHE) on all the synthesized Pt/Sn nanoparticles. In the case of methanol electrooxidation, it can be seen that the

179

maximum of activity between the synthesized nanoparticles is reached for $Pt_{80}Sn_{20}$ nanoparticles for all the explored potentials. This is because at room temperature methanol dehydrogenation can take place only on Pt sites so that a Pt-rich surface is more indicated for electrocatalysis under these conditions. It can also be seen that as soon as the Pt content is decreased to 60 at. % the bimetallic particles are less efficient than pure Pt. It can be considered that the electrocatalytic activity of a given type of particles depend on the balance between its adsorption properties and its tolerance to CO poisoning. It seems that since the Pt content is decreased to a value of 60 at. % the adsorption properties of nanoparticles are not sufficient to take advantage of the higher tolerance to surface poisoning due to occurrence of the bifunctional mechanism.
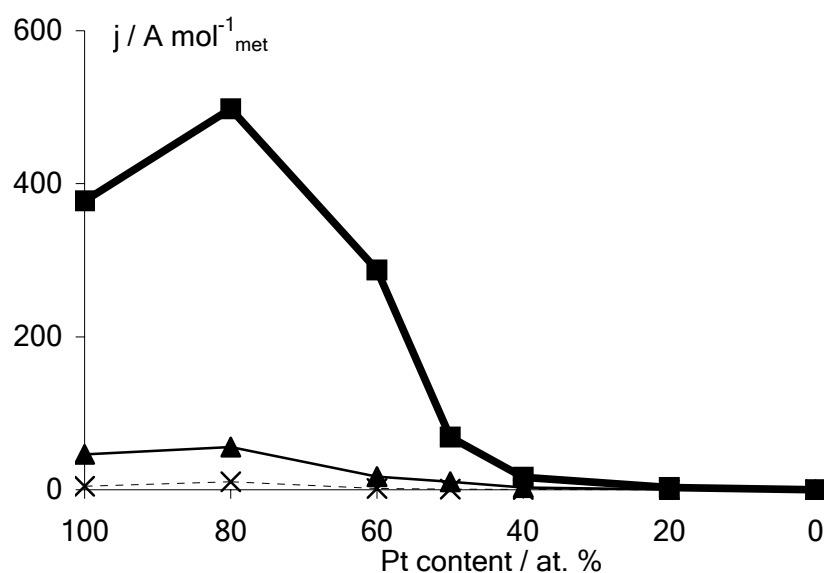

Figure 7.18: Specific molar current for MeOH electrooxidation on BDD-supported microemulsion-synthesized Pt/Sn nanoparticles. Recorded in 1 M $HClO_4$ + 0.1 M CH_3OH at 25°C at constant potentials of 0.4 (thin dashed line with cross markers), 0.5 (thin solid line with triangle markers) and 0.6 V vs. SHE (thick solid line with square markers) after 200 sec of electrolysis.

The case of ethanol electrooxidation at constant potential seems to be similar to that of methanol electrooxidation in the sense that the maximum of electrocatalytic activity is also reached for $Pt_{80}Sn_{20}$ nanoparticles; this fact can also be attributed to the superior adsorption properties of these particles compared to others of lower Pt contents. Nevertheless Fig. 7.19 needs some specific additional comments. Firstly, both $Pt_{60}Sn_{40}$ and $Pt_{50}Sn_{50}$ nanoparticles exhibit higher specific molar currents than Pt. Then for all the samples synthesized here the values of specific molar currents are always higher for ethanol electrooxidation than for methanol electrooxidation. It can be supposed that, in addition to the bifunctional mechanism and water activation

at lower potential values, Sn probably influences the scission of the ethanol molecule C-C bond. Therefore the low alcohol adsorption properties of these particles are certainly hidden by the fact that the C-C bond breaking is activated on these surfaces and that ethanol electrooxidation is more complete than on Pt. Lowering again the Pt content in bimetallic Pt/Sn nanoparticles the adsorption properties of the surface are decreased in such an extent that activation of the C-C bond breaking is not sufficient to ensure good electrocatalytic performance.
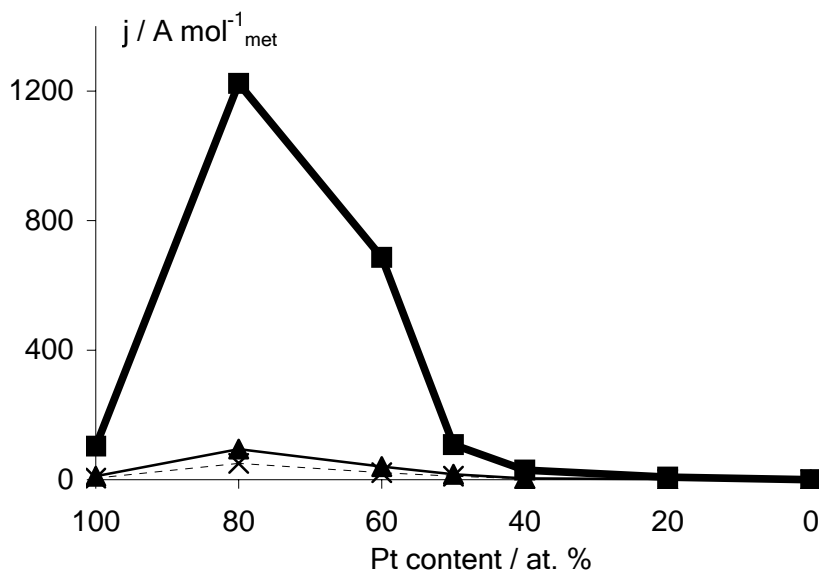

Figure 7.19: Specific molar current for EtOH electrooxidation on BDD-supported microemulsion-synthesized Pt/Sn nanoparticles. Recorded in 1 M $HClO_4$ + 0.1 M CH_3CH_2OH at 25°C at constant potentials of 0.4 (thin dashed line with cross markers), 0.5 (thin solid line with triangle markers) and 0.6 V vs. SHE (thick solid line with square markers) after 200 sec of electrolysis.

In order to further investigate the action mode of Pt/Sn surfaces on ethanol electrooxidation, the oxidation of known intermediates (acetic acid and acetaldehyde) was studied on BDD-supported $Pt_{80}Sn_{20}$ nanoparticles and the behaviour of these particles was compared to those of Pt under the same conditions. Figure 7.20 shows the CV recorded on both Pt and $Pt_{80}Sn_{20}$ nanoparticles for acetaldehyde electrooxidation. Measurements done in the presence of acetic acid are not shown here because no peaks associated with oxidation processes could be observed on both the two types of surfaces. It can be seen on the CV shown in Fig. 7.20 that the electrooxidation of acetaldehyde effectively takes place on both Pt and $Pt_{80}Sn_{20}$ nanoparticles and that the specific molar currents on the bimetallic surface are almost the double than those observed on Pt. Enhancement of electrocatalytic activity by Sn addition to Pt toward acetaldehyde electrooxidation has ever been reported and attributed to inhibition of poison formation [51]. However, regarding the values of

specific molar currents of Fig. 7.20, it can be said that the difference of electrocatalytic activity between the two types of particles toward ethanol electrooxidation can not solely be attributed to the fact that $Pt_{80}Sn_{20}$ oxides more efficiently C_2 intermediates. It must be considered that Pt/Sn promotes also probably the direct scission of the ethanol C-C bond when the molecule is adsorbed on the surface. Finally the strong cathodic current observed in the 0-0.4 V potential region for the bimetallic sample certainly comes from the residual surfactant that is less easily removed from this surface. Potential is indeed cycled in the supported electrolyte up to a more limited anodic potential when BDD-supported Pt/Sn nanoparticles are used in order to avoid tin dissolution.
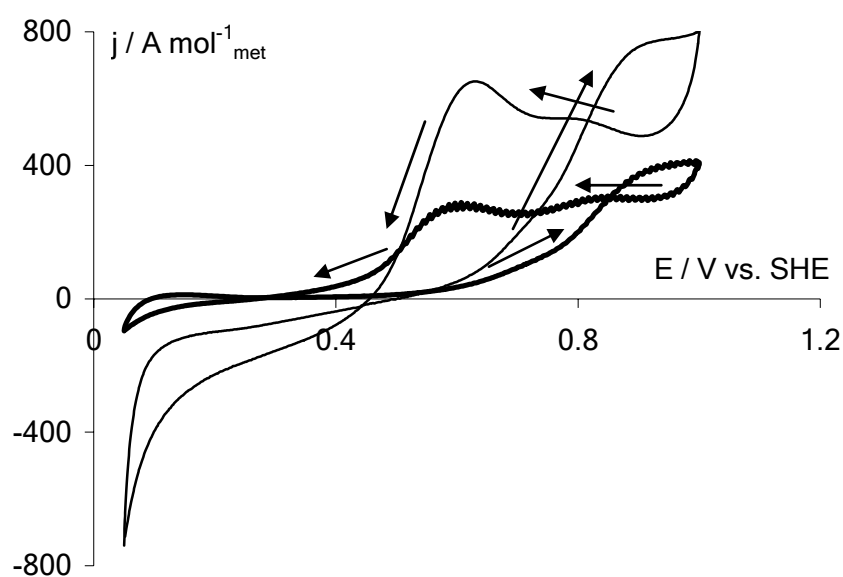
Figure 7.20: CV of BDD-supported Pt (thick line) and $Pt_{80}Sn_{20}$ (thin line) nanoparticles in the presence of acetaldehyde. Recorded in 1 M $HClO_4$ + 0.1 M C_2H_4O at 20 mV s^{-1} and 25°C.

In order to further investigate both methanol and ethanol electrooxidation processes on microemulsion-synthesized Pt/Sn nanoparticles, electrochemical impedance spectroscopy (EIS) measurements have been carried out. EIS experiments have been performed at potentials of 0.4 and 0.6 V vs. SHE (before and after water activation on Pt) both on Pt and $Pt_{80}Sn_{20}$ nanoparticles, using potential modulations of 10 mV with a frequency range comprised between 100 kHz and 0.01 Hz. The aim was to obtain additional evidences on the influences of the applied potential and the catalytic surface on the oxidation mechanism, and particularly on the action mode of Sn toward ethanol electrooxidation.

Figures 7.21 and 7.22 show the Nyquist plots for methanol electrooxidation at 0.4 and 0.6 V vs. SHE, respectively, recorded on both Pt and $Pt_{80}Sn_{20}$ nanoparticles

supported on BDD. It can be seen that at 0.4 V (Fig. 7.21), both the two Nyquist plots exhibit similar semi-circular shape. It can also been observed that on $Pt_{80}Sn_{20}$ the impedance arc diameter is much lower than in the case of Pt, indicating a smaller resistance to charge-transfer for methanol oxidation on the bimetallic surface. The large diameter of the impedance arc on Pt can be attributed to surface poisoning by strongly adsorbed intermediates (CO). Moreover no terminating inductive loop can be observed whatever the type of particles used is; this pseudo-inductive behaviour has been ascribed to surface reactions between adsorbed species, and more specifically in this case between CO and oxygenated species. This indicates that this surface reaction does not take place, as expected, on Pt because the applied potential is not sufficient to allow water activation and the subsequent generation of oxygen-containing species. Surprisingly the induction loop is also absent when methanol oxidation is performed at 0.4 V on $Pt_{80}Sn_{20}$ although it is known that water is activated at this potential value (see Fig. 7.15). Increasing the applied potential up to values for which water is activated on Pt (0.6 V vs. SHE, Fig. 7.22), the induction loop appears at Pt nanoparticles whereas it is still not present at $Pt_{80}Sn_{20}$. It indicates that Pt/Sn particles do not behave in the same manner that both Pt and Pt/Ru (see Chapter 6). A specific effect induced by tin addition can reasonably be postulated. As main differences between the two types of bimetallic particles, the unalloyed nature of Pt/Sn and the higher XPS chemical shift of the Pt*4f* signal can be mentioned. Moreover both the impedance arc diameter and the polarization resistance decrease with increasing potential for the two types of particles, indicating that charge-transfer resistance decreases and methanol oxidation rate increases concomitantly. It must also be pointed out that at this potential value, both the charge-transfer resistance and the polarization resistance are lower in the case of Pt nanoparticles. This seems to indicate that, at least in the case of methanol electrooxidation for which there is no need in the activation of a C-C bond breaking, superior adsorption properties are preferable to any ligand effect as soon as water is dissociation activated.

Figure 7.21: EIS Nyquist plot of MeOH electrooxidation on Pt (triangle markers) and $Pt_{80}Sn_{20}$ (square markers) at 0.4 V vs. SHE. Recorded in 1 M $HClO_4$ + 0.1 M CH_3OH at 25°C.

Figure 7.22: EIS Nyquist plot of MeOH electrooxidation on Pt (triangle markers) and $Pt_{80}Sn_{20}$ (square markers) at 0.6 V vs. SHE. Recorded in 1 M $HClO_4$ + 0.1 M CH_3OH at 25°C.

The electrooxidation of ethanol has also been studied on Pt/Sn by means of EIS. Figures 7.23 and 7.24 show the Nyquist plots for ethanol electrooxidation at 0.4 and 0.6 V vs. SHE, respectively, recorded on both Pt and $Pt_{80}Sn_{20}$ nanoparticles. For an applied potential of 0.4 V (Fig. 7.23), it can be seen than both the two Nyquist plots exhibit a semi-spherical shape. However in the case of Pt the value of the impedance arc diameter is so high that the semi-circle is not closed, indicating slow oxidation

rate and high charge-transfer resistance. These values are much lower for $Pt_{80}Sn_{20}$ nanoparticles, and the absence of the terminal inductive loop at low frequencies indicating surface reaction between adsorbates can be noticed. It can be supposed that Pt/Sn acts, in the case of ethanol oxidation electrocatalysis, via a specific effect and that this effect directly allows the activation of the C-C bond breaking of the ethanol molecule. However this action mode can be of several natures. It was for instance pointed out that a specific and weakly-bonded adsorbed CO state exists on Pt/Sn surfaces [50, 52, 53]. Therefore Pt/Sn is well-known to be a very efficient catalyst toward CO oxidation and it is possible that CO_{ads} coming from ethanol dehydrogenation could be eliminated more easily and rapidly so that an eventual surface reaction could not be observed by EIS. Another explanation involved the increase of the lattice parameter of the crystalline surface, due to addition of tin, which forces stretching and thus weakening of the C-C bond of the ethanol molecule in order to allow its adsorption on the surface. However a true alloy is not synthesized in our case so that this explanation is certainly not applicable to this system. Nevertheless it can reasonably be said that the microemulsion method allows the formation of bimetallic Pt/Sn nanoparticles with good surface dispersion of the two metals. The specific effect of tin addition on Pt has certainly an electronic origin, not of same nature than those of ruthenium, and this requires large interface between the two metals.
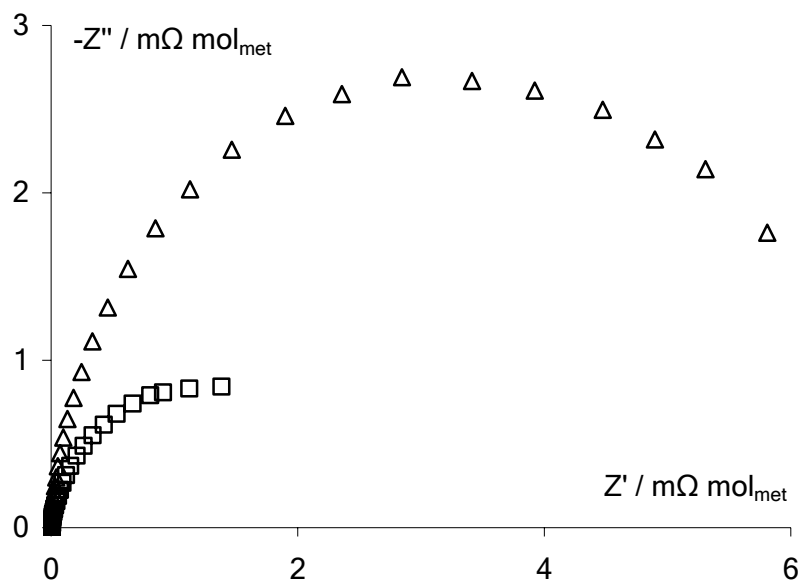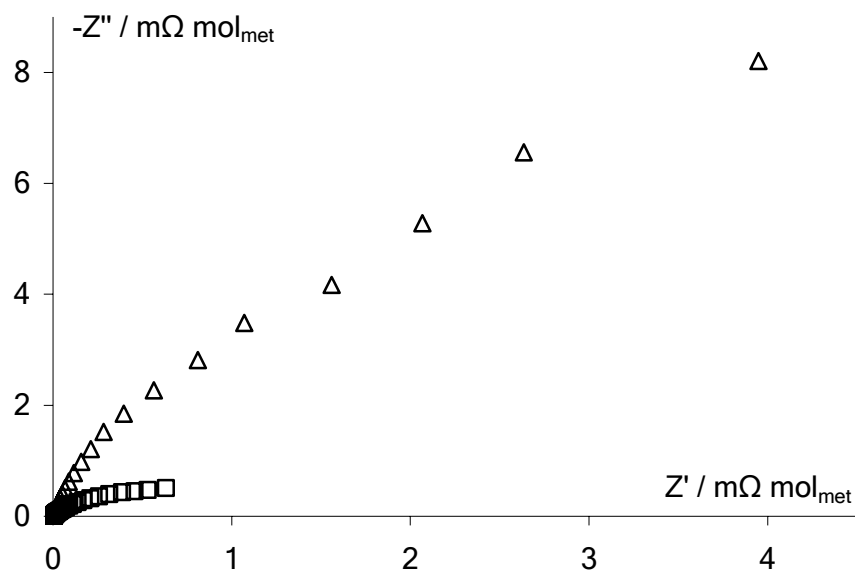
Figure 7.23: EIS Nyquist plot of EtOH electrooxidation on Pt (triangle markers) and $Pt_{80}Sn_{20}$ (square markers) at 0.4 V vs. SHE. Recorded in 1 M $HClO_4$ + 0.1 M CH_3CH_2OH at 25°C.
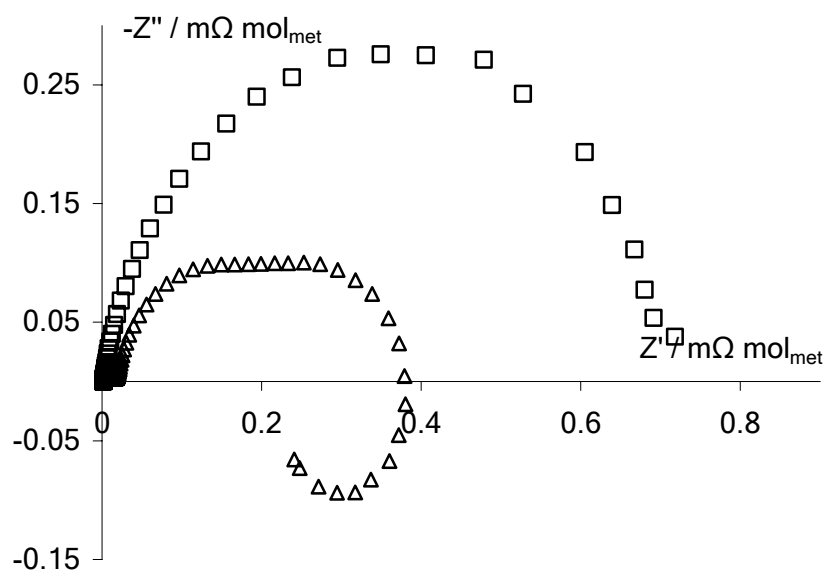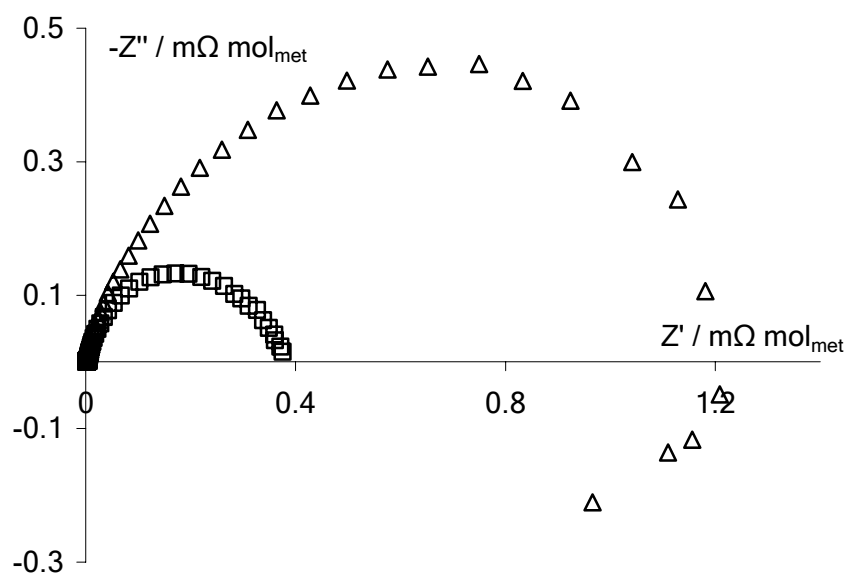

Figure 7.24: EIS Nyquist plot of EtOH electrooxidation on Pt (triangle markers), and $Pt_{80}Sn_{20}$ (square markers) at 0.6 V vs. SHE. Recorded in 1 M $HClO_4$ + 0.1 M CH_3CH_2OH at 25°C.

4. CONCLUSIONS

During this Chapter Pt/Sn nanoparticles of different compositions, synthesized following the microemulsion route, have been deposited on the BDD electrode for their electrochemical and electrocatalytic characterization. These Pt/Sn nanoparticles have also been physically characterized. The choice of synthesizing bimetallic Pt/Sn

nanoparticles was motivated by the well-known superior electrocatalytic activity of this type of surface toward ethanol electrooxidation. It is also, to the best of our knowledge, the first time that Pt/Sn nanoparticles have been synthesized using the microemulsion method.

It was shown by TEM measurements that particles were of spherical shape, with very little aggregation observable, and of diameter in the 2-5 nm size domain. Size distributions of the different samples were all similar and quite narrow; the observed size distributions of nanoparticles reflected those of inverse micelles in the initial microemulsions. The narrow size distributions of particles indicate that the microemulsion method allows fine size control by appropriate choice of the water-to-surfactant molar ratio value. XRD measurements have shown that bimetallic Pt/Sn particles are formed rather than true alloys. Particles are certainly composed of crystalline Pt islands together with crystalline Sn islands. Atomic quantification of elements present in the particles have been performed by XPS and EDX; the results obtained using both the two methods have shown that compositions of particles were in all the cases close to the nominal ones (*i.e.* ratio between metallic precursors initially introduced in the microemulsion). Moreover it was shown that Pt in particles was mainly metallic; the detected Pt^{II} species were presumably formed by interactions with atmospheric oxygen. Finally XPS was used to estimate an "electronic effect" of Sn on Pt. Pt*4f* doublet chemical shifts to lower values of binding energies were attributed to an electronic transfer from Sn to Pt that can lead to the modification of Pt properties and weakening of the Pt-CO bond. Regarding the quite important values of displacements it can be said that the two metals are certainly well dispersed at the nanoparticles surface.

CV recorded on BDD-supported Pt/Sn nanoparticles in 1 M $HClO_4$ have shown the gradual loss of Pt character of the surface when the Sn content is increased. More particularly the peaks attributed to H adsorption-desorption processes on Pt became worse-defined until no peaks can be attributed to these phenomena for Sn-rich nanoparticles. Such measurements gave also an idea about the most appropriate electrocatalysts for methanol and ethanol oxidation. CV performed in the presence of alcohols have confirmed the results obtained in the electrolyte; the surfaces with a marked Pt surface character exhibited the higher specific molar currents both for methanol and ethanol electrooxidation, Pt and $Pt_{80}Sn_{20}$ being the most efficient electrocatalysts for methanol and ethanol oxidation, respectively. It must be pointed out that, for a given type of Pt/Sn bimetallic nanoparticles, the specific molar currents for ethanol electrooxidation were always higher than those for methanol electrooxidation. The electrooxidation of acetaldehyde, a known ethanol

oxidation intermediate, was performed with higher activity on the bimetallic surface but could not explain solely the observed difference between methanol and ethanol electrooxidation. This seems to indicate that Pt/Sn surfaces are probably able to activate, at least partially, more efficiently the ethanol molecules C-C bond scission. Moreover the well-known beneficial effect of Sn addition to Pt was clearly observable in chronoamperometric and linear sweep (at slow scan rate) analyses. It was shown by these purposes that, using bimetallic Pt-rich nanoparticles, the onset of ethanol electrooxidation was appreciably shifted to lower potentials and that the tolerance to surface poisoning was greatly enhanced. Further investigations on both methanol and ethanol electrooxidation processes on Pt and $Pt_{80}Sn_{20}$ nanoparticles were conducted using EIS. It was shown that the pseudo-inductive behaviour, sign of surface reaction between adsorbed CO and hydroxyl radicals from water activation, is only visible on pure Pt nanoparticles. This was an indication that the observed enhancement of electrocatalytic activity toward ethanol electrooxidation has other origins than those of Pt/Ru for instance. The specific effect of Sn addition to Pt has certainly an electronic origin, but not of same nature than that of Ru.

In order to summarise it can be said that the microemulsion method efficiently leads to bimetallic Pt/Sn nanoparticles of controlled composition and size. The Pt-rich bimetallic surfaces exhibit the better electrocatalytic activities and the higher tolerance to CO poisoning. It seems that these effects could mainly be attributed to a specific electronic effect, *i.e.* modification of Pt electronic properties (work function, adsorption properties...). Ethanol oxidation on microemulsion-synthesized Pt/Sn nanoparticles presumably most likely proceeds via the direct C-C bond scission when the molecule is dehydrogenated. It can be finally expressed that microemulsion-synthesized $Pt_{80}Sn_{20}$ nanoparticles are good electrocatalysts of ethanol oxidation.

5. REFERENCES

[1]   C. Lamy, E. M. Belgsir, in: W. Vielstich, H. A. Gasteiger, A. Lamm (Eds.), *Handbook of Fuel Cells - Fundamentals, Technology and Applications*, John Wiley & Sons, Ltd., New York (2003), p. 323.

[2]   A. Hamnett, in: W. Vielstich, H. A. Gasteiger, A. Lamm (Eds.), *Handbook of Fuel Cells - Fundamentals, Technology and Applications*, John Wiley & Sons, Ltd., New York (2003), p. 305.

[3]   A. Hamnett, in: A. Wieckowski (Ed.) *Interfacial Electrochemistry - Theory, Experiments, and Applications*, Marcel Dekker, Inc., New York (1999), p. 843.

[4]   G. Cao, *Nanostructures & Nanomaterials. Synthesis, Properties and Applications*, Imperial College Press, London (2004).

[5]   M. Watanabe, S. Motoo, *J. Electroanal. Chem.* **60** (1975), 267.

[6]   T. Frelink, W. Vissher, J. A. R. van Veen, *Surf. Sci.* **335** (1995), 353.

[7]   L. Dubau, F. Hahn, C. Coutanceau, J.-M. Léger, C. Lamy, *J. Electroanal. Chem.* **554-555** (2003), 407.

[8]   M. M. P. Janssen, J. Moolhuysen, *Electrochim. Acta* **21** (1976), 869.

[9]   S. Wasmus, A. Kuver, *J. Electroanal. Chem.* **461** (1999), 14.

[10]   P. Waszczuk, J. Solla-Gullón, H.-S. Kim, Y. Y. Tong, V. Montiel, A. Aldaz, A. Wieckowski, *J. Catal.* **203** (2001), 1.

[11]   W. Zhou, Z. Zhou, S. Song, W. Li, G. Sun, P. Tsiakaras, Q. Xin, *Appl. Catal. B* **46** (2003), 273.

[12]   W. J. Zhou, S. Q. Song, W. Z. Li, G. Q. Sun, Q. Xin, S. Kontou, K. Poulianitis, P. Tsiakaras, *Solid State Ionics* **175** (2004), 797.

[13]   F. Vigier, C. Coutanceau, F. Hahn, E. M. Belgsir, C. Lamy, *J. Electroanal. Chem.* **563** (2004), 81.

[14]   F. Vigier, C. Coutanceau, A. Perrard, E. M. Belgsir, C. Lamy, *J. Appl. Electrochem.* **34** (2004), 439.

[15]   L. Jiang, G. Sun, Z. Zhou, W. Zhou, Q. Xin, *Catal. Today* **93-95** (2004), 665.

[16]   G. A. Camara, T. Iwasita, *J. Electroanal. Chem.* **578** (2005), 315.

[17]   M. Boutonnet, J. Kizling, P. Stenius, *Colloids Surf.* **5** (1982), 209.

[18]   J. Solla-Gullón, V. Montiel, A. Aldaz, J. Clavilier, *J. Electroanal. Chem.* **491** (2000), 69.

[19]   H. Härelind Ingelsten, R. Bagwe, A. Palmqvist, M. Skoglundh, C. Svanberg, K. Holmberg, D. O. Shah, *J. Colloid Interface Sci.* **241** (2001), 104.

[20]   I. Capek, *Adv. Colloid Interface Sci.* **110** (2004), 49.

[21]   G. Siné, Ch. Comninellis, *Electrochim. Acta* **50** (2005), 2249.

[22]   K. C. Song, J. H. Kim, *J. Colloid Interface Sci.* **212** (1999), 193.

[23]   J. Solla-Gullón, A. Rodes, V. Montiel, A. Aldaz, J. Clavilier, *J. Electroanal. Chem.* **554-555** (2003), 273.

[24]   J. Solla-Gullón, F. J. Vidal-Iglesias, V. Montiel, A. Aldaz, *Electrochim. Acta* **49** (2004), 5079.

[25]   M.-L. Wu, D.-H. Chen, T.-C. Huang, *Chem. Mater.* **13** (2001), 599.

[26]   Y. V. Pleskov, *Russ. Chem. Rev.* **68** (1999), 381.

[27]   B. El Roustom, G. Fóti, Ch. Comninellis, *Electrochem. Comm.* **7** (2005), 398.

[28]   F. Montilla, E. Morallon, I. Duo, Ch. Comninellis, J. L. Vazquez, *Electrochim. Acta* **48** (2003), 3891.

[29]   D. Gandini, E. Mahé, P.-A. Michaud, W. Haenni, A. Perret, Ch. Comninellis, *J. Appl. Electrochem.* **30** (2000), 1345.

[30] R. Zana, J. Lang, in: S. E. Friberg, P. Bothorel (Eds.), *Microemulsion: Structure and Dynamics*, CRC Press, Boca Raton (1987), p. 153.

[31] M. Pandey, R. D'Cunha, A. K. Tyagi, *J. Alloys Compounds* **333** (2002), 260.

[32] K.-M. Lee, D.-J. Lee, H. Ahn, *Mater. Lett.* **58** (2004), 3122.

[33] A. S. Aricò, P. L. Antonucci, E. Modica, V. Baglio, H. Kim, V. Antonucci, *Electrochim. Acta* **47** (2002), 3723.

[34] J. S. Hammond, N. Winograd, *J. Electroanal. Chem.* **78** (1977), 55.

[35] A. W. C. Lin, N. R. Armstrong, T. Kuwana, *Anal. Chem.* **49** (1977), 1228.

[36] P. A. Grutsch, M. V. Zeller, T. P. Fehlner, *Inorg. Chem.* **12** (1973), 1431.

[37] K.-W. Park, J.-H. Choi, B.-K. Kwon, S.-A. Lee, Y.-E. Sung, H.-Y. Ha, S.-A. Hong, H. Kim, A. Wieckowski, *J. Phys. Chem. B* **106** (2002), 1869.

[38] Y. Takasu, Y. Fujii, K. Yasuda, Y. Iwanaga, Y. Matsuda, *Electrochim. Acta* **34** (1989), 453.

[39] J. Clavilier, D. Armand, *J. Electroanal. Chem.* **199** (1986), 187.

[40] T. Iwasita, B. Rasch, E. Cattaneo, W. Vielstich, *Electrochim. Acta* **34** (1989), 1073.

[41] T. Iwasita, E. Pastor, *Electrochim. Acta* **39** (1994), 531.

[42] A. Oliveira Neto, M. J. Giz, J. Perez, E. A. Ticianelli, E. R. Gonzalez, *J. Electrochem. Soc.* **149** (2002), A272.

[43] D. Cao, S. H. Bergens, *J. Power Sources* **124** (2003), 12.

[44] I. d. A. Rodrigues, J. P. I. De Souza, E. Pastor, F. C. Nart, *Langmuir* **13** (1997), 6829.

[45] W. J. Zhou, S. Q. Song, W. Z. Li, Z. H. Zhou, G. Q. Sun, Q. Xin, S. Douvartzides, P. Tsiakaras, *J. Power Sources* **140** (2005), 50.

[46] T. D. Tran, I. Londner, S. H. Langer, *Electrochim. Acta* **38** (1993), 221.

[47] C. Lamy, E. M. Belgsir, J.-M. Léger, *J. Appl. Electrochem.* **31** (2001), 799.

[48] J. M. Perez, B. Beden, F. Hahn, A. Aldaz, C. Lamy, *J. Electroanal. Chem.* **262** (1989), 251.

[49] H. Hitmi, E. M. Belgsir, J. M. Léger, C. Lamy, R. O. Lezna, *Electrochim. Acta* **39** (1994), 407.

[50] T. E. Shubina, M. T. M. Koper, *Electrochim. Acta* **47** (2002), 3621.

[51] M. Shibata, S. Motoo, *J. Electroanal. Chem.* **187** (1985), 151.

[52] B. D. Dunietz, N. M. Markovic, P. N. Ross Jr, M. Head-Gordon, *J. Phys. Chem. B* **108** (2004), 9888.

[53] H. A. Gasteiger, N. M. Markovic, P. N. Ross Jr, *Catal. Lett.* **36** (1996), 1.

Chapter 8   RESULTS: Deposition of Microemulsion-Synthesized Pt/Ru/Sn Nanoparticles on BDD Electrodes for Alcohol Electrooxidation

1. INTRODUCTION

Nanomaterials have received during the last years an increasing interest due to their different and sometimes novel properties compared to those of bulk materials [1]. In electrocatalysis special attention was focused on Pt nanoparticles due to their applicability for the Direct Alcohol Fuel Cell (DAFC) technology [2], most generally fed with methanol or ethanol. However the use of Pt nanoparticles in fuel cells is severely limited due to poisoning of the surface by strongly adsorbed intermediates (CO) that block the catalytic active sites [3]. In order to circumvent these limitations Pt-based alloys have been synthesized. Alloying Pt with other transition metals (Ru, Sn, Mo, W or Ni) enhances CO tolerance of pure Pt, Ru and Sn being the most popular alloying metals for the catalysis of methanol and ethanol electrooxidation, respectively [4-7]. The reasons for such an enhancement are still under debate and two main approaches are currently privileged: *(i)* the so-called bifunctional mechanism [8], during which Pt adsorbs methanol and the other metal dissociates water molecules at lower overpotentials than Pt, and *(ii)* the electronic (or ligand) effect, in which the Pt-CO bond is weakened by the modification of the electronic properties of Pt induced by the presence of the alloying metal [9].

The use of ternary and quaternary Pt-based alloys has been recently proposed [10-13] as a viable alternative to binary ones for fuel cells applications. Therefore, in addition of the binary Pt/Ru and Pt/Sn nanoparticles (see Chapters 6 and 7 of this manuscript, respectively), the microemulsion method has been used for the synthesis of ternary nanoparticles combining Pt, Ru and Sn. It was shown during this thesis that the action modes of Pt/Ru and Pt/Sn nanoparticles were not of same nature so that a cooperative effect between Ru and Sn could be expected. Obviously the use of such particles in catalysis requires the control of both their composition and size, which can be done using the microemulsion method as it was firstly reported by Boutonnet and co-workers [14]. This method has been successfully applied to the synthesis of nanoparticles of metals [15-17] and alloys [18-20] with very narrow size distribution.

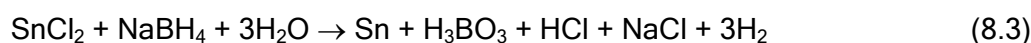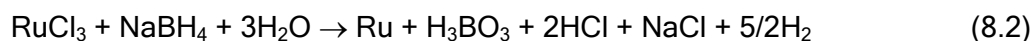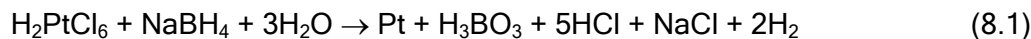As in the case of binary nanoparticles, the $Pt_{80}Ru_{10}Sn_{10}$ sample has been characterized by means of TEM, XPS, and electrochemical measurements (cyclic voltammetry and chronoamperometry) once deposited on BDD. The electrocatalytic behaviour of this ternary catalyst toward methanol and ethanol electrooxidation was investigated. Moreover the electrooxidation of acetic acid and acetaldehyde, well-

known intermediates in ethanol electrooxidation [21], was also studied to determined if an eventual enhanced electrocatalytic activity toward ethanol oxidation could be ascribed to oxidation of C_2 intermediates. The electrocatalytic activity of ternary nanoparticles was compared to those of bimetallic surfaces in order to determine if the beneficial effects of both Pt and Sn are combined.

2. EXPERIMENTAL

2.1. Nanoparticles synthesis

Platinum/Ruthenium/Tin nanoparticles were obtained by reduction of precursor salts mixture with sodium borohydride in a w/o microemulsion of water / tetraethyleneglycol-monododecylether (BRIJ$^{®}$ 30) / n-heptane, following Eqs. 8.1 to 8.3. On the basis of the results obtained from the electrocatalytic characterization of Pt/Ru and Pt/Sn nanoparticles (see Chapters 6 and 7) it was decided to keep a Pt content of 80 at. % in the ternary nanoparticles. Therefore as a preliminary attempt it was decided to synthesize a $Pt_{80}Ru_{10}Sn_{10}$ sample. The only difference with the synthesis of bimetallic nanoparticles was the presence in the aqueous phase of the microemulsion of a mixture of the three metallic precursors (H_2PtCl_6, $RuCl_3$ and $SnCl_2$) with appropriate ratios. The reduction of metal precursors was performed simultaneously following reactions 8.1 to 8.3:

$$H_2PtCl_6 + NaBH_4 + 3H_2O \rightarrow Pt + H_3BO_3 + 5HCl + NaCl + 2H_2 \qquad (8.1)$$

$$RuCl_3 + NaBH_4 + 3H_2O \rightarrow Ru + H_3BO_3 + 2HCl + NaCl + 5/2H_2 \qquad (8.2)$$

$$SnCl_2 + NaBH_4 + 3H_2O \rightarrow Sn + H_3BO_3 + HCl + NaCl + 3H_2 \qquad (8.3)$$

This method of synthesis was chose instead of mixing two microemulsions presented in Chapter 5 because $NaBH_4$ is a more powerful reducing agent that will avoid competition between reactions 8.1, 8.2 and 8.3 and allow the formation of true trimetallic particles. The microemulsions were prepared using ultra-pure water (Millipore$^{®}$ system). BRIJ$^{®}$ 30 and n-heptane were purchased from Fluka and Riedel-de-Haën, respectively, and were used as received. The metallic precursors were dissolved into the aqueous phase of one microemulsion that has a water-to-surfactant molar ratio (ω_0) fixed at 3.8. The quantity of surfactant represented 16.54 % of the volume of the microemulsion, and the aqueous phase was constituted of mixtures of 0.1 M solutions of the metallic salts. Relative amounts of the precursors solutions were adjusted depending on the desired alloy final composition. Only a $Pt_{80}Ru_{10}Sn_{10}$ (in atomic percents) trimetallic sample has been synthesized here. From a practical point of view, the surfactant and n-heptane were first mixed. Then the aqueous phase was slowly added and the solution vigorously stirred. This results in a

transparent, homogeneous and dark brown solution. The conditions for the synthesis of the Pt/Ru/Sn particles by the microemulsion method are summarized in Table 8.1.

	Pt/Ru/Sn nanoparticles
Vol. % surfactant	16.54
Vol. % n-heptane	80.46
Vol. % H_2O	3
$[PtCl_6^{2-}]_{aq}$ / M	0.1
$[RuCl_3]_{aq}$ / M	0.1
$[SnCl_2]_{aq}$ / M	0.1
$[NaBH_4]_{aq}$ / M	1
$[NaBH_4]_{aq}/[metal\ ions]_{aq}$	10

Table 8.1: Experimental parameters for the synthesis of Pt/Ru/Sn nanoparticles using the microemulsion method.

The synthesis was realised adding to the microemulsion the amount of solid sodium borohydride necessary to yield a concentration of 1 M of $NaBH_4$ in the aqueous phase. The general scheme of nanoparticles synthesis adding a solid reducing agent to a microemulsion is shown in Figure 8.1. It involves the following steps: (1) mixing of the microemulsion with the solid reducing agent that diffuses into the inverse micelles to react with the metallic precursors, (2) nucleation and (3) growth of the particles into the interior of the inverse micelles. Growth of the particles was finally stopped by the surfactant layer that stabilises the aqueous dispersion.
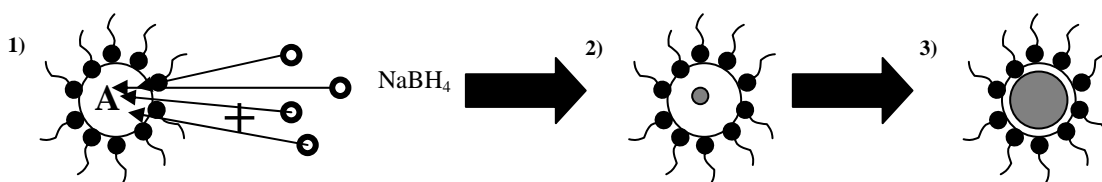

Figure 8.1: General scheme for the synthesis of Pt/Ru/Sn particles adding a solid reducing agent to a microemulsion. Steps of the process: **1)** mixing of the microemulsion with solid $NaBH_4$, diffusion into the inverse micelles and reaction, **2)** nucleation and **3)** growth of the particles. A = H_2PtCl_6 + $RuCl_3$ + $SnCl_2$ (aq.) in appropriate ratios, aqueous droplets are dispersed in n-heptane and stabilized by a BRIJ®-30 layer.

After complete reduction, that needs only a few minutes and is evidenced by colour change to dark black and gas release, acetone was added to the solution to cause phase separation and precipitation of the particles. The precipitate was rinsed several times with acetone and ultra-pure water, and then centrifuged for a few minutes to eliminate most of the surfactant. Finally particles were put in a small

volume of ultra-pure water as a suspension. The Pt contents of the final aqueous suspension were determined using AAS.

2.2.   BDD-Pt/Ru/Sn electrode preparation

BDD films were synthesised by the hot filament chemical vapour deposition technique (HF-CVD) on single crystal p-type Si <100> wafers (1-3 mΩcm, Siltronix). The doping level of boron expressed as B/C ratio was about 3500 ppm. The obtained diamond film thickness was about 1 μm with a resistivity in the range 10-30 mΩcm. This as-grown BDD contains some graphitic (sp^2) phase and is hydrogen terminated. Activation of BDD by anodic polarization (10 mA cm^{-2} in 1 M H_2SO_4 at 25 °C during 30 min) eliminates most of the sp^2 and adsorbed H from the surface, and allows obtaining of reproducible electrochemical measurements [22]. Pt/Ru/Sn nanoparticles were deposited onto the BDD substrate putting a droplet (5 μl) of the suspension onto diamond. The excess water was dried under nitrogen atmosphere. Finally the BDD-Pt/Ru/Sn electrode was transferred to the electrochemical cell for measurements.

2.3.   Measurements

Electrochemical measurements were conducted using the conventional three-electrode cell described in Chapter 3, with BDD-supported Pt nanoparticles as working electrode (exposed area of diamond: 0.4 cm^2), Hg/Hg$_2$SO$_4$.K$_2$SO$_4$(sat.) as reference and a platinum wire as counter electrode. All potentials reported here are plotted with respect to the Standard Hydrogen Electrode (SHE). All solutions were made in ultra-pure (Millipore® system) water using analytical grade reactants without further purification. Before any experiment the solution was saturated with nitrogen gas and measurements were conducted under a nitrogen atmosphere.

Physical characterization of particles was conducted by TEM, XPS and XRD, using the methods and apparatus described in Chapter 3. For TEM analysis, a small droplet of the particles suspension was put on an amorphous carbon-coated copper grid; the excess water was then removed and the grid placed in the vacuum chamber of the microscope for analysis. XRD measurements of particles were carried out with particles deposited on a BDD substrate, whereas XPS analyses were performed using a gold substrate due to the proximity of the C *1s* and Ru*3d* peaks.

3.   RESULTS AND DISCUSSION

The structure and composition of ternary nanoparticles were investigated by TEM and XPS, respectively. Figure 8.1 shows the TEM micrograph of the nanoparticulate catalyst deposited on the microscope grid. Particles are present as nano-sized

spheres, in the 2-5 nm diameter range as in the case of both monometallic and bimetallic nanoparticles. This indicates that the key-point for controlling the size of microemulsion-synthesized nanoparticles is the formulation of the starting microemulsion (water-to-surfactant molar ratio ω_0).
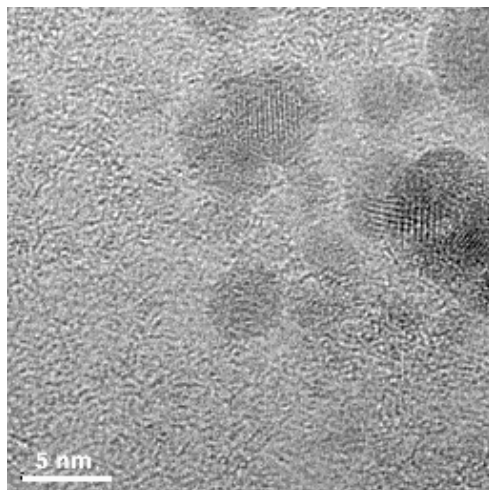
Figure 8.1: TEM image of microemulsion -synthesized $Pt_{80}Ru_{10}Sn_{10}$ nanoparticles.

Figure 8.2 represents the XPS survey of $Pt_{80}Ru_{10}Sn_{10}$ nanoparticles deposited on Au. Au was chose as substrate rather than BDD for XPS analyses due to the vicinity in binding energies of C *1s* and Ru*3d* XPS signals (around 280 eV). This spectrum shows the presence of Pt, Ru and Sn in the nanoparticles with relative atomic amounts of 90, 3 and 7 %, respectively. Such an impoverishment in Ru has ever been reported in Pt/Ru/Sn surfaces [23] and has been explained by the fact that Sn atoms repelled Ru from the surface.

Figure 8.2: XPS survey of $Pt_{80}Ru_{10}Sn_{10}$ nanoparticles deposited on Au.

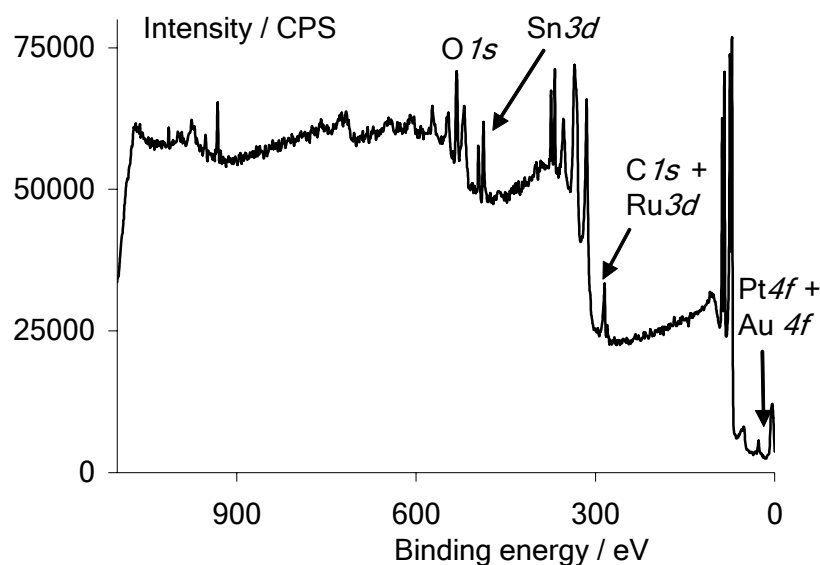Figure 8.3 represents the XPS chemical shift of the Pt$4f_{7/2}$ (Pt^0) line in the ternary sample as well as in Pt-rich binary and Pt particles (dashed vertical line on Fig. 8.3). It can be seen from this picture that in the case of binary samples the presence of the second metal lowers the binding energy. This phenomenon is more marked in the case of Sn (Pt$_{80}$Sn$_{20}$ particles), in which Pt$4f$ appears at a lower binding energy than in Pt$_{80}$Ru$_{20}$. The shift of the binding energy can be attributed to an e$^-$ d transfer from the second metal to Pt, which modifies the work function of Pt and thus weakens the Pt-CO bond of adsorbed intermediates [9]. As a general trend it can be said that the higher the electro-negativity difference between the second metal and Pt, the higher the shift in the binding energy of Pt. This explains the higher shift in Pt$_{80}$Sn$_{20}$ than in Pt$_{80}$Ru$_{20}$ (electronegativities of Pt, Ru and Sn are 2.2, 2.2 and 1.8, respectively). However in the case of the ternary sample the binding energy of Pt$4f$ moves back to its value in Pt nanoparticles. It seems that there is some kind of screening between Ru and Sn that may impeach electronic transfer to Pt, and that the electronic effect most likely occurs between Sn and Ru. However an eventual displacement of the Ru$3d$ signal should be very difficult to confirm due to the proximity of the C$1s$ contribution. This signal would indeed more or less completely hide that of Ru$3d$.
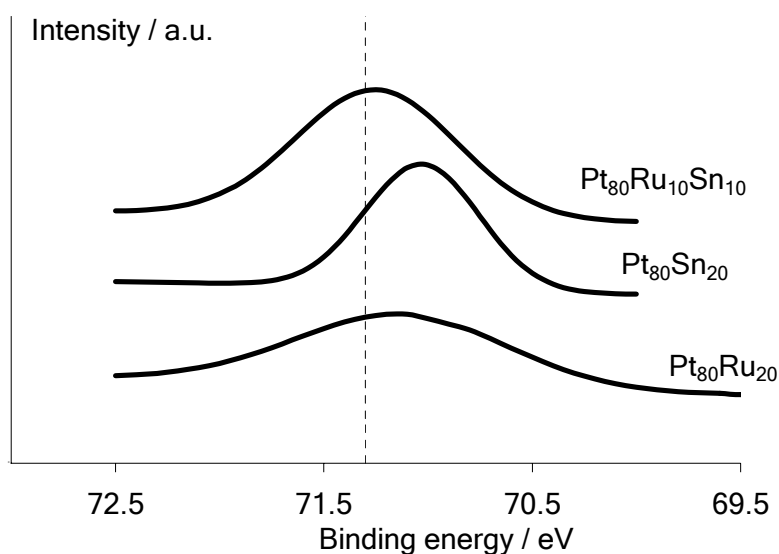
Figure 8.3: XPS chemical shift of the Pt $4f_{7/2}$ line of Pt^0 in Pt-rich ternary and binary nanoparticles supported on Au. The dashed vertical line represents the position of the signal in pure Pt nanoparticles.

The CV of a BDD-Pt (thin line) and a BDD-Pt$_{80}$Ru$_{10}$Sn$_{10}$ (thick line) electrode recorded in 1 M HClO$_4$ at 50 mV s^{-1} are shown in Figure 8.4. The CV of BDD-supported Pt shows two distinctive hydrogen adsorption/desorption peaks between 0.05 and 0.3 V. From 0.3 V to 0.7 V Pt is in its metallic state and the current density is very low. In the ternary alloy, the adsorption/desorption of hydrogen also happens in

the same potential region, but it is not well defined with a decreased resolution (one broad peak). It is worth noticed that the capacitive courant in the double layer region is larger for the alloy than for pure Pt, representing the higher capacitance of the BDD-$Pt_{80}Ru_{10}Sn_{10}$ electrode and therefore its ability to activate water at lower potential values. It is also important to notice that the potential window was limited in order to avoid formation of Pt oxides. This phenomenon can indeed induce Pt surface reorganization [24] and aggregation in the case of particles [25]; the use of such limited potential window also avoids dissolution of the alloying metals (especially Sn) that is one of the main limitation of using Pt alloyed with transition metals in acidic media. This limited scanning potential region for the study of ternary nanoparticles can also explain the more important cathodic current in the H adsorption-desorption region. Such a feature can be caused by surface impurities (*i.e.* the residual surfactant) that are less easily removed due to the lower potential reached in the anodic direction.
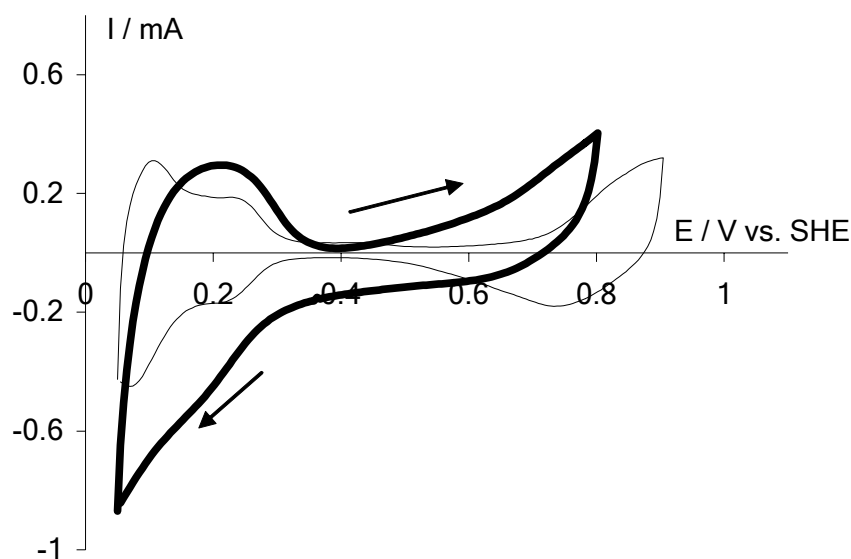
Figure 8.4: CV of BDD-supported Pt (thin line) and $Pt_{80}Ru_{10}Sn_{10}$ (thick line) electrodes. Recorded in 1 M $HClO_4$ at 50 mV s^{-1} and 25 °C.

The CV of Figure 8.5 show the electrooxidation of MeOH, EtOH, acetaldehyde and acetic acid on BDD-supported $Pt_{80}Ru_{10}Sn_{10}$ nanoparticles recorded at 25 °C and 20 mV s^{-1} in 1 M $HClO_4$ + 0.1 M electroactive species solutions. Specific molar currents are plotted with respect to the total amount of metals deposited on the diamond substrate (*i.e.* Pt + Ru + Sn), determined on the basis of AAS titration. It can be seen from the voltammograms of Fig. 8.5 that the specific molar current in the case of methanol oxidation is very high compared to those of other fuels. This ternary electrocatalyst is therefore more active toward methanol electrooxidation, and the

measured specific molar current of methanol oxidation is almost the double than that of ethanol oxidation. Although it was suggested that bimetallic Pt/Sn nanoparticles activate the breaking of the ethanol C-C bond scission, it seems that this is not the case with ternary Pt/Ru/Sn. Within the inset of Fig. 8.5 the difference between acetic acid and acetaldehyde electrooxidation is shown: the former exhibits a lower specific molar current but both can be considered as very low and negligible compared to those of methanol and ethanol. Moreover the CV for acetaldehyde electrooxidation at $Pt_{80}Ru_{10}Sn_{10}$ does not show the two oxidation peaks that were observed both at Pt and $Pt_{80}Sn_{20}$ (see Fig. 7.20 of this manuscript). It can therefore be reasonably stated that the ternary catalyst is inactive toward acetaldehyde and acetic acid electrooxidation. This can partially explains the lack of activity of Pt/Ru/Sn nanoparticles toward ethanol electrooxidation.
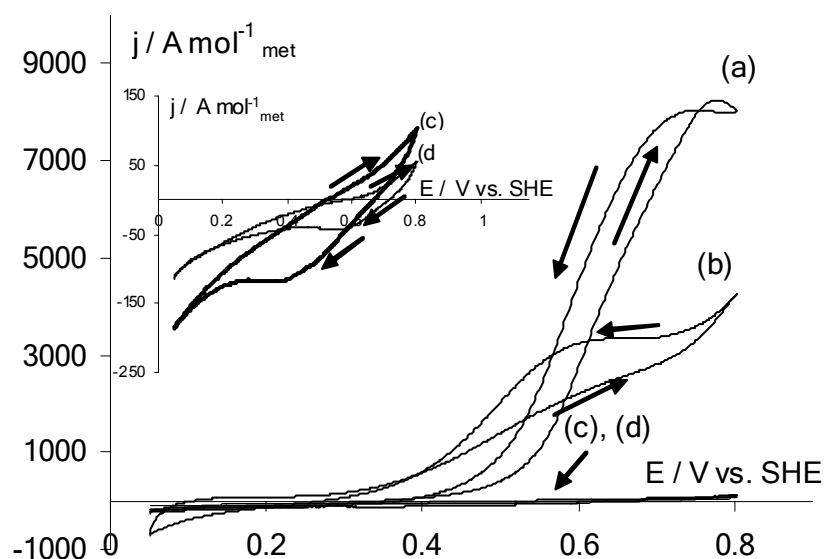
Figure 8.5: CV of BDD-supported $Pt_{80}Ru_{10}Sn_{10}$ nanoparticles in the presence of (a) methanol, (b) ethanol, (c) acetaldehyde and (d) acetic acid. Recorded in 1 M $HClO_4$ + 0.1 M electroactive species solutions at 20 mV s^{-1} in and 25°C.

From the previous equations the specific molar current of EtOH electrooxidation should theoretically be the double than that for MeOH electrooxidation. This is not the case; the specific molar current of methanol electrooxidation is roughly 3 times higher than that for ethanol (Fig. 8.5). For this reason, if a total oxidation of MeOH is

If one considers the total oxidation of methanol 6 electrons should be exchanged and 12 electrons in the case of the total electrooxidation of ethanol, as shown in Equations 8.4 and 8.5:

$$H_2O + CH_3OH \rightarrow CO_2 + 6e^- + 6H^+ \tag{8.4}$$

$$3H_2O + C_2H_5OH \rightarrow 2CO_2 + 12e^- + 12H^+ \tag{8.5}$$

considered (6e⁻), only 2e⁻ would be released from EtOH electrooxidation. A possible mechanism that gives this number of exchanged electrons should involve the formation of acetic acid and/or acetaldehyde as intermediates, as described in Equation 8.6:

$$C_2H_5OH \rightarrow (C_2H_4O \text{ and/or } CH_3COOH) + 2e^- + 2H^+ \qquad (8.6)$$
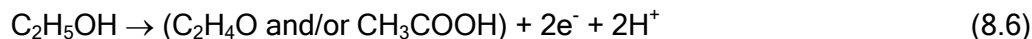
The CV of acetic acid and acetaldehyde in Fig. 8.5 do not show any oxidation of these two intermediates, meaning that EtOH electrooxidation may be stopped at these stages. Furthermore, as the specific molar current of EtOH electrooxidation is lower than that for MeOH electrooxidation, it can be concluded that ternary nanoparticles do not activate the ethanol C-C bond scission. The major issue in the development of Direct Ethanol Fuel Cells, as well as Fuel Cells fed with 2-propanol for instance, is the finding of catalyst capable of activation of the C-C bond breaking [26, 27]. Therefore this ternary catalyst cannot be considered as a good one for ethanol electrooxidation.

Figure 8.6 shows the linear sweep voltammograms of BDD-supported Pt (a), $Pt_{80}Sn_{20}$ (b) $Pt_{80}Ru_{10}Sn_{10}$ (c) nanoparticles in 1 M $HClO_4$ + 0.1 M EtOH solution. This figure reveals the shift in the onset of EtOH oxidation on the different types of surface. It can be seen that the onset of EtOH electrooxidation is appreciably shifted to lower potential values using a multi-metallic surface rather than Pt. The current increase demonstrates that the surface reaction occurs between adsorbed hydroxyl radicals and adsorbed CO (water activation thus takes place). The surface reaction on Pt particles only takes place when Pt activates water discharge at relatively high potentials (0.5 V) compared to that of alcohol dehydrogenation (around 0.05V), whereas in the case of the binary catalyst the second metal activates water at lower potentials (0.3 V). The use of ternary nanoparticles allows lowering again the potential onset of EtOH oxidation compared to $Pt_{80}Sn_{20}$ particles.
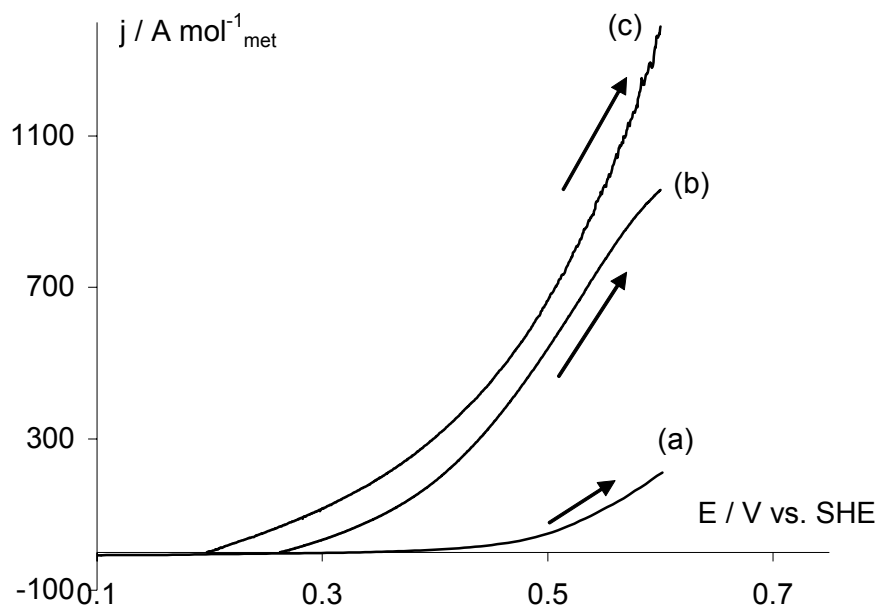
Figure 8.6: Polarization curves and onset of EtOH oxidation on BDD-supported Pt (a), $Pt_{80}Sn_{20}$ (b) and $Pt_{80}Ru_{10}Sn_{10}$ (c) nanoparticles. Recorded in 1 M $HClO_4$ + 0.1 M EtOH at $1mV\ s^{-1}$ and 25°C.

Electrochemical measurements have shown that for MeOH oxidation ternary $Pt_{80}Ru_{10}Sn_{10}$ particles are far more efficient than both Pt/Ru and Pt/Sn surfaces (specific molar currents of 8000, 3800 and 2300 A mol^{-1}_{met} by CV, respectively as it can be seen in Chapters 6 and 7). This means that the ternary catalyst is very efficient toward MeOH oxidation. The addition of the two metals together (Sn and Ru) has a beneficial effect on MeOH specific molar current. On the contrary the binary $Pt_{80}Sn_{20}$ catalyst is more efficient for EtOH oxidation than Pt/Ru surfaces, certainly because of the ability of Pt/Sn to promote the ethanol C-C bond breaking. Even if the use of ternary nanoparticles allows the shift of the onset potential of EtOH electrooxidation to lower values compared to that of bimetallic Pt/Sn, it seems, regarding the relative values of MeOH and EtOH oxidation specific molar currents, that the breaking of the ethanol C-C bond is not activated on $Pt_{80}Ru_{10}Sn_{10}$.

4. CONCLUSIONS

The particular effect of Sn addition on the electrocatalytic activity of Pt toward EtOH electrooxidation is certainly due to higher electronic interactions between Pt and Sn than between Pt and Ru. This can be seen on Figure 8.3, in which the chemical shift of the Pt$4f_{7/2}$ line of Pt^0 is more pronounced for the Pt-rich Pt/Sn surface, due to the higher difference of electronegativity (χ) between Pt and Sn. However in the case of $Pt_{80}Ru_{10}Sn_{10}$, the Pt $4f_{7/2}$ line moves back to its initial value in

Pt. It can be supposed here that the electronic transfer occurs between Sn and Ru (same $\Delta\chi$ of 0.4 as between Pt and Sn), thus modifying Ru electronic properties. Consequently a new $^\cdot$OH state can be created, weakly adsorbed on Ru and of higher mobility and reactivity. This new $^\cdot$OH state could explain both the reduced onset potential of EtOH electrooxidation and the enhanced electrocatalytic activity for MeOH electrooxidation, since these processes can be related to surface reaction between adsorbed CO and adsorbed $^\cdot$OH. However it seems that this electronic interaction between Sn and Ru hides the beneficial effect of Sn toward EtOH electrooxidation in bimetallic surface. Electronic transfer between Sn and Ru rather than Sn and Pt certainly impeaches modification of Pt electronic properties, leading to an almost unchanged behavior toward EtOH and consequently inability to promote the ethanol C-C bond scission. Obviously other experiments have to be performed to validate this assumption, for instance with varying the composition of the ternary particles but keeping the Pt content at a constant value of 80 at. % in order to maintain the alcohols superior adsorption properties of the surface (at room temperature).

5. REFERENCES

[1] G. Cao, *Nanostructures & Nanomaterials. Synthesis, Properties and Applications*, Imperial College Press, London (2004).

[2] W. Vielstich, H. A. Gasteiger, A. Lamm (Eds.), *Handbook of Fuel Cells - Fundamentals, Technology and Applications*, John Wiley & Sons, Ltd., New York (2003).

[3] A. Hamnett, in: A. Wieckowski (Ed.) *Interfacial Electrochemistry - Theory, Experiments, and Applications*, Marcel Dekker, Inc., New York (1999), p. 843.

[4] L. Dubau, F. Hahn, C. Coutanceau, J.-M. Léger, C. Lamy, *J. Electroanal. Chem.* **554-555** (2003), 407.

[5] S. L. Gojkovic, T. R. Vidakovic, D. R. Durovic, *Electrochim. Acta* **48** (2003), 3607.

[6] F. Delime, J.-M. Léger, C. Lamy, *J. Appl. Electrochem.* **29** (1999), 1249.

[7] C. Lamy, S. Rousseau, E. M. Belgsir, C. Coutanceau, J.-M. Léger, *Electrochim. Acta* **49** (2004), 3901.

[8] M. Watanabe, S. Motoo, *J. Electroanal. Chem.* **60** (1975), 267.

[9] K.-W. Park, J.-H. Choi, B.-K. Kwon, S.-A. Lee, Y.-E. Sung, H.-Y. Ha, S.-A. Hong, H. Kim, A. Wieckowski, *J. Phys. Chem. B* **106** (2002), 1869.

[10] W. C. Choi, J. D. Kim, S. I. Woo, *Catal. Today* **74** (2002), 235.

[11] M. Gotz, H. Wendt, *Electrochim. Acta* **43** (1998), 3637.

[12]   Z. Jusys, T. J. Schmidt, L. Dubau, K. Lasch, L. Jorissen, J. Garche, R. J. Behm, *J. Power Sources* **105** (2002), 297.

[13]   K. L. Ley, R. Liu, C. Pu, Q. Fan, N. Leyarovska, C. Segre, E. S. Smotkin, *J. Electrochem. Soc.* **144** (1997), 1543.

[14]   M. Boutonnet, J. Kizling, P. Stenius, *Colloids Surf.* **5** (1982), 209.

[15]   H. Härelind Ingelsten, R. Bagwe, A. Palmqvist, M. Skoglundh, C. Svanberg, K. Holmberg, D. O. Shah, *J. Colloid Interface Sci.* **241** (2001), 104.

[16]   S. Qiu, J. Dong, G. Chen, *J. Colloid Interface Sci.* **216** (1999), 230.

[17]   C.-C. Wang, D.-H. Chen, T.-C. Huang, *Colloids Surf. A* **189** (2001), 145.

[18]   J. Solla-Gullón, V. Montiel, A. Aldaz, J. Clavilier, *Electrochem. Comm.* **4** (2002), 716.

[19]   J. Solla-Gullón, F. J. Vidal-Iglesias, V. Montiel, A. Aldaz, *Electrochim. Acta* **49** (2004), 5079.

[20]   M.-L. Wu, D.-H. Chen, T.-C. Huang, *Chem. Mater.* **13** (2001), 599.

[21]   J. M. Perez, B. Beden, F. Hahn, A. Aldaz, C. Lamy, *J. Electroanal. Chem.* **262** (1989), 251.

[22]   D. Gandini, E. Mahé, P.-A. Michaud, W. Haenni, A. Perret, Ch. Comninellis, *J. Appl. Electrochem.* **30** (2000), 1345.

[23]   C. Stuhlmann, H. Hoffschulz, K. Wandelt, in: A. Wieckowski (Ed.) *Interfacial Electrochemistry - Theory, Experiments, and Applications*, Marcel Dekker, Inc., New York (1999), p. 805.

[24]   J. Clavilier, D. Armand, *J. Electroanal. Chem.* **199** (1986), 187.

[25]   Y. Takasu, Y. Fujii, K. Yasuda, Y. Iwanaga, Y. Matsuda, *Electrochim. Acta* **34** (1989), 453.

[26]   X. H. Xia, H.-D. Liess, T. Iwasita, *J. Electroanal. Chem.* **437** (1997), 233.

[27]   D. Cao, S. H. Bergens, *J. Power Sources* **124** (2003), 12.

Chapter 9   Theoretical Part

1.   INTRODUCTION

In this chapter theoretical considerations related to electrooxidation processes at Pt and Pt-based electrode surfaces will be presented. The case of oxidation of C_1 and C_2 alcohols at Pt-based surfaces will be specifically emphasized here as it is the main subject of this thesis. Firstly the bifunctional mechanism, as commonly proposed in literature, will be briefly presented (see also Chapter 2 of this thesis). Then a development of this mechanism will be investigated. For this purpose connections between classical liquid phase electrocatalysis and heterogeneous catalysis will be highlighted. A complex electrochemical reaction that involves adsorbed intermediates at the electrode surface will be regarded with the concepts and definitions of heterogeneous catalysis such as the donor-acceptor theory for instance [1-3]. Some limiting cases will be treated. Finally this treatment will be extended to the commonly accepted bifunctional mechanism of simple alcohols (methanol, ethanol...) electrooxidation at Pt-based surfaces and it was used in order to re-examine the results presented within the precedent chapters. The electronic (or ligand) effect will not be detailed within this chapter. This electronic effect consists in the modification of the Pt intrinsic electronic properties due to alloying and/or interacting with a second metal. As a consequence the Pt-CO bond strength is weakened and the removal of the poisoning intermediate becomes more facile. However this electronic effect remains difficult to estimate and its incorporation in the following treatment would have caused some additional problems.

2. THE BIFUNCTIONAL MECHANISM IN ELECTROCATALYSIS

The study of the electrochemical behaviour of platinum has attracted during the last decades a very large interest, and papers dealing with the characterization of Pt electrodes under different conditions (polycrystalline or single crystals, different supporting electrolytes) are numerous. Such an interest comes from the applicability of Pt surfaces in the Direct Alcohol Fuel Cell (DAFC) technology [4, 5] as Pt is considered as the only metal capable of alcohol dehydrogenation. Consequently the oxidation mechanisms of alcohols of interest for the DAFC (methanol, ethanol) have been extensively studied, and the question of reactions intermediates has been investigated experimentally by means of FTIR (Fourier Transform Infra-Red Spectroscopy), DEMS (Differential Electrochemical Mass Spectrometry) or electrochemical measurements [6-13]. Therefore the mechanism of methanol oxidation at Pt surfaces is well known and generally accepted to proceed via the

following sequence (Equations 9.1 to 9.3). This global mechanism is well summarized in the catalytic cycle of methanol electrooxidation on Pt presented in Figure 9.1. All the steps described within Eqs. 9.1 to 9.3 are clearly distinguishable on this picture in which the successive and fast dehydrogenation steps of methanol are detailed.
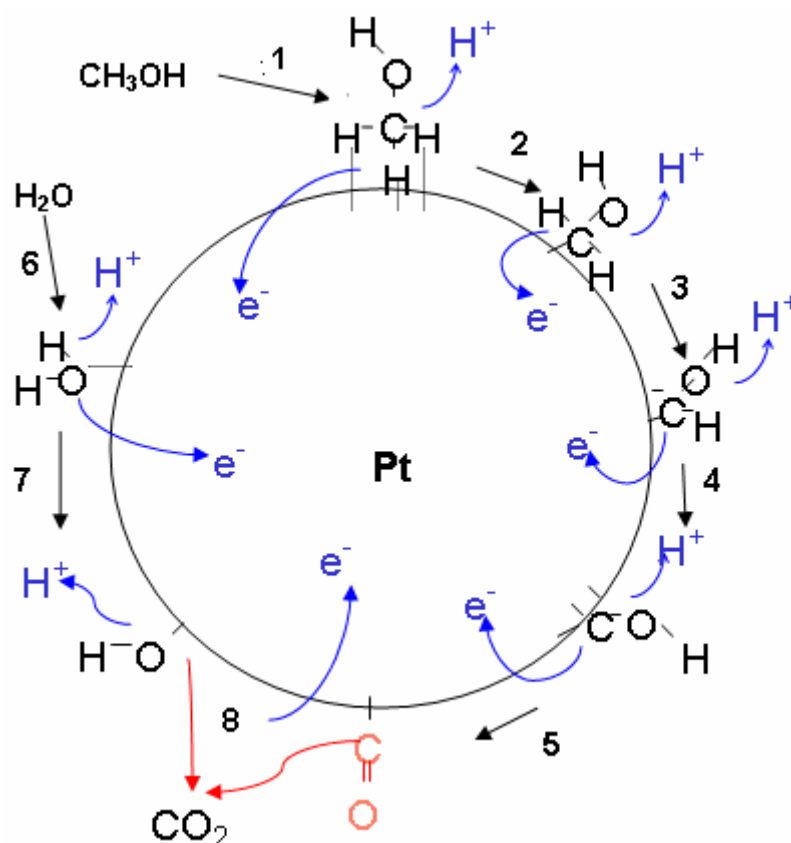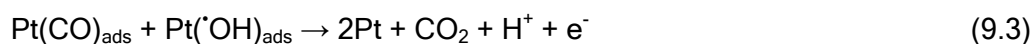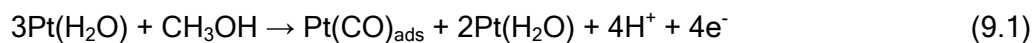
$$3Pt(H_2O) + CH_3OH \rightarrow Pt(CO)_{ads} + 2Pt(H_2O) + 4H^+ + 4e^- \quad (9.1)$$

$$Pt + H_2O \rightarrow Pt(^{\cdot}OH)_{ads} + H^+ + e^- \quad (9.2)$$

$$Pt(CO)_{ads} + Pt(^{\cdot}OH)_{ads} \rightarrow 2Pt + CO_2 + H^+ + e^- \quad (9.3)$$

Figure 9.1: Catalytic cycle of methanol electrooxidation on a Pt electrode. This cycle involves the following steps: adsorption (1) of one methanol molecule at three adjacent Pt sites, followed by the four successive and fast dehydrogenation steps (2-5) of adsorbed methanol leading to CO. In parallel water activation and adsorption (6) of hydroxyl radicals at Pt sites (7) take place and finally the surface reaction between adsorbed CO and $^{\cdot}OH$ yields free sites and CO_2 (8).

However the limitation of the Pt electrocatalyst comes from the fact that this metal is no able to dissociate water (Reaction 9.2) at potentials lower than 0.5 V vs. SHE (0.4V higher than the thermodynamic potential of methanol dehydrogenation). As a consequence the Pt surface is readily poisoned by adsorbed intermediates (CO) that block the catalytic sites of the surface, thus decreasing dramatically its electrocatalytic activity. In order to circumvent this problem, alloying (or mixing) Pt

with another metal capable of activating water dissociation at lower potential than Pt has been considered [14]. At this type of surface each one of the components has a specific role: Pt is charged of alcohol dehydrogenation and the second metal (Ru, Sn, Mo, W...) of water activation. The poisoning intermediate is then removed via a surface reaction between adsorbates. This bifunctional mechanism [15] is well described by Equations 9.4 to 9.6 and the catalytic cycle of Figure 9.2:

$$3Pt(H_2O) + CH_3OH \rightarrow Pt(CO)_{ads} + 2Pt(H_2O) + 4H^+ + 4e^- \tag{9.4}$$

$$M + H_2O \rightarrow M(^{\bullet}OH)_{ads} + H^+ + e^- \tag{9.5}$$

$$Pt(CO)_{ads} + M(^{\bullet}OH)_{ads} \rightarrow Pt + M + CO_2 + H^+ + e^- \tag{9.6}$$
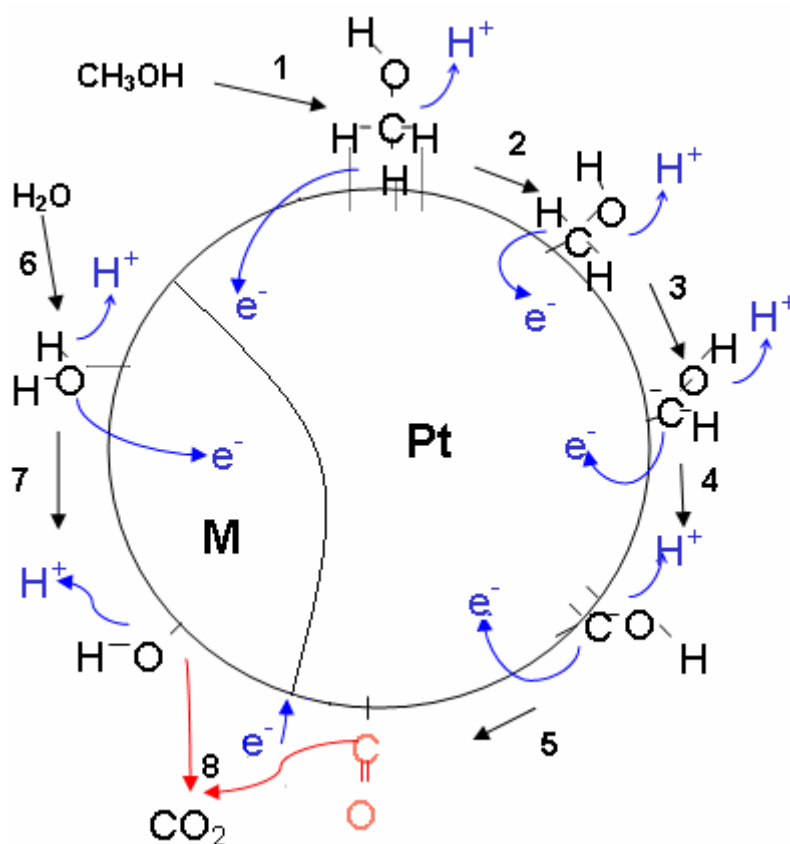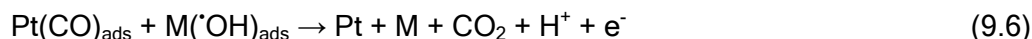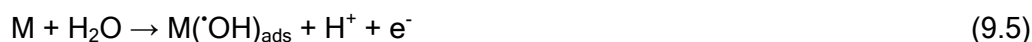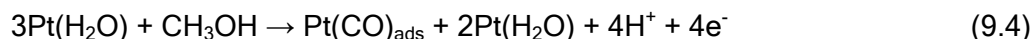
Figure 9.2: Catalytic cycle of methanol electrooxidation at a Pt/M bimetallic electrode. This cycle involves the following steps: adsorption (1) of one methanol molecule at three adjacent Pt sites, followed by the four successive and fast dehydrogenation steps (2-5) of adsorbed methanol leading to adsorbed CO at Pt. Water activation and adsorption (6) of hydroxyl radicals at M sites take place and finally the surface reaction (7) between adsorbed CO (Pt) and $^{\bullet}$OH (M) yields free sites and CO_2 (8).

3. PROPOSED OXIDATION MECHANISM

3.1. General case

As already stated in the Introduction of this Chapter, we propose here to point out the parallel between electrocatalysis on one hand and heterogeneous catalysis on

the other hand. For this purpose the works of Delmon et al. [1, 3] relative to gas phase reactions have been adapted to the electrochemical case. The mathematical model developed by this group to explain the catalytic synergy between MoO_3 and α-Sb_2O_4 towards n-ethyl formamide dehydration [3] has been more particularly regarded. The synergy between these two oxides was explained through a remote control by formation of mobile species (O spillover) at the controlling phase (donor: α-Sb_2O_4) surface that are transferred by diffusion to the controlled phase (acceptor: MoO_3) at which they react to form/regenerate active sites. The idea here is to extend this view to an electrochemical system. The general case of an electrochemical reaction with the involvement of adsorbed intermediate will thus be presented without further developments. The most specific case of methanol oxidation at Pt/Sn surface, which is of crucial interest in the framework of this thesis, will then be highlighted and developed within the next section.

The situation of this electrochemical reaction is depicted in Figure 9.3. The overall process can be described as the sequence of the following events: *(i)* electrochemical discharge of A to yield the adsorbed B species, *(ii)* electrochemical discharge of D leading to the adsorbed C species, and *(iii)* surface reaction between adsorbed species (B and C) to yield the final product P and regenerate free surface sites for adsorption processes.

Figure 9.3: Schematic view of an electrochemical reaction at a surface composed of a donor (Don) and an acceptor (Acc) phase.

However several facts, that make the system more complex, should be taken in mind:

- A can be discharged on both surfaces (donor and acceptor) with different rates
- D can be discharged on both surfaces (donor and acceptor) with different rates
- spillover of B from the acceptor to the donor or from the donor to the acceptor
- spillover of C from the donor to the acceptor or from the acceptor to the donor
- reaction between B and C on both surfaces (donor and acceptor)

In order to be treated and applied for methanol oxidation, the following simplifications (based on experimental results) can be brought to this system:

- B is formed only at the acceptor (Acc) and not adsorbed at the donor (Don) phase

- C is formed only at the donor (Don) and can be adsorbed at the acceptor (Acc) phase

- the reaction between B and C can take place only at the acceptor (Acc) phase or at the interface between the two phases

The electrochemical reaction (discharge of A) takes place only at the acceptor surface (Acc) and yields to B (Equation 9.7):

$$A_{sol} \rightarrow B^{Acc} + ne^- \tag{9.7}$$

The adsorption of C (by oxidation of D) to form a highly mobile and reactive species C occurs at the donor phase (Don) and only at the donor phase (Equation 9.8). Both reactions 9.7 and 9.8 are electrochemical, hence potential-dependent.

$$D_{sol} \rightarrow C^{Don} + n'e^- \tag{9.8}$$

Both species B and C may freely diffuse over their respective surface. Species B may not cross the border of the acceptor phase; hence it does not exist at the donor surface, while species C may be transferred from the donor phase to the acceptor phase (spillover) then transported by diffusion over this latter. Finally, B and C species can react with each other at the donor/acceptor interface or on the acceptor to yield the final product P (Equation 9.9) and create/regenerate active sites available for further adsorption.

$$B + C \rightarrow P \tag{9.9}$$

From a kinetic point of view, the overall mechanism can be described by the following relations. At the donor phase, the rate of formation R_C of active species C (in mol s^{-1}) is given by Equation 9.10:

$$R_C = k_C \, S^{Don} \, \Gamma_C^{Don} \, (1 - \theta_C^{Don}) \tag{9.10}$$

where k_C is the electrochemical rate constant of C formation at the donor phase (s^{-1}), S^{Don} is the surface area of the donor (m^2), Γ_C^{Don} is the saturation concentration of C at the donor phase (mol m^{-2}), and θ_C^{Don} is the fraction of surface sites occupied by C. The rate constant k_C is potential-dependent according to Equation 9.11 [16]:

$$k_C = k_C^{ox} \exp\left[(-\alpha_C^{Don} n' FE) / RT\right] \tag{9.11}$$

where k_C^{ox} is the standard rate constant of D oxidation (C formation) in s^{-1}, α_C^{Don} is the anodic transfer coefficient relative to C formation at the donor phase, n' is the number of exchanged electrons in the formation of C (oxidation of D), F is the Faraday's constant ($\approx$ 96500 C mol^{-1}), E is the applied potential vs. a reference electrode (V), R is the molar gas constant (8.314 J mol^{-1} K^{-1}) and T is the temperature (K). The rate of electrochemical formation of B at the acceptor surface is given by Equation 9.12, in which k_B is potential-dependent according to Equation 9.13 [16]:

$$R_B = k_B \, S^{Acc} \, \Gamma_B^{Acc} \, (1 - \theta_B^{Acc}) \tag{9.12}$$

$$k_B = k_B^{ox} \exp[(-\alpha_B^{Acc} nFE) / RT] \tag{9.13}$$

where S^{Acc} is the surface area of the acceptor (m^2), Γ_B^{Acc} is the saturation concentration of B at the acceptor phase (mol m^{-2}), θ_B^{Acc} is the fraction of the acceptor surface sites occupied by B at the acceptor phase, k_B^{ox} is the standard rate constant of A oxidation (B formation) in s^{-1}, α_B^{Acc} is the anodic transfer coefficient of B formation at the acceptor phase and n is the number of exchanged electrons during the oxidation of A (formation of B).

The rate of transfer of species C (in mol s^{-1}) via spillover from the donor to the acceptor is given by Equation 9.14:

$$R_{sp} = k_{sp} L ([C]^{Don} - [C]^{Acc}) \tag{9.14}$$

where k_{sp} is the spillover transfer coefficient of C (m s^{-1}), L is the characteristic length of the donor/acceptor double phase boundary (m) which accounts for not only the geometrical length but also the quality of the contact between the two phases, and $[C]^{Don}$ and $[C]^{Acc}$ are the surface concentrations of C at the donor and acceptor phases (mol m^{-2}), respectively.

Finally, the rate of surface reaction between B and C, that may take place at the acceptor or at the donor/acceptor interface, can be expressed by Equation 9.15:

$$R_r = k_r S_r [C] [B] \tag{9.15}$$

where k_r is the reaction rate constant (m^2 mol^{-1} s^{-1}) of reaction 9.9, S_r is the area of the surface where the reaction occurs (m^2), and [B] and [C] are the surface concentration of B and C at the reaction surface.

The aim of this model is also to evaluate the influence of experimental parameters such as the applied potential, the relative quantities of the two phases and the quality of the dispersion between them on the overall reaction kinetics. For this purpose a dimensionless parameter λ can be defined (Equation 9.16)

$$\lambda = R_r / R_{sp} \tag{9.16}$$

which is the ratio of the rate of surface reaction (Equation 9.15) and the rate of spillover (Equation 9.14). Several limiting cases can be treated according to the value of λ.

(i)   λ >> 1, the reaction (Equation 9.9) is fast compared to spillover of reactive species that is consequently the rate-determining step (rds). In this case the reaction takes place at the interface between the two phases.

(ii)   λ << 1, transfer by spillover of reactive species is fast compared to the reaction rate and the surface reaction between adsorbed species is the rds. In this case transfer of species by spillover from the donor phase to the acceptor phase and it can be considered that the reaction takes place at the acceptor phase.

This model will be applied during the next section, as it is the main subject of this thesis, on the real case of methanol oxidation at a Pt/Sn surface. In this view of methanol oxidation at Pt/Sn, Pt is considered as the acceptor phase (Acc) whereas Sn is regarded as the donor phase (Don). The limiting cases will be treated according to real limiting situations that can come from the employed metal (Sn) or applied potential for instance.

3.2. Application to methanol oxidation (Pt/Sn system)

The view of the electrochemical reaction described above can be extended to the oxidation of methanol at a Pt/Sn bimetallic surface, where Pt is the acceptor and Sn the donor. The aim of this treatment is to link the bifunctional theory of methanol electrocatalysis [15] with the concepts of heterogeneous catalysis. Fundamentally the role of each of the two metals is the same as in the bifunctional mechanism; however the oxygenated species that react at the surface with the adsorbed poison [17] are supposed here to be species transported by spillover. For simplicity it is supposed that they are, as commonly accepted, adsorbed hydroxyl radicals that come from water discharge at Sn (donor) sites.

This situation is described by the scheme of Figure 9.4. As already stated Pt is considered to be the acceptor (Acc) whereas Sn is the donor (Don). At Sn hydroxyl radicals (species that spillover) are formed from water discharge (Equation 9.17):

$$H_2O \rightarrow {}^{\bullet}OH^{Sn} + H^+ + e^- \qquad \text{(takes place only on Sn)} \qquad (9.17)$$
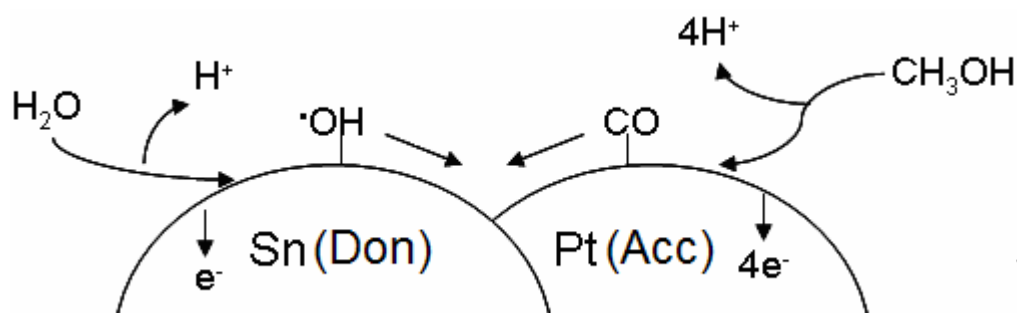
Figure 9.4: Schematic view of methanol oxidation at a surface composed of a Sn (donor) and a Pt (acceptor) phase.

As water is the solvent, there is no limitation by diffusion of water molecules from the bulk solution to the surface so that the rate of formation of adsorbed hydroxyl radicals can simply be expressed as:

$$R_{OH} = k_{OH} \, S^{Sn} \, \Gamma_{OH}{}^{Sn} \, (1 - \theta_{OH}{}^{Sn}) \qquad (9.18)$$

where k_{OH} is the electrochemical rate constant of ${}^{\bullet}OH$ formation (s^{-1}) that depends on the applied potential according to Equation 9.19, S^{Sn} is the surface area of the Sn

phase (m^2), Γ_{OH}^{Sn} is the saturation surface concentration of $^{\bullet}OH$ at Sn phase (mol m^{-2}) and θ_{OH}^{Sn} is the fraction of Sn surface sites occupied by $^{\bullet}OH$ species.

$$k_{OH} = k_{OH}^{ox} \exp [(-\alpha_{OH}^{Sn} FE) / RT] \qquad (9.19)$$

At the Pt (acceptor) sites, methanol dissociatively adsorbs to form CO that blocks the catalytic sites. This process is accompanied by the release of four protons and electrons as described in Equation 9.20:

$$CH_3OH_{sol} \rightarrow CO^{Pt} + 4H^+ + 4e^- \text{ (takes place only on Pt)} \qquad (9.20)$$

The rate of CO formation can thus be expressed according to Equation 9.21:

$$R_{CO} = k_{CO} S^{Pt} \Gamma_{CO}^{Pt} (1 - \theta_{CO}^{Pt}) \qquad (9.21)$$

where k_{CO} is potential-dependent according to Equation 9.22, and S^{Pt} is the surface area of the Pt phase (m^2):

$$k_{CO} = k_{CO}^{ox} \exp [(-4\alpha_{CO}^{Pt} FE) / RT] \qquad (9.22)$$

Then the rate of spillover of $^{\bullet}OH$ species from the donor to the acceptor is given by Equation 9.23:

$$R_{sp} = k_{sp} L ([^{\bullet}OH]^{Sn} - [^{\bullet}OH]^{Pt}) \qquad (9.23)$$

Finally the rate of surface reaction between adsorbed carbon monoxide and hydroxyl radicals (Reaction 9.24)

$$CO + {}^{\bullet}OH \rightarrow CO_2 + H^+ + e^- \qquad (9.24)$$

can be expressed according to Equation 9.25:

$$R_r = k_r S_r [^{\bullet}OH] [CO] \qquad (9.25)$$

Obviously it is possible to assume that, at steady-state conditions, the rate of formation of reactants are equal to their rate of consumption, *i.e.*:

$$R_{OH} = R_r = R_{CO} \qquad (9.26)$$

The aim of this model is also to evaluate the influence of the applied potential, the relative quantities of the two metals and the quality of the dispersion between them. For this purpose two real cases, that depend on the employed alloying metal and applied potential, can be treated.

(i) $\lambda \gg 1$, the surface reaction (Eq. 9.24) is very fast compared to spillover of $^{\bullet}OH$ species (Eq. 9.23) and the reaction takes place at the Pt/Sn interface, considering that *(i)* CO is not formed and not adsorbed on Sn, *(ii)* $^{\bullet}OH$ is not formed on Pt but can adsorb on it, and *(iii)* CO diffusion on Pt is fast relative to reaction (9.24).

In this case it is possible to write that, under steady-state conditions, the rate of $^{\bullet}OH$ formation at Sn is equal to the rate of $^{\bullet}OH$ spillover from Sn to Pt, *i.e.*:

$$R_{OH} = R_{sp} \qquad (9.27)$$

which means that:

$$k_{OH} S^{Sn} \Gamma_{OH}^{Sn} (1 - \theta_{OH}^{Sn}) = k_{sp} L ([^{\bullet}OH]^{Sn} - [^{\bullet}OH]^{Pt}) \qquad (9.28)$$

It can be assumed that $[^\bullet OH]^{Sn} \gg [^\bullet OH]^{Pt}$ and, as $\Gamma_{OH}{}^{Sn} \theta_{OH}{}^{Sn} = [^\bullet OH]^{Sn}$, Eq. 9.28 can be simplified into:

$$k_{OH} S^{Sn} (1 - \theta_{OH}{}^{Sn}) = k_{sp} L \theta_{OH}{}^{Sn} \tag{9.29}$$

Therefore it comes that:

$$\theta_{OH}{}^{Sn} = \frac{k_{OH}S^{Sn}}{k_{OH}S^{Sn} + k_{sp}L} \tag{9.30}$$

By replacing $\theta_{OH}{}^{Sn}$ by its expression in Eq. 9.18 it comes that:

$$R_{OH} = \frac{i_{OH}}{F} = \Gamma_{OH}{}^{Sn} \frac{k_{OH}S^{Sn}k_{sp}L}{k_{OH}S^{Sn} + k_{sp}L} \tag{9.31}$$

and therefore it becomes possible to relate the measured current with the applied potential as described in Equation 9.32 in which k_{OH} is potential-dependent:

$$i_{OH} = \Gamma_{OH}{}^{Sn}F\frac{k_{OH}S^{Sn}k_{sp}L}{k_{OH}S^{Sn} + k_{sp}L} \tag{9.32}$$

Two limiting cases can be treated here:

a) at high potential it is possible to assume that $^\bullet OH$ spillover is very slow compared to $^\bullet OH$ formation, so that:

$$k_{sp}L \ll k_{OH}S^{Sn} \tag{9.33}$$

In this case $\theta_{OH}{}^{Sn}$ tends to unity and both R_{OH} and R_{sp} tend to zero. It means that formation of $^\bullet OH$ at the donor surface is inhibited, due to saturation of the donor surface by adsorbed hydroxyl radicals.

b) on the contrary when $^\bullet OH$ spillover is very fast compared to $^\bullet OH$ formation at low potentials, it is possible to write that:

$$k_{sp}L \gg k_{OH}S^{Sn} \tag{9.34}$$

Hence $\theta_{OH}{}^{Sn}$ tends to zero, and the rate of $^\bullet OH$ formation equals:

$$R_{OH} = k_{OH}S^{Sn}\Gamma_{OH}{}^{Sn} \tag{9.35}$$

In this case the rate is independent of the contact length and quality between donor and acceptor (L) and depends only on the applied potential and on the available active sites at the donor surface ($S^{Sn}\Gamma_{OH}{}^{Sn}$).

(ii) $\lambda \ll 1$, the spillover of $^\bullet OH$ species is fast compared to the rate of the overall reaction at the acceptor.

In this case it is possible to write that, under steady-state conditions, the quantity of $^\bullet OH$ formed at Sn sites is equal to the quantity of $^\bullet OH$ reacting at Pt sites:

$$R_{OH}(Sn) = R_r(Pt) \tag{9.36}$$

which means that:

$$k_{OH} S^{Sn} \Gamma_{OH}{}^{Sn} (1 - \theta_{OH}{}^{Sn}) = k_r S^{Pt} [^\bullet OH]^{Pt} [CO]^{Pt} \tag{9.37}$$

This expression can be written as:

211

$$k_{OH}\, S^{Sn}\, \Gamma_{OH}^{Sn}\, (1 - \theta_{OH}^{Sn}) = k_r\, S^{Pt}\, \theta_{OH}^{Pt}\, \theta_{CO}^{Pt}\, (\Gamma_{OH}^{Pt})^2 \qquad\qquad (9.38)$$

This is a Langmuir-Hinshelwood type kinetics. Three cases can be found depending on the applied potential:

a) at low potential it can be assumed that $\theta_{OH}^{Pt} \approx 0$ and hence that the reaction rate is low.

b) at high potential it can be assumed that $\theta_{OH}^{Pt} \approx 1$, hence θ_{CO}^{Pt} tends to zero and again the reaction rate is low.

c) at intermediate potentials the condition $\theta_{OH}^{Pt} = \theta_{CO}^{Pt}$ can be fulfilled where the rate reaches a maximum.

4. DISCUSSION OF THE PROPOSED MODEL

The aim of this section is to discuss, on the basis of the experimental results obtained in the framework of the thesis, the validity and limitations of the model proposed above. More particularly experimental findings such as the influence of the applied potential, influence of the acceptor (Pt) / donor (M) molar ratio and contact quality on the electrocatalytic behaviour of the various Pt-based nanoparticles synthesized here will be regarded and compared with the predictions of the model. Some other parameters, such as the influence of the temperature, will also be discussed and compared with the predictions of our model. Two main cases can be discriminated depending on the value of the dimensionless parameter λ:

$$\lambda = R_r \text{ (eq.9.23)} / R_{sp} \text{ (eq. 9.24)} \qquad\qquad (9.16)$$

When the dimensionless parameter λ is much higher than unity, the surface reaction between adsorbed intermediates is very fast compare to spillover of reactive species and therefore the reaction takes place at the acceptor/donor interface. In this case at high potentials the rate of ˙OH formation is very fast compared to that of ˙OH spillover, and therefore R_{OH} at the donor (M) tends to zero. Formation of ˙OH at the donor surface is inhibited due to surface saturation by already adsorbed hydroxyl radicals that can not react with CO due to their low spillover rate. The formation of surface metal oxides at high potentials can also be considered. This may explain in some extent the current decrease that follows the first oxidation peak observed by CV (see Fig. 7.13 for instance). From this point of view the nature of the surface on which oxygen-containing species are formed is of secondary importance. The key point is that since the donor phase is passivated by oxygen-containing species the reaction can not take place and therefore the current decreases. On the other hand, when rate of spillover of reactive species (˙OH) is very fast compared to that of their formation, the rate then depends only on the applied potential and on the available active sites at the donor phase, and is independent of the contact length and quality between the

donor and the acceptor phases. This may be the case of Pt/Ru surfaces. It is indeed well accepted in literature that Pt/Ru is the most efficient system for the electrocatalysis of methanol oxidation. The studied Pt/Ru surfaces have been synthesized using various experimental techniques and moreover the question of the necessity of alloying the metals together has also been pointed out. The microemulsion-synthesized Pt/Ru nanoparticles studied during this work have also exhibited superior electrocatalytic activity toward methanol oxidation and from this point of view the results presented in this thesis on the study of Pt/Ru nanoparticles seem to be consistent with both the literature and the model. Pt/Ru electrocatalysts could therefore certainly be considered as surfaces on which the surface reaction between adsorbed intermediates is very fast compared to spillover of reactive species.

If λ is much lower than unity then the spillover of reactive species is very fast compared to the overall reaction at the acceptor. The surface reaction is a Langmuir-Hinshelwood type reaction and depending on the applied potential three cases can be defined. At low potential values it can be assumed that the $^{\bullet}OH$ coverage is negligible so that the reaction rate is low. However the use of a bimetallic surface with a donor phase that allows water activation (and hence oxygen-containing species formation) at lower potential values contributes to the enhancement of the reaction rate. From this point of view a high M (Sn) content should be desired. However it must be kept in mind that CO must also be formed at the acceptor (Pt) phase so that an ideal balance between the surface alcohol adsorption properties on one hand and abilities to form oxygen-containing species on the other hand must be found. Within the synthesized bimetallic nanoparticles during this thesis, it appears that the most efficient ones toward alcohol electrooxidation at room temperature are Pt-rich ones, presumably due to their superior properties of dissociative alcohol adsorption. On the contrary at high potential values it can be considered that the platinum phase surface is saturated by oxygen-containing species so that in this case also the reaction rate is low. Alcohol dissociative adsorption is hence inhibited and from this point of view both the Pt/M ratio and the contact length and quality between the two phases appear of secondary importance. This is not the case at intermediate potential values, for which the rate reaches a maximum. In this case again an ideal balance between surface adsorption properties and water activation abilities must be found.

However it must be mentioned that this model has its limitations. The mathematical treatment developed above is indeed based on an over-simplified view of the whole process. It has been considered that the formation of CO from methanolic dissociative adsorption could only take place at Pt sites and could not be

adsorbed at Sn sites, and that ˙OH formation could occur only at Sn sites and could be adsorbed at Pt sites. Consequently it has been stated that the surface reaction between these adsorbed intermediates could only occur at the Pt/Sn interface or at the Pt phase. Moreover the diffusion of adsorbed intermediates over the surfaces on which they have been respectively formed has not been taken into account and neglected compared to spillover of reactive species. Obviously the situation is not so simple; at high potential values hydroxyl radicals can for instance be formed at both donor (M) and acceptor (Pt) sites. A more accurate model would consider all these parameters, but the mathematical treatment of such a more realistic view would be quite more complex. It can also be seen that the influence of the Pt/M molar ratio does not appear clearly. Finally it can also be supposed from the model that an increase in temperature will induce a concomitant increase in rates of reaction. However, and it remains another limitation to this model, the reaction rate of the surface reaction (Eq. 9.9) and the adsorption properties of both the acceptor and the donor phases change with the temperature (different activation energies). Consequently the simplifications performed above would be no longer valid. Therefore an accurate treatment of the influence of the temperature on the overall reaction must consider the temperature dependence of the surface reaction rate and of adsorption properties, and on the subsequent changes in the reactive species surface coverage, of the two respective phases.

5. CONCLUSIONS

During this part of the thesis a theoretical model for the electrooxidation of methanol at Pt/M (M = Ru, Sn) surfaces has been proposed and developed. The basic idea was to establish the parallel between electrocatalysis on one hand and heterogeneous catalysis on the other hand, which has never been done to the best of our knowledge. For this purpose the donor-acceptor theory of heterogeneous catalysis has been applied and adapted to the case of an electrochemical reaction involving adsorbed intermediates (methanol electrooxidation at Pt/M surfaces). The model is based on the assumption that hydroxyl radicals (or other oxygen-containing species involved in the CO oxidative removal) can be considered as spillover species. Starting from this consideration, Pt was regarded as the acceptor and M (Ru, Sn) as the donor (supplier of oxygen-containing species) phase. The development of this model has allowed the establishments of relationships between the applied potential and the measured oxidation current in a number of real limiting cases. The model appears to be consistent with the conclusions from results presented in this work. Further improvements of the model would take into account the possible

formation of hydroxyl radicals at Pt sites at high potentials or the diffusion of reactive species over the surface on which they have been formed for instance. A more precise study of the influence of the temperature, taking into account the temperature dependence of the adsorption properties of both the acceptor (Pt) and the donor (Sn) phases and of the surface reaction rate, could also be integrated into the model. In this case also the influence of the Pt/Sn ratio should appear more obvious.

6. LIST OF SYMBOLS

Roman symbols

E	Applied potential vs. a reference	V
L	Characteristic length of donor/acceptor interface	m
i	Measured oxidation current	A
k	Reaction rate constant	s^{-1} or m^2 mol^{-1} s^{-1}
n (n')	Number of exchanged electrons	
R	Reaction rate	$mol\ s^{-1}$
R	Molar gas constant	$8.314\ J\ mol^{-1}\ K^{-1}$
S	Surface area	m^2

Greek Symbols

α	Anodic transfer coefficient
λ	Reaction rate to spillover rate ratio
θ	Fraction of occupied sites
Γ	Saturation surface concentration $mol\ m^{-2}$

Superscript

Acc	Relative to the acceptor phase
Don	Relative to the donor phase
ox	Relative to an oxidation process
Pt	Relative to Pt sites
Sn	Relative to Sn sites

Subscript

B	Relative to B formation (discharge of A)
C	Relative to C formation (discharge of D)
CO	Relative to CO formation
r	Relative to the surface reaction between adsorbed intermediates

OH   Relative to ˙OH formation

sp   Relative to spillover from acceptor to donor

7.   REFERENCES

[1]   B. Delmon, *Surf. Rev. Lett.* **2** (1995), 25.

[2]   M. P. Kiskinova, *Poisoning and Promotion in Catalysis based on Surface Science Concepts and Experiments*. Studies in Surface Science and Catalysis, ed. B. Delmon, J. T. Yates. Vol. 70, Elsevier, Amsterdam (1992).

[3]   F. Melo Faus, B. Zhou, H. Matralis, B. Delmon, *J. Catal.* **132** (1991), 200.

[4]   A. Hamnett, in: W. Vielstich, H. A. Gasteiger, A. Lamm (Eds.), *Handbook of Fuel Cells - Fundamentals, Technology and Applications*, John Wiley & Sons, Ltd., New York (2003), p. 305.

[5]   N. A. Hampson, M. J. Willars, B. D. McNicol, *J. Power Sources* **4** (1979), 191.

[6]   G. R. Mundy, R. J. Potter, P. A. Christensen, A. Hamnett, *J. Electroanal. Chem.* **279** (1990), 257.

[7]   T. Iwasita, R. Dalbeck, E. Pastor, X. Xia, *Electrochim. Acta* **39** (1994), 1817.

[8]   P. A. Christensen, A. Hamnett, J. Munk, G. L. Troughton, *J. Electroanal. Chem.* **370** (1994), 251.

[9]   T. Iwasita, E. Pastor, *Electrochim. Acta* **39** (1994), 531.

[10]   X. H. Xia, T. Iwasita, F. Ge, W. Vielstich, *Electrochim. Acta* **41** (1996), 711.

[11]   J. Munk, P. A. Christensen, A. Hamnett, E. Skou, *J. Electroanal. Chem.* **401** (1996), 215.

[12]   X. H. Xia, H.-D. Liess, T. Iwasita, *J. Electroanal. Chem.* **437** (1997), 233.

[13]   L. Dubau, F. Hahn, C. Coutanceau, J.-M. Léger, C. Lamy, *J. Electroanal. Chem.* **554-555** (2003), 407.

[14]   A. B. Anderson, E. Grantsharova, S. Seong, *J. Electrochem. Soc.* **143** (1996), 2075.

[15]   M. Watanabe, S. Motoo, *J. Electroanal. Chem.* **60** (1975), 267.

[16]   A. J. Bard, L. R. Faulkner, *Electrochemical Methods - Fundamentals and Applications (2nd edition)*, John Wiley & Sons, Inc., New York (2001).

[17]   A. Hamnett, in: A. Wieckowski (Ed.) *Interfacial Electrochemistry - Theory, Experiments, and Applications*, Marcel Dekker, Inc., New York (1999), p. 843.

Chapter 10 General Discussion

1. INTRODUCTION

The aim of this Chapter is double: *(i)* to link, together and within the current scientific background, summarize and discuss the different results obtained in the framework of this thesis and *(ii)* to discuss the model of methanol electrooxidation at Pt/Sn (and generally Pt/M) surfaces proposed here. The main aspects of the results to be developed here are the following:

- the justification of the choice of the BDD electrode as substrate.

- the discussion of the choice of the microemulsion method for nanoparticles synthesis, in terms of obtained dimensions and size distribution, composition...

- the comparison and discussion of the respective electrocatalytic activities of the different types of nanoparticles synthesized here.

For these purposes the results obtained on the electrochemical and electrocatalytic characterization of the different BDD-supported Pt-based nanoparticles will be firstly presented and discussed. The response of BDD-supported Pt nanoparticles will be firstly treated, both without and with methanol added to the solution. The case of bimetallic Pt/M nanoparticles (M = Ru or Sn) will be then highlighted and then extended to trimetallic Pt/M$_1$/M$_2$ particles. Finally the proposed oxidation model will be discussed on the basis of the obtained results.

2. BDD AS SUBSTRATE FOR THE STUDY OF NANOPARTICLES

The behaviour of Pt nanoparticles synthesized via the microemulsion synthesis has been investigated once they were deposited on the BDD substrate electrode. The choice of this substrate was motivated by its outstanding properties of chemical inertness, low background current, large electrochemical window available between evolution of hydrogen and oxygen, or high mechanical resistance to both chemical and electrochemical attacks [1, 2]. It was expected that these properties could allow the study of supported particles avoiding the problems usually encountered when common substrates are used. It is for instance well known that graphite or glassy carbon (GC) substrates present various surface functional groups and can undergo corrosion while using gold substrates can lead to surface oxides formation or electronic exchange between Au and supported Pt particles. For instance the lowering of the vibrational frequencies of CO on Pt particles at low particle coverage was attributed to a contribution of the gold substrate [3]. It was considered that since the work function of CO-covered polycrystalline Pt (5.95 eV) is higher than those of

gold (5.1 eV) a transfer of negative charge from the gold substrate to the Pt particles appeared possible. Although the work function of BDD is not accurately known it can be reasonably expected that the use of such substrate will allow the study of the behaviour of supported particles without any major interferences.

The voltammetric response of microemulsion-synthesized Pt nanoparticles deposited on BDD is shown in Figure 10.1. As it is well-known from the literature the shape of the voltammogram of Pt nanocrystallites is different from bulk polycrystalline Pt [4]. When the particle size becomes smaller and smaller the interpretation of the signal is not so easily correlated to geometrical shape and therefore the determination of the crystalline coherent dominium is not so obvious. As a justification of the choice of the diamond substrate, it is important to notice the low background current in the double-layer region that avoids the masking of the H adsorption/desorption peaks (between 0.05 and 0.5 V approximately). This is one of the advantages of using BDD as substrate rather than a substrate such as GC that exhibits a large double-layer capacity that can mask the H adsorption/desorption features of Pt and therefore lowers the quality and significance of the obtained voltammograms.
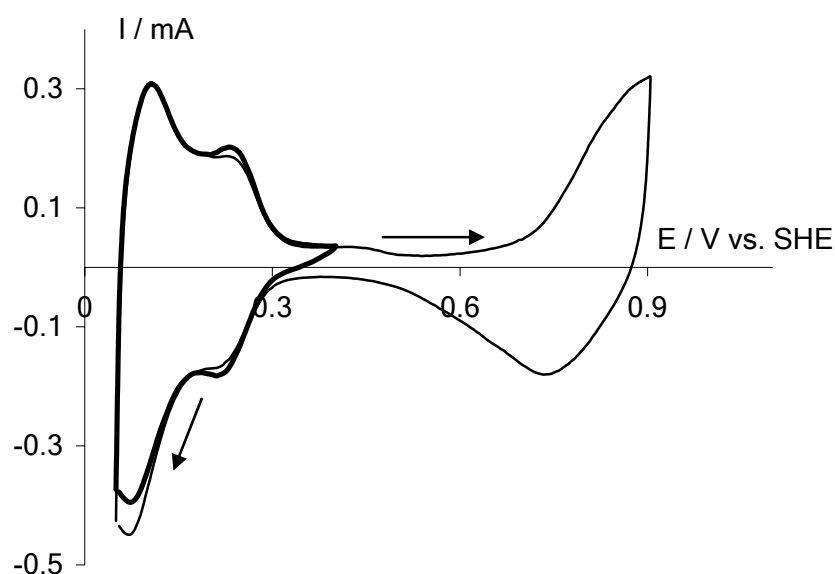

Figure 10.1: CV of microemulsion Pt nanoparticles deposited on BDD support. Recorded in 1 M HClO$_4$ at 50 mV s^{-1} and 25°C.

3. Pt-BASED ELECTROCATALYSTS SYNTHESIS IN MICROEMULSION

The microemulsion method of synthesis has been used during this work for the preparation of Pt and Pt-based (Pt/Ru, Pt/Sn and Pt/Ru/Sn) nanoparticles. In the case of pure Pt nanoparticles, this method of synthesis has led to nanosized particles

(diameter typically between 2 and 5 nm, see Chapter 5 of this manuscript) with narrow size distribution. The synthesis of binary (Pt/Ru and Pt/Sn) and ternary (Pt/Ru/Sn) nanoparticles using the same technique and the same microemulsion formulation has led to nanoparticles of mean diameter in the same size domain with similar size distribution. Moreover, for a given Pt/M combination, the composition of the microemulsion aqueous phase (ratio between the metallic precursors) does not influence the size of the resulting nanoparticles. This indicates that the key parameter for controlling the size of nanoparticles synthesized by this method is to control the size of the initial aqueous nanodroplets. For this purpose control over the water-to-surfactant molar ratio (ω_0) is sufficient, and modulations of the nanoparticles size can be achieved in a certain extent by modifying this experimental parameter.

Moreover it has been showed that the effective compositions of bimetallic nanoparticles determined both by EDX and XPS were in all cases very close to those expected from the metallic salts ratios introduced in the aqueous phases of the starting microemulsions. However there are two remarks to this finding: *(i)* such measurements concern the whole depth of the nanoparticles so that their surface state and composition are not accurately known, and *(ii)* the determined composition of the Pt/Ru/Sn sample was slightly different than those expected, with an impoverishment in Ru presumably due to the fact that Sn atoms repelled Ru from the surface [5]. Another limitation was the inability to synthesize pure Sn nanoparticles by this method, whereas Sn is present in Pt/Sn nanoparticles with correct proportions. It is believed that this is because the formation of preliminary Pt nuclei catalyses the reduction of Sn^{2+} ions. In order to summarize, it can be said that the microemulsion method is an efficient and convenient way to synthesize Pt-based nanocatalysts of controlled compositions and dimensions, with narrow size distribution.

4. BEHAVIOUR OF Pt-BASED NANOPARTICLES

4.1. BDD-supported Pt nanoparticles

The electrocatalytic behaviour of Pt nanoparticles has been mainly determined towards the electrooxidation of methanol and ethanol, which are the main reactions of interest for the Fuel Cell technology [4]. For instance the j-t curve for methanol electrooxidation at 0.6 V vs. SHE at a BDD-Pt electrode is shown in Figure 10.2. This j-t curve exhibit the common shape for this kind of experiment, *i.e.* a sharp decrease in oxidation current followed by a "steady-state" plateau. This feature has been attributed in literature to the rapid formation of strongly adsorbed intermediates (CO) that poison the surface and block the active sites [6]. However the determination of

an instantaneous current ($i_{t=0}$) as proposed by Wieckowski et al. [6] seems difficult here due to the low temporal resolution of the measurements performed here.
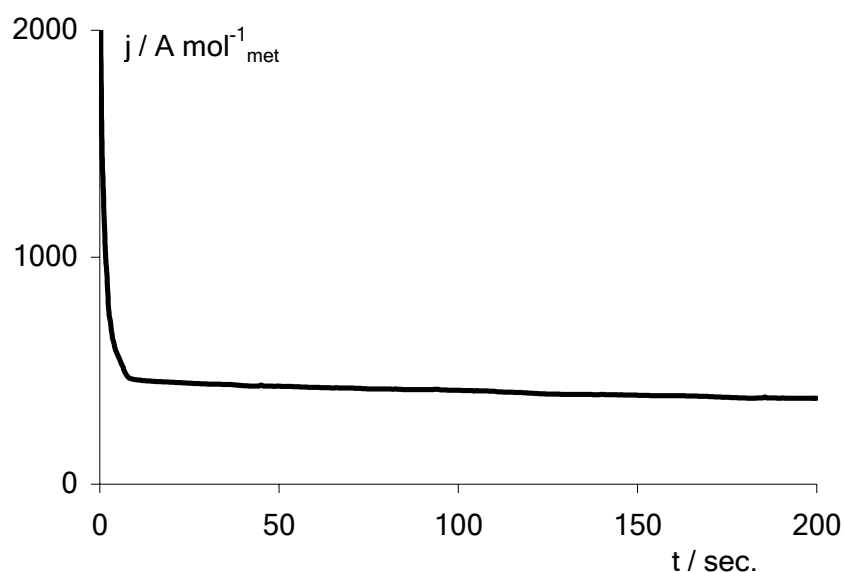

Figure 10.2: j-t transient for the electrooxidation of MeOH at a constant potential of 0.6 V vs. SHE on BDD-supported microemulsion-synthesized Pt nanoparticles. Recorded in 1 M $HClO_4$ + 0.1 M CH_3OH at 25°C.

Methanol dehydrogenation does not require the participation of an oxygen-containing species. However the complete oxidation of methanol producing CO_2 requires the oxidation of CO that needs one extra oxygen to fulfill the reaction stoechiometries and it is commonly accepted that the removal of adsorbed CO is only feasible through a surface reaction between the poison and oxygenated species coming from water. However there are up to now some discussions upon the nature of this oxygenated species since this question is of considerable mechanistic interest. There are three possible oxygen sources for oxygen-containing species able to oxidize adsorbed CO: *(i)* hydroxyl radicals from water dissociation, *(ii)* oxygen contained in reversible Pt surface oxides and *(iii)* interfacial or near surface bulk water molecules. As already stated, the most commonly accepted explanation for CO oxidation to CO_2 at high potential values is the one involving water dissociation to form hydroxyl radicals. These hydroxyl radicals can then react at the surface with adsorbed CO, leading to CO_2 and free Pt sites on which further methanol dehydrogenation steps can be performed again. However it was shown by voltammetric studies of methanol oxidation on single-crystals Pt electrodes that the methanol oxidation current in the reverse scan (negative going) could not be correlated with a water discharge process that would occur in the absence of methanol [6]. The water discharge can take place to yield high coverage $H_2O^{\delta+}$ species or low coverage Pt-OH_{ads}. Adsorbed CO from methanol dehydrogenation

surface water coexist at the surface catalytic sites of platinum. At the voltammetric peak beginning the electrode potential is sufficiently positive to make the adsorbed CO and water molecules more reactive. As a result the oxygen transfer from water to methanolic CO may occur without water decomposition [7]. This can explain the shape of the CV relative to methanol oxidation on BDD-supported microemulsion-synthesized Pt nanoparticles in which it can be seen that the two oxidation peaks are not located at the same potentials and do not occur with the same intensity (see Figure 10.3). These two peaks correspond to two different events, *i.e.* methanolic CO oxidation by two different mechanisms (oxidation by adsorbed OH from water dissociation for the forward scan peak and directly by water molecules without water dissociation for the reverse scan peak).
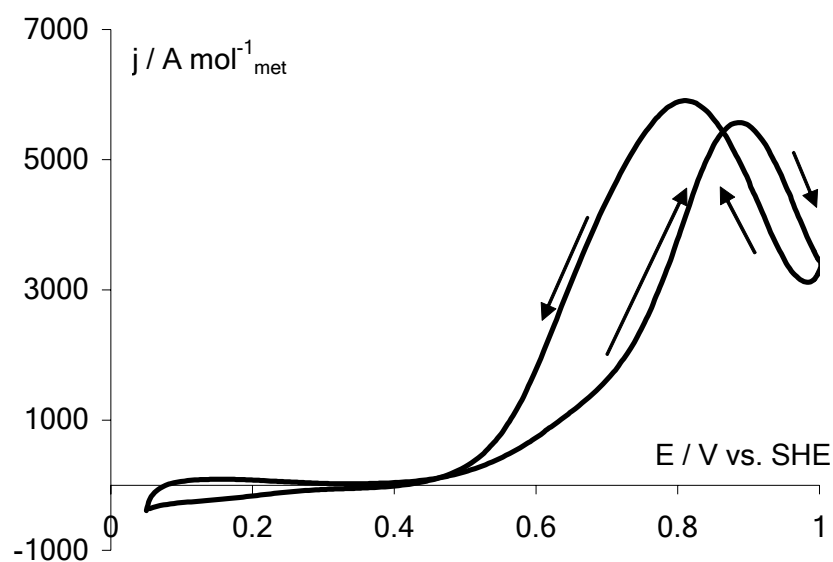

Figure 10.3: CV for the electrooxidation of MeOH on microemulsion-synthesized Pt nanoparticles deposited on a BDD electrode. Recorded in $HClO_4$ 1 M + CH_3OH 0.1 M at v = 20 mV s^{-1} and T = 25°C.

Moreover it was shown that activation by electrogenerated hydroxyl radicals (high overpotential at BDD) of the microemulsion-synthesized Pt nanoparticles results in both an increase in the specific molar oxidation currents and lowering of the onset of oxidation. This was attributed to additional cleaning of particles by hydroxyl radicals and participation of these radicals to the overall oxidation process.

4.2. BDD-supported Pt/M and Pt/M$_1$/M$_2$ nanoparticles

The study of the electrocatalytic behaviour of microemulsion-synthesized nanoparticles has been extended during this thesis to both bimetallic Pt/M (Pt/Ru and Pt/Sn) and trimetallic Pt/M$_1$/M$_2$ (Pt/Ru/Sn) nanoparticles deposited on the BDD

electrode. Some bimetallic Pt-based systems (Pt/Ru, Pt/Sn, Pt/Mo...) are well-known to improve the electrocatalytic activity of pure Pt thanks to the bifunctional mechanism [8] and/or the electronic (ligand) effect [9]. Although both these two effects can occur simultaneously, the first reason for alloying Pt with other metals was to decrease the activation energy required for water discharge in order to allow the formation of oxygenated species necessary for the oxidative removal of adsorbed CO. Historically Pt/M alloys or bimetallic surfaces have thus been considered as electrocatalysts for fuel cells applications due to the occurrence of the bifunctional mechanism, and a wide range of Pt/M combinations have been systemically evaluated with respect to their ability to activate water dissociation [10]. The effectiveness of an electronic effect depends on the intrinsic electronic properties of the second metal (work function...) as well as on the structure of the catalytic surface (alloy, mixture or other). Finally it must be pointed out that the use of Pt/M catalyst is dramatically limited in acidic media by the corrosion of transition metals at high potential (this is for instance the case of Sn). Ideally a good knowledge of the true surface (composition, dispersion of the two metals, crystalline structure...) should be necessary; however this requirement is often difficult to fulfill in the case of nanocatalysts due to the performance of analysis tools available. From this point of view cyclic voltammetry can provide precious insights on the surface state of supported nanoparticles. Typical CV in pure supporting electrolyte have thus been carried out on BDD-supported Pt and Pt/Ru nanoparticles and the samples with marked Pt surface character have been identified (see Fig. 6.11, and Fig. 7.11 for the characterization of Pt/Sn nanoparticles). It was believed that these Pt-rich nanoparticles should be more active than others due to their superior alcohol adsorption properties.

It is indeed commonly assumed that methanol adsorption proceeds similarly on Pt/Ru and Pt. The electrooxidation process at Pt/Ru is believed to occur via a bifunctional mechanism [8] in which the adsorption of methanol takes place mainly at the Pt sites whereas the generation of oxygen-containing species takes place mainly at the Ru sites. The subsequent reaction of oxidative removal of CO is a Langmuir-Hinshelwood reaction between adsorbed intermediates. The effectiveness of this bifunctional mechanism is well illustrated by Figure 10.4 in which the linear sweep voltammograms for methanol oxidation at Pt and $Pt_{80}Ru_{20}$ nanoparticles deposited on BDD are shown. It can be seen that the onset of methanol electrooxidation is appreciably shifted to lower potential values on the bimetallic nanoparticles (from approximately 0.52 V to 0.43 V at a specific molar current of 50 A mol^{-1}_{met}). According to the bifunctional mechanism [8], Ru allows the activation of water at lower potentials

than Pt. Consequently the surface reaction between adsorbed CO and adsorbed OH radicals can take place earlier at Pt/Ru. Pt sites are then free for further dissociative adsorption and the oxidation current is increased.
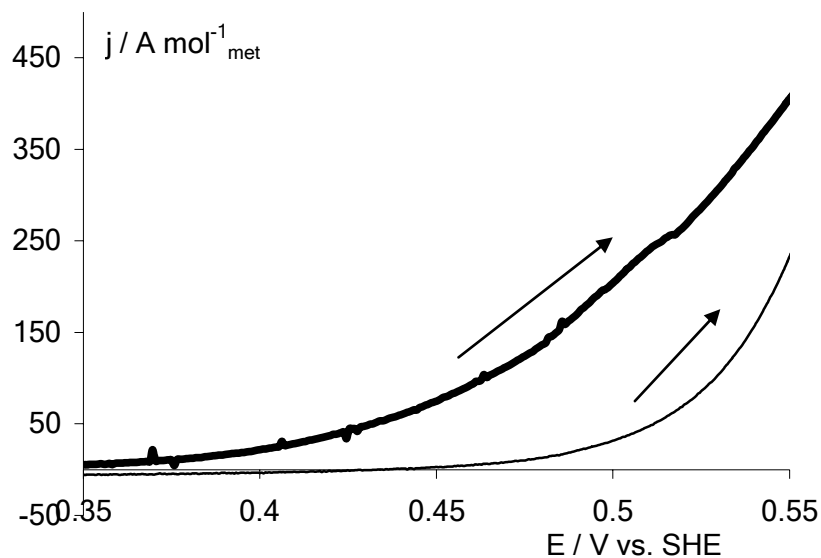

Figure 10.4: Polarization curves and onset of MeOH electrooxidation on microemulsion-synthesized Pt (thin line) and $Pt_{80}Ru_{20}$ (thick line) nanoparticles deposited on BDD. Recorded in 1 M $HClO_4$ + 0.1 M CH_3OH at 1 mV s^{-1} and 25°C

At a Pt/Ru surface the existence of two types of adsorption sites can be considered: *(i)* Pt sites on which adsorption can occur and *(ii)* electroinactive Ru sites. Ru atoms are considered to "dilute" the Pt surface, thus diminishing the probability to find three adjacent Pt sites for methanol adsorption. Assuming that: *(i)* no adsorption take place at all at Ru sites, *(ii)* the first adsorption step (initial scission of methyl hydrogen) is rate-determining, *(iii)* there is no interaction between adsorbed species and *(iv)* no surface diffusion can be postulated, Christov et al. have simulated methanol adsorption at Pt/Ru surfaces [11]. It was shown in this study that the optimum composition of Pt/Ru alloys for methanol oxidation at room temperature should be between 10 and 30 at. % in Ru. This corresponds well with the obtained results within the framework of this thesis. Figure 10.5 indeed shows the evolution of the specific molar current for methanol oxidation on BDD-supported microemulsion Pt/Ru nanoparticles with the atomic Pt content. This specific molar current decreases with the increase in Ru content at the surface. The higher current density is reached for pure Pt due to its superior adsorption properties compared to Pt/Ru. Within the Pt/Ru nanoparticles synthesized here $Pt_{80}Ru_{20}$ is the one exhibiting the larger oxidation current density. It seems obvious from Fig. 10.5 that decreasing the surface Pt content results in the decrease the adsorption abilities of the particles, thus

decreasing their electrocatalytic activity. It must be pointed out also than on pure Ru no alcohol electrooxidation occurs (data not shown), due to inability of Ru to adsorb methanol. However, it must be pointed out that the maximum observed here should be shifted to higher Ru contents ($\approx$ 50 at. %) at higher temperatures, due to possible adsorption at the Ru sites [12].
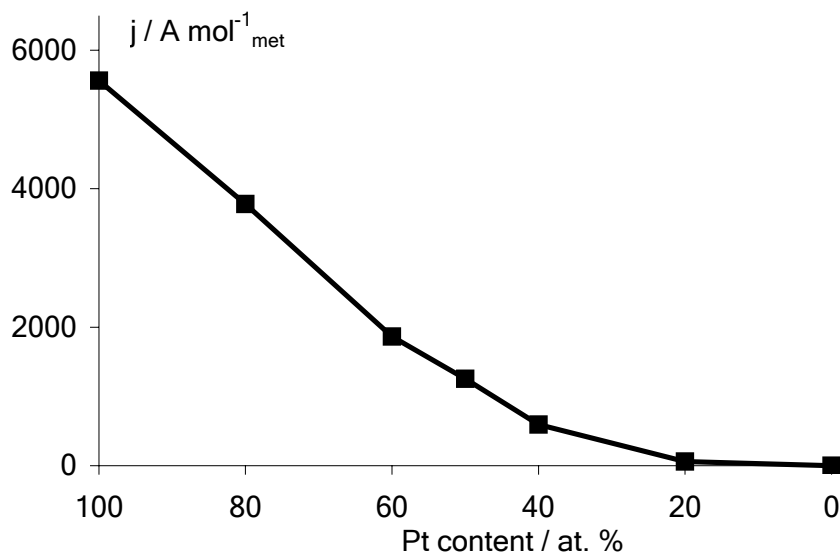

Figure 10.5: Evolution of the specific molar current for the electrooxidation of MeOH on BDD-supported microemulsion-synthesized Pt/Ru nanoparticles. Recorded by CV in 1 M $HClO_4$ + 0.1 M CH_3OH at 20 mV s^{-1} and 25°C.

It was shown by XRD measurements that microemulsion-synthesized Pt/Ru nanoparticles are alloyed ones (see Chapter 6 of this thesis) so that an electronic effect can reasonably be expected in addition of the cooperative effect already seen above. The electronic effect consists in the weakening of the Pt-CO bond strength due to modifications of the electronic properties of Pt that are induced by electronic transfer from the alloying metal to Pt. The effectiveness of this electronic transfer has been determined by XPS measurements, in which a shift of the Pt*4f* signal position to lower binding energies was observed. Occurrence of the electronic effect can be noted on Figure 10.6, which shows the chronoamperometric curves for methanol oxidation at 0.6 V vs. SHE on both Pt and $Pt_{80}Ru_{20}$ nanoparticles. At this potential value, water dissociation is activated on the two surfaces, *i.e.* the surface reaction between the adsorbed poison and oxygenated species can take place. The two curves exhibit a similar profile with a sharp current decay that can be attributed to surface poisoning by adsorbed intermediates [13]. However the current decay is far less pronounced in the case of the alloyed surface. It seems to indicate that $Pt_{80}Ru_{20}$ is more CO-tolerant than Pt, *i.e.* that the surface reaction between CO_{ads} and oxygen-containing species proceeds more efficiently and rapidly at $Pt_{80}Ru_{20}$. A reason for

such an enhanced CO-tolerance could be the existence of weakly bonded CO at $Pt_{80}Ru_{20}$; these weakly adsorbed CO would be more reactive and mobile than those adsorbed on pure Pt explaining the more facile removal of CO on the alloy.
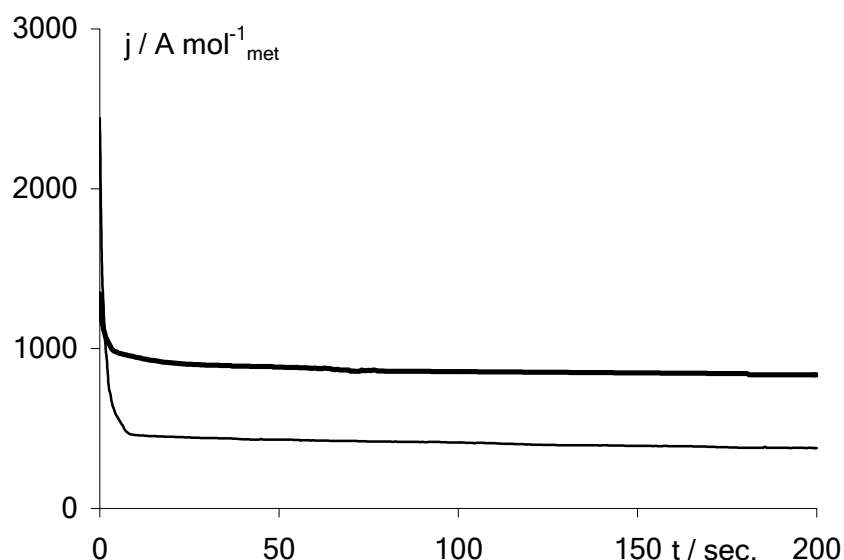

Figure 10.6: Chronoamperometric curves at 0.6 V vs. SHE for the electrooxidation of MeOH on BDD-supported microemulsion-synthesized Pt (thin line) and $Pt_{80}Ru_{20}$ (thick line) nanoparticles. Recorded in 1 M $HClO_4$ + 0.1 M CH_3OH at 25°C.

Therefore it seems that both the cooperative and ligand effects occur simultaneously at microemulsion-synthesized Pt/Ru alloys. The combination of these two effects explains the enhanced electrocatalytic activity of Pt/Ru alloys. However the relative importance of the two effects is difficult to estimate. Finally it must be said that Pt/Ru are not good electrocatalysts for ethanol electrooxidation. Pt/Ru alloys are effectively more tolerant to surface poisoning from ethanol dissociative electrosorption than pure Pt, but addition of Ru does not activate the C-C bond scission of the ethanol molecule. Specific molar currents for ethanol electrooxidation represent in all cases the third than those for methanol oxidation. It can therefore be reasonably postulated that, on Pt/Ru as well as on Pt, ethanol oxidation is incomplete and leads to C_2 species (acetaldehyde and/or acetic acid) rather than CO_2.

So the use of microemulsion-synthesized Pt/Sn nanoparticles has been considered more specifically for the catalysis of ethanol oxidation. Pt/Sn surfaces have indeed exhibited superior electrocatalytic activity toward ethanol oxidation in some studies. However these results are still subject of discussion, as some other groups have not observed any enhancement in electrocatalytic activity, or even worse activity. This fact points out the crucial importance of the Pt/Sn electrocatalyst preparation method. It can be considered that methanol dissociative adsorption proceeds at Pt/Sn similarly than on Pt and Pt/Ru surfaces; the primary role of Sn is to

promote water dissociation at lower potential values than possible on pure Pt in order to generate oxygenated species able to oxidize the adsorbed poison. However the behaviour of Pt/Sn surfaces is somewhat different than that of Pt/Ru in the sense that quantum calculations have shown that CO is exclusively adsorbed on Pt sites whereas oxygen-containing species are exclusively located at Sn sites [14]. On the contrary at Pt/Ru, CO exhibit a preference for Pt sites and OH for Ru sites, but both Pt-OH and Ru-CO groups can be found in small amounts. Removal of adsorbed CO is thus supposed to proceed via the surface reaction between adsorbed CO at Pt and adsorbed OH at Sn and to follow a Langmuir-Hinshelwood mechanism. This reaction can take place only at the Pt/Sn interface. Thus it requires high mobility of reactants (weakly bonded reactants at the surface) and/or good dispersion of the two metals. An important interface between Pt and Sn is thus needed. From this point of view an ideal structure should be an alloy (solid solution of the two metals). Moreover with an alloy an electronic effect (weakening of the Pt-CO bond) can reasonably be expected. The wide range of methods used for the preparation of Pt/Sn electrocatalytic surfaces can thus explain the large discrepancy in literature results. The knowledge and the control of the surface state are therefore important requirements in the preparation of such surfaces and the use of appropriate synthesis methods is a crucial parameter.

As already stated above, the dissociative adsorption of methanol proceeds at Pt/Sn similarly than both at Pt and Pt/Ru. Therefore, as it was observed in the case of methanol oxidation at Pt/Ru, it can reasonably be expected that the addition of Sn to the Pt lattice will dilute the Pt surface, hence decreasing the probability of alcohol adsorption at the Pt sites. This is effectively observed in the case of methanol oxidation (see thick line with square markers in Fig. 10.7) for which the specific molar current decreases with the Pt content. However the behaviour of Pt/Sn nanoparticles is somewhat different toward ethanol electrooxidation in the sense that the specific molar currents observed for ethanol electrooxidation is higher than those for methanol electrooxidation. It can reasonably be supposed that addition of Sn to Pt activates the breaking of the C-C bond of ethanol, leading to a more complete oxidation and explaining the higher specific molar currents obtained for ethanol electrooxidation. Pt-rich nanoparticles ($Pt_{80}Sn_{20}$) are again the most active ones due to their superior adsorption properties.
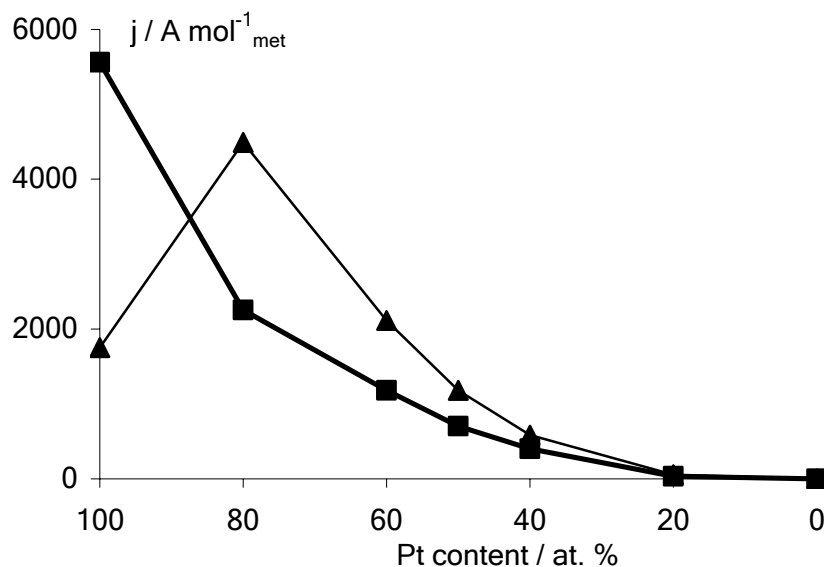
Figure 10.7: Evolution of the specific molar current for the electrooxidation of MeOH (thick line with square markers) and EtOH (thin line with triangle markers) on BDD-supported microemulsion-synthesized Pt/Sn nanoparticles. Recorded by CV in 1 M $HClO_4$ + 0.1 M Alcohol at 20 mV s^{-1} and 25°C.

There is a specific effect of Sn toward ethanol electrooxidation that does not occur when Ru is added to Pt. Nevertheless, as in the case of Pt/Ru nanoparticles, the bifunctional mechanism plays a role in the enhanced electrocatalytic activity of Pt/Sn. This is well illustrated by Figure 10.8, which shows the linear sweep voltammograms for EtOH oxidation at Pt and $Pt_{80}Sn_{20}$ nanoparticles deposited on BDD. It can be clearly seen that the onset of ethanol electrooxidation is largely shifted to lower potential values on the bimetallic surface. To reach a specific molar current of 200 A mol$^{-1}_{met}$ a potential of 0.6 V is necessary at Pt whereas a value of 0.4 V is sufficient at $Pt_{80}Sn_{20}$ nanoparticles. The observed current increase needs the availability of free adsorption sites (Pt) that can be regenerated by the surface reaction between oxygenated species from water dissociation and adsorbed intermediates poisoning the surface. It is also possible that surface Sn oxides are involved; it was indeed showed by XPS that Sn is present in Pt/Sn nanoparticles in an oxidized form. The relative starting potentials of current increases on Pt and $Pt_{80}Sn_{20}$ nanoparticles thus indicates that the activation of water takes place earlier on the bimetallic surface than on pure Pt and illustrates the role of Sn in Pt/Sn nanoparticles.
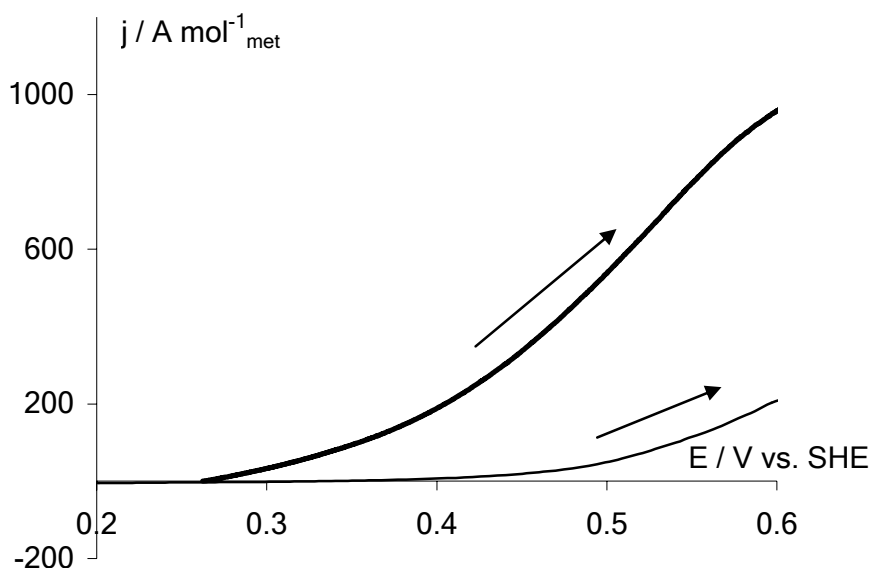
Figure 10.8: Polarization curves and onset of EtOH electrooxidation on microemulsion-synthesized Pt (thin line) and $Pt_{80}Sn_{20}$ (thick line) nanoparticles deposited on BDD. Recorded in 1 M $HClO_4$ + 0.1 M CH_3CH_2OH at 1 mV s^{-1} and 25°C.

The specific action of Sn that can explain the activation of the C-C bond breaking during ethanol electrooxidation needs to be elucidated. It has been shown by XRD that Pt/Sn nanoparticles are not true alloys but should be most likely regarded as a mixture of Pt and Sn islands. Therefore an electronic effect between Sn and Pt should not be reasonably considered as truly effective. However a strong shift to lower values of binding energies of the Pt*4f* signal was observed in XPS measurements, indicating e⁻ d transfer from Pt to Sn. The chemical Pt*4f* shift is of larger importance in the case of Pt/Sn nanoparticles than for Pt/Ru nanoparticles due to the larger difference in electronegativities between Sn and Pt than between Ru and Pt. It can so be concluded that electronic interactions between the two metals occur; obviously such electronic interactions can take place only at the interface between the two metals. The microemulsion method presumably leads to the synthesis of bimetallic Pt/Sn nanoparticles with both the two metals well dispersed at the surface, *i.e.* large interface between the two metals is available. This is also an important requirement in the sense that the surface reaction between oxygen-containing species at Sn sites and CO at Pt sites can proceed exclusively at the Pt-Sn interface.

Therefore the electronic effect may play a role in the enhanced electrocatalytic activity of Pt/Sn toward ethanol electrooxidation compare to both those of Pt and Pt/Ru. However it can be stated that the electronic interactions between Sn and Pt are not of same nature than those between Ru and Pt. This seems obvious considering that Pt/Ru nanoparticles do not activate the scission of the ethanol C-C bond as it can be deduced from the relative specific molar currents obtained for the

oxidation of methanol and ethanol. This can come either from the electronic structure of the second metal in particles or the structure of particles themselves (alloy or not).

The fact that Ru and Sn do not affect Pt in the same way justifies the choice of realizing ternary nanoparticles combining Pt, Ru and Sn. It can indeed be postulated that the two metals would not compete and that it would be possible to combine the advantages of the two types of bimetallic particles within the ternary sample. It was also chosen to keep an important Pt content in order to take advantage of the superior adsorption properties of Pt-rich surfaces at room temperature, and therefore only a nominal $Pt_{80}Ru_{10}Sn_{10}$ sample was synthesized. In this case, the Pt *$4f_{7/2}$* line moves back to its initial value in pure Pt compare to what was observed in $Pt_{80}Sn_{20}$. It can be supposed that the electronic transfer occurs between Sn and Ru (same $\Delta\chi$ of 0.4 as between Pt and Sn), thus modifying the electronic properties of Ru rather than those of Pt. Consequently a new ˙OH state can be created, weakly adsorbed on Ru and of higher mobility and reactivity. This new ˙OH state could explain both the reduced onset potential of EtOH electrooxidation and the enhanced electrocatalytic activity for MeOH electrooxidation, since these processes can be related to surface reaction between adsorbed CO and adsorbed ˙OH. However it seems that this electronic interaction between Sn and Ru hides the beneficial effect of Sn toward EtOH electrooxidation in bimetallic surface. Electronic transfer between Sn and Ru rather than Sn and Pt certainly impeaches modification of the electronic properties of Pt, leading to unchanged behavior toward EtOH and consequently inability to promote the C-C bond scission. Obviously other experiments have to be performed to validate this assumption, for instance with varying the composition of the ternary particles but keeping the Pt content at a constant value of 80 at. % in order to maintain the surface alcohols adsorption properties. Moreover, it must be pointed out that the structure of the surface is not accurately known and that this parameter would be of great importance in the understanding of the electrocatalytic behaviour of these ternary nanoparticles.

Finally it was attempted to realize a new type of Pt-based particles deposited on BDD. Pt particles were electrodeposited on pre-deposited Au particles on BDD following a procedure from our group [15]. The aim was to combine the electrocatalytic properties of Pt particles with those of Au particles toward CO oxidation [16-19]. Ideally this kind of catalyst would allow dissociative methanol adsorption at Pt sites and oxidative removal of adsorbed CO at Au sites. This requires both an electronic effect (adsorbed CO must be weakly bonded to Pt in order to migrate to Au sites) and another type of cooperative effect (Pt dissociatively adsorbs methanol, Au oxides the resulting adsorbed CO). Moreover some preliminary

calcination tests of the Au/Pt deposit (600°C in air for 1 h) were performed in order to yield a structure in which the two metals would be closely related (alloy for instance). The objective of this calcination procedure was to enhance the electronic effect and to increase the interface between the two metals.

The CV of both the calcinated and non-calcinated Au/Pt deposit on BDD, recorded in 1 M HClO$_4$, are shown in Figure 10.9. The two reduction peaks of metal oxides are clearly visible and distinguishable on the CV of the non-calcinated BDD-Au/Pt electrode (thick solid line in Fig. 10.9). The reduction of Au oxides occurs at ≈ 1.1 V and that of Pt oxides at ≈ 0.6 V. This is indicative that both the two metals are present and accessible to the electrolyte, so that the deposit is certainly composed of Au particles deposited together with Pt particles. Similar profile of CV of Au/Pt surface has been observed in sulphuric acid [20]. Calcination of the deposit at 400°C for 1 h yields to a decrease in the intensity of the reduction peak of Pt oxides whereas the Au oxides reduction peak remains almost constant. It seems that calcination results in the exaltation of the Au character of the BDD-Au/Pt electrode, certainly due to surface segregation and coverage of Pt particles by Au leading to a core-shell structure. The melting point of small (< 50 nm) gold particles is indeed around 400°C [21] whereas those for Pt particles of the same size is around 900°C; this can explain the more or less complete Pt deposit coverage by gold depending on the calcination conditions.
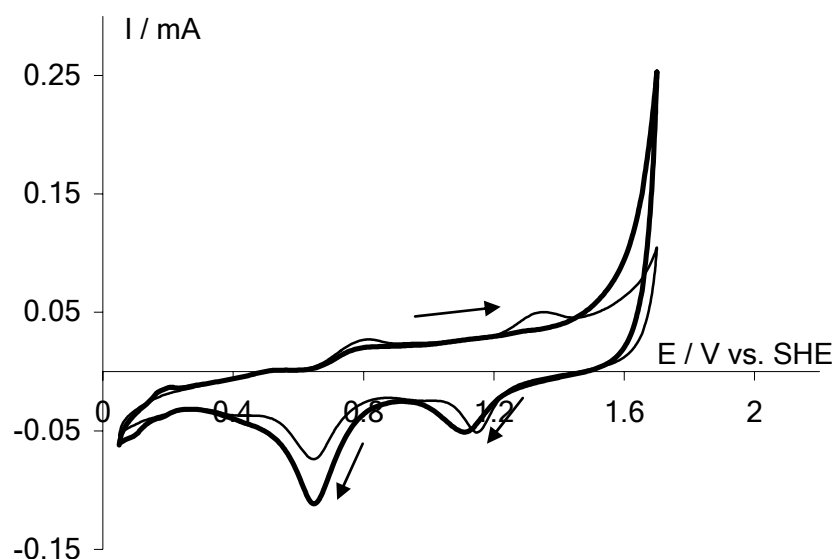

Figure 10.9: CV of Au/Pt (thick solid line) and calcinated Au/Pt (1 h in air at 400°C, thin solid line) particles deposited on BDD. Recorded in 1 M HClO$_4$ at 50 mV s^{-1} and 25°C. Parameters for sputtering: dc mode, discharge of 330 V under 10^{-2} mbar argon pressure at room temperature for 20 sec., followed by calcination at 600°C in air for 1 h. Parameters for electrodeposition: potential step of 5 sec. from 1 to 0.02 V vs. SHE in 1 M HClO$_4$ + 2 mM H$_2$PtCl$_6$ solution.

The behaviour of both calcinated and non-calcinated BDD-Au/Pt electrodes toward methanol and ethanol electrooxidation has also been investigated. Figure 10.10 shows the CV recorded on the two types of bimetallic deposits on BDD toward methanol electrooxidation. Specific molar currents are plotted here with respect to the total amount of deposited metals (*i.e.* Pt + Au) deduced from integration of I-t transients (Pt) and sputtering conditions (Au). The current values for non-calcinated Au/Pt deposit are lower than those observed for electrodeposited Pt alone; however these normalisations are taking into account the gold deposit that is not active for dissociative adsorption of alcohols. Neglecting Au deposited on BDD and considering Pt as the only metal present leads to specific molar currents comparable to those of electrodeposited Pt alone. This indicates that the Au deposit does not influence strongly the behaviour of Pt when the two types of metallic particles are only co-deposited on the diamond substrate. This is the reason why we have attempted to realize a structure in which the two metals would be more closely related. However the calcination carried out under our preliminary conditions dramatically decreases the activity of the deposit both toward methanol and ethanol electrooxidation. It can be postulated that such heat treatment results in melting of Au nanoparticles that cover the Pt deposit and leads to a core-shell structure with a Pt core; the surface capable of alcohol adsorption decreases and the electrocatalytic activity is decreased concomitantly.
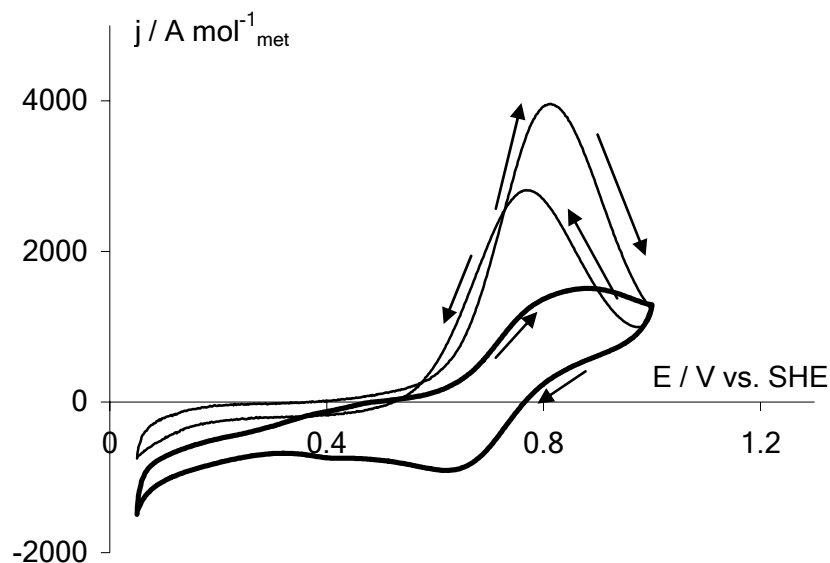
Figure 10.10: CV of MeOH electrooxidation on Au/Pt particles (thin solid line) and calcinated Au/Pt (thick solid line) deposited on BDD. Recorded in 1 M $HClO_4$ + 0.1 M CH_3OH at 20 mV s^{-1} and 25°C. Parameters for sputtering: dc mode, discharge of 330 V under 10^{-2} mbar argon pressure at room temperature for 20 sec., followed by calcination at 600°C in air for 1 h. Parameters for electrodeposition: potential step of 5 sec. from 1 to 0.02 V vs. SHE in 1 M $HClO_4$ + 2 mM H_2PtCl_6 solution.

Heat treatment using other conditions could be a solution to realize a more efficient Au/Pt bimetallic surface for electrocatalysis of methanol or ethanol electrooxidation. Requirements for such surface would be to preserve its adsorption properties and to allow fast and effective migration of adsorbed CO from Pt sites to Au sites where it can be easily oxidized. In particular the use of a temperature for which both the two metals melt (at least 900°C) should be tested in the next future. However the changes that the diamond substrate can undergo under such conditions (in particular surface oxide formation) must also be taken into account as they could greatly influence the behaviour of the supported particles (metal-support interactions).

5. DISCUSSION OF THE PROPOSED MODEL

During this thesis a theoretical model for methanol electrooxidation at a Pt/M (Sn) surface has been proposed and developed. The idea was to extend the concepts of heterogeneous catalysis to the specific case of an electrochemical reaction involving adsorbed intermediates. More specifically the donor-acceptor theory of heterogeneous catalysis has been applied and adapted here, considering Pt as the acceptor phase and Sn as the donor phase (supplier of oxygen-containing species able to spillover from the donor to the acceptor phase). This view is not so far from that of the bifunctional mechanism [8], in which the alloying metal of a Pt/M catalyst

activates water dissociation at lower potential values than possible at Pt sites. Several assumptions have been done in order to simplify the treatment. It was therefore considered that CO is not formed and not adsorbed at Sn sites, $^{\bullet}$OH is not formed at Pt sites but adsorbed on them and the reaction between CO and $^{\bullet}$OH occurs at Pt or at the interface between Pt and Sn. It has also been supposed that the oxygen-containing species was hydroxyl radicals as mainly accepted in literature, although the involvement of activated water molecules or surface metal oxides can also be considered. The model has been applied to the treatment of some real limiting cases.

If the surface reaction between adsorbed CO and $^{\bullet}$OH is very fast compared to the spillover of reactive species, then the reaction takes place at the Pt/Sn interface. In this case the current is proportional to the contact length and quality. The dependence of current toward contact length and quality may be at the origin of the differences in the electrocatalytic behaviour of Pt/Sn catalysts as observed by several groups [22-27]. It seems therefore that, for this kind of electrocatalysts, the preparation mode of the surface plays a crucial role in its response and that an experimental preparation procedure that allows the obtaining of bimetallic surfaces in which the two metals are ideally (alloys) or at least well dispersed is highly desirable. The controversial results on electrocatalysis by Pt/Sn were indeed obtained using surfaces that were prepared using various experimental techniques so that no definitive conclusions could be drawn from these works. However it seems that the microemulsion method alloys the synthesis of Pt/Sn nanoparticles in which the two metals are well dispersed. On the contrary when spillover of reactive species is supposed to be fast compared to the rate of the surface reaction between adsorbed intermediates the contact quality does not appear in the expression of the rate (and hence in the expression of the current). Therefore for Pt/M surfaces at which the spillover of reactive species is fast compared to CO oxidation rate the quality of the interface between the two phases appears to be of secondary importance. Therefore it can reasonably be stated that the preparation mode of the surface does not play a key role in the electrocatalytic behaviour of the surface. Moreover it can be supposed that Pt/Ru electrocatalysts are in this category, explaining the large consensus on the superior electrocatalytic properties of Pt/Ru systems compare to those of pure Pt [8, 28-31] whatever the preparation procedure is.

In order to be further developed, the proposed model would take into account the possible occurrence of $^{\bullet}$OH formation at Pt sites at high potential values or the diffusion of reacting species over the surface on which they have been formed. The influence of the Pt/M ratio should also appear more clearly. Finally, in order to more

precisely study the influence of the temperature on the process, the temperature dependence of the adsorption properties of both the acceptor (Pt) and the donor (Sn) phases could also be integrated into the model

6.   REFERENCES

[1]   Y. V. Pleskov, *Russ. Chem. Rev.* **68** (1999), 381.

[2]   Y. V. Pleskov, in: R. C. Alkire, D. M. Kolb (Eds.), *Advances in Electrochemical Science and Engineering*, Wiley-VCH, Weinheim (2002), p. 209.

[3]   K. A. Friedrich, F. Henglein, U. Stimming, W. Unkauf, *Colloids Surf. A* **134** (1998), 193.

[4]   W. Vielstich, H. A. Gasteiger, A. Lamm (Eds.), *Handbook of Fuel Cells - Fundamentals, Technology and Applications*, John Wiley & Sons, Ltd., New York (2003).

[5]   C. Stuhlmann, H. Hoffschulz, K. Wandelt, in: A. Wieckowski (Ed.) *Interfacial Electrochemistry - Theory, Experiments, and Applications*, Marcel Dekker, Inc., New York (1999), p. 805.

[6]   E. Herrero, K. Franaszczuk, A. Wieckowski, *J. Phys. Chem.* **98** (1994), 5074.

[7]   A. Wieckowski, *J. Electroanal. Chem.* **78** (1977), 229.

[8]   M. Watanabe, S. Motoo, *J. Electroanal. Chem.* **60** (1975), 267.

[9]   K.-W. Park, J.-H. Choi, B.-K. Kwon, S.-A. Lee, Y.-E. Sung, H.-Y. Ha, S.-A. Hong, H. Kim, A. Wieckowski, *J. Phys. Chem. B* **106** (2002), 1869.

[10]   A. B. Anderson, E. Grantsharova, S. Seong, *J. Electrochem. Soc.* **143** (1996), 2075.

[11]   M. Christov, K. Sundmacher, *Surf. Sci.* **547** (2003), 1.

[12]   H. A. Gasteiger, N. M. Markovic, P. N. Ross Jr, E. J. Cairns, *J. Electrochem. Soc.* **141** (1994), 1825.

[13]   A. Hamnett, in: A. Wieckowski (Ed.) *Interfacial Electrochemistry - Theory, Experiments, and Applications*, Marcel Dekker, Inc., New York (1999), p. 843.

[14]   T. E. Shubina, M. T. M. Koper, *Electrochim. Acta* **47** (2002), 3621.

[15]   B. El Roustom, G. Fóti, Ch. Comninellis, *Electrochem. Comm.* **7** (2005), 398.

[16]   R. Grisel, K.-J. Weststrate, A. Gluhoi, B. E. Nieuwenhuys, *Gold Bull.* **35** (2002), 39.

[17]   G. C. Bond, *Gold Bull.* **34** (2001), 117.

[18]   T. Kobayashi, M. Haruta, S. Tsubota, H. Sano, B. Delmon, *Sensors Actuators B* **1** (1990), 222.

[19]   T. Kobayashi, M. Haruta, H. Sano, M. Nakane, *Sensors Actuators* **13** (1988), 339.

[20]   H. Moller, P. C. Pistorius, *J. Electroanal. Chem.* **570** (2004), 243.

[21]   P. Buffat, J.-P. Borel, *Phys. Rev. A* **13** (1976), 2287.

[22]   M. M. P. Janssen, J. Moolhuysen, *Electrochim. Acta* **21** (1976), 861.

[23]   T. Frelink, W. Visscher, J. A. R. van Veen, *Electrochim. Acta* **39** (1994), 1871.

[24]   T. Frelink, W. Vissher, J. A. R. van Veen, *Surf. Sci.* **335** (1995), 353.

[25]   Y. Morimoto, E. B. Yeager, *J. Electroanal. Chem.* **444** (1998), 95.

[26]   Y. Morimoto, E. B. Yeager, *J. Electroanal. Chem.* **441** (1998), 77.

[27]   F. Vigier, C. Coutanceau, F. Hahn, E. M. Belgsir, C. Lamy, *J. Electroanal. Chem.* **563** (2004), 81.

[28]   J. Munk, P. A. Christensen, A. Hamnett, E. Skou, *J. Electroanal. Chem.* **401** (1996), 215.

[29]   M. Watanabe, M. Uchida, S. Motoo, *J. Electroanal. Chem.* **229** (1987), 395.

[30]   H. A. Gasteiger, N. Markovic, P. N. Ross Jr, E. J. Cairns, *Electrochim. Acta* **39** (1994), 1825.

[31]   N. Fujiwara, K. A. Friedrich, U. Stimming, *J. Electroanal. Chem.* **472** (1999), 120.

Chapter 11 Perspectives

1. INTRODUCTION

The aim of this final Chapter of the thesis is to propose some possible further developments to this work. For this purpose some perspectives to this work are also proposed; more particularly the BDD substrate surface has been treated by electrochemical polishing [1] and plasma fluorination [2]. These pre-treated BDD electrodes can be used as substrates for the study of supported catalytic nanoparticles. It has indeed be showed that electrochemical treatment of a GC substrate can greatly influence the electrocatalytic activity of supported Pt nanoparticles [3]. Moreover Pt nanoparticles have also been synthesized using the dendrimeric route [4] as a new preparation method in order to decrease the mean diameter and improve the size distribution of the obtained particles. Finally, on the basis of recent works from literature, some new catalyst formulations (Pt skin layer or use of non-noble metal catalysts in basic medium) can be imagined for further use as DAFC anode catalysts.

The role of the substrate on the response of supported particles (metal-support interaction) has indeed be recently the subject of numerous questions and papers [5, 6], and the possibility to modify the BDD surface properties in a controlled way would be a convenient way to elucidate the above problem. Moreover the history of the BDD electrode can have a great influence on its intrinsic electrochemical response and the importance of surface pre-treatments of the diamond electrode has been pointed out in many papers [7-10]. It is well-known that diamond surfaces can easily be oxidized and modified by oxygen functionalities (hydroxyl and carboxyl groups) by electrochemical polarisation or plasma treatment [11]. The role of surface non-diamond carbon (sp^2) impurities on the electron-transfer kinetics of both *outer-sphere* and *inner-sphere* model redox couples has been also emphasized in a recent paper from our laboratory [12]. As a general trend, it can be said that the electrochemical properties of the BDD electrodes strongly depend on its surface state (hydrogenated ↔ hydrophobic and oxidized/oxygenated ↔ hydrophilic), and also on the way the modification was obtained [13]. In our group, BDD electrodes are usually polarized anodically under mild conditions (10 mA cm^{-2} during 30 min in 1 M H_2SO_4), process that results in the elimination of most of the sp^2 carbon surface impurities [14].

Diamond polishing remains a very difficult task due to the hardness of this material. Many polishing techniques have been used [15]; however they all have their disadvantages. Mechanical polishing, used for a long time to polish single-crystal diamonds, can need several days and subsurface microcracking can occur due to the

applied force. Thermochemical polishing, using hot transition metals or rare earths plates, can lead to diamond contamination by the plate material [16]. Laser polishing, proposed in the case of curved and localized surfaces [17-19]; can result in cracks that affect the adhesion between the diamond film and the substrate. Electropolishing is a well-known technique for smoothing and brightening electrode surfaces [20, 21], but there are until now only few reports on electropolishing of polycrystalline diamond surfaces [1]. Fluorination of diamond surfaces have recently received some interest because this process has permitted to obtain low internal stress [22], best performance in terms of wear resistance and friction [23], low dielectric constant [24]. Moreover the fluorinated surface was found to be highly hydrophobic [25]. However until now only a few papers deal with the electrochemical characterization of fluorinated BDD [2, 26].

2. PERSPECTIVES

2.1. Treatment of substrate surface

2.1.1. Electropolishing of BDD

Polishing of as-grown BDD electrodes was electrochemically performed on samples from CSEM (Centre Suisse d'Electronique et Microtechnique, Neuchâtel). The synthesis and characteristics of these BDD electrodes are more detailed in within the experimental sections of the results Chapters of this thesis. A constant anodic current density (1 A cm^{-2}) was applied to the diamond electrode immersed in a 3 M acetic acid in 1 M H_2SO_4 solution, a commonly used electropolishing medium, which was continuously stirred and maintained at 40°C. The exposed area of diamond was 1 cm^2 and a platinum wire was used as counter electrode. The influence of this treatment on BDD was studied by means of electrochemical measurements, XPS and SEM, using the experimental methods and set-ups described in Chapter 3. The C $1s$ peak in XPS spectra was deconvolved using the CasaXPS$^{®}$ software. Electropolished BDD electrodes were characterized after different polarization times. Electrochemical measurements were conducted using the conventional three-electrode cell described in Chapter 3, with treated BDD as working electrode (exposed area of diamond: 1 cm^2), Hg/Hg$_2$SO$_4$.K$_2$SO$_4$(sat.) as reference and a platinum wire as counter electrode. All potentials reported here are plotted with respect to the Standard Hydrogen Electrode (SHE). All solutions were made in distilled water using analytical grade reactants without further purification.

SEM micrographs of BDD electrodes before and after different treatment times in 3 M acetic acid + 1 M H_2SO_4 at 1 A cm^2, as well as after treatment at 1 A cm^{-2} in 1 M

H_2SO_4, are shown in Fig. 11.1. The surface of the non-treated electrode (Fig. 11.1.A) consists of a polycrystalline diamond film of randomly oriented crystallites. The surface appears to be quite rough and crystallites size is inhomogeneous, ranging typically from 200 to 800 nm. Even after long polarization times in 1 M H_2SO_4 (256 h for Fig. 11.1.B), the BDD surface remains unchanged due to its well-known corrosion resistance in acidic media. There is no evidence in this case of any polishing or smoothing of the diamond surface. On the contrary, a short polarization time (4 h, see Fig. 11.1.C), under the same current and temperature conditions, is sufficient to significantly polish the diamond electrode in an acetic acid medium that is commonly used as electropolishing electrolyte. At this stage it was observed that the crystallites size strongly decreases and that edges were significantly smoothed. After 17 h of this treatment (Fig. 11.1.D), the morphology of the BDD surface has completely changed. The polycrystalline morphology is no longer visible and crystals edges are smoother; these are typical results of polishing processes and loss of material.
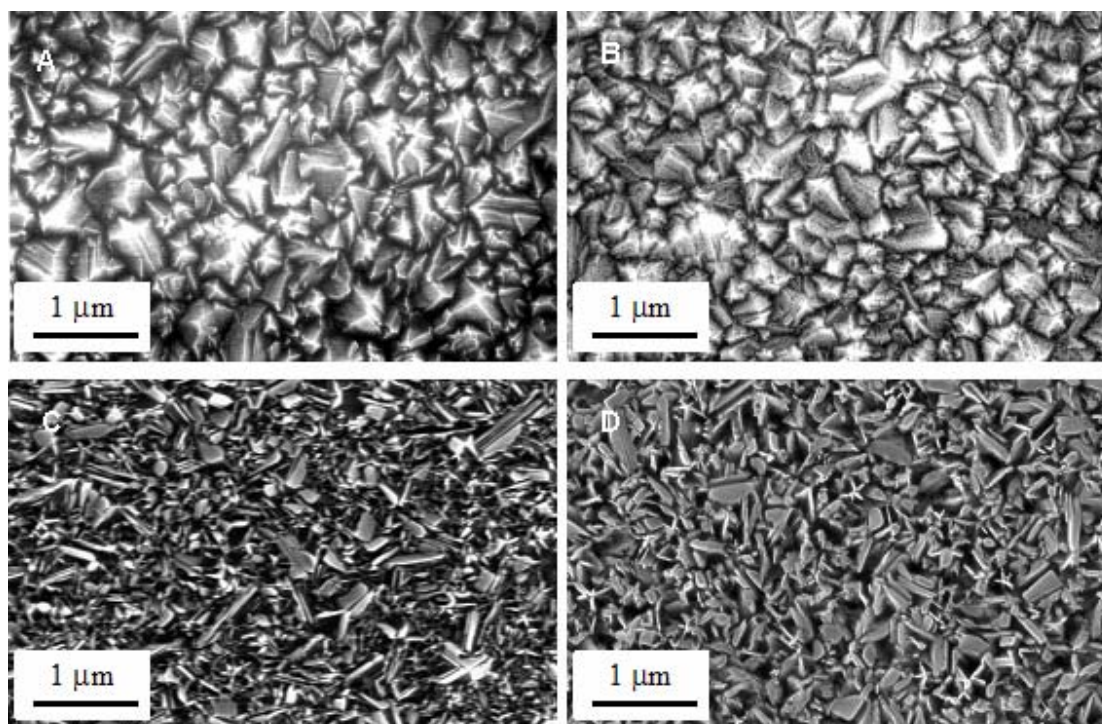

Figure 11.1: SEM micrographs of BDD surfaces (**A**) before any treatment; after electropolishing for (**B**) 256 h in 1 M H_2SO_4, (**C**) 4 h in 3 M CH_3COOH + 1 M H_2SO_4 and (**D**) 17 h in 3 M acetic acid + 1 M H_2SO_4. Applied current: i = 1 A cm^{-2}, T = 40°C.

Influence of polarization treatment on the diamond surface composition and bonds has also been studied by XPS. The XPS surveys of BDD electrode before and after electropolishing in acetic acid are shown in Figure 11.2. The survey spectrum of the non-treated electrode (curve a on Fig. 11.2) only shows a very low O *1s* peak at 532 eV in addition of the predominant C *1s* peak located at approximately 285 eV,

indicating that the surface is free of detectable impurities. After 4h of electropolishing (curve b in Fig. 11.2), the intensity of the O *1s* peak increased due to oxidation of the diamond surface. The O *1s*/C *1s* atomic concentration ratio, calculated from XPS data, have increased ten times (from 0.02 to 0.21) during polarization, indicating that this electrochemical treatment implies significant oxidation of the surface making it more hydrophobic. The appearance of peaks due to the contributions of S*2p* (169 eV) and Si*2p* (102 eV) can also be noticed, and are certainly due to some exchange with the electrolyte (H_2SO_4) or the substrate. Such evolution continues increasing the electropolishing time, as it can be seen from the survey of a BDD electrode treated during 17 h (curve c in Fig. 11.2).
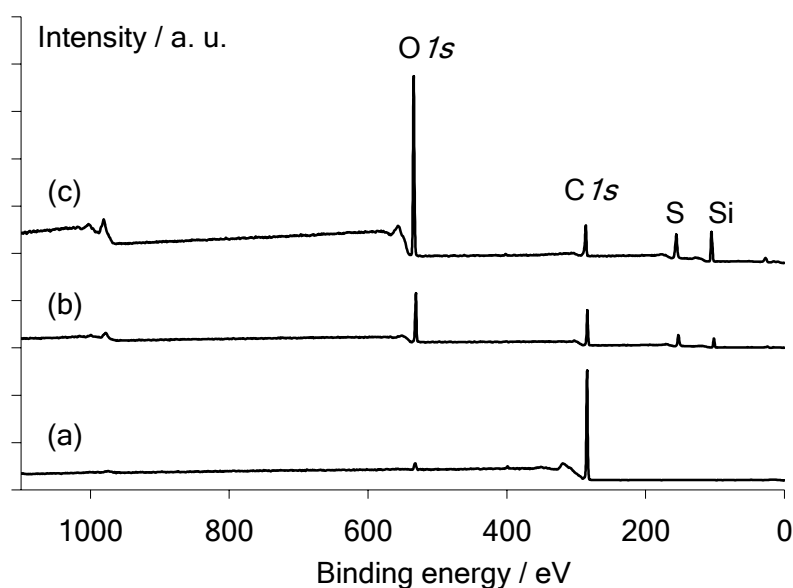

Figure 11.2: XPS spectra of a BDD electrode before (**a**), after (**b**) 4 h and (**c**) 17 h of electropolishing in 3 M CH_3COOH + 1 M H_2SO_4 at 1 A cm^{-2} and 40°C.

The surface chemical bonds were specifically investigated by the deconvolution of the C *1s* peak of BDD electrodes after different electropolishing times. Figures 11.3 and 11.4 show the deconvolved XPS C *1s* peak of a BDD electrode after 0 and 4 h of electropolishing, respectively. The C *1s* spectrum of the non-treated electrode (Fig. 11.3) exhibits a predominant sharp peak, due to simple C-C bonds, placed here for commodity at 0 eV. In addition of this peak, a second broad peak can be observed at +0.5 eV and assigned to a specific surface state that only involves carbon and hydrogen [27]. During the electropolishing process significant surface changes occur. After 4 h of polarization (Fig. 11.4) the broad peak at +0.5 eV is no longer observable. Two new peaks with shifts of +1 and +1.9 eV were observed, and can be attributed to the contributions of oxygenated functionalities such as hydroxyl and ether groups [28]. Formation of oxygenated surface groups during anodic polarization of BDD has

been reported [11]. No additional significant qualitative changes in the surface chemical bonds were observed for more prolonged polarization times (17h of electropolishing, data not shown).
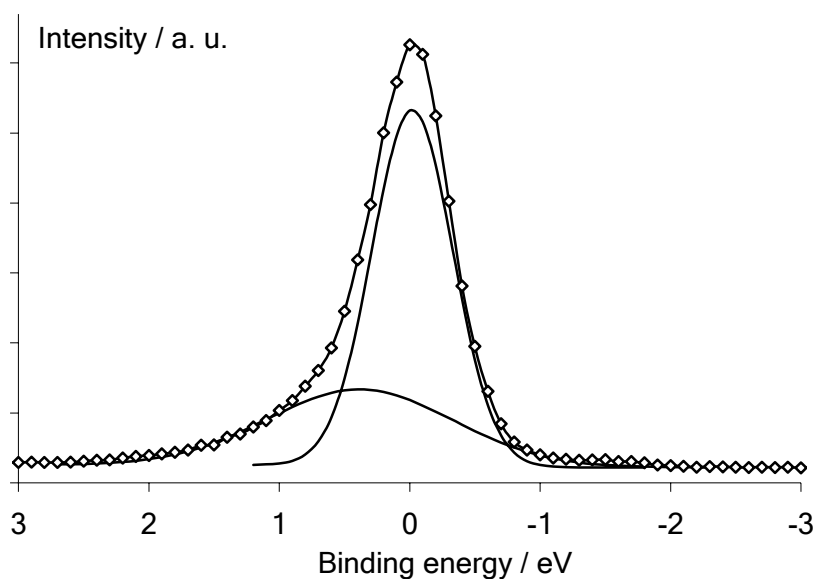

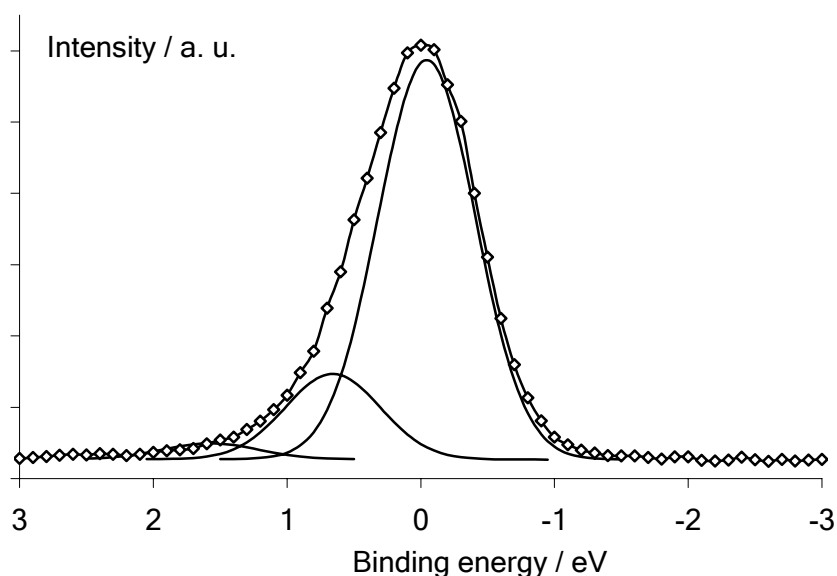**Figure 11.3**: Deconvolved XPS C *1s* peak of a non-treated BDD electrode.

Figure 11.4: Deconvolved XPS C *1s* peak of a BDD electrode after 4 h of electropolishing in 3 M CH_3COOH + 1 M H_2SO_4, at 1 A cm^{-2} and 40°C.

Cyclic voltammograms in the stability domain of the supporting electrolyte (0.5 M H_2SO_4) of a non-treated and an electropolished (4 h in 3 M CH_3COOH + 1 M H_2SO_4 at 1 A cm^{-2} and 40 °C) BDD electrode are shown in Figure 11.5. The voltammogram of the non-treated electrode (thin line in Fig. 11.5) was rather featureless, which is typical for diamond, reflecting the ideally polarization nature of the thin solid-

241

electrolyte interface. After electropolishing in acetic acid medium (4h, thick line in Fig. 11.5) it can be seen that both the current density and the total voltammetric charge significantly decreased.
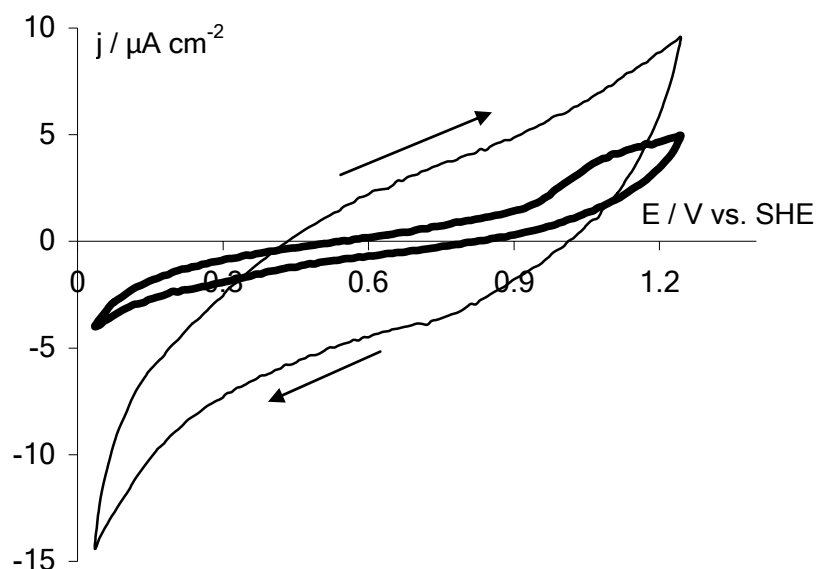

Figure 11.5: CV recorded in 0.5 M H$_2$SO$_4$ on a BDD electrode before (thin line) and after 4 h (thick line) of electropolishing in 3 M CH$_3$COOH + 1 M H$_2$SO$_4$ at 1 A cm^{-2} and 40°C. Scan rate of 100 mV s^{-1}.

The double-layer capacitance, related to the microscopic area and to the roughness of the electrode, was also evaluated by CV using Equation 11.1:

$$i_{tot} = 2\, C_{dl}\, v \tag{11.1}$$

where i_{tot} is the total anodic current density (A cm^{-2}), C$_{dl}$ is the double-layer capacitance (F cm^{-2}) and v is the scan rate (V s^{-1}). The evolution of the double-layer capacitance during the electropolishing treatment is shown in Figure 11.6. A significant decreased can be noticed in the value of the double-layer capacitance as a result of the electropolishing process. After 17 h of electropolishing the double-layer capacitance reached a value of approximately 0.9 μF cm^{-2} comparable to that of the single-crystal diamond. The decreases both in the voltammetric charge and in the double-layer capacitance result from oxidative removal by gasification of non-diamond impurities (sp^2 sites) and from etching of the surface, which was also evidenced by SEM measurements.
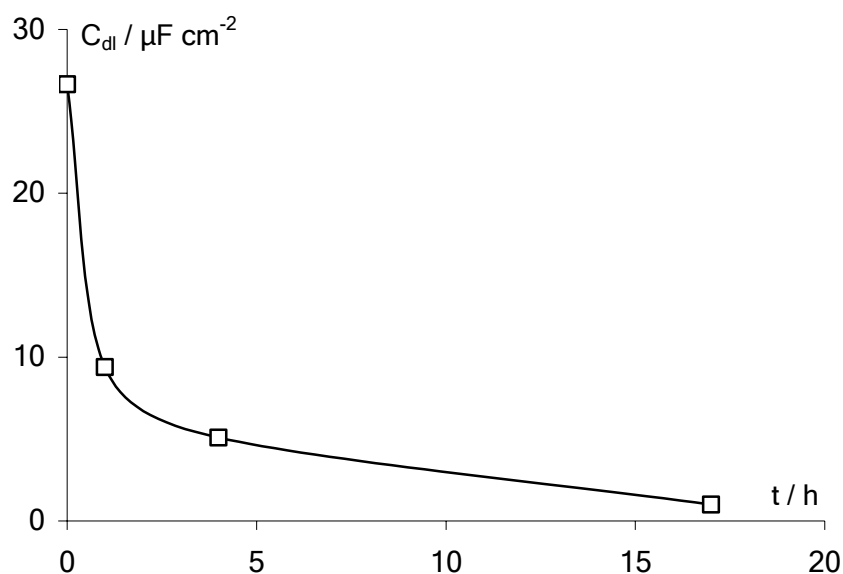
Figure 11.6: Evolution of the double layer capacitance of BDD in 0.5 M H_2SO_4 during electropolishing in 3 M CH_3COOH + 1 M H_2SO_4 at 1 A cm^{-2} and 40°C.

The electrochemical behaviour of the BDD electrode as a function of electropolishing was also investigated, in order to confirm elimination of C sp^2 surface groups, in the presence of model couples for *outer-sphere* reactions ($Fe(CN)_6^{3-}$/$Fe(CN)_6^{4-}$) and *inner-sphere* (benzoquinone/hydroquinone (BQ/HQ)) reactions. It has indeed been showed in our laboratory that non-diamond impurities on the diamond surface play a significant role in the electrochemical response of the BDD electrode [12, 29], and especially on the observed electron transfer kinetics. Figure 11.7 shows that on non-polished electrode (thin line) the $Fe(CN)_6^{3-}$/$Fe(CN)_6^{4-}$ couple is strongly irreversible (ΔE_p = 240 mV). After 4 h of electropolishing in 3 M CH_3COOH in 1 M H_2SO_4 at 1 A cm^{-2} and 40°C, the system becomes more irreversible (ΔE_p = 900 mV), as it can be seen on thick line in Fig. 11.7, indicating a slower electron transfer. This is in agreement with literature results [8, 30] and have been attributed to changes in surface functional groups and removal of non-diamond (sp^2) carbon impurities. Even for an *inner-sphere* reaction, there is a correlation between non-diamond surface impurities and the electrode response as it was shown that electropolishing of the diamond electrode surface implies increase in separation between anodic and cathodic peaks of the BQ/HQ couple (data not shown).
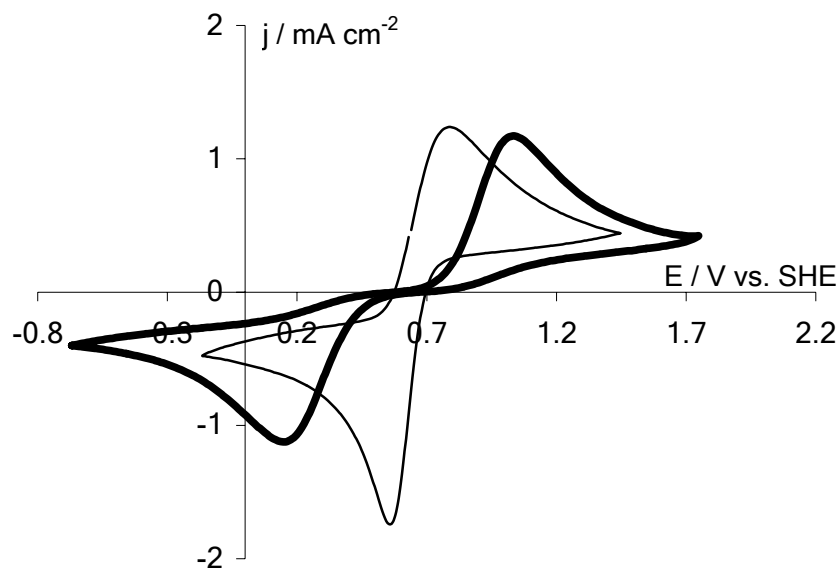
Figure 11.7: CV recorded in 0.5 M H_2SO_4 + 10 mM $Fe(CN)_6^{3-}/Fe(CN)_6^{4-}$ on a BDD electrode before (thin line) and after 4 h (thick line) of electropolishing in 3 M CH_3COOH + 1 M H_2SO_4 at 1 A cm^{-2} and 40°C, scan rate of 100 mV s^{-1}.

2.1.2. BDD fluorination

Fluorination of the BDD electrodes was directly conducted at the end of the diamond deposition (HF-CVD) procedure. F-BDD electrodes were obtained by the postdeposition treatment of BDD films in a radio-frequency (rf, 14.56 MHz) plasma reactor using a CF_4-He mixture (ratio 2:1) as precursor atmosphere. This treatment was applied during 5 minutes at a plasma power of 100 W under a constant pressure of 8 x 10^{-3} mbar. The SEM micrographs of a F-BDD electrode (data not shown) are essentially identical to those taken from a non-fluorinated surface (see Fig. 11.1.A. for instance). Therefore fluorination has no significant effect on the electrode morphology.

The XPS spectra of a CVD diamond film before and after fluorination are shown in Figure 11.8. C *1s* and O *1s* peaks at 285 and 532 eV, respectively, are present on the spectra of both the two types of diamond films. The F *1s* peak, located at 689 eV, is clearly observable on spectrum B of the F-BDD electrode, confirming the surface fluorination after the plasma surface treatment. Quantitative analysis has revealed that the atomic concentration of fluorine was of the order of 6 %, and that the surface oxygen concentration was not changed by the fluorination. This indicates that oxygen-containing groups were not affected by the fluorination.
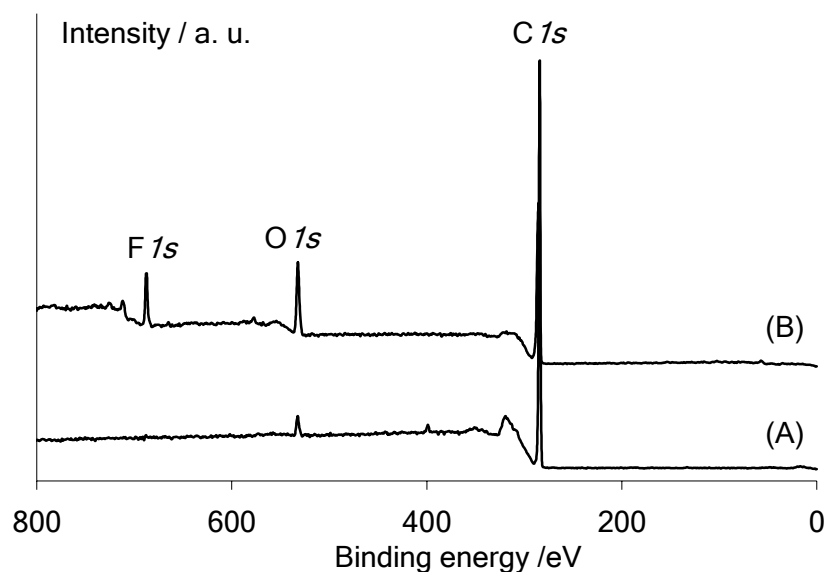
Figure 11.8: XPS spectra of BDD electrode before (A) and after fluorination (B).

Surface chemical bonds have also been investigated by XPS. The result of the deconvolution of the C *1s* peak of a F-BDD electrode, is shown in Figure 11.9. It can be deduced from this picture that the C *1s* peak in the whole signal is constituted by three different contributions. Besides the main peak located at 285 eV, due to C-C and C-H bonds [31], it is possible to observe two other peaks at higher binding energies, which correspond to C-CF (287 eV) and C-F (289 eV) bonds [32]. There was no evidence for the presence of C-F$_2$ (291.9 eV) or more fluorinated groups at the surface.
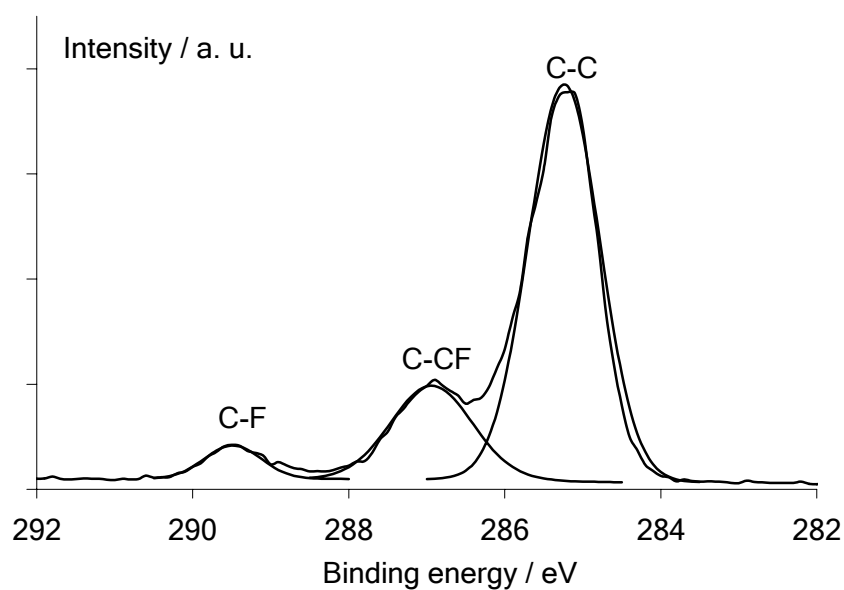

Figure 11.9: Deconvolved C *1s* XPS peak of fluorinated BDD.

Figure 11.10 shows the voltammograms corresponding to the non-fluorinated (thin line) and the F-BDD (thick line) electrodes recorded in 1 M HClO$_4$ at 100 mV s^{-1}. As previously reported in literature [33, 34], the BDD electrode exhibits a wide potential window between -0.5 and 2.3 V vs. SHE without significant water decomposition. This suggests that the BDD surface has weak adsorption properties and undergoes little interaction with dissolved species. Fluorination does not imply significant modification of the electrochemical behaviour of the electrode in the anodic region as no difference can be observed in the oxygen evolution overpotential. However the hydrogen evolution overpotential was appreciably shifted to a more negative value of approximately -1.25 V vs. SHE. The inhibiting influence for hydrogen evolution can be related to the presence of carbon-fluorine bonds that are making the surface more hydrophobic. Therefore fluorination decreases the adsorption strength of both water molecules and atomic hydrogen on the electrode surface, steps that are essential in the hydrogen evolution reaction.
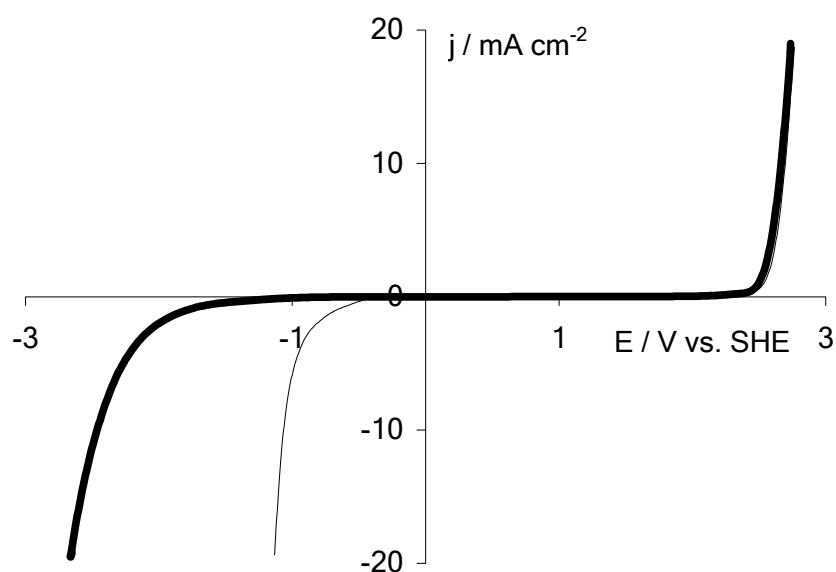

Figure 11.10: Linear potential sweep voltammograms of a BDD (thin line) and F-BDD (thick line) electrode recorded in 1 M HClO$_4$ at 100 mV s^{-1}.

Due to the very negative overpotential needed for hydrogen evolution, F-BDD can be expected to be an excellent cathode for reactions that require very negative potentials such as deposition of some metals or reduction of nitrate. Therefore the fluorinated diamond electrode has been tested in such applications. For instance the deposition of nickel (E^0 = -0.25 V vs. SHE) that is impeached by hydrogen evolution on many electrode materials is feasible on F-BDD. Figure 11.11 shows cathodic polarization curves recorded at 100 mV s^{-1} on a F-BDD electrode in 1 M HClO$_4$ solutions containing different concentrations of NiSO$_4$. in the presence of Ni^{2+} ions,

the cathodic current density at a given potential was significantly higher than the background (curve a in Fig. 11.13) and this was attributed to the reduction of nickel as indicated in Equation 11.2:
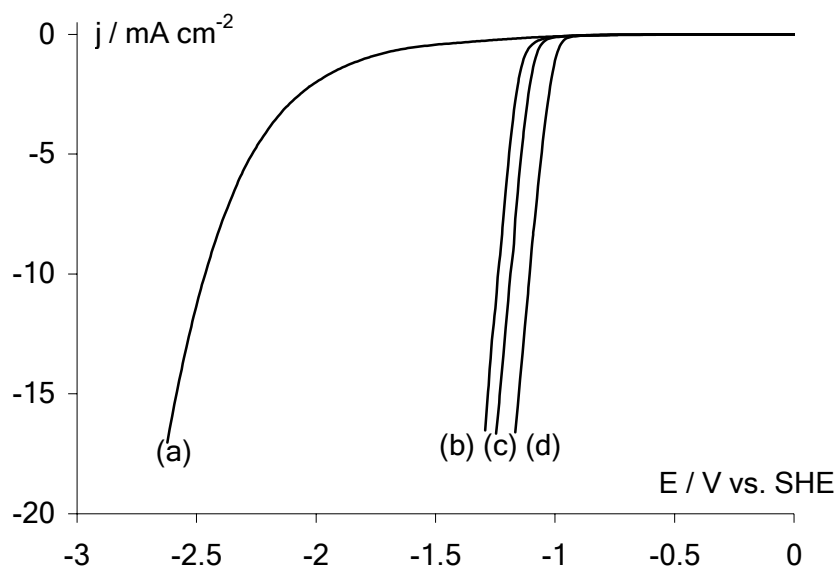
$$Ni^{2+} + 2e^- \rightarrow Ni \qquad\qquad (11.2)$$

Figure 11.11: Linear potential sweep voltammetry of F-BDD electrode in 1 M HClO$_4$ with different NiSO$_4$ concentrations. [NiSO$_4$] = 0 (a), 0.05 (b), 0.1 (c) and 0.5 M (d); scan rate of 100 mV s^{-1}.

Moreover, it can be seen from CV recorded in 0.05 M NiCl$_2$ solution in 1 M HClO$_4$ (thick line in Fig. 11.12) that the current at the reverse scan was higher than in the forward one, indicating an increase in the electrode area due to nickel deposition on the surface during the forward scan. Similar behaviour was also observed in the case of zinc (data not shown).
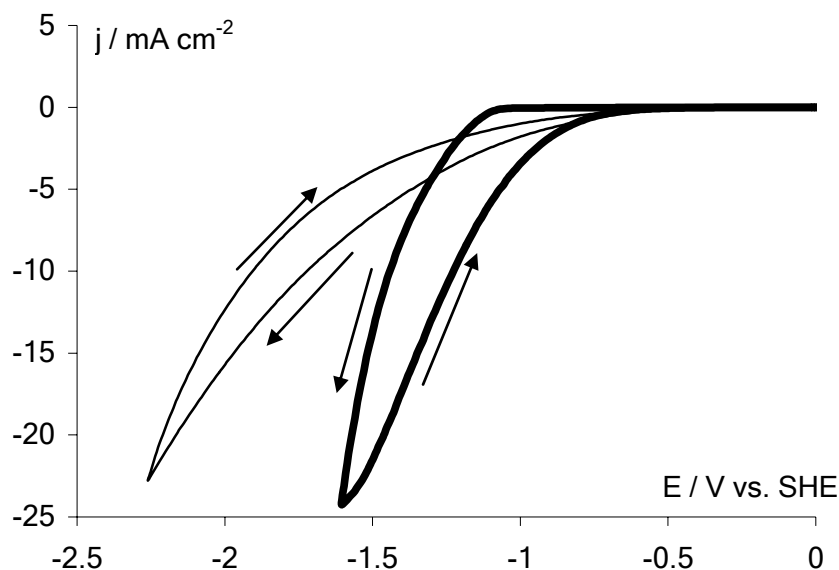
Figure 11.12: CV of a F-BDD electrode in 1 M HClO$_4$ with different NiCl$_2$ concentrations. [NiCl$_2$] = 0 (thin line) and 0.05 M (thick line); scan rate of 100 mV s^{-1}.

In order to summarize, it can be said that the fluorinated diamond electrode exhibit a more negative overpotential for hydrogen evolution than the non-fluorinated one, allowing its use for reactions that need highly cathodic potentials.

2.2. Dendrimeric synthesis of Pt nanoparticles

Some preliminary tests have been done on Pt synthesis using the dendrimeric technique. The synthesis of Pt particles via the dendrimeric route was performed according to a published procedure [4]. A polyamidoamine (PAMAM) amine-terminated dendrimer of 4th generation (G$_4$-NH$_2$) diluted at 10 % wt. in methyl alcohol (Aldrich Chemicals) was used as dendrimer source. The complex structure of such kind of polymer is illustrated in Figure 11.13. It looks like a dendrite and exhibits a lot of channels and cavities where for instance metallic ions can complex.
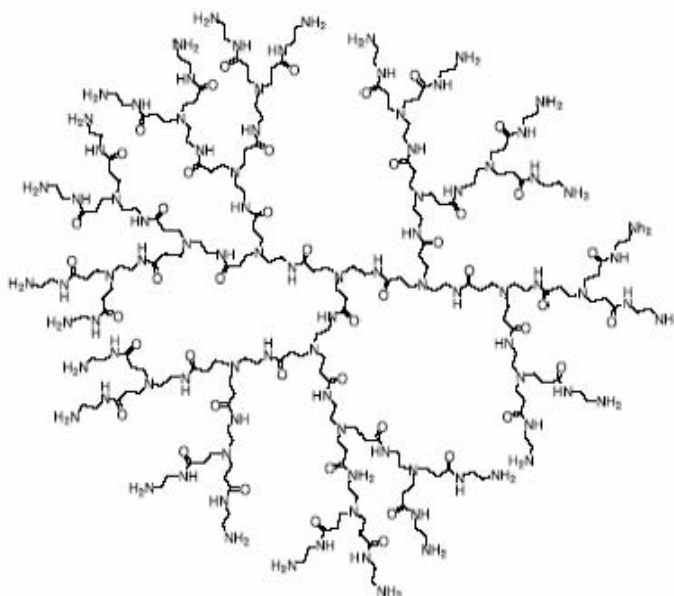
Figure 11.13: Structure of an amine-terminated PAMAM dendrimer [35].

Practically, the methyl alcohol solvent was removed and the quantity of dendrimer necessary to yield a 2.5-50 μM solution was diluted in ultra-pure water (Milli-Q). The pH of the solution was adjusted to 5 by addition of HCl in order to favour complexion of Pt^{4+} ions with internal NH_2 groups of the dendrimer rather than external NH_2 terminations. A solution of 0.1 M H_2PtCl_6 in ultra-pure water was added to the dendrimeric solution in order to yield a Pt^{4+}/G_4-NH_2 molar ratio ranging from 30 to 60 (labelled Pt_{30} and Pt_{60}). This mixture was then continuously stirred during 4 days. Finally a 0.1-0.5 M solution of $NaBH_4$ (Aldrich) in ultra-pure water was added (quantity necessary to have the reducing agent twenty times in excess) in order to reduce the complex ion and the pH of the solution was adjusted to 8. This procedure results in the formation of dendrimer-encapsulated Pt nanoparticles (Pt DENs), and its schematic principle is given in Figure 11.14. Similarly than the microemulsion method, the synthesis of nanoparticles within dendrimer is a way providing compartmentalized and isolated nanoreactors for the reduction of metallic precursors.
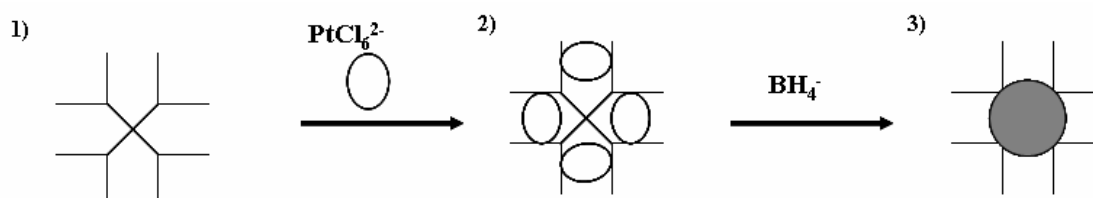

Figure 11.14: Schematic principle of Pt nanoparticles synthesis following the dendrimeric route. Steps of the procedure: **1)** mixing of a dendrimer solution with a metallic ion solution to yield a **2)** complex ion, reduced by addition of solid $NaBH_4$ to give a **3)** dendrimer-encapsulated nanoparticle.

Figure 11.15 shows a TEM micrograph of Pt_{30} nanoparticles synthesis using the dendrimeric method. It can be seen on this image that particles are well isolated (due to the high repulsive forces between NH_2 terminations of the polymers) and of well-defined spherical shape. Moreover the size distribution of such particles (based on measurements carried out on more than 100 individual particles) shows that the diameter of such particles is limited to the 1-4 nm with very narrow distribution. The narrower distribution of dendrimer-synthesized nanoparticles compare to microemulsion-synthesized ones reflects the higher degree of uniformity of the dendrimers compare to inverse micelles in microemulsions. Increasing the Pt^{4+}/G_4-NH_2 molar ratio up to a value of 60 only results in the increase of the mean size of the particles and displacement of the size distribution to slightly higher values of diameter (data not shown).
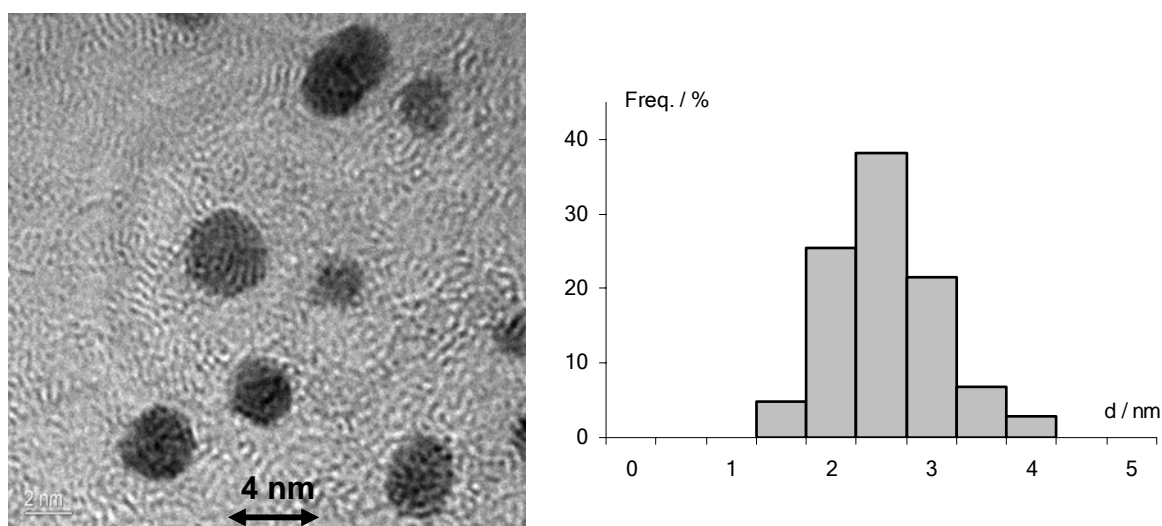

Figure 11.15: TEM micrograph and size distribution of Pt nanoparticles synthesized via the dendrimeric route. Pt^{4+}/G_4-NH_2 ratio = 30.

In spite of the very promising size characteristics of Pt DENs, the electrochemical and electrocatalytic characterization of these particles was problematic. Two main issues were encountered: *(i)* the high hydrophilicity of dendrimers that made the deposit unstable on BDD and *(ii)* the "closed" structure of these polymers, which only allow the passage of electroactive species through small channels. The first problem could be solved stabilizing the Pt DENs deposit on BDD by an additional Nafion® layer as it was ever done in the case of microemulsion-synthesized Pt nanoparticles [36]. The second problem is quite more complicated to solve, and this is the reason why, to the best o our knowledge, DENs have been mainly used in the catalysis of gas-phase reactions [37-39]. Some attempts to remove these encapsulating polymers have therefore been done. It was tried to oxidize the dendrimers by heat

250

treatment in air at 425°C during 4 h followed by reduction at 100°C in hydrogen atmosphere during 1 h to avoid irreversible Pt oxides formation [40]. Figure 11.16 shows CV of Pt_{60} dendrimer-synthesized nanoparticles deposited on BDD in pure supporting electrolyte. These voltammograms exhibit the well-known H adsorption-desorption features (successive peaks at 0.05-0.3 V vs. SHE) attributable to Pt. However it appeared that this treatment did not yield reproducible results and the CV shown in Fig. 11.17 were only obtained a few times among the entire tests performed using the same conditions. Moreover no peaks for alcohols (methanol or ethanol) oxidation could be observed. This seems to indicate that the encapsulating dendrimers were not sufficiently removed from the nanoparticles surface, impeaching the adsorption of electroactive species on the catalytic sites. Therefore some additional oxidative treatments must be performed in order to completely remove the dendrimers and to obtain a clean and available catalytic surface. Such treatments can be for instance hydrolysis of dendrimers within the Pt DENs solution, dendrimers electrochemical oxidation or heat treatments with optimized temperature and time conditions. In addition of complete removal of dendrimers, these treatments should also avoid the formation of irreversible Pt oxides or aggregation of particles.
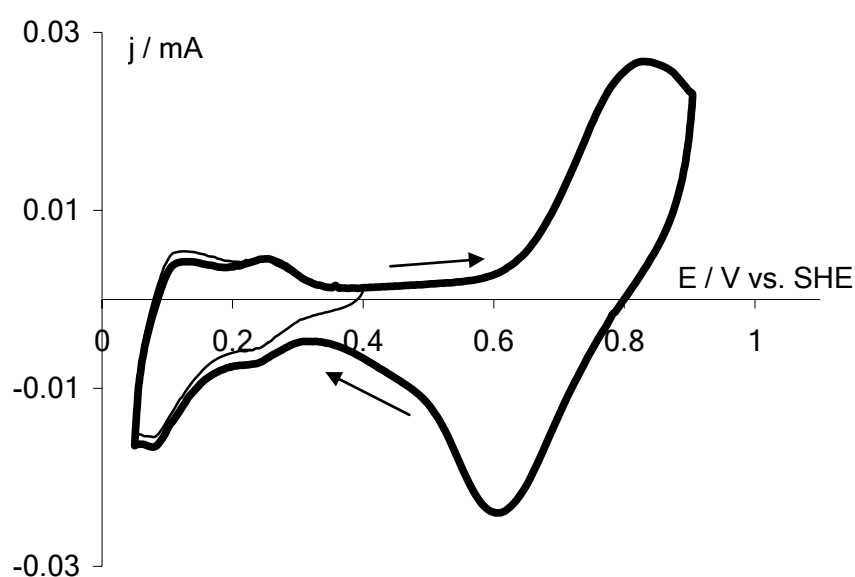
Figure 11.16: CV of Nafion®-coated BDD-supported Pt nanoparticles synthesized via the dendrimeric route (Pt^{4+}/G_4-NH_2 ratio = 60). Post-treatment: calcination at 425°C during 4 h followed by reduction at 100°C in H_2 atmosphere during 1 h. Recorded in 1 M $HClO_4$ at 50 mV s^{-1} and 25°C.

2.3. New catalysts formulations

Another way that is currently followed in order to increase fuel cells performances up to levels that would allow commercial applications is the development of new

catalyst formulations. Considerable efforts have indeed been done in the development of Pt/M (M = Ru, Sn, Mo...) electrocatalysts but there are still some severe limitations to their use such as the dissolution of the alloying metal when operating under acidic conditions. Consequently some new catalysts are needed to avoid these problems. For instance the development of "Pt skin layers" has been recently reported by Watanabe et al. [41, 42]. Briefly, it consists in alloying Pt with a second transition metal (including non-precious ones such as Fe), which forms Pt skin layers as the result of the latter dissolution and the reconstruction of remaining Pt atoms. It has been claimed that the modification of the electronic structure of the skin layer by the underlying alloy results in an important enhancement of the electrocatalytic activity toward methanol oxidation, but also toward O_2 reduction [41] and CO oxidation [42]. However these are at the moment preliminary results that have to be completed.

A way that is also currently studied is the development of non-noble metal catalysts, especially for working in basic media. The use of Pt-free catalysts has indeed the great advantage of significantly decrease the cost of the fuel cell anode. Moreover it was showed that platinum is strongly passivated during ethanol oxidation in alkaline media [43] so that alternative catalysts are required for this purpose. Therefore ethanol oxidation has been studied in 1 M KOH on titanium promoted by RuO_2/Ni system and GC coated by RuNi nanoparticles [44, 45]. However these catalysts have only exhibited low activities. Nevertheless in some recent work it was showed that RuNi catalysts (dispersed Ru decorated by Ni oxides) display good specific activity toward ethanol oxidation in concentrated KOH [46]. The optimum catalyst composition was found to be 20-40 at. % in Ni, and the change of ruthenium properties in RuNi as compared to pure Ru was pointed out. However works on DAFC operating with basic media are quite scarce at the moment, and the difficulty in such systems is that CO_2 is accumulated in the anodic fuel cell compartment (carbonate formation). Nevertheless it seems that it could be a interesting approach for further developments of the DAFC technology.

3. CONCLUSIONS

During this part of the thesis, Pt nanoparticles have been synthesized by the dendrimeric method and the BDD electrode surface has been treated by electropolishing or plasma fluorination. The influence of such treatments on the electrode properties was studied by electrochemical measurements, XPS and SEM.

Anodic polarization (1 A cm^{-2} at 40°C in 3 M CH_3COOH + 1 M H_2SO_4) of the BDD electrode resulted in etching and smoothing of the surface, as revealed by SEM

micrographs. Moreover the surface was enriched in oxygen-containing groups such as hydroxyl and ether groups. Removal of non-diamond (C sp^2) surface impurities was confirmed by decrease in double-layer capacitance of the electrode in pure electrolyte (H$_2$SO$_4$ 0.5 M) and by increase of irreversibility of both *outer-sphere* and *inner-sphere* model redox couples. Fluorination, which was realized by postdeposition plasma treatment under CF$_4$-He precursor atmosphere, had no influence on the surface morphology of the electrode. However fluorine is well present on the surface and is involved in C-CF and C-F bond types. The most remarkable effect of fluorination on the diamond electrode is an appreciable shift of the overpotential for hydrogen evolution to more negative values. This new property was used to perform on the F-BDD cathode reactions that require negative potentials to take place and that are impeached on most electrodes due to hydrogen evolution. F-BDD electrode has been here successfully used to realize the deposition of nickel. The use of such BDD electrodes as substrates for the electrochemical study of Pt-based nanoparticles would be of great interest as many authors have recently claimed the importance of the substrate surface state in the electrochemical and electrocatalytic response of supported nanoparticles. It was for instance showed that electrochemical treatment of a GC substrate (oxidation at 2 V vs. SCE during 95 s.) results in an enhancement of more than one order of magnitude of the electrocatalytic activity of supported Pt [3].

Although the dendrimeric method allows the synthesis of true Pt nanoparticles (1.5-4 nm in diameter with very narrow size distribution), due to the large degree of uniformity of dendrimers, it has been observed that such nanoparticles were not efficient for electrocatalytic applications. It is believed that this is because the dendrimer matrix that encapsulates the particle makes it inaccessible to the electroactive species to be oxidized. Therefore it appears necessary to remove the dendrimer once the particles synthesis is achieved. For this purpose some preliminary tests have been conducted, however the calcination conditions that were applied were not sufficient to obtain a completely free catalytic surface and reproducible results. The use of more severe calcination conditions would certainly lead to particles aggregation that is a non-desired effect. So that other dendrimer removal ways must be considered and hydrolysis by a more acidic solution could be tested. The use of such nanoparticles in electrocatalysis would be interesting in the sense that they exhibit lower dimensions and narrower size distribution than microemulsion-synthesized ones.

4. REFERENCES

[1]   M. Panizza, G. Siné, I. Duo, L. Ouattara, Ch. Comninellis, *Electrochem. Solid-State Lett.* **6** (2003), D17.

[2]   G. Siné, L. Ouattara, M. Panizza, Ch. Comninellis, *Electrochem. Solid-State Lett.* **6** (2003), D9.

[3]   V. M. Jovanovic, S. Terzic, A. V. Tripkovic, K. D. Popovic, J. D. Lovic, *Electrochem. Comm.* **6** (2004), 1254.

[4]   H. Ye, R. W. J. Scott, R. M. Crooks, *Langmuir* **20** (2004), 2915.

[5]   C. G. Vayenas, S. Bebelis, C. Pliangos, S. Brosda, D. Tsiplakides, *Electochemical activation of catalysis. Promotion, Electrochemical Promotion, and Metal-Support Interactions.*, Kluwer Academic / Plenum Publishers, New York (2001).

[6]   A. S. Aricò, V. Antonucci, P. L. Antonucci, in: A. Wieckowski, E. R. Savinova, C. G. Vayenas (Eds.), *Catalysis and Electrocatalysis at Nanoparticle Surfaces*, Marcel Dekker, New York (2003), p. 613.

[7]   T. N. Rao, D. A. Tryk, K. Hashimoto, A. Fujishima, *J. Electrochem. Soc.* **146** (1999), 680.

[8]   M. C. Granger, M. Witek, J. Xu, J. Wang, M. Hupert, A. Hanks, M. D. Koppang, J. E. Butler, G. Lucazeau, M. Mermoux, J. W. Strojek, G. M. Swain, *Anal. Chem.* **72** (2000), 3793.

[9]   Y. Einaga, R. Sato, H. Olivia, D. Shin, T. A. Ivandini, A. Fujishima, *Electrochim. Acta* **49** (2004), 3989.

[10]   H. B. Suffredini, V. A. Pedrosa, L. Codognoto, S. A. S. Machado, R. C. Rocha-Filho, L. A. Avaca, *Electrochim. Acta* **49** (2004), 4021.

[11]   C. H. Goeting, F. Marken, A. Gutierrez-Sosa, R. G. Compton, J. S. Foord, *Diamond Rel. Mater.* **9** (2000), 390.

[12]   I. Duo, A. Fujishima, Ch. Comninellis, *Electrochem. Comm.* **5** (2003), 695.

[13]   S. Ferro, A. De Battisti, *Electrochim. Acta* **47** (2002), 1641.

[14]   D. Gandini, E. Mahé, P.-A. Michaud, W. Haenni, A. Perret, Ch. Comninellis, *J. Appl. Electrochem.* **30** (2000), 1345.

[15]   A. P. Malshe, B. S. Park, W. D. Brown, H. A. Naseem, *Diamond Rel. Mater.* **8** (1999), 1198.

[16]   J. A. Weima, J. von Borany, R. Grötzschel, W. R. Fahrner, *J. Electrochem. Soc.* **149** (2002), G301.

[17]   S. Tezuka, M. Yoshikawa, *New Diamond* **17** (1990), 36.

[18]   M. Rothschild, C. Arnone, D. J. Ehrlich, *J. Vac. Sci. Technol. B* **4** (1986), 310.

[19] V. N. Tokarev, J. I. B. Wilson, M. G. Jubber, P. John, D. K. Milne, *Diamond Rel. Mater.* **4** (1995), 169.

[20] D. Landolt, *Electrochim. Acta* **32** (1987), 1.

[21] O. Piotrowski, C. Madore, D. Landolt, *Electrochim. Acta* **44** (1999), 3389.

[22] L. G. Jacobsohn, D. F. Franceschini, M. E. H. Maia da Costa, F. L. Freire Jr., *J. Vac. Sci. Technol. A* **18** (2000), 2230.

[23] F. L. Freire Jr., M. E. H. Maia da Costa, L. G. Jacobsohn, D. Franceschini, *Diamond Rel. Mater.* **10** (2001), 125.

[24] J. A. Theil, *J. Vac. Sci. Technol. B* **17** (1999), 2397.

[25] R. S. Butter, D. R. Waterman, A. H. Lettington, R. T. Ramos, E. J. Fordham, *Thin Solid Films* **311** (1997), 107.

[26] H. B. Martin, A. Argoitia, J. C. Angus, U. Landau, *J. Electrochem. Soc.* **146** (1999), 2959.

[27] L. Ley, R. Graupner, J. B. Cui, J. Ristein, *Carbon* **37** (1999), 793.

[28] D. D. Haasz, S. Chiu, J. E. Pierre, *J. Vac. Sci. Technol. A* **14** (1996), 184.

[29] I. Duo, *Control of electron transfer kinetics at boron-doped diamond electrodes by specific surface modification*, PhD Thesis, Ecole Polytechnique Fédérale de Lausanne, (2003).

[30] F. Marken, C. A. Paddon, D. Asogan, *Electrochem. Comm.* **4** (2002), 62.

[31] P. Merel, M. Tabbal, M. Chaker, S. Moisa, J. Margot, *Appl. Surf. Sci.* **136** (1998), 105.

[32] S. Agraharam, D. W. Hess, P. A. Kohl, S. A. Bidstrup Allen, *J. Vac. Sci. Technol. A* **17** (1999), 3265.

[33] Y. V. Pleskov, in: R. C. Alkire, D. M. Kolb (Eds.), *Advances in Electrochemical Science and Engineering*, Wiley-VCH, Weinheim (2002), p. 209.

[34] Y. V. Pleskov, *Russ. Chem. Rev.* **68** (1999), 381.

[35] F. Aulenta, W. Hayes, S. Rannard, *Eur. Polymer J.* **39** (2003), 1741.

[36] G. Siné, Ch. Comninellis, *Electrochim. Acta* **50** (2005), 2249.

[37] R. M. Crooks, M. Zhao, L. Sun, V. Chechik, L. K. Yeung, *Acc. Chem. Res.* **34** (2001), 181.

[38] H. Lang, R. A. May, B. L. Iversen, B. D. Chandler, *J. Am. Chem. Soc.* **125** (2003), 14832.

[39] R. W. J. Scott, A. K. Datye, R. M. Crooks, *J. Am. Chem. Soc.* **125** (2003), 3708.

[40] D. S. Deutsch, G. Lafaye, D. Liu, B. Chandler, C. T. Williams, M. D. Amiridis, *Catal. Lett.* **97** (2004), 139.

[41] T. Toda, H. Igarashi, M. Watanabe, *J. Electroanal. Chem.* **460** (1999), 258.

[42]   H. Uchida, H. Ozuka, M. Watanabe, *Electrochim. Acta* **47** (2002), 3629.

[43]   S.-M. Park, N. Chen, N. Doddapaneni, *J. Electrochem. Soc.* **142** (1995), 40.

[44]   J.-W. Kim, S.-M. Park, *J. Electrochem. Soc.* **146** (1999), 1075.

[45]   J.-W. Kim, S.-M. Park, *Electrochem. Solid-State Lett.* **3** (2000), 385.

[46]   M. R. Tarasevich, Z. R. Karichev, V. A. Bogdanovskaya, E. N. Lubnin, A. V. Kapustin, *Electrochem. Comm.* **7** (2005), 141.

Curriculum Vitae

Guillaume Siné
Rue du Centre 3
CH-1030 Bussigny

Personal information

Born on November 18th 1979, in Hyères, France
Nationality: French
Single

Education

1996-2002	University Bordeaux I, France
2002-2005	École Polytechnique Fédérale de Lausanne, Switzerland - Institute of Chemical Science and Engineering - Group of Electrochemical Engineering

Academic degrees

1999	DEUG, Chemistry and Physical Chemistry (University Bordeaux I, France)
2000	Licence, Physical Chemistry (University Bordeaux I, France)
2001	Maîtrise, Physical Chemistry (University Bordeaux I, France)
2002	DEA, Structures, Materials and Molecular Processes (University Bordeaux I, France)
2005	Ph. D, Investigation of Pt-Based Nanoparticles on Boron-Doped Diamond Substrate for Applications in Electrocatalysis (École Polytechnique Fédérale de Lausanne, Switzerland).

Professional experience

2001	Chemistry Department, University of Reading (UK). Training period of six months.
2002	Ecole Nationale Supérieure de Chimie-Physique de Bordeaux (ENSCPB). Training period of six months.

Publications

G. Siné, L. Ouattara, M. Panizza, Ch. Comninellis, *Electrochemical Behavior of Fluorinated Boron-Doped Diamond*, Electrochem. Solid-State Lett. **6**, D9 (2003).

M. Panizza, G. Siné, I. Duo, L. Ouattara, Ch. Comninellis, *Electrochemical Polishing of Boron-Doped Diamond in Organic Media*, Electrochem. Solid-State Lett. **6**, D17 (2003).

G. Siné, Ch. Comninellis, *Boron-Doped Diamond Supported Pt Nanoparticles Synthesized in Compartmentalized Nanoreactors for Electrocatalysis*, Grundlagen und Anwendungen der Elektrochemishen Oberflächentechnik, GDCh Monographie Bd. 32, 185 (2005).

G. Siné, Ch. Comninellis, *Nafion®-Assisted Deposition of Microemulsion-Synthesized Platinum Nanoparticles on BDD: Activation by Electrogenerated ˙OH Radicals*, Electrochim. Acta **50**, 2249 (2005).

Oral presentations

<u>G. Siné</u>, Ch. Comninellis, *Boron-Doped Diamond Supported Pt Nanoparticles Synthesized in Compartmentalized Nanoreactors for Electrocatalysis*, Grundlagen und Anwendungen der Elektrochemishen Oberflächentechnik, GDCh Meeting, Graz (Austria), 08 – 10 September 2004.

<u>Ch. Comninellis</u>, G. Siné, I. Duo, B. El Roustom, *Deposition of Nanoparticles on Boron-Doped Diamond Electrodes for Electrocatalysis*, 21st Century COE KEIO-LCC International Symposium, KEIO University (Japan), 4 - 5 March 2005.

<u>G. Siné</u>, Ch. Comninellis, *Caractérisation Électrochimique et Activité Électrocatalytique de Nanoparticules Bimétalliques à Base de Pt Déposées sur l'Électrode BDD*, Journées d'Électrochimie 2005, St-Malo (France), 5 – 8 July 2005.

Posters

B. El Roustom, G. Siné, G. Fóti, Ch. Comninellis, *Préparation de Nanoparticules d'Au et d'Au-Pt sur des Électrodes BDD*, Journées d'Électrochimie 2005, St-Malo (France), 5 – 8 July 2005.